

Chipless RFID Sensor Systems for Structural Health Monitoring

Adi Mahmud Jaya Marindra

A thesis submitted for the degree of Doctor of Philosophy



Intelligent Sensing and Communication Research Group

School of Engineering

Newcastle University

September 2020

CERTIFICATE OF ORIGINALITY

This is to certify that all the works submitted in this thesis are my own works except as specified in acknowledgments. Neither the work nor the thesis has been submitted to any other institution for another degree. I am responsible for all the works in this thesis.

A handwritten signature in black ink, appearing to read 'Adi Mahmud Jaya Marindra', with a stylized flourish at the end.

Adi Mahmud Jaya Marindra

Abstract

Defects in metallic structures such as crack and corrosion are major sources of catastrophic failures, and thus monitoring them is a crucial issue. As periodic inspection using the non-destructive testing and evaluation (NDT&E) techniques is slow, costly, limited in range, and cumbersome, novel methods for in-situ structural health monitoring (SHM) are required. Chipless radio frequency identification (RFID) is an emerging and attractive technology to implement the internet of things (IoT) based SHM. Chipless RFID sensors are not only wireless, passive, and low-cost as the chipped RFID counterpart, but also printable, durable, and allow for multi-parameter sensing.

This thesis proposes the design and development of chipless RFID sensor systems for SHM, particularly for defect detection and characterization in metallic structures. Through simulation studies and experimental validations, novel metal-mountable chipless RFID sensors are demonstrated with different reader configurations and methods for feature extraction, selection, and fusion. The first contribution of this thesis is the design of a chipless RFID sensor for crack detection and characterization based on the circular microstrip patch antenna (CMPA). The sensor provides a 4-bit ID and a capability of indicating crack width and orientation simultaneously using the resonance frequency shift. The second contribution is a chipless RFID sensor designed based on the frequency selective surface (FSS) and feature fusion for corrosion characterization. The FSS-based sensor generates multiple resonance frequency features that can reveal corrosion progression, while feature fusion is applied to enhance the sensitivity and reliability of the sensor. The third contribution deals with robust detection and characterization of crack and corrosion in a realistic environment using a portable reader. A multi-resonance chipless RFID sensor is proposed along with the implementation of a portable reader using an ultra-wideband (UWB) radar module. Feature extraction and selection using principal component analysis (PCA) is employed for multi-parameter evaluation.

Overall, chipless RFID sensors are small, low-profile, and can be used to quantify and characterize surface crack and corrosion undercoating. Furthermore, the multi-resonance characteristics of chipless RFID sensors are useful for integrating ID encoding and sensing functionalities, enhancing the sensor performance, as well as for performing multi-parameter analysis of defects. The demonstrated system using a portable reader shows the capability of defects characterization from a 15-cm distance. Hence, chipless RFID sensor systems have great potential to be an alternative sensing method for in-situ SHM.

I dedicate this thesis to my loving parents, wife, and daughter

Acknowledgment

First and foremost, the highest praise and gratitude be to the Almighty Allah, and blessings and peace be upon His prophet Muhammad SAW. I thank Allah for the strength, health, and blessings bestowed upon me during this long but fulfilling pathway.

I am indebted to my home country and my sponsor, Indonesia Endowment Fund for Education (LPDP). I would like to thank my home institution, Institut Teknologi Kalimantan (ITK), for all the supports. I thank the former vice-rector of ITK, Subchan, Ph.D., my former supervisors, Dr. Pornanong Pongpaibool from NECTEC Thailand and Dr. Sathaporn Promwong from KMITL Thailand, for their help in the process of my Ph.D. applications.

I would like to express my heartfelt gratitude to my respected supervisor, Professor Gui Yun Tian, for his concerns, advice, and encouragement. He has been giving me constant support through brainstorming and opportunities since I started my study with him. I thank him for showing me his dedication to research, discipline, passion, and wisdom. It is indeed a great privilege to have been one of Prof Tian's students.

Superb colleagues and people have surrounded me in Newcastle. I would like to acknowledge my lab mates: Ruslee Sutthaweekul, Denis Ona, Mohammed Buhari, Ali Sunny, Kongjing Li, Aobo Zhao, Chaoqing Tang, Xiaotian Chen, Monika Roopak, Yachao Ran, Junzhen Zhu, Qiuji Yi, Lawal Daura, Jumamah Abdulwali, and other colleagues in Newcastle University. I would like to thank the admin staff, IT supports, and technicians, especially Paul Killan and Jeffrey Warren, for their excellent technical assistance. During the COVID-19 outbreak, I received helps from my colleagues in Thailand on accessing CST Studio Suite; therefore, I acknowledge Bancha Luadang, Tom Tanaporn, and Arnon Sakonkanapong. I would also like to thank the Indonesian communities for the togetherness in Newcastle.

My thanks to Dr. Cristian Ulianov, who involved me in several projects within the NewRail (Newcastle Centre for Railway Research). It has been an invaluable experience for working with him on RFID, IoT, and sensors-related projects for railway applications. I would also like to thank my colleagues, whom I have worked with at the NewRail: Paul Hyde, Altan Onat, and Nagvendra Kanoje.

Last but not least, my profound thankfulness to all my family for their love and prayers; my parents, Sumardiyana and Indrayati; my parents in law, Winarno and Cucu Maryati; my brothers and sisters. Finally, but most importantly, I would like to express my deepest gratitude to my dear wife Wieta Martiane, and my beloved daughter Dahayu Areta Marindra. All the works and achievements I have made until today have invisible parts of their contributions.

Table of Contents

Abstract	i
Acknowledgment	iii
Table of Contents	iv
List of Figures	viii
List of Tables	xv
List of Abbreviations	xvi
List of Publications and Awards	xviii
Chapter 1 Introduction	1
1.1 Background and Motivation	1
1.2 Aim and Objectives	5
1.3 Main Achievements	5
1.4 Thesis Organization.....	6
Chapter 2 Literature Review	8
2.1 Crack and Corrosion Defects in Metallic Structures.....	8
2.1.1 Crack and Challenges Related to Sensing	9
2.1.2 Corrosion and Challenges Related to Sensing.....	10
2.2 Traditional NDT&E Techniques for Defect Detection	13
2.2.1 Visual Testing (VT).....	14
2.2.2 Penetrant Testing (PT).....	15
2.2.3 Magnetic Flux Leakage (MFL)	16
2.2.4 Ultrasonic Testing (UT).....	17
2.2.5 Eddy Current Testing (ECT)	18
2.2.6 Microwave and Millimeter-wave NDT	20
2.2.7 Thermography	21
2.2.8 Radiography (X-Rays and Gamma Rays)	22
2.2.9 Summary of Traditional NDT&E Techniques for Defect Detection	23
2.3 SHM and Its Relation to NDT&E	25
2.4 SHM Technologies and Trend Towards the Internet of Things (IoT) based SHM	27
2.4.1 Wired SHM	28
2.4.2 Fiber Optic Sensors (FOS)	29
2.4.3 Wireless Sensor Networks (WSN)	30
2.4.4 The Internet of Things (IoT) based SHM.....	32
2.5 Chipped RFID Technology, Chipped RFID Sensors, and State-of-the-Art Chipped RFID Tag Antenna-based Sensors for SHM.....	35

2.5.1	Brief Fundamentals of Chipped RFID Technology	35
2.5.2	Chipped RFID Sensors	40
2.5.3	State-of-the-Art Chipped RFID Tag Antenna-based Sensors for SHM	41
2.6	Chipless RFID Technology, Chipless RFID Sensors, and State-of-the-Art Chipless RFID and Antenna Sensors for SHM	49
2.6.1	Brief Fundamentals of Chipless RFID Technology	50
2.6.2	Chipless RFID Sensors	55
2.6.3	State-of-the-Art Chipless RFID Sensors and Antenna Sensors for SHM	56
2.7	Research Gap, Problems, and Challenges Identified	61
Chapter 3	Research Methodology and the Proposed Chipless RFID Sensor System for Defect Detection and Characterization	63
3.1	Research Methodology	63
3.1.1	Study 1: Chipless RFID sensor for crack detection and characterization based on circular microstrip patch antenna (CMPA)	65
3.1.2	Study 2: Chipless RFID sensor for corrosion characterization based on frequency selective surface (FSS) and feature fusion	65
3.1.3	Study 3: Robust characterization of defects in a realistic environment using a portable reader, multi-resonance chipless RFID sensor, and Principal Component Analysis	65
3.2	Background of the Proposed Chipless RFID Sensor System for Defect Detection and Characterization	66
3.2.1	Design Approaches for Metal-mountable Chipless RFID Sensors	67
3.2.2	Chipless RFID Reader Mechanism	72
3.2.3	Signal Pre-processing, Feature Extraction, Selection, and Fusion	75
3.3	Chapter Summary	77
Chapter 4	Chipless RFID Sensor for Crack Detection and Characterization Based on Circular Microstrip Patch Antenna (CMPA)	78
4.1	Chipless RFID Sensor System and Crack Detection Approach Using CMPA	78
4.2	Design of the Chipless RFID Sensor based on CMPA	80
4.3	Simulation Studies of CMPA for Crack Characterization	83
4.3.1	Effects of Substrate's Thickness on RCS and Sensitivity	85
4.3.2	Effects of Substrate's Dielectric Constant on RCS and Sensitivity	86
4.4	Experimental Studies and Results	87
4.4.1	Readability of the Chipless RFID Sensor	89

4.4.2	Experimental Studies Using Man-made Crack and Natural Fatigue Crack Samples.....	92
4.4.3	Experimental Study in Multipath Environment	94
4.5	Discussions	95
4.6	Chapter Summary	97
Chapter 5	Chipless RFID Sensor for Corrosion Characterization Based on Frequency Selective Surface (FSS) and Feature Fusion	99
5.1	Chipless RFID Sensor System, Corrosion Detection Approach Using FSS, and Feature Fusion	99
5.1.1	Corrosion Detection Approach Using FSS.....	101
5.1.2	Feature Fusion Using Simple Sum and Confidence Weighted Averaging (CWA)	102
5.2	Design of the Chipless RFID Sensor based on FSS	103
5.3	Simulation Studies of FSS for Corrosion Characterization.....	105
5.4	Experimental Study and Results.....	107
5.5	Discussions	112
5.6	Chapter Summary	114
Chapter 6	Robust Characterization of Defects in Realistic Environment Using Multi-resonance Chipless RFID Sensor, Portable Reader, and Principal Component Analysis	115
6.1	Chipless RFID Sensor System Using Multi-resonance Sensor, Portable Reader, and PCA	116
6.1.1	Defect Sensing Approach Using RF Encoding Particles	117
6.1.2	Portable Chipless RFID Sensor Reader Implemented Using a UWB Radar Module.....	119
6.1.3	Multi-parameter Analysis Using Principal Component Analysis (PCA).....	121
6.2	Design of Multi-resonance Chipless RFID Sensor Based on RF Encoding Particles	123
6.3	Simulation Studies of Multi-resonance Chipless RFID Sensor for Crack and Corrosion Characterization.....	125
6.3.1	Simulation Study of Crack Characterization	125
6.3.2	Simulation Study of Corrosion Characterization	126
6.3.3	Effects of Substrate Thickness on RCS and Sensitivity	127
6.3.4	Effects of Patch Width on RCS and Sensitivity	128
6.4	Experimental Studies and Results	129
6.4.1	Experimental Study Using the Crack Samples.....	131

6.4.2 Experimental Study Using the Corrosion Samples	135
6.5 Discussions	136
6.6 Chapter Summary	137
Chapter 7 Conclusions and Future Works.....	139
7.1 Conclusions	139
7.2 Limitations.....	142
7.3 Recommendations for Future Works	143
References.....	145
Appendix A: The Dual-polarized Broadband Vivaldi Antennas Used in Chapter 5	164
Appendix B: The Broadband Antipodal Vivaldi Antenna Used in Chapter 6	167
Appendix C: Specifications of the Salsa Cayenne Radar Module for Portable Chipless RFID Sensor Reader Used in Chapter 6	169
Appendix D: Matlab Codes for Collecting Signal Data Using the Portable Chipless RFID Sensor Reader in Chapter 6.....	170

List of Figures

Figure 1.1 Catastrophic accidents due to crack and corrosion: (a) The I-35 Mississippi River Bridge collapse due to fatigue crack [4]. (b) Damage of a turbine engine of Airbus A330 in Manchester due to fatigue crack initiated by corrosion [5]. (c) A pipeline failure in California due to corrosion and crack [6].....	1
Figure 1.2 Statistical data of mechanical failure mechanisms showing the domination of crack and corrosion as the sources of catastrophic accidents [7].....	1
Figure 2.1 Surface cracks: (a) Schematic representation of different types of surface cracks. (b) The visual appearance of tiny surface cracks in metal [34].	9
Figure 2.2 Different models of corrosion: (a) two layers. (b) non-layer. (c) three layers [39].	11
Figure 2.3 Various traditional NDT&E techniques with different working principles, most of which are based on electromagnetics.	13
Figure 2.4 Illustration of visual testing of aircraft components using an endoscope by an operator [51].	14
Figure 2.5 Basic steps of penetrant testing [59].	15
Figure 2.6 MFL testing: (a) Basic principle. (b) A large MFL tool for pipeline inspection [62], [63].	16
Figure 2.7 Basic principle of ultrasonic testing showing a UT probe emitting a sound wave and receiving the reflected echo signal that indicates a defect [68].....	17
Figure 2.8 The difference between bulk ultrasonic and guided wave testing in terms of detection range [78].	18
Figure 2.9 Principle of eddy current testing using a coil probe that induces eddy currents in metal under test [84].	19
Figure 2.10 Microwave and millimetre-wave NDT: (a) General setup diagram for the evaluation of complex permittivity of material [99]. (b) Illustration of a real setup using an open-ended waveguide probe [98].	20
Figure 2.11 Principles of thermography: (a) Passive thermography. (b) Active thermography using a flash lamp as the external heating source [108].	22
Figure 2.12 Principle of radiographic inspection [68].	23
Figure 2.13 Example of an SHM system in Tsing Ma Bridge with numerous sensors distributed over the bridge [119].	25
Figure 2.14 The relationship between NDT&E, CM, and SHM [120].	26
Figure 2.15 Trends of SHM technologies from old SHM, new SHM, to future SHM [121]–[123].	27

Figure 2.16 FOS mounted onto structures to monitor temperature and strain. (a) FOS mounted onto cages of reinforcement piles. (b) FOS mounted onto a steel pipe [129].	29
Figure 2.17 SOFO interferometric sensor system. Courtesy of Smartec. [119], [130].	29
Figure 2.18 Conceptual diagram of wired sensors and wireless sensor networks (WSN)	31
Figure 2.19 Wireless sensor node: (a) Functional block diagram. (b) A commercial wireless sensor node platform (Imote2) [119], [138].	31
Figure 2.20 Application areas of IoT [19].	33
Figure 2.21 Framework overview of the IoT based SHM [147].	33
Figure 2.22 Typical concept of an RFID system and the main components [149].	36
Figure 2.23 Coupling mechanism in RFID. (a) Inductive coupling. (b) Radiative coupling	37
Figure 2.24 Classification of chipped RFID with the illustration of tags [151].	38
Figure 2.25 Topologies for chipped RFID sensing. (a) connecting the sensor to the antenna. (b) connecting the sensor to the chip [160].	40
Figure 2.26 RFID sensor applications [162].	40
Figure 2.27 Concept of passive RFID sensor networks for the Internet of Things (IoT) based structural health monitoring (SHM) of heterogeneous infrastructures consisting of perception, network, and application layers [21].	42
Figure 2.28 Principle of passive chipped RFID tag antenna-based sensor system for SHM based on backscatter communication [21].	42
Figure 2.29 General operating principle of a chipless RFID system [201].	50
Figure 2.30 Classification of chipless RFID with the illustration of tags extracted from [207]–[212].	52
Figure 2.31 Generic principle of a chipless RFID sensor system [27].	55
Figure 2.32 Relevant problems and challenges for research on chipless RFID sensor systems for SHM.	62
Figure 3.1 Diagram of the research methodology.	64
Figure 3.2 Operating principle of a chipless RFID sensor system for defect detection and characterization.	66
Figure 3.3 Microstrip patch antenna: (a) General geometrical representation. (b) Typical shapes for microstrip patch elements [238].	68
Figure 3.4 A metal-mountable chipless RFID tag based on MPA comprising four inset-fed rectangular patches with distinct sizes on a ground plane [241], [242]. The patch size determines the resonance frequencies used for ID encoding.	69

Figure 3.5 FSS: (a) FSS periodic structure consisting of complimentary array elements, their equivalent circuits, and the frequency responses. (b) Various shapes of FSS elements [243], [245], [246].	70
Figure 3.6 A metal-mountable chipless RFID tag based on FSS comprising periodic multiple square ring elements on a dielectric substrate and a ground plane. The RCS and reflection coefficient show multiple resonances for ID encoding [244].	70
Figure 3.7 Chipless RFID tags based on REP: (a) Dipole resonators. (b) C-shaped resonators [217].	71
Figure 3.8 Metal-mountable chipless RFID tags based on REP: (a) Circular ring resonators. (b) Dipole resonators. (c) L-shaped resonators [217].	71
Figure 3.9 Arrangement of transmitter, target, and receiver for the radar range equation. In a chipless RFID system, the target is a chipless RFID tag or sensor [238].	73
Figure 3.10 Two optional devices to implement a chipless RFID reader: (a) A VNA connected to antennas with bistatic configuration [217]. (b) A commercially available portable radar module [248], a similar radar module was used for a chipless RFID reader in [247].	75
Figure 4.1 (a) Illustration diagram of a chipless RFID sensor system for crack detection and characterization using CMPA. (b) The structural configuration of CMPA when applied for crack sensing on a metallic structure.	79
Figure 4.2 Geometry of the proposed chipless RFID sensor consisting of tip loaded dipoles for ID encoding and CMPA for crack sensing. The sensor has a partial ground plane on the backside to protect the ID signature from changes due to a crack.	80
Figure 4.3 Simulation setup of the chipless RFID sensor in CST Microwave Studio.	81
Figure 4.4 Simulated RCS spectrum of the chipless RFID sensor showing two sets of resonance frequency for ID encoding and crack sensing.	82
Figure 4.5 Simulated surface current distributions of the chipless RFID sensor showing the concentration of current at each resonance on the backing metal slab.	82
Figure 4.6 Simulated RCS spectra of the chipless RFID sensor showing the resonance frequency shift for different crack orientations and widths. (a) Horizontal crack. (b) Vertical crack. (c) Diagonal crack. The insets show the amount of resonance frequency shifts and linear fitting lines.	83
Figure 4.7 Simulated surface current distribution on the metallic structure under the CMPA, showing the current flows for different crack orientations. (a) Without crack: at 4.70 GHz. (b) With a 2-mm horizontal crack: at 4.43 GHz. (c) With a 2-mm vertical crack:	

at 4.84 GHz. (d) With a 2-mm diagonal crack: at 4.30 GHz (left) and 4.77 GHz (right).	85
Figure 4.8 Effects of the substrate’s thickness on: (a) RCS of the chipless RFID sensor, showing that the resonance of CMPA moves towards a higher frequency with a shallow resonance when the substrate thickness decreases. (b) The sensitivity of CMPA to crack, showing that the sensitivity increases when the substrate thickness decreases.....	86
Figure 4.9 Effects of the substrate’s dielectric constant on: (a) RCS of the chipless RFID sensor, showing that the substrate with a high dielectric constant generates a shallow resonance magnitude and vice versa. (b) The sensitivity of CMPA to crack, showing that the sensitivity to crack remains similar for different substrate’s dielectric constants.....	87
Figure 4.10 Crack samples. (a) Man-made crack samples. (b) Natural fatigue crack sample.	88
Figure 4.11 Experimental setup using the bistatic radar configuration. (a) Schematic diagram of the experimental setup. (b) Photograph of the experimental setup in the anechoic chamber.	88
Figure 4.12 Comparison between the simulated and measured RCS spectra of the chipless RFID sensor.....	90
Figure 4.13 Measured RCS spectra with different reading distances.....	90
Figure 4.14 Measured RCS spectra of the chipless RFID sensor placed on different sizes of metal plate samples showing an unreadable sensor when the metal size is large.	91
Figure 4.15 Measured RCS of the chipless RFID sensor placed on metal plate samples of different sizes. The RCS is calibrated with the response of each metal plate sample. .	91
Figure 4.16 Measured RCS spectra of the chipless RFID sensor for different crack orientations and widths, showing good agreement between simulations and measurements. (a) Horizontal crack. (b) Vertical crack. (c) Diagonal crack.	93
Figure 4.17 Measured RCS spectra of the chipless RFID sensor when placed on a natural fatigue crack sample showing detection of a submillimeter crack using the resonance frequency shift.....	93
Figure 4.18 Experimental setup outside the anechoic chamber to represent a multipath environment.....	94
Figure 4.19 Measured RCS spectra of the chipless RFID sensor on horizontal crack samples of different widths in a multipath environment. The resonances for ID signature are hard to detect due to the high noise level.	95
Figure 5.1 Illustration diagram of a chipless RFID sensor system for corrosion characterization using FSS and feature fusion.....	100

Figure 5.2 Corrosion sensing approach: (a) Simplified model of a corrosion undercoating with FSS-based chipless RFID sensor on corroded steel covered by a paint coating, (b) Equivalent-circuit model of FSS grounded on a corroded and coated steel.	101
Figure 5.3 Design and geometry of the multi-resonance FSS-based chipless RFID sensor with periodically arranged 2×2 unit cells. Each unit cell comprises three Z-shaped patches; one of them (Z-shaped patch A) is the longest, and the other two (Z-shaped patch B and C) are of the same lengths.	104
Figure 5.4 Simulated cross-polar RCS of the FSS-based chipless RFID sensor for the different number of unit cells. The greater number of unit cells exhibits higher resonance magnitudes.	105
Figure 5.5 Simulated surface current distributions of the FSS-based chipless RFID sensor: (a) at 3.06 GHz. (b) at 3.85 GHz. (a) at 4.88 GHz.	105
Figure 5.6 Simulation setup of the FSS-based chipless RFID sensor for corrosion characterization in CST Microwave Studio.	106
Figure 5.7 Simulated cross-polar RCS of the FSS-based chipless RFID sensor against variations of corrosion rust thickness showing three resonance shifts. Three resonance shift features allow for feature fusion to enhance the sensitivity and reliability of the sensor. The insets show the resonance frequency shifts and linear fitting lines.	106
Figure 5.8 Effects of the substrate thickness on: (a) RCS of the FSS, showing that the resonance magnitudes decrease with the decrease of substrate thickness. (b) The sensitivity to corrosion thickness, showing that the sensitivity increases when the substrate thickness decreases.....	107
Figure 5.9 Corrosion undercoating samples with different exposure periods to a marine atmosphere.	108
Figure 5.10 Experimental setup in a laboratory environment using VNA and dual-polarized Vivaldi antennas.	108
Figure 5.11 Measured transmission coefficient ($ S_{21} $) averaged from 10 repeated measurements of the FSS-based chipless RFID sensor for different corrosion undercoating samples: (a) Raw (uncalibrated) $ S_{21} $. (b) Calibrated $ S_{21} $ by subtracting the raw $ S_{21} $ with the $ S_{21} $ response of the sample.	109
Figure 5.12 Characterized corrosion progression indicated by: (a) Resonance frequency features. (b) Fused resonance frequency feature using simple sum. (c) Fused resonance frequency feature using CWA. The fused features show less overlapped and smaller error bars than individual features.....	110

Figure 6.1 Illustration diagram of a chipless RFID sensor system using a multi-resonance sensor, portable reader, and principal component analysis (PCA). Principal components (PCs) represent the extracted features used for evaluating the most contributing physical parameters contained in signal data.	116
Figure 6.2 Monocycle Gaussian UWB pulse generated by the Xethru1 chip of the Salsa Cayenne radar module. (a) Time-domain pulse waveform. (b) Normalized power spectral density (PSD).	120
Figure 6.3 Geometry of the multi-resonance chipless RFID sensor.	123
Figure 6.4 Simulated cross-polar RCS spectrum of the multi-resonance chipless RFID sensor placed on metal.	124
Figure 6.5 Simulated surface current distributions of the multi-resonance chipless RFID sensor showing the concentration of currents on the backing metal slab formed by the diagonal dipole and L-shaped patches: (a) at 2.29 GHz. (b) at 2.73 GHz. (c) at 3.11 GHz. (d) at 3.74 GHz. (e) at 4.51 GHz. (f) at 5.1 GHz.	125
Figure 6.6 Simulated cross-polar RCS of the multi-resonance chipless RFID sensor for different crack orientations and crack widths (o = orientation, w = width): (a) 0° crack orientation. (b) 45° crack orientation. (c) 90° crack orientation. (d) 135° crack orientation.	126
Figure 6.7 Simulated cross-polar RCS of the multi-resonance chipless RFID sensor showing that all six resonances shifted to lower frequencies with the increase of corrosion thickness.	127
Figure 6.8 Effect of substrate thickness on: (a) RCS. (b) Sensitivity to crack. (b) Sensitivity to corrosion. Instead of using the full design with six resonances, the simulations were performed with diagonal dipole patches of the same length as representative resonant elements for the chipless RFID sensor.	128
Figure 6.9 Effect of patch width on: (a) RCS. (b) Sensitivity to crack, showing that 2-mm patch width results in an optimum sensitivity. (c) Sensitivity to corrosion, showing that the patch width does not affect the sensitivity.	129
Figure 6.10 Man-made crack samples with three different widths and four different orientations.	130
Figure 6.11 Corrosion undercoating samples with different exposure periods to a marine atmosphere.	130
Figure 6.12 Experimental setup of a chipless RFID sensor system for characterization of crack and corrosion. Experiments for corrosion were repeated for different orientations corrosion samples.	131

Figure 6.13 The measured received signals after pre-processing from the multi-resonance chipless RFID sensor mounted on crack samples with different crack orientations and crack widths: (a) 0° crack orientation. (b) 45° crack orientation. (c) 90° crack orientation. (d) 135° crack orientation. The signals were taken without calibration (background subtraction). The pink boxes with numbers mean to highlight the resonances generated by the chipless RFID sensor.....	132
Figure 6.14 A block diagram illustrating the process of principal component analysis (PCA) after collecting the measured signals.	133
Figure 6.15 PCA features for different crack samples: (a) PC1. (b) PC2. (c) PC3. (d) PC4. (e) PC5. (f) PC6.	134
Figure 6.16 The measured received signals after pre-processing from the multi-resonance chipless RFID sensor mounted on different corrosion progression samples: (a) with the samples oriented horizontally. (b) with the samples oriented vertically. The signals were taken without calibration (background subtraction). The pink boxes with numbers mean to highlight the resonances generated by the chipless RFID sensor.	135
Figure 6.17 PCA features from different coated corrosion samples and different sample orientations: (a) PC1. (b) PC2. (c) PC3. (d) PC4.	136

List of Tables

Table 2.1 Electrical resistivity and the dielectric constant of materials related to corrosion rust measured at room temperature (25°C) [40]–[46].	12
Table 2.2 Advantages and disadvantages of traditional NDT&E techniques.	24
Table 2.3 List of chipped RFID tag antenna-based sensors for crack detection and characterization. The highlighted rows are chipped RFID tag antenna-based sensors for crack detection in metals.	46
Table 2.4 List of chipped RFID tag antenna-based sensors for corrosion detection and characterization.	48
Table 2.5 A comparison of chipped and chipless RFID [203].	51
Table 2.6 List of chipless RFID sensors and antenna sensors for crack detection and characterization. The highlighted row shows the only chipless RFID sensors for crack detection before 2016. The sensor was proposed for crack detection in concrete and using time-domain chipless RFID.	57
Table 2.7 List of chipless RFID sensors and antenna sensors for corrosion detection.	60
Table 4.1 Dimensions of the proposed chipless RFID sensor (in mm).	80
Table 4.2 Comparison of this work with chipped RFID tag antenna-based sensors for crack detection and characterization.	96
Table 5.1 Dimensions of the FSS-based chipless RFID sensor with 2x2 unit cells (in mm).	104
Table 5.2 Sensitivity and standard deviation of individual resonance frequency features and the fused features.	111
Table 5.3 Summary of several RFID sensors for corrosion characterization.	112
Table 6.1 Specification of UWB radar module for chipless RFID sensor reader.	119
Table 6.2 Dimensions of the multi-resonance chipless RFID sensor (in mm).	123
Table 7.1 Comparisons of chipless RFID sensor systems and results in Chapters 4, 5, and 6	140

List of Abbreviations

ADC	Analog to Digital Converter
AID	Analog Identifier
ASIC	Application Specific Integrated Circuit
ASK	Amplitude Shift Keying
BINDT	British Institute of Non-Destructive Testing
CFRP	Carbon Fiber Reinforced Composite
CM	Condition Monitoring
CMOS	Complementary Metal Oxide Semiconductor
CMPA	Circular Microstrip Patch Antenna
CNT	Carbon Nano Tube
CST	Computer Simulation Technology
CUI	Corrosion Under Insulation
CW	Continuous wave
CWA	Confidence Weighted Averaging
DC	Direct Current
DWT	Discrete Wavelet Transform
EBG	Electromagnetic Band Gap
ECPT	Eddy Current Pulsed Thermography
ECT	Eddy Current Testing
EM	Electromagnetic
EMI	Electromagnetic Interference
EPC	Electronic Product Code
FBG	Fiber Bragg Grating
FCC	Federal Communication Commission
FD	Frequency Domain
FMCW	Frequenc Modulated Continuous Wave
FOS	Fiber Optic Sensor
FSS	Frequency Selective Surface
GFRP	Glass Fiber Reinforced Polymer
GPS	Global Positioning System
HF	High Frequency
HIS	High Impedance Surface
IC	Integrated Circuit
ID	Identity/Identification
IDC	Inter-digital Capacitor
IFF	Identification Friend or Foe
IR	Impulse Radio
ISM	Industrial, Scientific and Medical
LC	Inductor (L) Capacitor (C)
LF	Low Frequency
LVDT	Linear Variable Differential Transformer
MEMS	Micro-Electro-Mechanical Systems
MFL	Magnetic Flux Leakage
MIMO	Multiple Input Multiple Output

MPA	Microstrip Patch Antenna
NDT	Non-destructive Testing
NDT&E	Non-destructive Testing and Evaluation
NFC	Near Field Communication
PC	Principal Components
PCA	Principal Component Analysis
PCB	Printed Circuit Board
PDMS	Polydimethylsiloxane
PEC	Pulsed Eddy Current
PEDOT	Poly(3,4-ethylenedioxythiophene)
PIFA	Planar Inverted-F Antenna
PRF	Pulse Repetition Frequency
PSD	Power Spectral Density
PT	Penetrant Testing
PVA	Polyvinyl Alcohol
PZT	Lead zirconate titanate
QNDE	Quantitative Non-destructive Evaluation
RCS	Radar Cross Section
REP	RF Encoding Particles
RF	Radio Frequency
RFID	Radio Frequency Identification
RLC	Resistor (R) Inductor (L) Capacitor (C)
RSSI	Received Signal Strength Indicator
SAW	Surface Acoustic Wave
SCC	Stress Corrosion Cracking
SHM	Structural Health Monitoring
SNR	Signal to Noise Ratio
SOFO	Surveillance d'Ouvrages par Fibres Optiques
SRR	Split Ring Resonator
SVD	Singular Value Decomposition
SWB	Super Wide Band
TDM	Time Division Multiplexing
TDR	Time Domain Reflectometry
TM	Transverse Magnetic
TOF	Time of Flight
UAV	Unmanned Aerial Vehicle
UGWT	Ultrasonic Guided Wave Testing
UHF	Ultra High Frequency
USB	Universal Serial Bus
USRP	Universal Software Radio Peripheral
UT	Ultrasonic Testing
UV	Ultraviolet
UWB	Ultra Wide Band
VNA	Vector Network Analyzer
VT	Visual Testing
WSN	Wireless Sensor Network

List of Publications and Awards

Journal publications:

1. J. Zhang, G. Tian, A. M. J. Marindra, A. Sunny, and A. Zhao, “A Review of Passive RFID Tag Antenna-Based Sensors and Systems for Structural Health Monitoring Applications,” *Sensors*, vol. 17, no. 2, p. 265, Jan. 2017.
2. A. M. J. Marindra and G. Y. Tian, “Chipless RFID Sensor Tag for Metal Crack Detection and Characterization,” *IEEE Transactions on Microwave Theory and Techniques*, vol. 66, no. 5, pp. 2452–2462, May 2018.
3. A. M. J. Marindra and G. Y. Tian, “Multiresonance Chipless RFID Sensor Tag for Metal Defect Characterization Using Principal Component Analysis,” *IEEE Sensors Journal*, vol. 19, no. 18, pp. 8037–8046, Sep. 2019.
4. A. M. J. Marindra and G. Y. Tian, “Chipless RFID Sensor for Corrosion Characterization Based on Frequency Selective Surface (FSS) and Feature Fusion,” *Smart Materials and Structures*, vol. 29, no. 12, pp. 125010, Oct. 2020.

Conference publications:

1. R. Sutthaweeikul, A. M. J. Marindra, and G. Y. Tian, “Study of microwave responses on layered woven CFRP composites,” in *2017 9th International Conference on Information Technology and Electrical Engineering (ICITEE)*, 2017.
2. A. M. J. Marindra, R. Sutthaweeikul, and G. Y. Tian, “Depolarizing Chipless RFID Sensor Tag for Characterization of Metal Cracks Based on Dual Resonance Features,” in *2018 10th International Conference on Information Technology and Electrical Engineering (ICITEE)*, 2018. [Best Paper Award].

Awards:

1. 2nd Position Award at the Live Demo Session of the IEEE International “Sensors and Measurements” Student Contest during IEEE Sensors 2017, presenting the project “SOUNNETIC: Turning Motion into Music by Means of Multi-Sensor Fusion” in Glasgow, UK, October 30, 2017.
2. 1st place for ‘Best Poster’ in the Communication, Sensors, Signal and Information Processing group at the School of Electrical and Electronic Engineering – Annual Research Conference 2017.
3. 2nd place for ‘Best Presentation’ in the Intelligent Sensing and Communications group in the Electrical and Electronic Engineering at the School of Engineering – Annual Research Conference 2018.

4. 3rd place for ‘Best Paper’ in in the Intelligent Sensing and Communications group in the Electrical and Electronic Engineering at the School of Engineering – Annual Research Conference 2018.
5. ‘Best Paper’ Award in the 10th International Conference on Information Technology and Electrical Engineering (ICITEE), held by Electrical Engineering and Information Technology Department, Faculty of Engineering, Universitas Gadjah Mada, in Bali, 26 July 2018.

Involvement in projects with NewRail (Newcastle Centre for Railway Research):

1. Cargo condition monitoring using RFID technology in INNOWAG (Innovative Monitoring and Predictive Maintenance Solutions on Lightweight Wagon) project, funded by the Shift2Rail Joint Undertaking under the European Union’s Horizon 2020. (January 2019 to June 2019).
2. Vehicle Dynamics: ARSS (Active Radius Steering Suspension) sensors and instrumentation systems, funded by Grand Central, UK, in collaboration with Rail Safety and Standards Board (RSSB) and LIEBHERR, Switzerland. (July 2019 to December 2020).

Chapter 1 Introduction

1.1 Background and Motivation

The rapid development of technology and engineering systems makes our environment replete with large-scale and complex structures that are designed to carry heavy loads and operated for a long-term period. Examples include buildings, bridges, pipelines, wind turbines, powerplants, rails, aircraft, and many more. Although these structures are designed to work safely under appropriate loading conditions, deteriorations and damages can occur during their operation [1]. Structural damage problem arises from metals as the constitutive materials of large structures. Metallic materials are subject to deterioration, such as fatigue and corrosion, which can be caused by cyclic loads, chemicals, and continuous exposure to aggressive environmental conditions. Cracks due to fatigue and corrosion can affect the mechanical performance of structures and thus are among the common reasons for failures in aircraft and pipelines [2], [3].

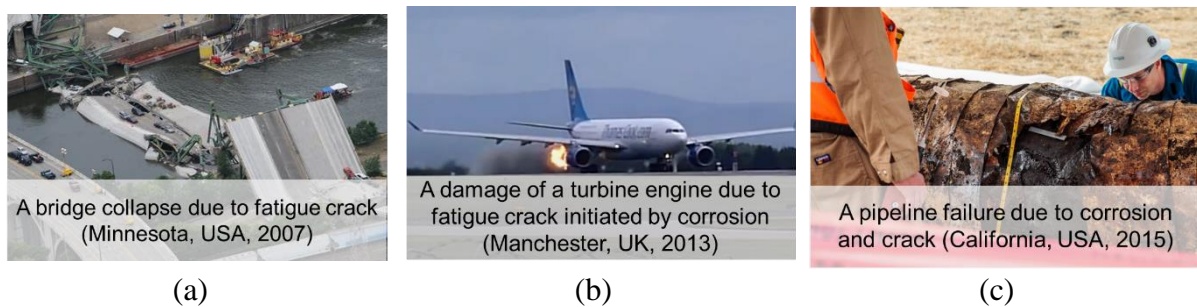


Figure 1.1 Catastrophic accidents due to crack and corrosion: (a) The I-35 Mississippi River Bridge collapse due to fatigue crack [4]. (b) Damage of a turbine engine of Airbus A330 in Manchester due to fatigue crack initiated by corrosion [5]. (c) A pipeline failure in California due to corrosion and crack [6].

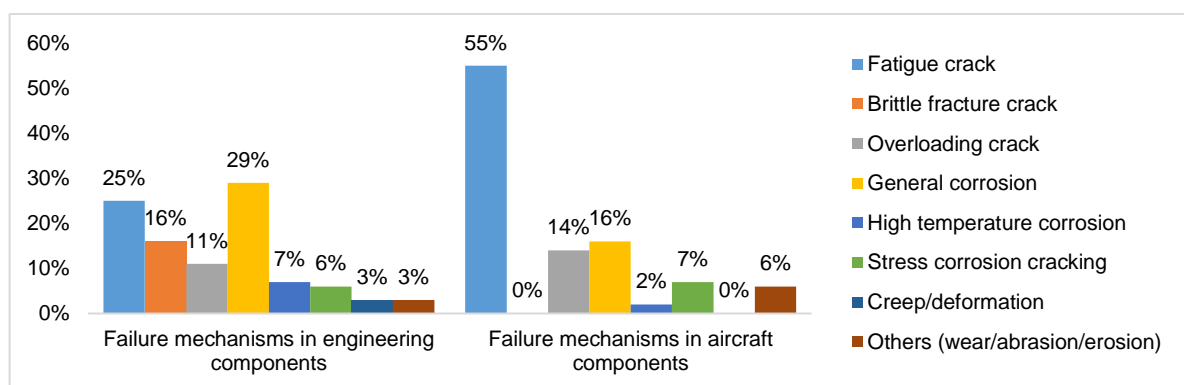


Figure 1.2 Statistical data of mechanical failure mechanisms showing the domination of crack and corrosion as the sources of catastrophic accidents [7].

There have been numerous catastrophic accidents caused by crack and corrosion defects; a few incidents are illustrated in Figure 1.1. On 1 August 2007, during the rush hour traffic after 6 pm, the Interstate 35W bridge over the Mississippi River, Minneapolis, USA, suddenly collapsed. There were 111 vehicles on the bridge at the time, causing 13 people died and 145

injured. According to the inspections carried out in 2001 and 2006, the bridge was rated “structurally deficient” as fatigue crackings were found in the cross girder at the end of the approach spans. On 24 June 2013, an Airbus A330 got a serious incident at Manchester Airport, UK, when the right engine caught fire at a speed of 190 km/h during take-off. The crew brought the aircraft to an emergency stop on the runway using the unaffected left engine. Investigation revealed that there had been a failure of a turbine blade caused by high cycle fatigue crack propagation initiated by corrosion. More recently, on 19 May 2015, there was a discharge of 540 m³ of crude oil from a pipeline failure in Santa Barbara, California, USA. Santa Barbara is one of the most biologically diverse coastlines in the United States. The investigation indicated that the ruptured pipeline was severely corroded, having the pipe thickness reduced by about 45%. Additionally, there was a crack propagation, which created a hole approximately six inches long on the pipeline.

Based on statistical data of mechanical failure mechanisms for past catastrophic accidents [7], crack and corrosion are the major “culprits” for failures in engineering and aircraft components, as shown in Figure 1.2. Cracks due to fatigue, brittle fracture, and overloading were the reason for 52% of failures. At the same time, corrosions in various forms, i.e., general corrosion, high-temperature corrosion, and stress corrosion cracking (SCC), were the reason for 42% of failures in engineering components. The data also shows that crack has caused 69% of failures in aircraft components, while corrosion has contributed 25% to the total. Hence, crack and corrosion are serious concerns for structural health and, therefore, need to be monitored in a timely fashion. Without timely detection of damage states in structural components and materials, structures are more prone to failure, which can cause economic losses and jeopardize human and environmental safety.

A subject that studies the implementation of damage identification strategy through data acquisition from sensors to assess the health of a structure is structural health monitoring (SHM) [8], [9]. In recent years, SHM becomes a multi-disciplinary area of growing interest that involves several techniques and technologies, including materials, sensors, electronics, signal processing, and data science [10], [11]. With SHM, anomalies can be detected in time, thus enabling more efficient maintenance and reducing operational costs. Also, observation of structural health allows us to prevent catastrophic failures by reacting properly before the damage becomes severe. SHM for assessing the global condition of a structure by measuring, for example, vibration levels during operation, has been a relatively mature field. This type of SHM is unlikely to be sensitive to detect local damages unless it is exceptionally severe and dramatically affects the operation of the monitored structure. SHM that aims for local defect

detection, such as crack and corrosion detection, is still limited in standards and applications [12].

This far, assessment of defects in metallic materials relies on scheduled manual inspections using the traditional non-destructive testing and evaluation (NDT&E) techniques, such as ultrasonic testing [13] and eddy-current testing [14]. Other NDT&E methods such as pulsed eddy current (PEC) [15], eddy current pulsed thermography (ECPT) [16], microwave testing [17] have been developed for monitoring of structural defects with a proper resolution, sensitivity, and reliability. However, these NDT&E techniques are limited in range, time-consuming, and expensive for continuous monitoring of large-scale structures. Furthermore, periodic inspections using NDT&E techniques are cumbersome due to the requirement of sizeable equipment and often need to be carried out in a laboratory environment. The techniques are practically troublesome to be employed for continuous monitoring when the structure is in operation. Therefore, there is an inevitable requirement to further scale NDT&E techniques into a holistic and continuous approach for early detection of defects and in-situ SHM.

The internet of things (IoT) [18]–[20] has the potential to bridge the gap between NDT&E and SHM through one of its primary key enabling technologies, radio frequency identification (RFID). The IoT is considered the future of the internet and will comprise a vast amount of intelligent communicating “things” with embedded and sophisticated sensing and actuation. RFID, which was initially developed for object identification and asset tracking, is attractive for deploying wireless, passive, and low-cost sensors on heterogeneous engineering infrastructures. The standard chipped RFID systems, including the low-frequency (LF) RFID and the ultra-high-frequency (UHF) RFID, have been investigated for defect detection through antenna-based sensors [21]. Chipped RFIDs have been standardized and widely accepted throughout the industry. With the availability of the IC chips and off-the-shelf readers, research on chipped RFID for SHM applications is growing in the last few years.

Although the studies on chipped RFID sensors have proved their viability for SHM; however, there are at least three shortcomings in applying chipped RFIDs. First, the use of silicon chip makes chipped RFID sensors not cost-effective in manufacturing and unable to work in harsh environments, such as in the high-temperature condition. Typical RFID chips can work within the temperature range of -40°C up to 85°C . In an environment where the temperature may exceed this range, e.g., surrounding oil and gas pipelines, RFID chips may get damaged, and the material that bonds the chip to the antenna may not be in a solid-state and thus unable to conduct RF energy. Second, the detection capability of chipped RFID tag antenna-based sensors is limited to only one parameter detection. Since the chipped RFID standards operate in a

narrowband spectrum, the number of resonances and sensing features that can be occupied is limited. Whereas in fact, defects in metallic structures may have multiple parameters to detect. Third, the RFID antenna-based sensing exploits the level of impedance matching between antenna and chip, thus creating a trade-off between sensing sensitivity and the communication range [17]. Although ideally, the reading range of chipped UHF RFID tags can be greater than 10 m, it is not the case when the tag antenna is used as a sensor. Sensitive changes in antenna characteristics used for sensing lead to impedance mismatch between the chip and the antenna, and at once, degrade the reading range. Furthermore, studies in chipped RFID tag antenna sensors for SHM have revealed problems and challenges associated with the size and profile of the antenna sensor, reading distance, sensitivity, and resolution.

Chipless RFID, the next generation of RFID, offers numerous advantages over the chipped RFID [22], [23]. While it was initially developed for replacing item barcodes like the chipped RFID, chipless RFID is seen as a technology for IoT-based smart sensing [24]. The idea of eliminating chip and electronics in chipless RFID opens the possibility to bring the cost of tags and sensors to the lowest. In the context of SHM, the low-cost aspect will be beneficial for the massive deployment of chipless sensors to safety-critical areas on a large structure. The absence of chip and electronics also makes chipless tags and sensors printable, embeddable, and durable in harsh environments. The printable and embeddable aspects provide a possibility to integrate sensors into materials, enabling new functional materials and smart structures. Another exciting benefit is its multi-parameter sensing capability. Chipless RFID is designed to encode information using resonances within a broadband frequency range. The broadband operation allows chipless RFID to detect multiple physical variables and incorporate more resonances and sensing features within the sensor's frequency signature [25].

Despite the appealing advantages, chipless RFID for SHM received little attention. Chipless RFID for the purpose of object identification has not been mature yet for commercialization and is still being intensively studied [26]. Furthermore, the exploration of chipless RFID for sensing applications currently puts the highest emphasis on environmental sensors, such as temperature, humidity, and gas sensors [27]. To date, there has been insufficient research that examines chipless RFID sensors for SHM, particularly for defect detection and characterization. Hence, the design and development of chipless RFID sensor systems for crack and corrosion is an open challenge. Metal-mountable sensor designs, reader configurations, as well as signal processing methods, including feature extraction, selection, and fusion, need to be investigated. Considering the potential of chipless RFID sensors and challenges in their

application for SHM, the aim and objectives of this research are outlined in the following section.

1.2 Aim and Objectives

This research aims to design and develop chipless RFID sensor systems for SHM, particularly for crack and corrosion detection and characterization. Novel metal-mountable chipless RFID sensor designs, reader configurations, as well as feature extraction, selection, and fusion, are investigated.

In order to study different metal-mountable chipless RFID sensors and systems with case studies, the research is divided into the following objectives:

1. To design a chipless RFID sensor that provides ID encoding and sensing functionality based on the circular microstrip patch antenna (CMPA) for crack detection and characterization. (Chapter 4)
2. To observe the resonance frequency of CMPA against the crack orientation and the crack width in simulation and experiment. (Chapter 4)
3. To design a chipless RFID sensor for corrosion characterization based on frequency selective surface (FSS) that provides multiple resonances for sensing. (Chapter 5)
4. To examine multiple resonance frequency features from the FSS against corrosion thicknesses and progression in simulation and experiment, and to apply feature fusion for enhancing sensitivity and reliability. (Chapter 5)
5. To design a multi-resonance chipless RFID sensor based on depolarizing RF encoding particles (REPs) for robust detection and characterization of defects. (Chapter 6)
6. To implement a portable chipless RFID reader using an ultra-wideband (UWB) radar module and to undertake experiments with crack and corrosion in a realistic environment. (Chapter 6)
7. To evaluate crack and corrosion defects using feature extraction and selection based on principal component analysis (PCA). (Chapter 6)

1.3 Main Achievements

The achievements and contributions of this thesis to the body of knowledge is represented by several achievements as follows:

1. This thesis presents a comprehensive and systematic literature review in NDT&E techniques, SHM technologies, and state of the art of RFID based sensors for SHM. Various traditional NDT&E techniques, especially the electromagnetic means, are

surveyed. In order to emphasize the novelty of chipless RFID technology as a new method for SHM, the state of the art of chipped RFID sensors and chipless RFID sensors are reviewed. Parts of the literature survey on RFID tag antenna-based sensors for SHM were published in the *Sensors MDPI Journal* in 2017 [21].

2. This thesis demonstrates the novel use of the frequency signature-based chipless RFID sensor system for metal crack detection and characterization. A chipless RFID sensor employing a CMPA is proposed exploiting the resonance frequency shift feature to indicate the crack width and crack orientation. The sensing principle based on CMPA, simulation model, and the experiments, provides a proof of concept and guideline in the application of chipless RFID for SHM. The study was published in the *IEEE Transactions on Microwave Theory and Techniques* in 2018 [28].
3. In regards to corrosion characterization, a novel chipless RFID sensor based on FSS is presented in this thesis. The structure of FSS is related to metasurfaces, which is a trending scientific topic in recent years. Furthermore, multiple feature extraction and feature fusion are introduced to find a reliable interpretation of corrosion progression. Multiple feature extraction and feature fusion have rarely been explored for chipless RFID sensors. The study was published in the *IOP Smart Materials and Structures* in 2020 [29].
4. This thesis demonstrates a robust chipless RFID sensor system using a portable reader in a realistic environment. A novel multi-resonance chipless RFID sensor and feature extraction using PCA are proposed for multiparameter analysis of defects. The proposed sensor is multifunctional and tested for characterizations of crack and corrosion. Moreover, the application of feature extraction using PCA for chipless RFID sensors is novel. The demonstration of a portable reader for defects characterization underpins the practicality of chipless RFID sensor systems for SHM applications. This study was published in *IEEE Sensors Journal* in 2019 [30].

1.4 Thesis Organization

This thesis is divided into seven chapters, with the contents of the six following chapters are organized as follows.

Chapter 2 reviews the existing literature on the traditional NDT&E techniques, SHM technologies, and RFID sensors for SHM. Mechanism and characteristics of crack and corrosion, as well as their challenges related to sensing, are described. Various traditional NDT&E techniques for defect detection are surveyed, followed by a summary of their advantages and disadvantages. Then, the relationship between NDT&E and SHM and the trend

of SHM technologies towards IoT based SHM are discussed. State of the art of chipped RFID tag antenna-based sensors and chipless RFID sensors for SHM are reviewed. Then, the chapter highlights the research gap, as well as the relevant problems and challenges identified for the research in this thesis.

Chapter 3 describes the research methodology and the working principle of the proposed chipless RFID sensor system for defect detection and characterization. The selected problems and challenges to be tackled, the research methodology, and the three studies carried out in this thesis are specified. The theoretical backgrounds and approaches related to the design and development of chipless RFID sensor systems are elaborated.

Chapter 4 presents a chipless RFID sensor design using the circular microstrip patch antenna (CMPA) and resonance frequency shift feature for crack detection and characterization. By using the principle of patch antennas, this study presents a proof-of-concept of the application of the frequency signature-based chipless RFID for crack detection and characterization.

Chapter 5 explores the frequency selective surface (FSS) based chipless RFID sensor, multiple features extraction, and fusion for corrosion characterization. The study investigates sensor design and principle using FSS as well as the extraction of multiple features and fusion using simple sum and CWA to enhance the sensitivity and reliability of the sensor.

Chapter 6 demonstrates a multi-resonance chipless RFID, portable reader, and feature extraction using PCA for robust and multi-parameter defect sensing. The study proposes a chipless RFID sensor design by integrating several RF encoding particles that generate multiple resonances for sensing. The multi-resonance sensor design and the feature extraction method using PCA address the issue of robustness and multiparameter analysis in a chipless RFID sensor system. Implementation of a portable reader using a UWB radar module is presented to show the applicability in a realistic environment.

Chapter 7 concludes the findings and contributions of the research, as well as limitations and recommendations for future works.

Chapter 2 Literature Review

As highlighted in the previous chapter, defects such as crack and corrosion are crucial issues for metallic infrastructures. In order to avoid catastrophic structural failures, it is vital to detect, characterize, and monitor defects. Thus far, NDT&E techniques have been the traditional means to detect defects based on different principles and instruments. However, inspection using NDT&E techniques is costly in labor, slow, limited in range, and the sizeable equipment makes it difficult to perform continuous and in-situ monitoring. Since SHM technologies for automatic and in-situ monitoring of defects are currently limited, RFID can play a strategic role in bridging the gap between NDT&E and SHM. RFID technology is a key enabling technology for the internet of things (IoT), and therefore, RFID sensors have gained attention for SHM in recent years.

This chapter presents a comprehensive and systematic literature review from NDT&E techniques to state of the art of RFID technologies for SHM. The review begins with the basics of crack and corrosion defects in metallic structures and the challenges they pose related to sensing. Then, a survey of traditional NDT&E techniques for defect detection is provided in Section 2.2 with a summary of their advantages and disadvantages. Next, SHM and its relation to NDT&E are explained in Section 2.3, followed by SHM technologies, i.e., distributed fiber optic sensors (FOS) and wireless sensor network (WSN), and the trend towards the IoT based SHM, in Section 2.4. After that, chipped and chipless RFID are discussed in Sections 2.5 and 2.6, respectively, including the fundamentals of the technologies, sensor applications, and state-of-the-art developments of chipped and chipless RFID sensors for SHM. Lastly, the identified research gap, problems, and challenges associated with chipless RFID sensor systems for defect detection are outlined in Section 2.7.

2.1 Crack and Corrosion Defects in Metallic Structures

Crack and corrosion are two types of defects in metallic structures, which have been recognized as the sources of structural failures. Repeated application of loads and exposure to the aggressive environmental condition can lead to the occurrence of crack and corrosion, degrading the integrity of metallic structures. The degradation can start in the form of small defects, getting more prominent over time, and then cause catastrophic failures. Crack and corrosion occur as different phenomena, but they both pose severe threats to the safety of infrastructures. This section briefly discusses the crack and corrosion mechanism in metallic structures, their general characteristics, and the challenges they pose related to sensing.

2.1.1 Crack and Challenges Related to Sensing

The occurrence of a crack in metallic materials is often associated with fatigue, which happens due to cyclic loadings when a structure is in operation. Nonetheless, a crack can also be originated from poor quality manufacturing and overloading. Extensive metallurgical investigations discovered that metal fatigue damage is a surface phenomenon, where bands of slip lines form on the surface grains under fatigue loading. Eventually, these slip lines turn into cracks, which then increase in depth and propagate across the material, creating a fracture [31]. The fatigue cracking mechanism is complicated as it can involve five stages, i.e., early cyclic formation and damage, microcrack nucleation, short crack propagation, macrocrack propagation, and final fracture [32]. Fatigue cracks initiate primarily at the surface of a material in the short fatigue life regime but may shift to the subsurface in the long-life range. Both surface and subsurface cracks have negative impacts on metals. Since subsurface crack presents a higher challenge in terms of detection, the following discussion will be limited to the characteristics of surface crack.

Surface crack is defined as a material “discontinuity” originating from the outer boundary of a solid due to the high stress [33]. It can significantly reduce the service life of structures leading to premature failures. In some materials like steel, surface defects can present not only because of repeated loading but also since the manufacturing stage due to the poor quality during continuous casting. Figure 2.1 shows schematic representation and visual appearance of surface crack in a slab. Surface cracks can appear in different orientations and positions; there are transverse crack, longitudinal crack, corner crack, and edge crack. Meanwhile, their sizes can range from a few tens of centimeters to a few centimeters, while the depths of cracks are up to a few hundred micrometers [34].

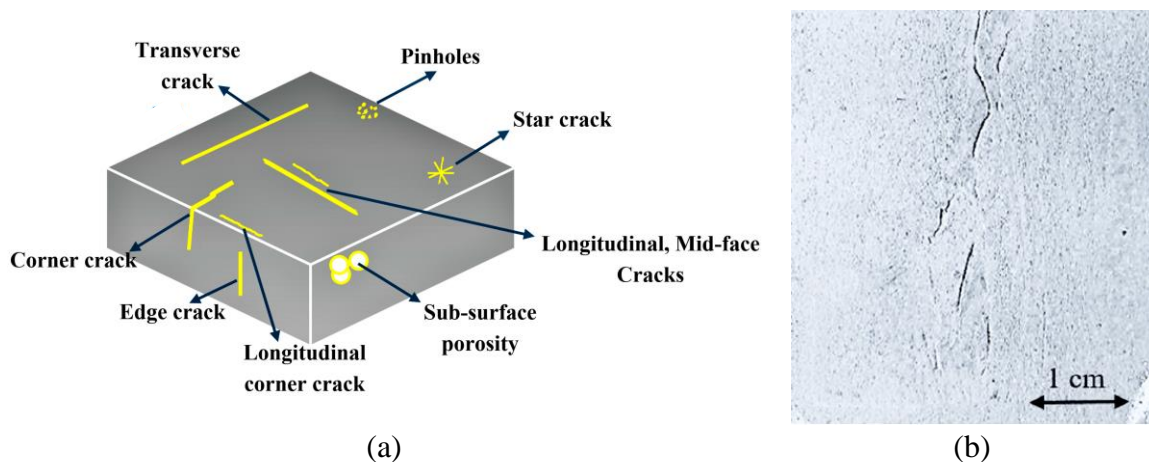


Figure 2.1 Surface cracks: (a) Schematic representation of different types of surface cracks. (b) The visual appearance of tiny surface cracks in metal [34].

Since a crack present physical discontinuity in a material, crack sensing is possible yet challenging. The microscopic size of the crack in the early stage and its multiaxial characteristics are challenges for sensing. In order to detect a tiny crack in its early formation, it is required for any crack sensing system to have high sensitivity and high resolution. From a fracture mechanics point of view, crack location, size, and orientation have to be known to predict the effect of the crack on structural integrity. Crack size involves multidimensional measures, i.e., length, width, and depth, and can change from microscopic to macroscopic as the crack grows. Crack orientation is also an attribute that needs attention as it determines the direction of the crack propagation. Hence, the geometrical complexity of cracks requires the sensor system to have the capability of multi-parameter sensing.

2.1.2 Corrosion and Challenges Related to Sensing

Corrosion is the chemical or electrochemical reaction between a material and environment that changes the properties and produces a deterioration of the material. It is inevitable destruction and unintentional attack of all metals, except noble metals such as gold, platinum, and silver [35]. The deterioration usually comes in the form of rusts in the materials. Steel, which is a mixture of iron and carbon, is the most commonly used metallic material to produce engineering structures due to its low cost and mechanical strength. However, the most considerable disadvantage of steel is its low resistance to corrosion. Steel is frequently used outdoor and exposed to water, soil, chemicals, or highly polluted atmospheres, where corrosion is much more severe than in clean environments [36].

Corrosion in an aqueous solution can demonstrate the corrosion mechanism in general. When steel is in contact with an acid solution, it acts as an anode and cathode of an electrolytic process. The metal atoms at the anode site lose electrons, which are then absorbed by other metal atoms at the cathode site. The anode and cathode are in contact through the electrolyte, conducting exchanges to balance their positive and negative charges [37]. This reaction is responsible for the metal loss and the formation of rust in the corrosion process. The anodic and cathodic reactions during the corrosion process of iron and steel are the same under various conditions. At the anodic areas, an anodic reaction occurs where the iron releases electrons [38]:



At the cathodic areas, reduction of oxygen takes place:



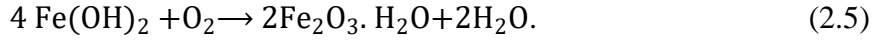
However, there are different versions of the rust formation mechanism. In [38], the resulting OH ions react with the positive ions produced in the anodic areas:



With oxygen in the air, $\text{Fe}(\text{OH})_2$ oxidizes to $\text{Fe}(\text{OH})_3$ and loses its water as



The oxygen in the air converts ferrous hydroxide $4\text{Fe}(\text{OH})_2$ to hydrated ferric oxide $2\text{Fe}_2\text{O}_3 \cdot \text{H}_2\text{O}$ as



The Fe_2O_3 is the composition of hematite and maghemite, which are two oxides compounds found in rust layers. Other chemical compounds can be found in rust layers. Another model, Evans' model in [39], explains the rust formation based on magnetite (Fe_3O_4) and FeOOH . In Evans' version, after anodic reaction in (2.1), the anodic dissolution of iron is balanced by the cathodic reduction of Fe_3O_4 in the rust layer:



When the pore structure is partially dry, oxygen has free access to the pores and re-oxidizes the magnetite, and forms FeOOH :



The cycle of FeOOH reduction and Fe_3O_4 oxidation can start again after wetting.

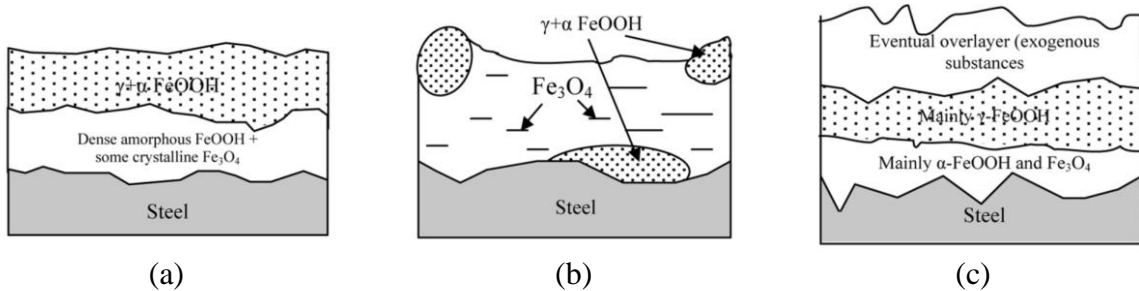


Figure 2.2 Different models of corrosion: (a) two layers. (b) non-layer. (c) three layers [39].

As the corrosion mechanism is complex and involves the formation of many chemical compounds, rust as the corrosion product has a complicated morphology. The structure of the rust layer in steel is debatable, but studies have observed that corrosion is a combination of several substances and is a multilayer structure. Figure 2.2 shows different models of corrosion [39]. The first model in Figure 2.2(a) illustrates corrosion as a two-layer structure: the inner layer is a mixture of crystalline Fe_3O_4 and amorphous FeOOH , while the outer layer is loose crystalline $\alpha\text{-FeOOH}$ $\gamma\text{-FeOOH}$. The second model in Figure 2.2(b) shows that corrosion has no layer but FeOOH compounds surrounded by Fe_3O_4 . The third model in Figure 2.2(c) exhibits corrosion consist of three layers: the inner layer is mainly goethite ($\alpha\text{-FeOOH}$) and magnetite

(Fe₃O₄), while the outer layer is mainly lepidocrocite (γ-FeOOH), and the outermost layer is other substances such as chlorides, silica, and alumina. Table 2.1 lists electrical resistivity and the dielectric constant of materials related to corrosion rust measured at room temperature (25°C) [40]–[46].

Table 2.1 Electrical resistivity and the dielectric constant of materials related to corrosion rust measured at room temperature (25°C) [40]–[46].

Material	Electrical resistivity (Ωm) measured with direct current (DC)	Dielectric constant (measured at particular frequencies in Hz)	Refs
hematite (α-Fe ₂ O ₃)	$(1.58-5.62) \times 10^4$	12 (at 6×10^{10} Hz)	[40]–[42]
amorphous Fe ₂ O ₃	2.12×10^3	4.5 (at 10^5-10^7 Hz)	[40], [41], [45]
magnetite (Fe ₃ O ₄)	$1.58 \times 10^{-4} - 0.1$	20 (at 10^5-10^7 Hz)	[40], [41], [44]
goethite (α-FeOOH)	$(1.30-2.33) \times 10^5$	11 (frequency of the measurement not available)	[40], [43]
lepidocrocite (γ-FeOOH)	$(0.20-0.80) \times 10^5$	2.6 (frequency of the measurement not available)	[40], [43], [46]
Iron	1.0×10^{-7}	–	[40], [41]
Steel	4.6×10^{-7}	–	[40], [41]
Air	4×10^{13}	1	[40], [41]

In long-term exposure to corrosive solutions or atmospheres, steel will continue to corrode over the exposure time. Two general stages of corrosion growth include the initiation and propagation stage. In the initiation stage, corrosion proliferates, forming rust and covering parts of the metal surface. The propagation stage is the condition when corrosion reaches a steady-state and tends to propagate. The effect of long-term atmospheric exposure to metal loss due to corrosion can be expressed by

$$C = At^B \quad (2.8)$$

where C is metal loss, t is exposure time, and A and B are constants that represent corrosion behavior over time. As a rule, B is less than 1. It can vary between 0.3 and 0.7 for rural, urban, and industrial environments and between 0.6 and 0.9 for marine atmospheres.

Concerning sensing for SHM, the detection of corrosion progression is crucial. The unmonitored metal loss due to corrosion can degrade the integrity of structures leading to structural failures. The metal loss and formation of rusts in the corrosion process are physical changes in materials, indicating the viability of corrosion sensing. However, with the existence of rust on the surface of the steel, the structure becomes multilayer, i.e., steel, Fe₃O₄, FeOOH, and other substances. The appearance of corrosion starts with very thin rust, which will grow and spread along with the exposure time. The challenge of corrosion sensing, therefore, is associated with the capability of detecting corrosion progression from the changes in multilayer

materials with different layer properties. Hence, the sensor’s sensitivity is of uttermost importance to be able to detect the corrosion progression in a timely manner.

2.2 Traditional NDT&E Techniques for Defect Detection

Monitoring the performance of a structure, damage detection, and prognosis and prediction of the remaining service life of a structure have been of significant importance since decades ago. The practice started as non-destructive testing and evaluation (NDT&E) and later diverged to structural health monitoring (SHM) [47]. NDT&E is the science and practice of testing and evaluating properties, including physical, chemical, mechanical, or geometrical, of material without compromising the utility and usefulness of the component under evaluation [48]. NDT&E has been practiced for many decades for detecting defects in materials, including crack and corrosion. NDT&E is widely used in global industries dealing with large physical infrastructures, for example, aviation, automotive, rail, oil and gas, power generation, manufacturing, marine, military, and utility industries.

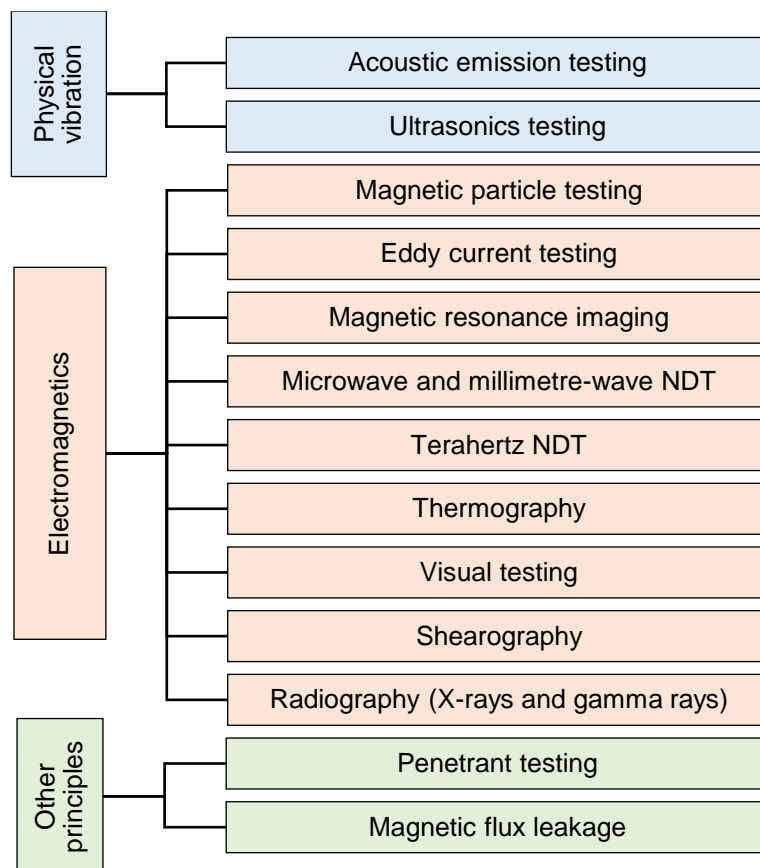


Figure 2.3 Various traditional NDT&E techniques with different working principles, most of which are based on electromagnetics.

Different from NDT&E, SHM aims at the in-service implementation of the damage detection system using installed sensors on the structure with the least manual intervention [49]. Although NDT&E can be considered as part of the SHM process, NDT&E techniques tend to be used for

off-site inspection after manufacturing and not to be performed continuously during the service operation of the structure. There is a wide range of existing and well-established NDT&E techniques, as listed in Figure 2.3. The techniques work based on physical vibration or sound waves, electromagnetics, and chemicals as in penetrant testing. This review is to provide a broad insight into NDT&E techniques that have existed in the literature, their underlying principles, and some recent advances in the field. A summary of the advantages and disadvantages of NDT&E techniques is discussed to highlight the difficulties in applying them for SHM.

2.2.1 Visual Testing (VT)

VT is an NDT method used to test the surface condition of a component performed by operators using eyes and optical aids. VT can be simple and straightforward. An operator in enough lighting can inspect a clean component with simple defects such as misalignment, weld globules, incorrect grinding without equipment. The operator often needs to use optical tools to aid the inspection, ranging from magnifier, fiberscope, or remote video system. VT is technically divided into direct viewing and remote viewing. The direct viewing method is viewing the tested component in the immediate presence of the operator. It can be unaided or aided using magnifying lenses, microscopes, telescopes, or cameras. Remote viewing is performed when the inspected location is difficult to access or when the inspection is not in the immediate presence of the operator. A few examples of tools for aiding remote viewing include borescope, fiberscope, endoscope, and video camera [50].



Figure 2.4 Illustration of visual testing of aircraft components using an endoscope by an operator [51].

The advantages of visual testing are mainly simplicity and the ability to inspect internal parts of components. It can be simple but effective to detect macroscopic flaws such as poor welds and often without expensive equipment. VT can be used to inspect any component on its clean surface, while it also can inspect internal parts of components using aiding tools. However, VT relies totally on human vision sense since the justification is performed manually by trained

operators. Many factors can lead to mistakes in defect detection using VT, such as lighting, cleanliness of the component, and human errors. Furthermore, VT cannot see subsurface defects or defects covered by dirt, paint, or coating.

The traditional VT for inspection of fatigue cracking in infrastructures is studied in recent years [52]. Nowadays, with the improvement of technology in sensing, measurement, and computing power, the traditional VT based on human eyes is frequently replaced by automation [53]. These advances significantly change the traditional VT to machine vision technology [54]. The modern VT uses a camera mounted on an unmanned aerial vehicle [55] and exploits video feature tracking for detecting cracks on large infrastructures [56]. By capturing video data with a camera, defects can be characterized by using trained algorithms such as the deep neural network [57]. Nevertheless, visual testing using either human or machine vision depends on the light condition, surface condition, and colors of the inspected component.

2.2.2 Penetrant Testing (PT)

PT is a simple NDT method used to locate and expose surface opening discontinuities using a penetrating liquid and is based on capillary action. As illustrated in Figure 2.5, PT involves several major steps: pre-cleaning, penetrant application, excess penetrant removal, developer application, inspection/interpretation, and final cleaning. The liquid is applied on the surface of the material and given time to soak into cavities of cracks. The surplus penetrant on the surface is removed, then a developer makes the penetrant that enters the crack visible [58]. Insufficient developer thickness may not draw the penetrant out of the crack, while excessive coating thickness may mask indications.

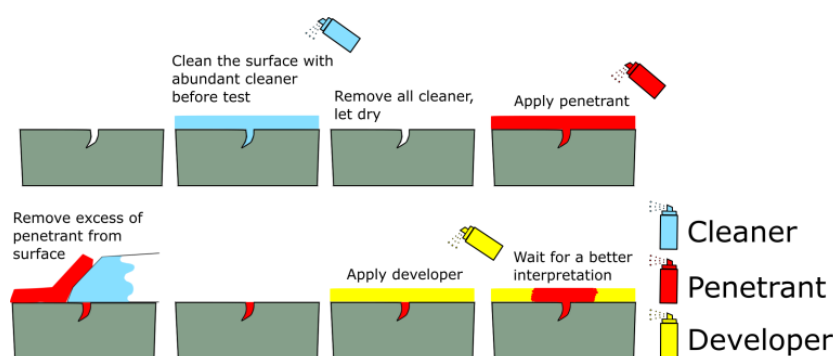


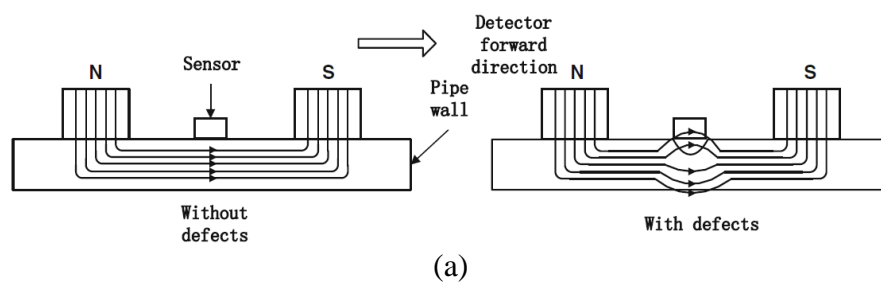
Figure 2.5 Basic steps of penetrant testing [59].

There are two types of penetrants: dye penetrants and fluorescent penetrants. Dye penetrants give a colored indication, while fluorescent penetrants need a source of ultraviolet light for viewing with a bright glowing indication in a darkened room. Fluorescent penetrants are more sensitive than dye penetrants. PT has several advantages for inspection, such as high sensitivity to small surface discontinuities, quick and inexpensive, and can test metal and non-metallic

materials. The disadvantages are the requirement of the operator and the need for surface preparation and cleaning. PT is used extensively in the aviation and automotive industries. PT has not changed much over the years; penetrants are developed to be more sensitive, but the process remains the same. One of the recent advances in the field of PT is the bacteria-based fluorescent penetrant, which can achieve comparable detection of submillimeter cracks to conventional penetrants [60]. Furthermore, there has been an effort to automate the defect detection in PT using image processing and the Random Forest algorithm [61].

2.2.3 Magnetic Flux Leakage (MFL)

MFL is an NDT&E method working based on the high-permeability characteristics of ferromagnetic materials. The principle of MFL is illustrated in Figure 2.6(a). When external magnetic fields temporarily magnetize a ferromagnetic material, the magnetic field will be mostly constrained inside the material if it is continuous and has no defect. When there is a defect in the material, the magnetic lines will change the paths due to the low permeability and large magnetic resistance of the defect [62]. The magnetic flux from the defect will diffuse and form magnetic flux leakage above the surface of the component, signaling the presence of defects like crack, corrosion, pitting, and wall loss. MFL is one of the most popular methods for pipeline inspection [63]. It is also extensively applied in pressure vessels, rails, and train wheels. An MFL tool for pipeline inspection is shown in Figure 2.6(b). It comprises a drive section, a central magnetizer, and a data logger.



(b)
Figure 2.6 MFL testing: (a) Basic principle. (b) A large MFL tool for pipeline inspection [62], [63].

MFL can examine many types of defects, including surface cracks, stomata, cavities, and corrosion pitting. It detects not only external but also internal defects. A disadvantage of MFL is the requirement of strong magnets to achieve magnetic saturation in the materials. The tool needs to be running on and in contact with the tested structure using rolling wheels. MFL relies

on qualitative analysis of signal because there is no direct correspondence between defects and the MFL signal. Besides, MFL is only applicable for ferromagnetic materials and sensitive to the movement velocity of the MFL tool.

Recent studies are conducted to advance the capabilities and tackle the disadvantages of MFL. It was demonstrated that MFL could detect rail defects with a depth of up to 20 mm under the upper rail edge [64]. The reduction of the velocity impact on the MFL signal was attempted using compensation by finding the relations between the MFL signals and the velocity [65]. Regarding corrosion detection, a quantitative evaluation of corrosion degrees of steel bars using MFL was studied [66]. A quantitative analytical model was developed but only limited to specific corrosion samples used in the experiments.

2.2.4 Ultrasonic Testing (UT)

Ultrasonic testing (UT) is an NDT technique that uses high-frequency sound waves, typically between 0.5 and 25 MHz, to detect surface and subsurface defects in sound conducting materials [67]. The principle is similar to echo sounding and is depicted in Figure 2.7 [68]. A UT probe emits sound waves passing through the material. The surface of the tested component must be clean and smooth with a couplant applied to exclude air between the probe and component under test. When the sound wave hits a defect, it will be reflected partly to the receiver in the probe and plotted on a graph. The size and position of the defect can be interpreted from the signal by a skilled operator. Time of flight (TOF) feature from the sound waves is commonly used in ultrasonic testing for determination of size and position of defects such as weld imperfections, cracks, and stress corrosion cracking [69]–[71].

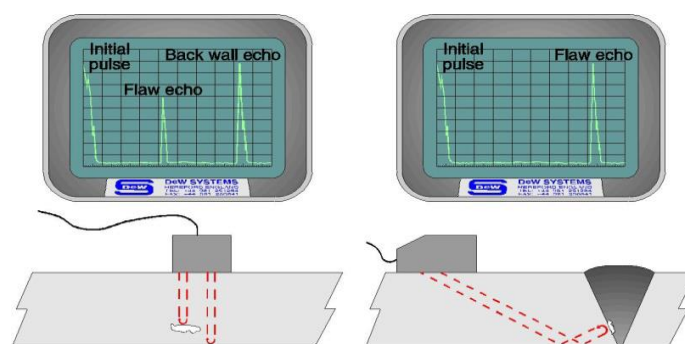


Figure 2.7 Basic principle of ultrasonic testing showing a UT probe emitting a sound wave and receiving the reflected echo signal that indicates a defect [68].

The advantage of UT is that it can scan for defects both on and underneath the surface. On the other hand, not all materials are receptive to ultrasonic testing. The probe must be in contact with the couplant medium and material surface to perform scanning. Moreover, the surface must be smooth and free from spatters and strikes. It also has the disadvantage that it requires

a good deal of skill and training to perform testing. Recent advances in UT show efforts in improving detection accuracy, sensitivity, and resolution using phased array UT [72], [73], laser UT [74], and signal processing methods such as focusing method and time-frequency analysis [75]–[77].

While UT is intended for defect detection in the short-range, it branches out to ultrasonic guided wave testing (UGWT) for long-range ultrasonic inspection. Guided waves can propagate long distances in thin-walled structures such as plates and pipelines. Compared to UT, the propagation direction of ultrasonic guided waves is parallel to the examined structure rather than penetrating through the thickness, as shown in Figure 2.8. However, there is a trade-off between the coverage and the sensitivity to detect small defects.

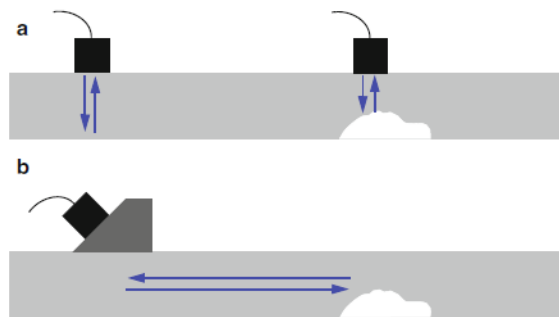


Figure 2.8 The difference between bulk ultrasonic and guided wave testing in terms of detection range [78].

Due to the capability of monitoring large structures from one sensor position, UGWT has been researched for SHM [79], [80]. Monitoring on large structures require lower frequencies to achieve a long propagation distance, but the sensitivity will be sacrificed due to the large wavelength. UGWT has been applied to crack and corrosion detection on buildings and bridges [81]. While giving benefit in terms of coverage than UT, wave propagation of UGWT is more complex and depends on the geometry of the structure and excitation frequency. In line with these limitations, signal processing for localization of damages using UGWT [82] is crucial, especially in complex structures [83].

2.2.5 Eddy Current Testing (ECT)

ECT works based on the induction of electrical currents in conductive material and observing the interaction between the induced currents, called eddy currents, and the material. ECT is widely used for surface and near-surface defect detection. As illustrated in Figure 2.9, eddy currents are induced by alternating electromagnetic fields generated by the excitation coil of an ECT probe. The presence of defects can be monitored simultaneously by measuring changes in

probe responses [84]. Typical frequencies used in ECT lie in the region of 200 Hz to 6 MHz, depending on the type and thickness of the material being tested.

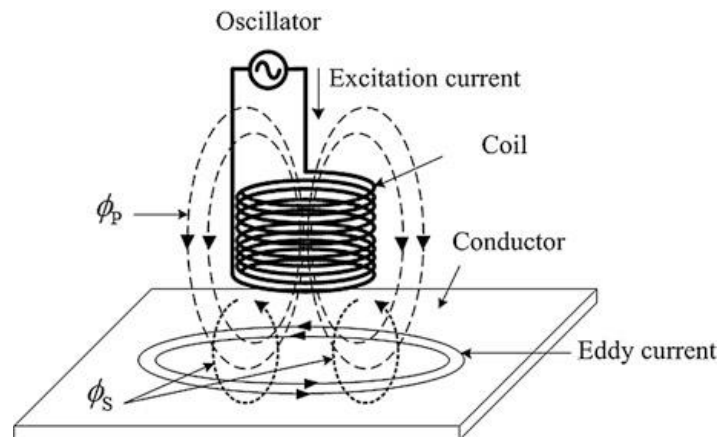


Figure 2.9 Principle of eddy current testing using a coil probe that induces eddy currents in metal under test [84].

Based on the excitation, ECT can be divided into single-frequency ECT, multi-frequency ECT, pulsed ECT, and swept frequency ECT. Multi-frequency ECT uses excitation current signals at several frequencies at the same time. It can obtain defect information from different depths due to the different penetration of different frequencies [85]. However, the multi-frequency eddy current provides the limited capability of quantification of defects. Then, pulsed ECT or PEC is developed to overcome the drawback of limited data and features in multi-frequency ECT [15]. The excitation signal of pulsed ECT is a square wave with a certain duty cycle, and thus the response signal contains rich frequency components for sensing information. Pulsed ECT has considerable achievements in the detection of cracks and corrosion in structures [86]. Since pulsed ECT suffers from decayed signals at higher frequencies, sweep frequency ECT (SFECT) has been developed as alternatives for inspection of material thickness and multilayered structures [87]. Recently, the SFECT is further extended by exploiting the principle of wireless power transfer (WPT). WPT based ECT can enrich the sensing features by having two resonances generated by a pair of Tx-Rx coils [88].

In general, ECT has advantages by offering a non-contact and sensitivity to surface and near-surface defects. Portable ECT instruments are available for rapid inspection by the operator. It can be embedded with a machine for automatic scanning and a thorough evaluation of conductive materials. Several disadvantages of ECT are that it can test only conductive materials, flaws parallel to the probe may be undetectable, and limited lift-off. As the probe is lifted away from the material under test, less magnetic flux reaches the material until, at some distance, eddy current is no longer formed in the material. Lift-off is the main aspect that affects ECT signals causing errors in data interpretation [89], [90]. Recent advancements in ECT are

in numerical simulation [91], optimization of probe design and configuration [92], improvements in signal conditioning circuitry [93], as well as signal processing algorithms for the development of quantitative non-destructive evaluation (QNDE) [94].

2.2.6 Microwave and Millimeter-wave NDT

Microwave and millimeter-wave NDT are electromagnetic NDT techniques operated in frequencies ranging from 300 MHz to 300 GHz, corresponding to wavelengths of 1 m and 1 mm, respectively [95]. Microwave frequencies span from 300 MHz to 30 GHz while millimeter wave ranges from 30 to 300 GHz. Microwave and millimeter-wave NDT are well-suited for inspecting dielectric materials due to their ability to penetrate and their sensitivity to changes of dielectric properties of these materials. On the other hand, these frequencies cannot penetrate highly conductive materials but are sensitive to surface defects, pitting, and surface roughness in metals [96]. Microwave and millimeter-wave NDT have been reported for the detection of surface-breaking cracks and corrosion [97], [98].

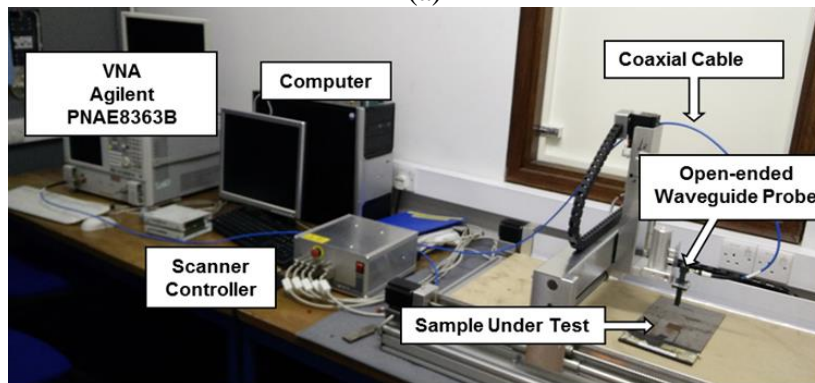
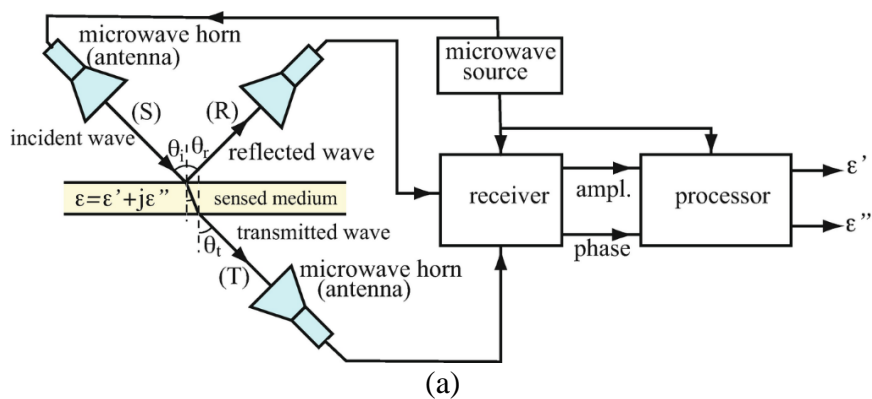


Figure 2.10 Microwave and millimetre-wave NDT: (a) General setup diagram for the evaluation of complex permittivity of material [99]. (b) Illustration of a real setup using an open-ended waveguide probe [98].

Microwave and millimeter-wave NDT techniques work based on the interaction between high-frequency electromagnetic waves with materials, such as scattering, attenuation, reflection, transmission, and resonance. The systems can be configured using sources, antennas, and data processing unit. A general setup diagram of microwave and millimeter-wave NDT based on

reflection and transmission is shown in Figure 2.10(a). With different configurations of antennas, reflection and transmission responses can be used for evaluating the dielectric constant and loss tangent of a material. Apart from permittivity measurement, microwave and millimeter-wave NDT are also used for microscopy allowing quantitative measurement below the wavelength of the used frequencies. This uses sub-wavelength antennas such as an open-ended waveguide, open-ended transmission line, coaxial tip, or resonant probe [99]. An example of a microwave microscopy setup using an open-ended waveguide is depicted in Figure 2.10(b). The system employs a VNA to collect scattering parameters data and a scanner allowing 2D or 3D imaging of the tested material.

The advantages of microwave and millimeter-wave NDT are that they are non-contact methods and can detect defects on dielectric materials and surface defects in metal with high accuracy and sensitivity even under dielectric coating or paint. However, these techniques are also sensitive to distance variations, and thus the lift-off should be consistent during testing. Some recent advances in microwave and millimeter-wave NDT are the near-field inspection of materials with a complex geometry such as multi-layered and curved structures [100], which introduces variations from multiple physical sources, 3D reconstruction of materials [101], high-resolution imaging using radar [102], and utilization of artificial intelligence approaches [103].

2.2.7 Thermography

Thermography is an imaging technique using the thermal radiation of an object to determine its characteristics. Heat can be transmitted by radiation, convection, and conduction. In thermography, the heat energy transmitted by radiation is of interest and utilized for material inspection. This radiated energy is called infrared, which is the electromagnetic spectrum between the millimeter-wave and visible light with a wavelength of 0.75 μm to 100 μm . There are two basic types of thermography: passive and active. Both passive and active thermographies use an infrared (IR) camera containing many IR sensors, which can measure small temperature differences [104], [105].

Principles of passive and active thermography are illustrated in Figure 2.11. In passive thermography, the temperature of an object is directly measured without using external heating. It is generally used to detect hot spots to indicate problems in electrical and mechanical components. A control PC is used to trigger the IR camera for capturing IR radiation from the test object and save the thermal data. The principle of active thermography is slightly different. It excites the material under test using a thermal source, which can be light, laser, ultrasound, eddy-current, or microwave. In Figure 2.11(b), flash lamps are employed as the external heating

source. Defects can be detected using the temperature variations caused by the presence of discontinuities within a material. Thermography has been demonstrated as an effective method for NDT of cracks and corrosion [106], [107].

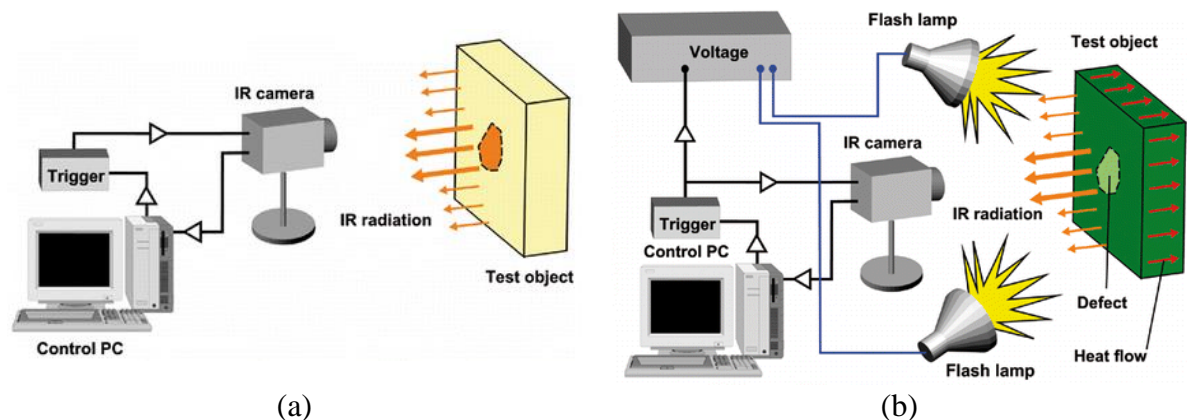


Figure 2.11 Principles of thermography: (a) Passive thermography. (b) Active thermography using a flash lamp as the external heating source [108].

Like the other NDT&E techniques, thermography has advantages and disadvantages. Both passive and active thermography are versatile as they can be applied to a wide range of components and many NDT&E applications. Inspection can be performed remotely with a high stand-off distance, quick, and even in a high-temperature environment. Thermal imaging of defects can be carried out on composite materials and allow accurate interpretation. The disadvantages of thermography are that the equipment is expensive, the reflective surface can lead to false hot spots, and the interpretation of results may be difficult due to many parameters involved. Recent advancements in thermography for NDT are the 3D reconstruction of subsurface defects [109], inspection and data analysis of challenging aerospace structures [110], and UAV thermographic system for inspection of large structures [111].

2.2.8 Radiography (X-Rays and Gamma Rays)

Radiography is a volumetric NDT technique that uses X-rays or gamma rays to penetrate through a material and captures the internal form of the material. X-rays and gamma rays are electromagnetic spectra above ultraviolet (UV). It has the same physical nature as visible light, IR, and UV, but the wavelength is much shorter, allowing them to a certain extent to penetrate all materials. Radiography is one of the earliest NDT methods, but alternative methods replaced it due to the health and safety implications of handling radioactive materials [68]. Nevertheless, radiography remains one of the volumetric NDT techniques. Figure 2.12 shows a schematic diagram for the principle of radiographic inspection. A component under test is placed between a source of X-rays or gamma rays and a radiography film. An object with a high density, e.g., a thick object, absorbs more radiation, reducing radiation hitting the film, and thus produces a lighter image.

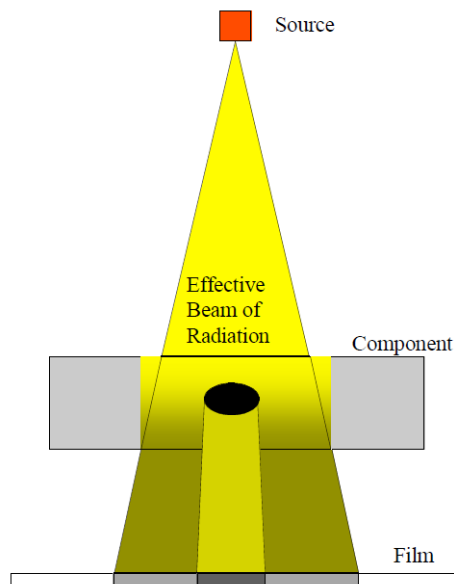


Figure 2.12 Principle of radiographic inspection [68].

Conversely, an object with a low density will absorb less radiation causing more radiation to hit the film and produces a darker image on the film. In radiographic inspection, radiation from the source passing through any defects will be less attenuated than the non-defected area. The defective area absorbs less radiation and gives greater exposure to the film. Thus, the radiograph is darker in the defective area. Radiography has demonstrated its capability for crack detection in aircraft wings [112] and steel corrosion inside concrete structures [113].

The advantages of radiography for NDT are that it can be used for most solid materials, and it can inspect internal defects. However, radiography also has several disadvantages. It can only detect defects in particular orientations and has difficulties in detecting small defects. It requires access to two sides of the tested material and is impractical to test components with complex geometry. Additionally, radiography requires safety consideration and high cost for NDT&E. Still, radiography is studied in recent years. Some advancements in radiography are in dynamic radiography for real-time characterization of cracks [114] and utilization of image processing and artificial intelligence for enhancing defect detection and visibility [115], [116].

2.2.9 Summary of Traditional NDT&E Techniques for Defect Detection

Some traditional NDT&E techniques for defect detection that have been discussed are summarized in Table 2.2. Their advantages and disadvantages in terms of capabilities in detecting defects in different materials, requirements, and costs are highlighted. In general, all the traditional NDT&E techniques can be used to inspect different types of defects in metallic materials with certain depths, lift-off, and requirements. VT, PT, microwave NDT, and millimeter-wave NDT are applicable for surface defects, especially surface-breaking cracks.

ECT is suitable for surface and near-surface defects. Subsurface and internal defects can be examined using MFL, UT, thermography, and radiography.

Table 2.2 Advantages and disadvantages of traditional NDT&E techniques.

NDT&E technique	Advantages	Disadvantages
Visual testing	Simple; able to detect surface defects in metallic and non-metallic materials	Manual inspection by an operator; applicable only on a clean and non-coated surface; difficult to detect small defects; depending on eyesight and light
Penetrant testing	Simple; inexpensive; able to detect small surface cracks in metallic and non-metallic materials	Manual inspection by an operator; applicable only on a clean, smooth, and non-coated surface
Magnetic flux leakage	Able to detect many types of surface and subsurface defects in ferromagnetic materials	Applicable for only ferromagnetic materials; using large magnets for magnetization; sensitive to the movement velocity of the tool
Ultrasonic testing	Able to detect surface and subsurface defects	Manual inspection by an operator; applicable only for sound conducting materials on a clean and non-coated surface; use of liquid couplant; guided wave testing has complexity in wave propagation along complex structures
Eddy current testing	Non-contact; sensitive to the surface and near-surface defects on conductive materials	Only for conductive materials; limited lift-off
Microwave and millimeter-wave NDT	Non-contact; able to detect defects in multi-layered dielectric materials and surface defects in metallic materials	Limited lift-off; sensitive to the variation of distance; strong interferences
Thermography	Quick; high stand-off distance; able to detect surface and subsurface defects	Expensive equipment; high power requirement; difficult interpretation of results
Radiography	Able to detect surface and subsurface defects on most solid materials	Expensive equipment; two-side access of the tested materials; difficult to detect small defects and to test components with complex geometry; radiation safety concern

Although the traditional NDT&E techniques have good sensitivity, resolution, and reliability for defect detection, there are issues in applying them for SHM. First, traditional NDT&E techniques are expensive for large-scale applications because of the requirement of operators, wiring, and high-cost equipment. For example, VT, PT, and UT require operators, while thermography and radiography involve expensive equipment. Second, these techniques are limited in range due to the requirement of power, sensitivity, and resolution. Probes in UT, MFL, ECT, and microwave and millimeter-wave NDT must be in contact with or in proximity to, typically in millimeters, the tested components. Third, NDT&E techniques are too cumbersome to monitor the growth of defects in large-scale structures continuously. The equipment is relatively large and wired, making them impractical to be mounted and distributed on infrastructures for in-situ monitoring. Instead of monitoring on the site, the inspection using NDT&E techniques often needs to be carried out in a laboratory environment. While

components are taken off from the site, the structure has to be out of service during the inspection.

2.3 SHM and Its Relation to NDT&E

As described in Chapter 1, SHM is the implementation of damage identification strategies through data acquisition from sensors to assess and monitor the health of a structure [8], [9]. SHM gathers several techniques, including structural dynamics, materials, sensor technologies, electronics, and signal processing, to diagnose structural health and to give a prognosis of its remaining life. The implementation of SHM systems generally involves four aspects: sensors and actuators, data acquisition systems, signal conditioning and processing, and statistical models [117]. The sensors are critical parts in SHM systems, which must be selected by considering variables to measure, constraints in the installation, and cost. Since sensors and some equipment need to be mounted permanently to the structure, SHM measurements demand cost-effective sensors. Besides, SHM needs continuous and reliable measurements over a long period during the operation of the infrastructure. Therefore, SHM systems should ideally fulfill these requirements: low-cost, able to perform continuous assessments, sensitive to low levels of damage and different damage types, insensitive to ambient loading conditions, measurement noise, and environmental condition changes [118]. The aspect of continuous assessment in SHM requires many sensors to be distributed and installed permanently over the structures, which can be achieved through wired or wireless connections.

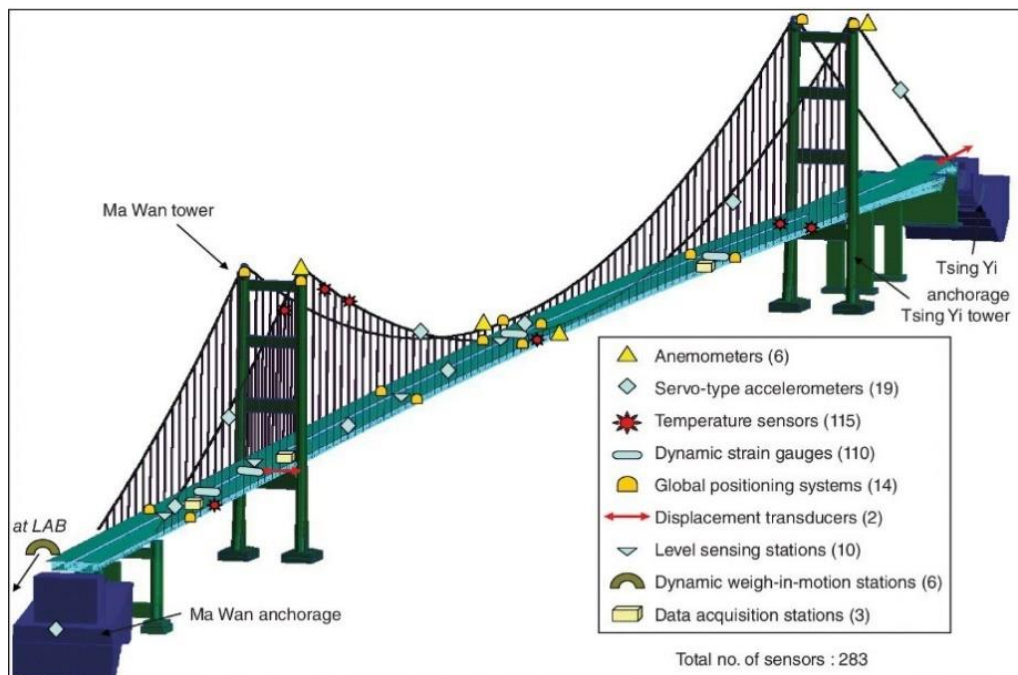


Figure 2.13 Example of an SHM system in Tsing Ma Bridge with numerous sensors distributed over the bridge [119].

As an example, Figure 2.13 shows an SHM system installed in Tsing Ma Bridge, which is a two-span suspension bridge providing services for both highway and railway traffic in Hongkong. The SHM system installed on the bridge consists of 283 sensors for eight types: anemometers, accelerometers, temperature sensors, strain gauges, GPS, displacement sensors, level sensing stations, dynamic weigh-in-motion stations [119]. The sensors analyze the global condition parameters, such as bridge responses and deformations, environmental conditions, traffic loads, and bridge features. Like the other typical SHM systems, however, there is no sensor dedicated to the detection and monitoring of local defects.

Regarding its essential function for diagnosis, SHM is similar to NDT&E. However, SHM is beyond NDT&E, and they are both complementary. The aspect of embedding sensors in SHM poses constraints that it is problematic to integrate an NDT&E system into a structure. Also, the prognosis aspect in SHM is not only about detecting defects on a structure but also includes the monitoring of its history through frequent or continuous inspections [9]. The British Institute of Non-destructive Testing (BINDT) describes the relationship between NDT&E, condition monitoring (CM), and SHM, as illustrated in Figure 2.14 [120]. NDT&E is mostly performed at the manufacturing stage to ensure that engineering components are free from defects. CM comes into play when the components are in service while the performance needs to be assessed during the operation. The data acquired from on-board CM can provide meaningful information, but periodic inspection using NDT&E techniques may also be used to interpret the structural condition. Covering both NDT&E and CM, SHM is the overall concept of using sensor systems to observe structural health conditions using the information gathered from both at the manufacturing stage and during operation.

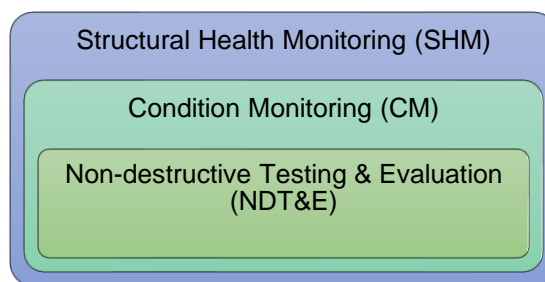


Figure 2.14 The relationship between NDT&E, CM, and SHM [120].

The gap between NDT&E and SHM is in the lack of techniques to perform in-situ and continuous monitoring of defects. The current SHM practice using CM is, in general, limited to monitoring the global condition of large structures, such as deformation, loads, environmental conditions, etc. [12]. Meanwhile, performing NDT&E only at the manufacturing stage is insufficient for timely detection and continuous assessment of defects. Also, as

highlighted in 2.2.9, periodic inspection using the traditional NDT&E techniques encounters problems associated with the high cost, limited lift-off, and troublesome installation due to the wiring and the sizeable equipment. Hence, there is a requirement to bridge the gap between NDT&E and SHM by developing new techniques for in-situ and continuous monitoring of defects in metallic infrastructures.

2.4 SHM Technologies and Trend Towards the Internet of Things (IoT) based SHM

Over the last decades, extensive efforts have been made in the development of SHM technologies. The research trends have changed during the past 40 years from old SHM, new SHM to emerging and future SHM, as illustrated in Figure 2.15. In the 1970s, studies and practices of the old SHM involve wired SHM and independent sensors for monitoring the global condition of infrastructures. It was the improvements of different types of sensors, such as piezoelectric ceramics and ultrasonic sensors, that enabled old SHM. The systems involved lengthy cables that both source power and collect data from each sensor individually. For the detection of local defects, periodic inspection using NDT&E techniques has been a routine to check up and maintain structural health. The major problems with the old SHM are messy wires, complex installation, and high cost.

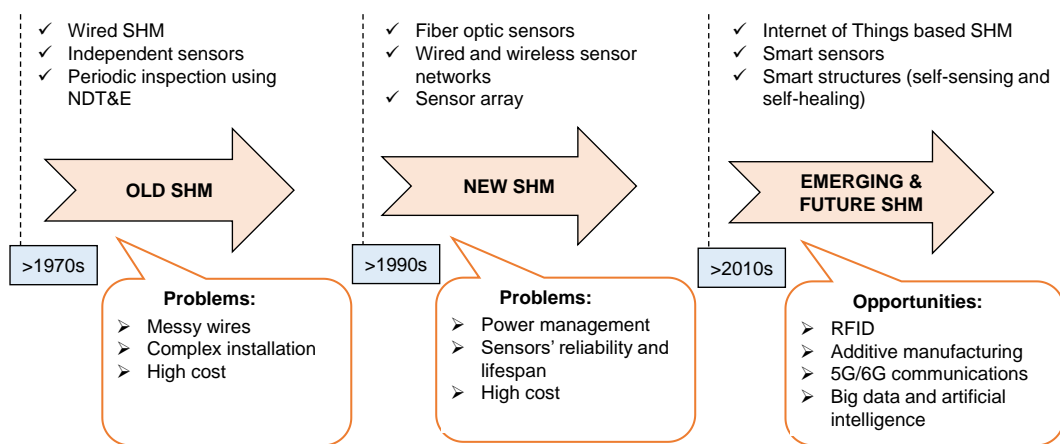


Figure 2.15 Trends of SHM technologies from old SHM, new SHM, to future SHM [121]–[123].

After the 1990s, the new SHM was influenced by the advancements in fiber optics, microprocessors, and wireless communications. Two popular technologies were fiber optic sensors (FOS) [124], [125], and wireless sensor networks (WSN) [126]. Sensors can be more densely distributed over the monitored infrastructures, enabling measurements from a wide range of locations. A single fiber optics can contain many sensors, while sensor arrays can be implemented using WSN with coordination among sensor nodes through wireless communications. FOS is small in size and lightweight so that it can be embedded into structures. Also, the immunity to electromagnetic interference ensures the data transfer from FOS fast and

reliable. Like wired SHM systems, however, FOS based SHM systems suffer from high cost, intricate wiring, and complicated installation. Whilst for WSN, the issue is related to power management since each wireless sensor node is battery powered, which leads to a limited lifetime. WSN do not have wiring issues as in FOS based SHM systems and wired SHM systems. Therefore, WSN offer reduced system cost, short deployment time, and easy installation. Although the cost is lower than wired SHM and FOS, however, the cost of WSN for large-scale deployment can still be relatively high. The system cost increases linearly with the number of distributed wireless sensor nodes, and thus, spatial granularity becomes a vital issue. WSN use battery-powered devices so that each wireless sensor node needs not only a set of electronic modules but also batteries and energy harvesters. Moreover, the battery-powered sensors used in WSN are at least twice more expensive than passive sensors. Hence, the costs of battery-powered devices and active sensors limit the granularity of their deployment.

The emerging and future SHM after the 2010s is towards the internet of things (IoT) based SHM [123]. Smart sensors are expected to be economically feasible, massively distributed in infrastructures, and connected to the internet. Future SHM will enable greater monitoring and smart structures with self-sensing and self-healing capability [121]. As one of the IoT key enabling technologies, WSN needs to be developed further for future SHM along with the advancements in energy harvesting and reduced size electronics with connectivity to the internet. Another IoT key enabling technology, i.e., RFID, will also play important roles for future SHM. RFID offers wireless, passive, and low-cost platforms for identification and sensing, which makes it possible to distribute a massive number of sensors in infrastructures. The trend towards the IoT based SHM is aided by other emerging technologies, including additive manufacturing, 5G/6G communications and beyond, big data, and artificial intelligence [127]. The following subsections describe the existing SHM technologies, including wired SHM, FOS, and WSN, as well as more details of the future IoT based SHM.

2.4.1 Wired SHM

In the past, SHM systems were designed using wired sensors. A traditional wired SHM system involves several components: a sensor system, a data processing system (including the data acquisition, transmission, and storage), and a structural health evaluation system. The data from different types of sensor systems are transmitted through coaxial cables and processed in the data processing system. There are many disadvantages of the wired SHM systems, such as high-cost, low-efficiency, labor-intensive and time-consuming deployment, susceptible to disturbance, and inflexibility [128]. The deployment is constrained to locations with access to the power grid as alternative portable power sources are rarely adequate. Another problem is

the wiring to supply power and interconnect the components. The wiring makes the installation complex, high-cost, and time-consuming.

2.4.2 Fiber Optic Sensors (FOS)

Fiber optics are known as a medium for data transmission in telecommunication using optical pulses transmitted over long distances. Since glass and polymer are sensitive to mechanical and physical perturbations, fiber optics can also be used as sensors [129]. Fiber optic sensors-based SHM systems have been practiced for real-time and continuous assessment of many civil infrastructures such as bridges, buildings, tunnels, pipelines, wind turbines, railway infrastructure, and geotechnical structures. Figure 2.16 shows two examples of FOS mounted onto cages of reinforced piles and a steel pipe to monitor temperature and strain. The integration of FOS allows for sensitive detection of strain in massive concrete structures. The sensors can also give precise deformation of piles during static loading as well as evaluation of the load-bearing capacity. For monitoring a steel pipe, FOS can also be embedded by sticking tape sensing fibers to adhere to the pipe spirally. The sensors can measure both strain and temperature distribution along the pipe structure [129].

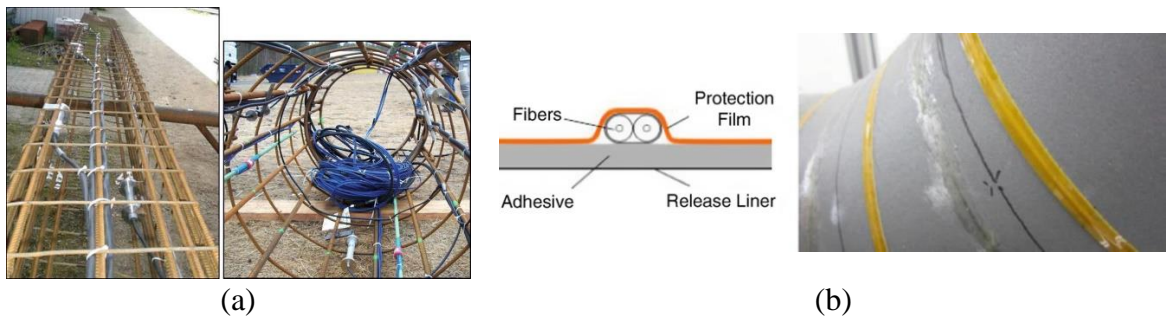


Figure 2.16 FOS mounted onto structures to monitor temperature and strain. (a) FOS mounted onto cages of reinforcement piles. (b) FOS mounted onto a steel pipe [129].

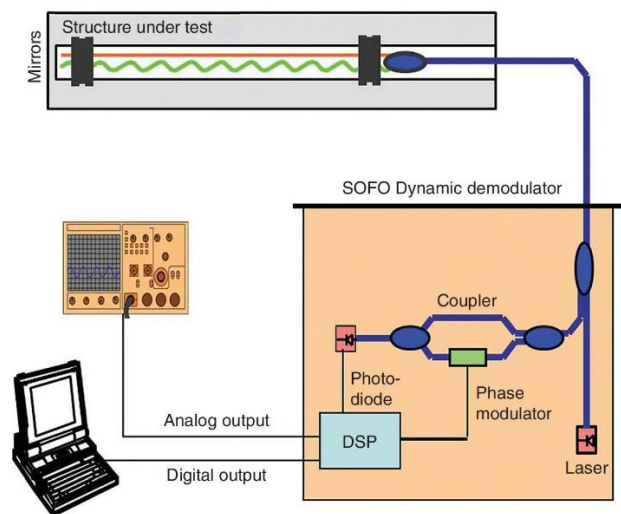


Figure 2.17 SOFO interferometric sensor system. Courtesy of Smartec. [119], [130].

Fiber optic sensors can be classified into three different classes: interferometric sensors, grating-based sensors, and distributed sensors [131]. Some typical fiber optic sensors for SHM applications include SOFO interferometric sensors, Fabry-Pérot interferometric sensors, Fiber Bragg Grating (FBG) sensors, and distributed Brillouin and Raman scattering sensors. In general, a FOS system consists of a light transmitter (e.g., laser), a receiver (e.g., photodiode), an optical fiber, a modulator element, and a signal processing unit. When strain or temperature variation occurs, the FOS embedded in the structure will expand or contract. With the change of the length of the optical fiber, the FOS modulates the light and reflects an optical signal to the signal processing unit for interpreting the physical quantities that represent the condition of the structure [132]. Figure 2.17 shows the Surveillance d'Ouvrages par Fibres Optiques (SOFO) system, which is the most successful low coherent interferometric sensor for SHM. Physical variation in structures is represented by the changes in the optical phase difference between two interference light waves. The systems have been deployed in more than hundreds of structures, including buildings, bridges, oil pipes, and tunnels [133]. SOFO interferometric sensors are long-gauge sensors with a measurement distance of up to 100 m and a resolution in the order of micrometers. For extended measurement ranges, the distributed Brillouin sensors can offer 30 km to 200 km with a spatial resolution from 1 m to 4 m [131].

FOS has been used for SHM because of its inherent advantages such as small size, lightweight, immunity to electromagnetic interference (EMI), embedding capability, and distributed measurement [132]. However, fiber optic sensors are expensive for widespread use in SHM and pose the complexity of wiring in the installation [130]. Despite the widespread use for strain and temperature measurement, FOS has been studied to monitor crack in concrete structures without the need for prior knowledge of the crack locations [134]. Several cracks can be detected, located, and monitored by a single fiber. The crack sensing can be either based on the fiber breakage or the intensity loss due to deformation. In addition, FOS has been investigated for corrosion detection using different mechanisms. Corrosion of the steel reinforcing bars in concrete structures can be measured from the expansive layer of corrosion products at the reinforcing bars and the surrounding concrete. In the other detection mechanisms, corrosion-induced damages and water ingress in a pipeline can also be detected using FOS [135], [136].

2.4.3 Wireless Sensor Networks (WSN)

WSN can solve the issue of wiring in the wired SHM systems. WSN can be defined as the networks of devices, which can sense the environment through sensors and communicate the data collected from the monitored field through wireless links [137]. The devices are usually called wireless sensor nodes. Different from wired SHM systems, WSN-based SHM systems

use wireless communication to transfer data from node to node and from node to the central data repository, as illustrated in Figure 2.18. With the ability to communicate wirelessly, a wireless sensor node is not merely a sensor but rather an autonomous data acquisition device to which several sensors (e.g., piezoelectric, accelerometers, etc.) can be attached alongside a wireless transceiver. As shown in Figure 2.19, a wireless sensor node functionally consists of several parts: sensing interface, computing core, actuation interface, and wireless radio. The computing core is usually a battery-powered microcontroller that can control actuators, collect and process data from several sensors, and transfer the data through a wireless radio transceiver [119], [138].

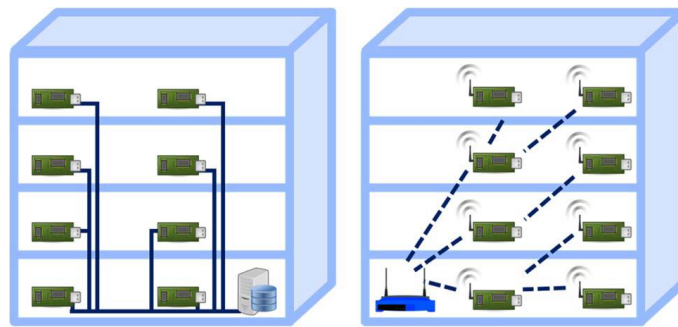
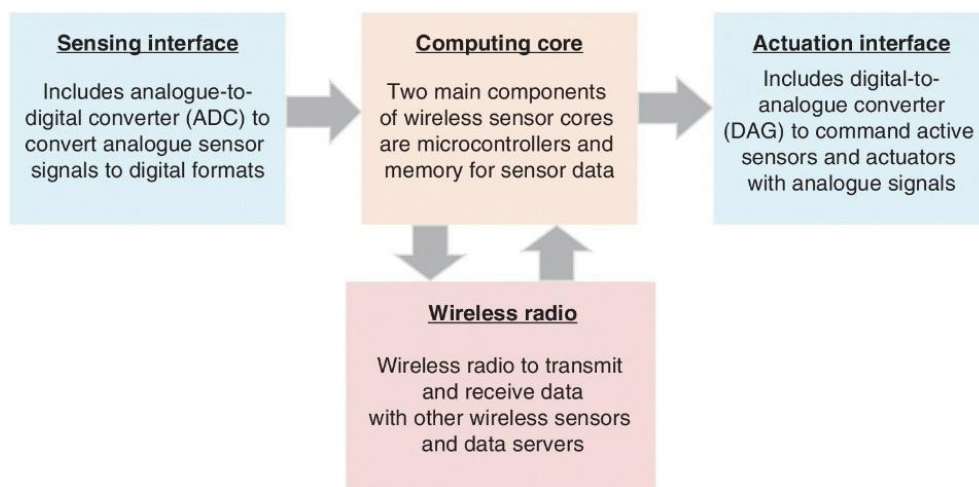
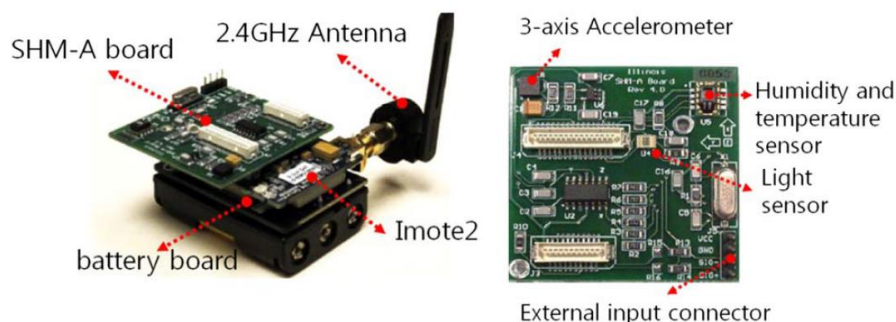


Figure 2.18 Conceptual diagram of wired sensors and wireless sensor networks (WSN) [138].



(a)



(b)

Figure 2.19 Wireless sensor node: (a) Functional block diagram. (b) A commercial wireless sensor node platform (Imote2) [119], [138].

Depending on the variables to measure, WSN based SHM systems can use a wide variety of sensors, including piezoelectric sensors, strain gauges, LVDT, and MEMS sensors. These sensors can measure diverse variables such as acceleration, angular velocity, displacement, deformation, temperature, humidity, pressure, gas, etc. For crack monitoring in concrete structures, WSN can use piezoelectric sensors made from lead zirconate titanate (PZT) material [139]. The presence of fractures changes the mechanical impedance of a structure, which is directly related to the electrical impedance of the piezoelectric sensor. For corrosion monitoring, several sensors can be used with WSN; for example, an electrical resistance sensor [140], [141], and the sensing electrodes made of graphite rod and carbon steel [142].

Several advantages have made WSN a compelling alternative to the wired based SHM. WSN based SHM systems offer reduced cost, short deployment time, and ease of installation. For example, the price for wired sensor networks can be \$10000 to \$25000, while a wireless sensor node is approximately \$500 [143]. Due to the low-cost feature and the ease of installation, the number of sensors and scalability of WSN can be higher to achieve finer grain of monitoring. However, the major constraint with WSN is the short lifespan due to the limited battery life. This poses the need for ultralow-power circuits and energy harvesters for WSN [138], [144]. Furthermore, the wireless data transfer leads to some drawbacks such as sensitivity to environmental effects, lower sensor data rate, unreliable connection, and difficult synchronization. Hence, there are still many challenges and open research issues for WSN, including limitation of sampling rate, power efficiency, data rate and throughput, fault tolerance, time synchronization, distributed processing, energy harvesting, and optimal sensor placement [145].

2.4.4 The Internet of Things (IoT) based SHM

The internet of things (IoT) is a paradigm to connect uniquely identifiable “things” or real-world objects to the internet [18]. The term “Internet of Things” was first introduced in 1999 by Kevin Ashton from Auto-ID center, Massachusetts Institute of Technology (MIT) [146]. The IoT enables “connectivity for anything from any time, anyplace connectivity for anyone.” With the implementation of IoT, the internet will sense information from the physical world, not only from people but also from a huge number of objects [19]. The revolution will be the interconnection between objects and to the internet, creating a smart environment. The integration of identification tags, sensors/actuators, and communication technologies are the foundation of IoT, which allows objects and devices to cooperate with each other and to be sensed by the internet [20]. Based on the impact of the data generated, the IoT will involve a wide range of application scenarios from individual to national level organizations, as shown

in Figure 2.20 [19]. Infrastructure and transportation are among a few application domains of IoT that have a close relation to SHM.



Figure 2.20 Application areas of IoT [19].

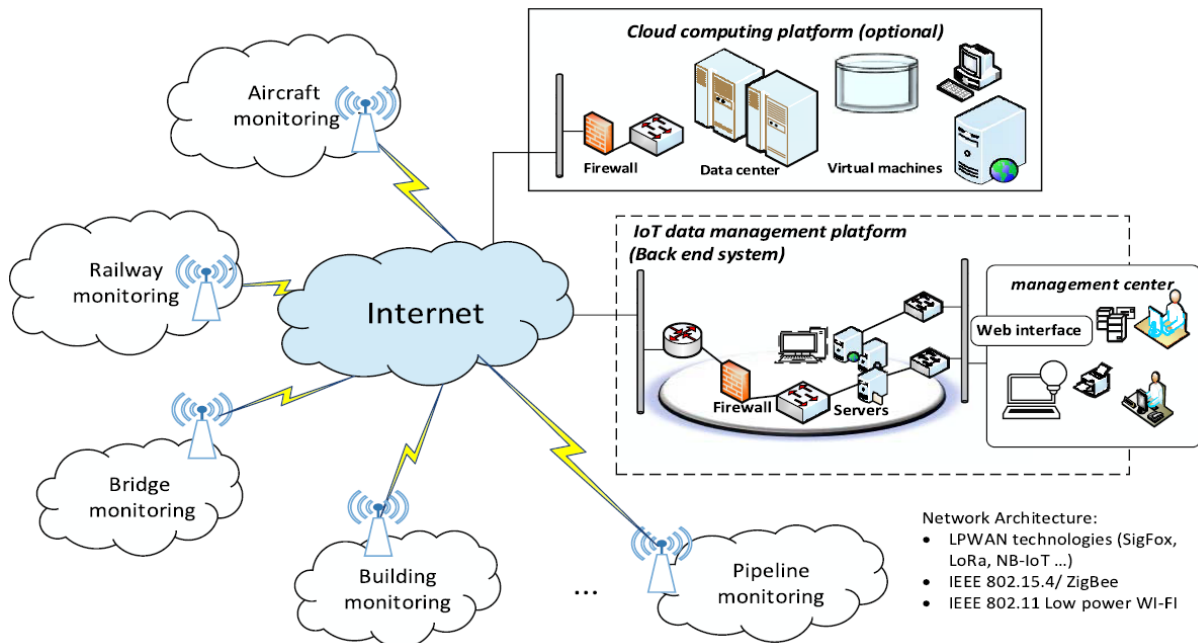


Figure 2.21 Framework overview of the IoT based SHM [147]

The IoT based SHM permits the adoption of new technologies to improve the efficiency and reliability of the developed monitoring system [123]. The IoT paradigm makes the sensors and

systems not only able to measure physical variables but also to interact and transmit the information to the internet for making decisions. Interaction between smart sensors needs IoT technologies to integrate the internet with SHM systems. The IoT based SHM can lead to a drastic reduction of the monitoring costs and increased safety due to continuous monitoring. The implementation can involve wireless technologies, eliminating the cabling requirement of the sensor networks, and enable the integration of monitoring systems into new and existing structures.

The framework overview of SHM systems in the IoT environment involves huge-scale sensor networks, as illustrated in Figure 2.21 [147]. IoT based SHM deploys sensors at strategic locations of the monitored structures and acquire appropriate data to be sent to the internet through wireless communication and networks. The network architecture may vary depending on the requirement of transmission distance, data rate, and availability of power. The IoT data management platform is responsible for data collection, storage, and processing to evaluate the condition of the monitored structures. Since the collected data is large, a big data cloud computing platform may be needed for data processing. The data is then visualized and presented via web interfaces or applications at the management center to be accessed by authorized users.

The above framework describes an overall concept of IoT based SHM and how future SHM systems will be interconnected through internet networks. IoT architecture comprises three layers, including the perception layer, network layer, and service layer [148]. Each layer can be realized with relevant key enabling technologies and is responsible for a specific function. As the primary function of the perception layer is to identify and sense objects, the enabling technologies include WSN and RFID. For the network layer, the enabling technologies are communication protocols such as IEEE802.15.4, ZigBee, LoWPAN, and messaging protocols, such as MQTT. The service layer is responsible for extracting valuable information from data and provides the interface between users and the IoT based SHM system. It is enabled by interface technology, service management technology, middleware technology, and resource management, and sharing technology.

Regarding the perception layer, WSN and RFID are two major enabling technologies for IoT. As discussed in the previous subsection, WSN is mainly used for interconnecting sensors through wireless communications and has been widely investigated for SHM. Adding internet connectivity to WSN through gateways would enable IoT based SHM. RFID technology was developed before WSN was known, but WSN has been explored for SHM earlier than RFID. It notably is because, in the past, RFID was initially developed for automatic object

identification and tracking until its versatility for sensing applications was explored in recent years. Since then, the RFID sensor network (RSN) is considered an enabling technology for IoT [148]. RFID, with the ability for both identification and sensing, could be a technology that shapes the emerging and future SHM.

2.5 Chipped RFID Technology, Chipped RFID Sensors, and State-of-the-Art Chipped RFID Tag Antenna-based Sensors for SHM

RFID initially emerged as a solution to the drawbacks of barcode technology, which has been used to identify items since the 1970s. Although the implementation through printing bar marks and spaces is very cheap, barcode labels have short-range line-of-sight readability and nonautomated tracking. Since the invention of RFID, electronic components, which later shrinkage into a tiny chip, were required to form unique identifiers using signal modulation. Therefore, the RFID that is commercially available now is known as chipped RFID. Whereas chipped RFID was developed for object identification, researchers gradually expand its application to wireless and passive sensing, from environmental sensing to SHM. Due to the low-cost nature of passive sensors, RFID is a viable solution for the spatial granularity issue of WSN. This section will cover the brief fundamentals of chipped RFID technology, including its invention, basic concept, and classification. The discussion is followed by chipped RFID sensors to explain how RFID purpose transformed from identification into various sensing applications. Then, state-of-the-art passive chipped RFID tag antenna-based sensors for SHM are reviewed, particularly for defect detection and characterization.

2.5.1 Brief Fundamentals of Chipped RFID Technology

Radio frequency identification (RFID) technology is a wireless data capturing technique that uses radio waves to identify objects automatically. The basic principles of RFID were developed by military research during World War II to identify friendly aircraft. In early 1940, a system called “Identification Friend or Foe (IFF)” was introduced in the Battle of Britain. The British Royal Air Force equipped airplanes with radio transponders, which replied to the incoming radar pulse with a unique echo signal that progressively increased in amplitude over time. The system allowed pilots and ground crews to identify and distinguish British airplanes from German Luftwaffe’s airplanes [149], [150]. After World War II, the birth of RFID was pioneered by a publication by Harry Stockman entitled “Communication by means of reflected power” in October 1948. The paper discussed the basic theory of backscatter communication. Since then, commercial applications of RFID technology were developed. The evolution of RFID technology involved the invention of the integrated circuit in the 1960s, the development

of RFID ASIC in 1975, and the advancement of low-power CMOS technology leading to the development of single-chip RFID transponders. By early 2000, modern passive RFID tags had entered in various commercial applications, such as automatic toll collection, smart cards, ticketing, contactless payment, vehicle access, animal tracking, industrial automation, and asset management [151].

The typical concept of an RFID system is depicted in Figure 2.22. An RFID system consists of three main components: RFID tag, RFID reader, and data processing subsystem. An RFID tag is a transponder, which contains unique ID data and is attached to the object to be identified. A tag integrates an antenna with an RFID IC or chip, in which the ID data is stored. An RFID reader is a transceiver that may be able to interrogate and read/write data from/to an RFID tag. The data processing subsystem is a unit that processes the data acquired from the reader into useful forms. The working principle is explained as follows: The reader transmits an interrogation signal to be received by the tag antenna. Then, the chip is activated using the energy harvested from the interrogation signal sent by the reader. When the chip wakes up, it modulates the signal and responds to the reader with the backscattered signal, which contains the unique ID number stored in the chip. The RFID reader passes the signal to the data processing subsystem, which will encode the ID, store it into the database, and send it via networks to application servers such as access control and supply chain management for further application-level operations [149].

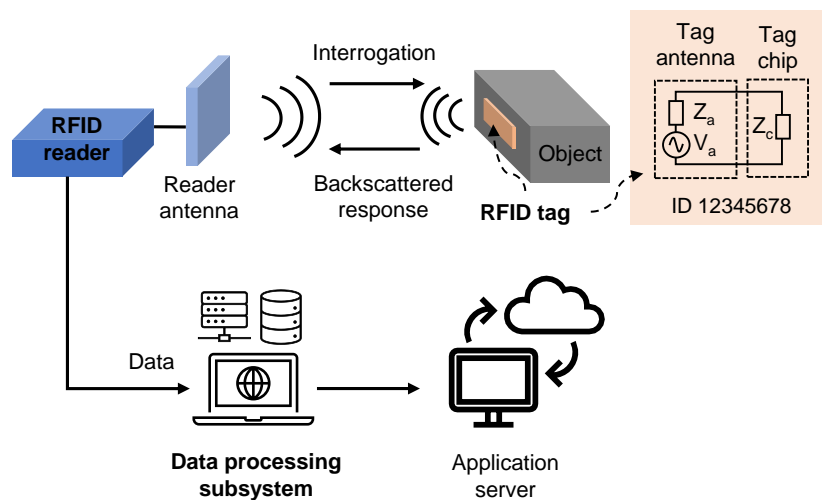


Figure 2.22 Typical concept of an RFID system and the main components [149].

RFID systems evolved with a variety of classifications, which differ in mechanisms and design requirements. Based on the tag power supply, RFID can be classified as active, passive, and semi-passive. Active RFID tags are outfitted with a power source, typically a battery, in order to supply energy to the transponder chip circuitry and to communicate with the reader. Active tags can communicate with the reader from a long distance, in hundreds of meters, with the

consequences of having an increased complexity, larger dimensions, higher cost, and limited lifetime. As opposed to the active tags, passive RFID tags do not have any independent power source to activate the transponder chip. The energy needed for the transponder activation is merely harvested from the interrogation signal coming from the reader. Without batteries, passive tags provide advantages in terms of dimensions, simplicity, cost, and lifetime. The consequence is that the read range is limited in order of centimeters to meters, which is enough for most applications. Semi-passive tags are equipped with a power source to feed the transponder chip but use the backscatter principle like the passive tags for communication with the reader. Semi-passive tags are typically employed in RFID tags interfaced with sensors, which need extra energy to read continuously and process signals from the sensors [151]. Among these three types of tags, passive tags are widely used in various applications.

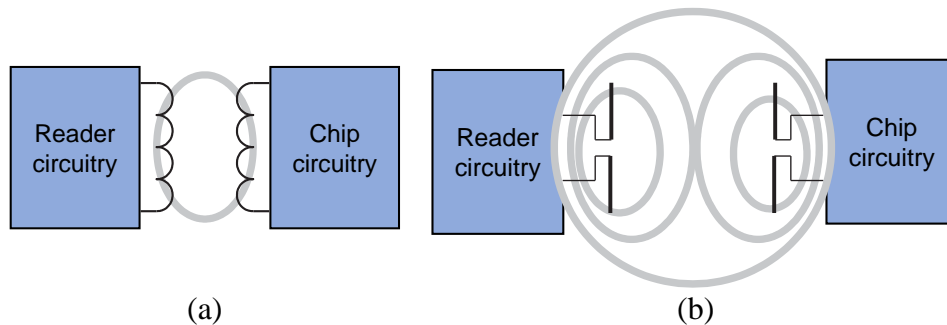


Figure 2.23 Coupling mechanism in RFID. (a) Inductive coupling. (b) Radiative coupling [149].

Another classification of RFID can be done based on the coupling mechanism between the tag and the reader. As illustrated in Figure 2.23, there are two types of coupling mechanisms for RFID: inductive coupling and radiative coupling. As an RFID tag uses a certain carrier frequency band to communicate with the reader, the coupling mechanism is determined by the size of the tag antenna relative to the wavelength. Tag antennas of low-frequency systems should be electrically smaller than the wavelength to limit the antenna size. Thus, the tag antenna is usually a small coil, which communicates through interacting magnetic fields in the vicinity of the reader coil. When the RFID tag antenna is a coil, the mechanism is, therefore, inductive coupling. For high-frequency systems, when the tag antenna size is comparable to the wavelength, the radiative coupling is used. The communication between the tag and reader uses radiating electromagnetic waves in the far-field zone of the antennas. While radiating fields decay with the square of the distance, near fields around an antenna attenuate with the cube of the distance. Therefore, the RFID systems relying on radiative coupling have the advantage of a longer reading range compared to the inductive coupling. Nevertheless, the inductive coupling mechanism allows much smaller coil antenna size and selective area of detection, which are useful for many applications such as for access control, smart card, and implanted tags for

animal tracking. The radiative coupling is useful for applications where long-range detection is necessary, such as in industrial automation and asset management.

Since different types of tags and the coupling mechanisms can fit in different applications, RFID systems have been developed using a wide range of frequency bands. The selection of a frequency band affects many aspects related to the physical behavior of electromagnetic fields. Coupling mechanism, the required antenna size, reading range, interaction with materials are among them. Based on the frequency bands, RFID systems can be classified as LF RFID, HF RFID, UHF RFID, and microwave RFID, as shown in Figure 2.24.

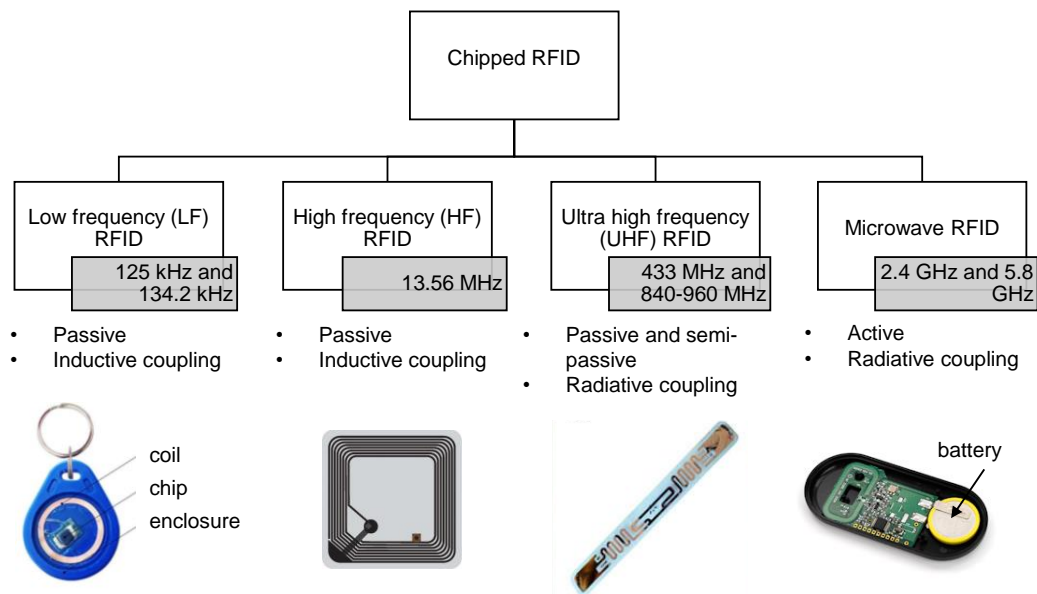


Figure 2.24 Classification of chipped RFID with the illustration of tags [151]

The low frequency (LF) RFID systems work at 125 kHz and 134.2 kHz and are usually passive. With a low frequency, LF RFID tags use coils and an inductive coupling mechanism to communicate with the reader. One of the benefits of LF RFID is its low interaction with various materials so that LF RFID tags can be attached or embedded in objects containing water, high-permittivity materials, and metals. However, LF RFID tags are readable only from a few centimeters, the reading speed is slow, and multiple tags reading is impractical. Moreover, LF RFID tags are relatively expensive as the construction of the coil antenna requires a winding process of copper wires. LF RFID is typically used for animal tracking, access control, and identification of pharmaceutical products.

High Frequency (HF) RFID systems operate at 13.56 MHz and use passive tags based on coil antennas and inductive coupling mechanism. Since the frequency is higher than the LF RFID, coils for HF RFID tags need a smaller number of turns. Thus, HF RFID tags can be realized as thin and inexpensive labels using printing technologies and provide a read range in order of tens of centimeters. Although an HF RFID tag can still be read when mounted on plastics, body,

and liquids, it is not readable when attached to metals. The typical applications of HF RFID are smart cards, electronic ticketing, product identification in supermarkets, and near field communication (NFC).

Ultra-high frequency (UHF) RFID systems operate in the frequency bands around 433 MHz for active tags and between 840 to 960 MHz for passive and semi-passive tags. UHF RFID passive tags use a radiative coupling to operate, allowing for a reading range of several meters to 15 meters in optimal configurations. In addition, UHF RFID tags can be manufactured as thin and inexpensive labels, making them fit with a wide variety of items. The sophisticated UHF RFID communication protocols with an anti-collision mechanism allow fast multiple readings of tags near the reader. However, UHF RFID systems are much more sensitive to the material of the tagged object and environmental conditions compared to LF and HF RFID. In general, the performance of UHF RFID tags degrades when in proximity to water, body, and metals. The optimized UHF RFID tag designs, such as metal-mountable tags, usually suffered from increased dimensions and cost. With the benefits of low-cost and long reading range, UHF RFID finds applications in the supply chain, asset and inventory management, car detection, and baggage tracking.

Microwave RFID systems use ISM frequency bands around 2.4 GHz and 5.8 GHz. Microwave RFID systems are typically designed based on active tags and aimed at tracking relatively expensive items from a long distance up to 100 m. Since a microwave RFID tag has a battery as a power source, it is possible to provide additional features by increasing the complexity of the tag circuit. Microwave RFID was the first RFID class to be deployed for commercial applications, such as highway toll collection in the 1980s. The technology is already mature and still widely used for transportation, access control, and tracking applications.

Ultimately, RFID technology is a breakthrough in embedded communication, which helps in the automatic identification of almost anything. Despite the widespread use in object identification applications, RFID implementation faces technical challenges, mainly in tag design and data management [149]. Several challenges are associated with tag cost, read range, tag form factor/size, performance near conductive objects, mobility, and reliability [152], [153]. Accordingly, many efforts have been made to overcome the challenges, including printed tags [154], miniaturized tags [155], and metal-mountable tags [156]. Regarding data management, some challenges include redundancy, uncertainties, the large volume of data, and data security and privacy [157]. Anti-collision algorithms, authentication, privacy protocols, localization, and performance tuning are among the solutions [158]. Nevertheless, many more specific challenges arise along with the expansion of RFID applications.

2.5.2 Chipped RFID Sensors

Chipped RFID technology, which was initially developed for object identification, provides the basic principle and platform for building low-cost and ubiquitous wireless sensing [159]. Typical RFID platforms have several critical advantages, including wireless, passive, low-cost, and low maintenance. These characteristics make passive RFID play a strategic role in overcoming the spatial granularity issue in distributed wireless sensors. The current wireless sensing platforms that use battery-powered sensors cost at least double compared to the passive ones [160]. In addition, the limited life of batteries poses issues in terms of maintenance cost and environmental risks due to the disposal of vast amounts of batteries. Meanwhile, passive RFID tags work on the principle of wireless backscatter communication to convey data without the requirement of a battery on the tag. The same mechanism of the RFID reader uses to collect data from tags can also be applied for sensing applications [161]. The passive backscatter communication principle enables data retrieval from many passive sensors using a single reader. With the wide acceptance throughout the industry, RFID sensors can be seamlessly integrated with off-the-shelves RFID systems. Moreover, RFID transponder chips, readers, and development kits are available in the market. These factors give RFID the potentials to extend its function from a tool for wireless identification into a sensing platform.

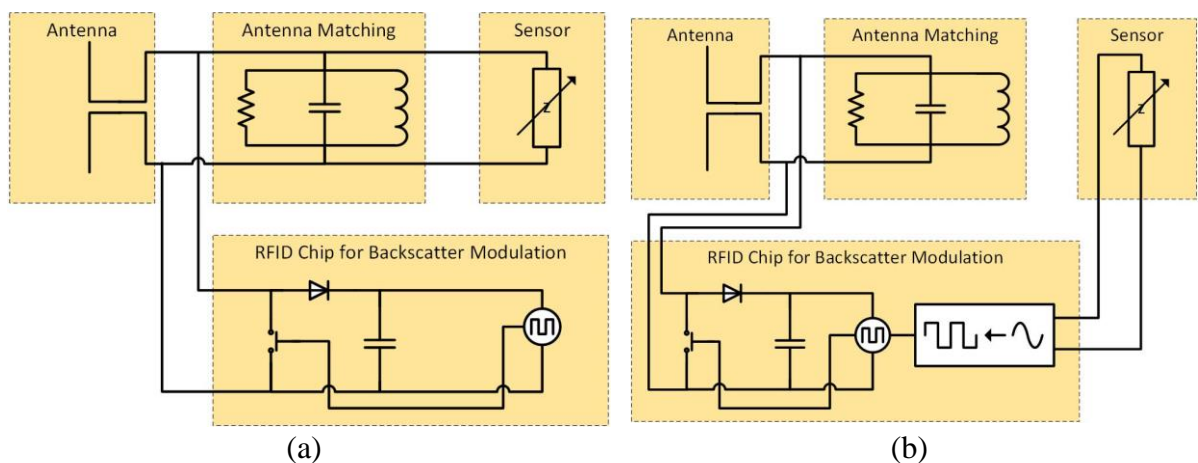


Figure 2.25 Topologies for chipped RFID sensing. (a) connecting the sensor to the antenna. (b) connecting the sensor to the chip [160].

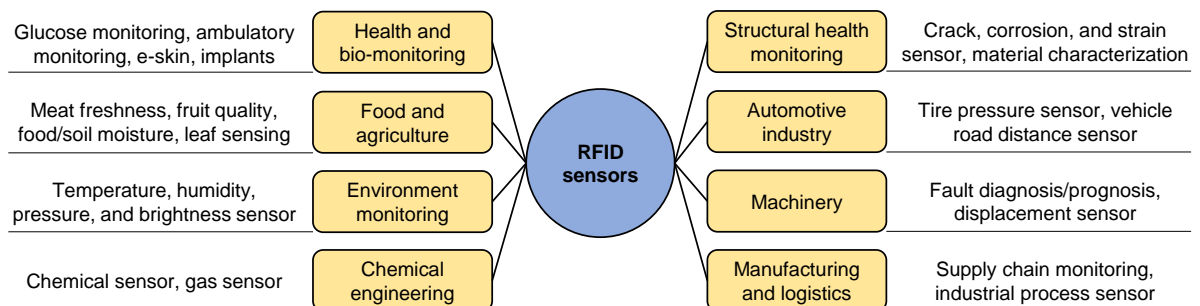


Figure 2.26 RFID sensor applications [162].

Besides its common use for identification and tracking, sensing can be performed using RFID by interfacing sensors to an RFID tag. As drawn in Figure 2.25, chipped RFID sensing can be implemented using different topologies depending on which the sensor is connected [159]: i.e., connecting the sensor to the antenna and connecting the sensor to the chip. First, the topology that connects the sensor to the antenna uses the variation of RCS of the “antenna mode” backscatter due to the load impedance mismatch caused by the sensor. This can be done, for example, by loading the antenna with sensing materials that can change the antenna impedance according to the measurand. While the ID from the chip uses time-domain modulation schemes such as ASK and PSK, the sensor varies the amplitude of the modulated signal over frequency. Both the identity of the tag and the sensor information can be extracted by using the time and frequency-modulated signals. Second, the topology that connects the sensor to the chip incorporates the sensor data directly into the digitally modulated backscatter signal. The sensor data is communicated as digital data along with the ID from the chip. The chip needs to employ a controller containing an analog to digital converter (ADC) to convert the sensor output to digital data. Since the RFID chip is an IC powered by RF energy, sensors and controllers can be interfaced or even integrated into the RFID chip. This topology is more robust and precise due to digital modulation in processing and communicating the sensor data. However, it is more expensive due to the higher complexity of electronics in the chip. Furthermore, the read range suffers as more power is required for signal conversion and computation in the chip.

Due to the benefits and convenience of using RFID for sensing, many research efforts have been made in RFID sensors, and thus plenty of novel applications can be found in the literature [163]. As illustrated in Figure 2.26, innovative applications of RFID sensors have been developed for a wide variety of functions and physical variables [162]. Just to mention but a few, RFID has been studied for applications including health monitoring [164], [165], environment monitoring [166], [167], chemicals detection [168], [169], food quality evaluation [170], [171], machine fault diagnosis [172], and SHM [173].

2.5.3 State-of-the-Art Chipped RFID Tag Antenna-based Sensors for SHM

Among many RFID sensor applications, SHM is one that attracts attention. RFID can be a backbone for building low-cost, passive, and large-scale wireless sensor networks for SHM. The concept of passive RFID sensor networks for the Internet of Things (IoT) based SHM is illustrated in Figure 2.27. In the future IoT [18], passive RFID sensor networks are used to connect heterogeneous engineering structures, including bridges, wind turbines, pipelines, and nuclear plants, to the internet [19]. RFID sensor systems act as the physical sensing layer, which continuously collects sensing information from massively distributed passive RFID sensors

[20]. Then, RFID readers send the data to the IoT cloud database through the network layer, which provides necessary networking support and connections for data transfer over wired and wireless networks. The application layer provides services for data management and interfaces for interaction with the users to monitor the health state of the infrastructures.

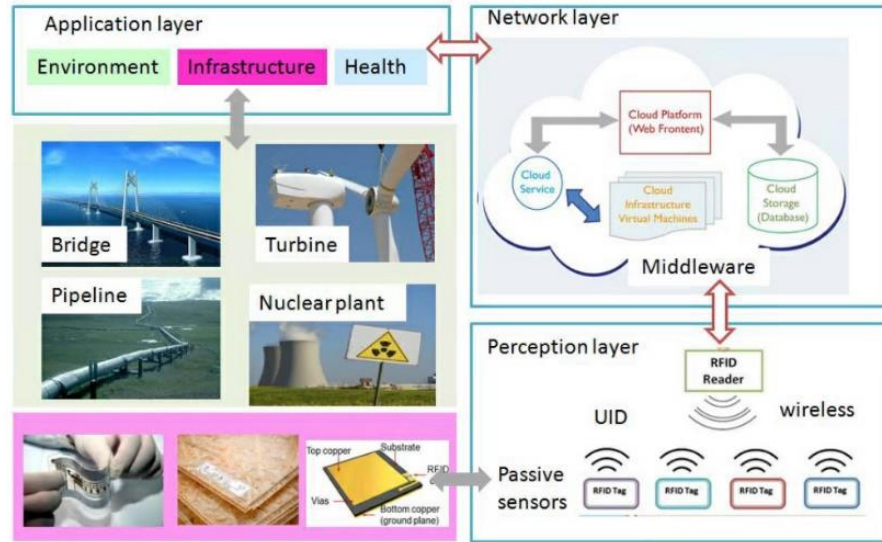


Figure 2.27 Concept of passive RFID sensor networks for the Internet of Things (IoT) based structural health monitoring (SHM) of heterogeneous infrastructures consisting of perception, network, and application layers [21].

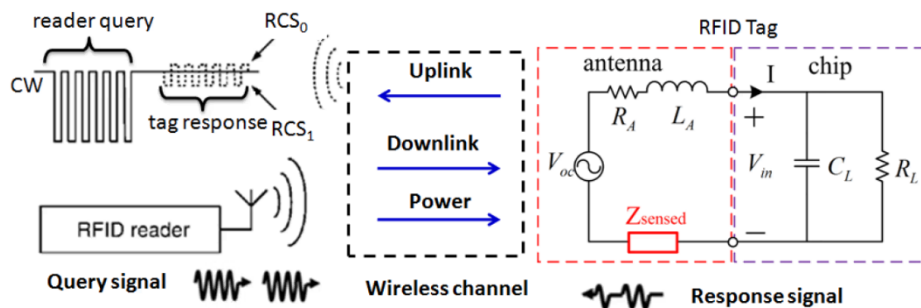


Figure 2.28 Principle of passive chipped RFID tag antenna-based sensor system for SHM based on backscatter communication [21].

Since engineering structures are usually large, the implementation of passive wireless sensor networks for SHM will be on a considerable scale. For massive use, therefore, sensors do not need to be exceptionally precise and sophisticated [174]. However, the sensors must be low-cost to be densely distributed at finer spatial granularity than the active and precise wired and wireless sensor systems. To enable such vision, therefore, RFID tag antenna-based sensors are attractive for SHM [21]. Analog processing of physical signals related to the reader-tag communication could obtain information about the environment around the antenna without additional sensors. While the tag ID information is digitally encoded, the strength of the

backscattered signal in the analog form is affected by the interaction with the surrounding materials, nearby objects, propagation channel, as well as position and orientation of the tag. The idea of using the RFID tag antenna as sensors is supported by the fact that antennas, in general, can be used for sensing purposes [175]. The capability of antenna sensors in detecting structural conditions, such as strain and crack, poses the principle for a unique sensing modality for SHM using “sensor-less” RFID tags. RFID tag antennas can be used as low-cost sensors by mapping some physical variables of interest to a controlled change in the RFID tag antenna's electrical properties [160].

The challenges of tag antenna-based sensors for defect detection are the requirement of metal-mountable and sensing-oriented antenna design. Typical RFID tag antennas do not work effectively on conductive materials. Therefore, tag antenna-based sensors should be designed to work in proximity to metal while its characteristics, e.g., impedance, change with the presence of defects. The principle of passive chipped RFID tag antenna-based sensor system is depicted in Figure 2.28. The RFID reader transmits continuous waves (CW) to activate nearby tags and a query asking the tags to respond with their IDs. An RFID tag antenna harvests RF energy from the reader. In order to maximize the power transfer in the tag, a tag antenna is designed to be conjugately matched with the chip input impedance. A proper matching between the tag chip impedance ($Z_c = R_c + jX_c$) and the tag antenna impedance ($Z_a = R_a + jX_a$) is denoted by a low reflection coefficient (Γ), which can be expressed as

$$\Gamma = \frac{Z_c - Z_a^*}{Z_c + Z_a} \quad (2.9)$$

When the tag chip gets enough power above the threshold, the tag chip alters its internal impedance to enable the re-radiation of CW provided by the reader. Depending on the type of modulation, i.e., ASK or PSK, the tag antenna emits an amplitude or phase-modulated backscattered signal controlled by the antenna loading. With the loading corresponds to ID bit ‘0’ and ‘1’, the signal arrived at the reader is the variation of RCS, i.e., RCS_0 and RCS_1 . It is important to notice that at the RFID tag, the measurand to sense is denoted as Z_{sensed} , which contributes to the electric property changes of the antenna sensor corresponding to its impedance variation. The reader can monitor the antenna parameters remotely based on RCS changes and hence the strength of the backscattered power.

There are at least two power parameters that can be captured by the RFID reader and used for defect sensing: the tag backscattered power denoted by the received signal strength indicator (RSSI) and the reader threshold transmitted power or the turn-on power [160]. In the reader-tag

communication, the defect or physical variable to be monitored can be denoted by Ψ . Thus, the power retrieved at the tag chip can be written as [174]

$$P_{\text{reader} \rightarrow \text{tag}}[\Psi] = \left(\frac{\lambda_0}{4\pi d} \right)^2 P_{in} G_{\text{reader}}(\theta, \phi) G_{\text{tag}}[\Psi](\theta, \phi) \tau[\Psi] \eta_p \quad (2.10)$$

where λ_0 is the free space wavelength at the operating frequency, d is the distance between the reader and the tag, P_{in} is the transmitted power input to the terminal of the reader antenna, G_{reader} is the gain of the reader antenna, G_{tag} is the gain of the tag antenna, θ and ϕ are the angles to account for the reader and the tag orientations and η_p is the polarization mismatch between the reader and the tag. τ is the power transmission coefficient of the tag related to the impedances of the tag chip and the tag antenna as [174]:

$$\tau[\Psi] = \frac{4R_c R_a[\Psi]}{|Z_c + Z_a[\Psi]|^2}. \quad (2.11)$$

Meanwhile, the power backscattered by the tag and collected by the reader is [174]:

$$P_{\text{reader} \leftarrow \text{tag}}[\Psi] = \frac{1}{4\pi} \left(\frac{\lambda_0}{4\pi d^2} \right)^2 P_{in} G_{\text{reader}}^2(\theta, \phi) \eta_p^2 \text{RCS}_{\text{tag}}[\Psi(\theta, \phi)] \quad (2.12)$$

where RCS_{tag} is the tag's radar cross section related to the modulation impedance Z_{mod} , which can be assumed equals to the chip impedance Z_c . RCS_{tag} can be written as [174]:

$$\text{RCS}_{\text{tag}}[\Psi] = \frac{\lambda_0^2}{4\pi} G_{\text{tag}}^2[\Psi](\theta, \phi) \left(\frac{2R_a[\Psi]}{|Z_{\text{mod}} + Z_a[\Psi]|} \right)^2. \quad (2.13)$$

The backscattered power $P_{\text{reader} \leftarrow \text{tag}}[\Psi]$ is measurable by the reader and termed as RSSI. Another measurable parameter at the reader is the reader threshold transmitted power or the turn-on power, which is the minimum input power at the reader that makes the tag to respond. The turn-on power can be derived as [174]:

$$P_{in}^{to}[\Psi] = \left(\frac{4\pi d}{\lambda_0} \right)^2 \frac{P_{\text{chip}}}{G_{\text{reader}}(\theta, \phi) G_{\text{tag}}[\Psi](\theta, \phi) \tau[\Psi]} \quad (2.14)$$

where P_{chip} is the threshold power of the chip specified by the chip sensitivity. P_{in}^{to} can be derived from the forward link $P_{\text{reader} \rightarrow \text{tag}}$ by considering $P_{\text{reader} \rightarrow \text{tag}} = P_{\text{chip}}$. From the turn-on power P_{in}^{to} , further parameters can be derived, such as the gain of the tag scaled by the impedance mismatch to the chip, i.e., the realized gain $\hat{G}_{\text{tag}} = G_{\text{tag}} \tau$. Furthermore, a non-dimensional indicator, namely Analog identifier (AID), can also be calculated as [174]:

$$AID[\Psi] = \frac{P_{\text{chip}}}{\sqrt{P_{\text{reader} \leftarrow \text{tag}}[\Psi] P_{\text{in}}^{\text{to}}[\Psi]}} = \frac{2R_c}{|Z_c + Z_a[\Psi]|} \quad (2.15)$$

Since AID is derived based on the forward and backward communication links between reader and tag, it reduces the influence of distance as well as the antenna gains and orientations of the reader and the tag. AID only depends on the tag antenna impedance and hence shows the impedance variation due to the defect or the monitored variable Z_{sensed} .

2.5.3.1 Chipped RFID Tag Antenna-based Sensors for Crack Detection and Characterization

The fact that 52% of structural failures are due to the formation of cracks and the availability of the sensing principle and measurable parameters have motivated researchers to study RFID tag antenna-based sensors for crack detection and characterization. Off-the-shelf chipped RFID tags and customized RFID tag antenna designs have been attempted. Moreover, different measured parameters and sensing features have been investigated. Table 2.3 presents a list of chipped RFID tag antenna-based sensors for crack detection and characterization.

RFID tag antenna-based sensors have been studied for detecting cracks in non-metallic materials, mostly concrete and wood, as well as metallic materials such as aluminum and steel. Due to the long reading range characteristic, most studies employed the UHF band. In 2013, *Yi et al.* demonstrated a UHF RFID tag antenna sensor capable of detecting crack from 2.1 m reading distance with good sensitivity and sub-mm crack resolution using resonance frequency shift [176]. However, the folded patch antenna sensor and the reader antenna used in the study are relatively large, and the crack is expected to break the antenna to be detected. The use of coupled UHF PIFA antennas was proposed by *Caizzone et al.* with a 1.5 m reading distance and 0.2 mm resolution exploiting realized gain and phase shift feature [177]. Two antennas were needed, and the phase shift feature, however, needs a fixed setup because of the influence of the wireless channel. It was also discovered that there is a trade-off between sensitivity and communication distance. A 3D UHF folded dipole antenna along with PCA feature extraction were introduced by *Zhang J. et al.* to mitigate the influence of the wireless channel [178]. The reading distance was 1 m, but the antenna profile was thick, and the resolution of the crack in the study was limited in mm. An attempt to use off-the-shelf UHF RFID dipole inlay tags formed as an array was reported by *Martinez-Castro et al.* [179]. RSSI variation was used to quantify the damage level from a 0.9 m reading distance. Indeed, an off-the-shelf inlay tag on a thin lossy substrate is not detectable on metallic materials. Consequently, a 12.7-mm thick

foam was needed in between tags and the metal, while the crack was only simulated by cutting parts of the tags.

Table 2.3 List of chipped RFID tag antenna-based sensors for crack detection and characterization. The highlighted rows are chipped RFID tag antenna-based sensors for crack detection in metals.

Ref	Year	Measurand	Sensor design			Measured parameter [feature]	Pros	Cons
			Band	Design	Size			
Yi [176]	2013	Strain and crack in aluminum	UHF	folded patch antenna	60 mm × 69 mm	Turn-on power [resonance frequency shift]	2.1-m reading distance; sub-mm crack resolution	Large sensor and reader antenna; crack breaks the antenna to be detected
Kalansuriya [180]	2013	Crack width in concrete beam	UHF	2D grid of dipole antenna	160 mm × 19 mm	Backscattered power [RSSI variation]	1-m reading distance; array sensor to determine crack propagation	Power is susceptible to wireless channel; not applicable to metal crack
Caizzone [181]	2014	Crack width in wood	UHF	Coupled dipole antennas	150 mm × 30 mm × 0.8 mm	Backscattered signal phase [phase shift]	0.3-mm crack resolution; stable communication	Two antennas required; fixed setup; not applicable to metal crack
Caizzone [177]	2015	Crack width in wood, concrete, aluminum	UHF	Coupled PIFA antennas	45 mm × 34 mm	Realized gain and phase of the tag [gain and phase shift]	0.2-mm resolution of crack width; 1.5 m reading distance	Two antennas required; fixed setup; trade-off between sensitivity and communication
Zhang J. [178]	2017	Crack depth in aluminum	UHF	3D folded dipole antenna	20 mm × 20 mm × 16 mm	Backscattered power [PCA]	PCA reduces wireless channel influence; 1-m reading distance	Thick antenna profile 16 mm; crack depth resolution only in mm
Martinez [179]	2017	Crack in steel girder	UHF	Off-the-shelf dipole inlay tag	70 mm × 17 mm × 0.8 mm	Backscattered power [RSSI variation]	Array sensor; 0.9-m reading distance	12.7-mm thick foam required between tag and metal; simulated crack by cutting the RFID tag
Omer [182]	2018	Crack depth in steel	UHF	Design undisclosed	Design undisclosed	Backscattered power over time [RSSI peak and skewness]	Time and frequency features; improved accuracy	0.3-m reading distance
Zhang J. [183]	2018	Crack depth in aluminum	UHF	circular patch antenna	67-mm diameter × 2mm	Turn-on power [resonance frequency shift]	Planar design; 1-m reading distance	Large sensor size; crack depth resolution only in mm
Sunny [184]	2018	Crack depth in aluminum	LF	Off-the-shelf coil tag	26-mm diameter	Signal envelop with sweep frequency [peak-to-peak amplitude and resonance frequency shift]	Robust (less affected by wireless channel); time and frequency features	40-mm reading distance
Bruciati [185]	2019	Crack in concrete beam	UHF	Off the shelf dipole inlay tag	70 mm × 17 mm × 0.8 mm	Backscattered power [RSSI variation]	0.88 m reading distance	not applicable to metal crack

In 2018, reduction of the wireless channel influence was again studied by *Omer et al.* using peak points and skewness of the time-varying RSSI data [182]. The method could improve the detection accuracy, but the reading distance was only 0.3 m. In the same year, *Zhang J. et al.* proposed a circular patch antenna [183], which was planar and had a lower thickness profile than his previous 3D folded dipole antenna in [178]. Although the profile was not thick, the antenna width and length were relatively large. In addition to the majority of studies conducted

in the UHF band, the feasibility of LF RFID for crack detection and characterization was investigated by *Sunny et al.* [184]. Off-the-shelf LF RFID coil was used, and peak-to-peak amplitude and resonance frequency features were analyzed. It demonstrated the principle and notably feature extraction method, but the reading distance was only 40 mm.

The studies on the RFID tag antenna sensors for crack detection and characterization have shown different antenna designs, different measured parameters, and features leading to pros and cons. The antenna size and profile, as well as the feature extraction method, provide advantages yet with consequences in terms of reading distance, sensitivity, crack resolution, and immunity to the wireless channel. The UHF RFID tag antenna sensors tended to be designed with a relatively large size and thick profile to give a sufficiently long reading distance, i.e., 1 to 2 m. With a long reading distance, the detection of crack with the sub-mm resolution was possible only if the crack broke the antenna sensor. Nonetheless, when the crack occurs around the antenna sensor, high sensitivity and sub-mm resolution were difficult to achieve at a long reading distance. In the aspect of feature extraction, resonance frequency shift and RSSI amplitude variation are typical. Statistical feature extractions, such as using PCA and analysis of time-frequency features, were demonstrated effective in reducing the wireless channel influence.

2.5.3.2 Chipped RFID Tag Antenna-based Sensors for Corrosion Detection and Characterization

Being the 42% cause of structural failures, RFID sensors for corrosion detection have attracted scientific interest in recent years. Since 2011, there have been studies on chipped RFID for detecting corrosion. Several studies use RFID tag antenna-based sensors, while some others integrate RFID systems with electrodes as the corrosion sensors [186]–[189]. The electrodes typically detect the presence of corrosion based on the voltage difference, which is fed to a microcontroller, RFID circuitry, and a coil antenna to pass the information to the reader. Although using the chipped RFID principle, these solutions are categorized as non-antenna-based sensors. In Table 2.4, chipped RFID tag antenna-based sensors for corrosion detection and characterization are listed and discussed.

A pioneering study on chipped RFID tag antenna-based sensors for corrosion detection and characterization was conducted by *Alamin et al.* in 2012, exploiting an off-the-shelf LF RFID coil tag and the peak amplitude feature [190]. The study demonstrated the ability to characterize corrosion progression from a 45-mm reading distance but faced an issue of dependency of the amplitude feature to the reading distance. In 2014, *He et al.* attempted the UHF band by applying the steel-filled composite paint to an off-the-shelf UHF metal-mountable tag. The

corrosion that occurred on the steel-painted tag changed its communication performance and could be detected by the reader through the read rate and the turn-on power. However, the study did not find any linear relationship between the read rate and the turn-on power, and the accelerated corrosion.

Table 2.4 List of chipped RFID tag antenna-based sensors for corrosion detection and characterization.

Ref	Year	Measurand	Sensor design			Measured parameter [feature]	Pros	Cons
			Band	Design	Size			
Alamin [190]	2012	Corrosion progression in steel	LF	Off-the-shelf coil tag	26-mm diameter	Signal envelope [peak amplitude]	Simple method	45-mm reading distance; reading distance dependent
He [191], [192]	2014	Corrosion progression in steel	UHF	Off-the-shelf metal-mountable tag coated using steel filled composite paint	148 mm × 18 mm × 4.1 mm	Read rate, turn-on power [read rate and turn on power level]	Reading distance 0.75 m	Non-linear relationship to corrosion
Sunny [193]	2016	Corrosion progression in steel	LF	Off-the-shelf coil tag	26-mm diameter	Signal envelope [transient response]	More robust than peak amplitude feature; enhanced sensitivity by adding a ferrite material	30-mm reading distance; reading distance dependent
Zhang H. [194]	2016	Corrosion progression in steel	HF	Off-the-shelf coil tag	50-mm diameter	Complex impedance [PCA]	Reading distance independent	25-mm reading distance
Zhang J. [195]	2016	Corrosion progression in steel	UHF	3D folded dipole antenna	20 mm × 20 mm × 16 mm	AID [PCA]	1-m reading distance; wireless channel-independent	Thick antenna profile 16 mm
Zhao [196]	2017	Corrosion progression in steel	UHF	meandered dipole patch antenna; folded meandered dipole patch antenna; meandered dipole T-shaped patch antenna	48 mm × 20 mm × 5 mm; 20 mm × 20 mm × 4.8 mm; 20 mm × 20 mm × 4.8mm	Turn-on power [resonance frequency shift and PCA]	0.66-m reading distance of; improvement of sensitivity to corrosion	Gain and reading range degrade with the antenna miniaturization
Sunny [197]	2019	Corrosion progression in steel	LF	Off-the-shelf LF RFID coil	26-mm diameter	Signal envelop with sweep frequency [fused peak-to-peak feature]	Temperature independent	30-mm reading distance

Sunny et al. observed other potential signal features in the LF RFID and proposed the transient response feature for corrosion detection. In addition, a ferrite layer was added to the LF RFID tag coil antenna, enhancing the sensitivity [193]. However, the reading distance was only 30 mm, and the corrosion detection was still reading distance dependent. *Zhang H. et al.* investigated the HF RFID by using an off-the-shelf HF RFID tag and its complex impedance retrieved using VNA [194]. By exploiting PCA based feature extraction, the system was claimed to be reading distance independent. However, the investigated reading distance was limited, only 5 mm to 25 mm. The limited reading distance was reasonable since it is well-known that the typical off-the-shelf HF RFID tags are hard to detect when attached to metals.

In contrast, a 3D UHF folded dipole antenna sensor demonstrated a 1-m reading distance for corrosion detection, as studied by *Zhang J. et al.* [195]. Moreover, the sensor was wireless channel-independent because the AID parameter was used along with PCA feature extraction. However, the antenna profile needed to be 16-mm thick to balance the sensing sensitivity and communication distance. A study on antenna sensor miniaturization by *Zhao et al.* showed that the sensor sensitivity could be slightly improved but at the expense of degrading the antenna gain, and thus shortening the reading distance [196].

The studies on chipped RFID tag antenna-based sensors for corrosion detection have been attempted in three RFID frequency bands, i.e., LF, HF, and UHF. Different RFID tag antennas, measured parameters, and features have demonstrated benefits and consequences in the reading distance, sensitivity, and robustness against unwanted influences. While the LF and HF RFIDs used off-the-shelf tags, studies at the UHF band employed customized metal-mountable tag antenna designs. The LF and HF RFIDs suffered from a limited reading distance, i.e., less than 45 mm. In contrast, the UHF RFID tag antenna could achieve a 1-m reading distance, but the antenna size and profile were relatively large. The UHF antenna sensors were as thick as 5 mm to 16 mm, and the size was often more significant than the corrosion to detect. Therefore, metal-mountable antenna sensor design, antenna size and profile, reading distance, and sensitivity are among the challenges chipped RFID tag antenna-based sensors for corrosion detection and characterization. In addition, unwanted external influences, such as wireless channel and temperature, pose the need for statistical feature extraction such as PCA and feature fusion for reliable and robust detection.

2.6 Chipless RFID Technology, Chipless RFID Sensors, and State-of-the-Art Chipless RFID and Antenna Sensors for SHM

Chipless RFID is a recent research area in automated wireless identification technology aimed at further reducing the cost of chipped RFID tags. The idea is to enable the development of wireless, passive, and electronic-free identification tags with the cost-competitive to that of barcodes. Compared to barcodes, chipless RFID tags have non-line-of-sight readability, and the detection can be automated. Due to the potentials, chipless RFID has also drawn scientific interest in various sensing applications. This section will cover the brief fundamentals of chipless RFID technology, discussing the basic concept and principle as well as the classification of chipless RFID tags. Then, chipless RFID sensors for a wide variety of applications are reviewed. Finally, state-of-the-art chipless RFID sensors and antenna sensors for defect detection and characterization are discussed.

2.6.1 Brief Fundamentals of Chipless RFID Technology

Chipped RFID has not yet been a full replacement of the barcode technology because of the higher price of chipped RFID tags. The major cost of a chipped RFID tag is contributed by the chip, particularly in the manufacturing and assembly process. The ASIC design and testing, as well as the chip assembly to the tag antenna, make it not possible to further lower the price of chipped RFID tags. Building a silicon fabrication plant costs billions of US dollars, while the fixed cost per wafer to fabricate silicon chips is around a thousand US dollars. In addition, other significant costs come from dividing the wafer, handling the die, and placing the chips onto the tag antenna. This makes chipped RFID tags have a minimum possible price of around US\$0.05. With the inevitable high cost of the chip for RFID tags, chipless RFID is an effort to push the RFID tags to the lowest, expectedly below US\$0.01 [22].

Chipless RFID technology was first developed by Richard Ribon Fletcher at the Massachusetts Institute of Technology (MIT) and published in his doctoral thesis in 2002 [198]. The thesis was entitled “Low-cost electromagnetic tagging: design and implementation,” in which several designs of chipless RFID tags and sensors were presented as low-cost alternatives to the chipped RFID tags and sensors. The research demonstrated the possibility of encoding information using a totally passive tag without any electronics and retrieving the data through RF interrogation. Afterward, a chipless RFID system was patented in 2005 by Michael Pettus, where the tag was comprised of multiple RF antenna structures to encode the tag ID. This system used a reader to scan an area and retrieves the tag ID using radar imaging techniques [199]. Since then, chipless RFID technology has been attaining a continuous growth of research interest globally. It is a technique of wireless identification using a tag that contains no electronic components and relies on its EM response for the identification [200].

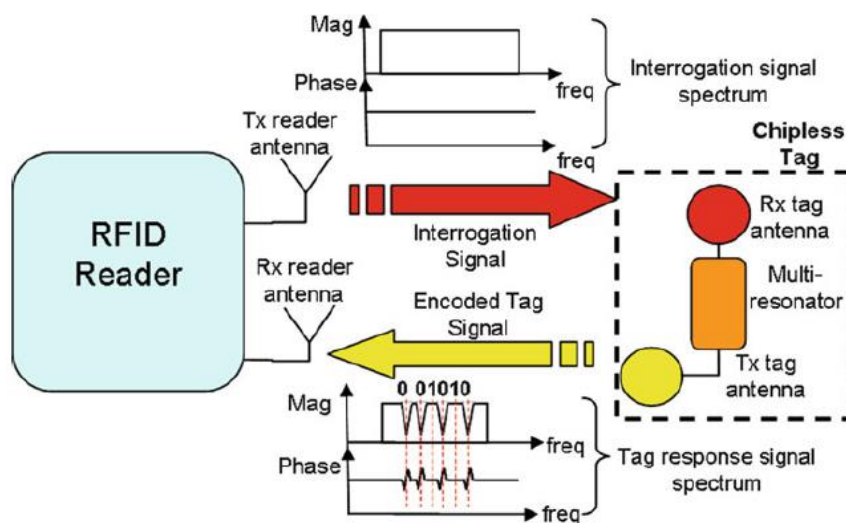


Figure 2.29 General operating principle of a chipless RFID system [201].

Until recent years, chipless RFID is still an object of intensive research [26]. The general operating principle is illustrated in Figure 2.29. Like the barcode and chipped RFID technologies, a chipless RFID system mainly consists of a tag and a reader. A chipless RFID tag does not need any IC and communication protocol. It is made of structures that form a signature that represents information when impinged by radio waves. The reader works similarly to a radar. It transmits radio waves to interrogate the tag and analyzed the backscattered signal to decode the information contained in the tag [202]. With the absence of a chip, chipless RFID tags are not only wireless, passive, and low-cost but also become simpler to fabricate and durable in harsh environments [23]. However, removing the chip causes a substantial technological break, where the communication is no longer using alternating load and digital modulation. A chipless RFID tag is fully analog and, therefore, akin to a radar target, where the ID or information is entirely governed by the geometry of the tag [202].

Table 2.5 A comparison of chipped and chipless RFID [203].

Parameter	Chipped RFID	Chipless RFID
Chip and communication protocol	UPC and EPC Gen 2, 3, 4	No chip and no communication protocol used
Data encoding principle	Encoded in chip	Encoded in physical signal/signature of the tag
Data capturing mechanism	Passive backscattering (modulated)	Passive backscattering
Frequency bands	Narrowband: LF (125 and 134.2 kHz), HF (13.56 MHz), UHF (433 MHz and 840-960 MHz), microwave (2.4 and 5.8 GHz)	Broadband: no standardization yet, usually in UWB bands (3.1-10.5, 22-26.5, and 60 GHz)
Reading distance	Up to 12 m	Up to 1 m in the UWB frequency range
Coding capacity	A few kilobits	A few tens of bits
Tag density	Up to 1000 tags at once with anti-collision protocol	Up to 3 tags at once with space-time-frequency localization
Cost of a tag	Minimum US\$0.05	Expectedly below US\$0.01

There are several core differences between the chipped RFID and the chipless RFID [203], [204], as summarized in Table 2.5. The most fundamental difference is the use of chip and communication protocol. Chipped RFID uses a microchip, which is standardized by EPC Global to define the physical and logical requirements, including the communication protocol between a reader and passive tags. Chipped RFID encodes data in the chip and uses a modulated backscattering mechanism to capture the data from the tag. Oppositely, chipless RFID does not use any chip and communication protocol to operate. The information is encoded solely in the physical signal or signature of the tag. Thus, the data is captured using passive backscattering and unmodulated as in the radar principle. In terms of the frequency band, chipped RFID occupies the narrow standardized bandwidths in LF, HF, UHF, and microwave. Meanwhile, chipless RFID requires large operational bandwidth, such as the UWB bands (3.1-10.5, 22-

26.5, and 60 GHz). As the technology is still in concept, there is no standard frequency band yet for chipless RFID. The large bandwidth has an implication on the allowed transmission power. Considering the transmitted power is limited to 10 dBm, it is only ten mW compared to the maximum 4W in the chipped RFID [204]. The microwave frequency bands also limit the tag size and thus reduce the backscattered radiation to the reader. Consequently, the read range of chipless RFID is mostly limited to 1 m in the UWB frequency range, while the chipped UHF RFID could reach a 12 m reading distance. The coding capacity of the commercially available chipped RFID tags can be in the order of a few kilobits. In chipless RFID, however, the coding capacity is strictly limited by the tag size and the signal domain to encode the data. Therefore, the coding capacity of chipless RFID is limited to a few tens of bits. This far, the highest coding capacity of low-cost chipless RFID is 80-bit in time-domain but at the expense of short reading range, long tag size, and the need of mechanical displacement of the tag while reading [205]. Another difference in performance is the tag density or the ability to read multiple tags. While the chipped UHF RFID can read up to 1000 tags at once with the anti-collision protocol, chipless RFID can differentiate only three tags at once [206]. Finally, the price of chipped RFID tags is US\$0.05 minimum, while the chipless RFID tag is potentially below US\$0.01 if printed on low-cost media such as a paper substrate.

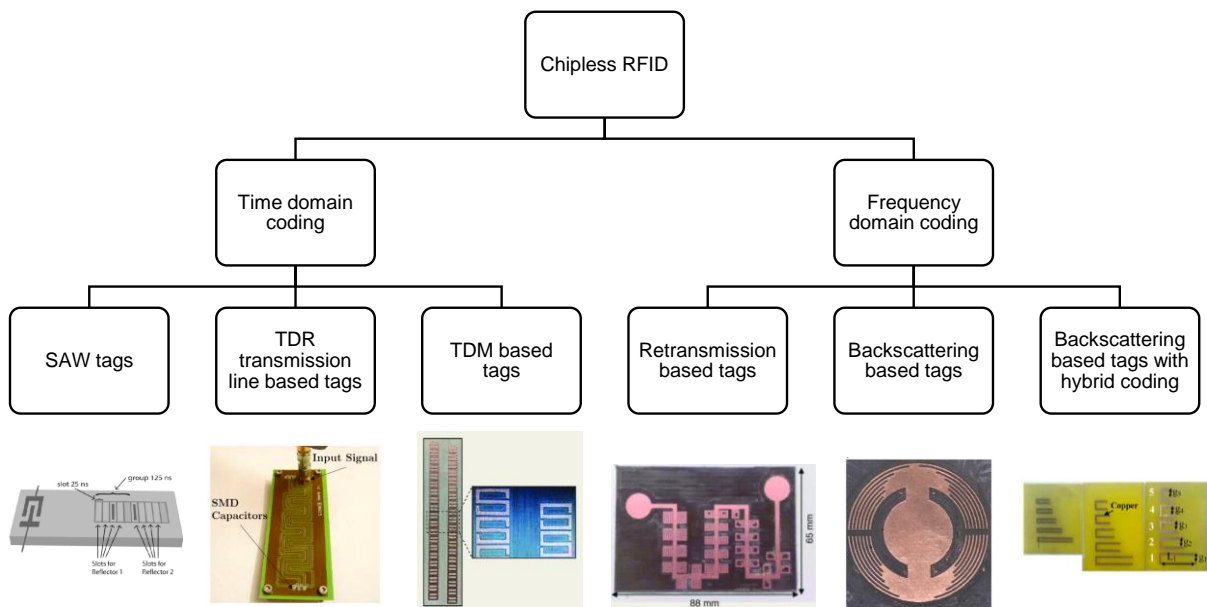


Figure 2.30 Classification of chipless RFID with the illustration of tags extracted from [207]–[212].

As shown in Figure 2.30, chipless RFID can be classified into two major classes based on the signal domain used for coding: time-domain coding and frequency domain coding [202]. The time-domain coding is based on the presence or absence of a pulse within the tag's echo. It uses

the reflectometry principle, and the tags generally comprise a transmission line connected to an antenna. Some parasitic elements are placed along the transmission line to produce pulses at certain timing moments. The advantage of the time domain coding is a fairly long read range in the order of a few meters. The precursors of time-domain chipless RFID tags are the surface acoustic wave (SAW) tags [207], [213], which typically work at 2.45 GHz, and the information capacity is relatively high, up to 256 bits. Although SAW tags are the only commercialized chipless RFID tags to date, the cost of SAW tags is very high because of the use of expensive piezoelectric substrate to transform the electromagnetic wave into an acoustic wave. For low-cost implementation, an alternative solution is the TDR tags based on the microwave transmission line, which contains discontinuities at certain positions to produce an echo that consists of delayed pulses [210]. To create measurable pulses, either the transmission line needs to be lengthy, or the pulses need to be narrow. Therefore, the bit encoding capability of TDR transmission line tags is generally limited [214]. Time-division multiplexing is an unconventional coding technique for near field chipless RFID applications. The operating principle is completely different from the SAW and the TDR transmission line tags. A TDM tag consists of a chain of resonant elements or metallic strips [209]. In order to read the tag, the tag needs to be mechanically displaced over the reader, which is made of a planar microwave resonant element coupled to a transmission line. While being displaced over the reader, the tag modulates the signal amplitude of the transmission line due to electromagnetic coupling between the resonators at the tag and the reader. TDM tags are low-cost and can overcome the limited capacity of the time domain coding. However, a TDM tag has a long dimension due to the chain of resonators. Furthermore, the reading mechanism is in near-field and requires mechanical displacement, and thus, TDM tags have limited applications [215].

Frequency domain coding relies on the presence or absence of distinctive patterns, like resonant peak or dip, at a predetermined frequency in the spectrum [216]. The tags that use frequency-domain coding are also known as the spectral signature or frequency signature tags. Frequency signature-based tags can be implemented using resonant structures tuned to resonate at different and predefined frequencies. In general, frequency-domain coding allows a greater coding capacity and density than time-domain coding for a limited tag area. However, it occupies a large bandwidth. Frequency signature tags have a shorter read range and sensitive to the environment. Calibration with the environment is often required to extract the information from the tag [202]. The first type of frequency signature tags is based on the retransmission approach. The retransmission-based tags are implemented using a planar filter connected to a receiving antenna and a transmitting antenna. The filter is loaded with multiple resonators, e.g., spiral resonators, to perform encoding [208]. The antennas are used to receive the interrogation signal

from the reader and retransmit it after being encoded by the loaded filter. The obvious downside of this type of tag is bulky because of the two antennas. The second approach is based on the backscattering approach through the singularities in the tag's RCS. This type of tag consists of resonant structures, which generates multiple resonances within the backscattered signal. The backscattering-based tags can be implemented using loaded antennas, resonators, or RF encoding particles (REPs) [217]. Since this strategy does not need antennas for retransmission, the tag size can be minimized.

Hybrid coding is a technique to increase the coding capacity of chipless RFID tags by assigning two or more logic states to a single resonant element [218]. This technique is mostly used as an extension of the frequency domain coding. It breaks the rule that one resonant element can represent only one resonance. With this strategy, the coding capacity can be increased for the limited available bandwidth as each resonant element can represent more than one bit. Hybrid coding can be implemented in various ways. A hybrid coding technique by exploiting the positions of the peak and the dip can be implemented using the C-shaped resonator via adjusting the length of the arms and size of the slot [219]. Peak frequency and peak amplitude of loop resonators can be used for hybrid coding by adding resistive bands [220]. Other techniques include combining frequency and phase deviation, frequency and polarization diversity, frequency and resonance depth, bandwidth division, and other techniques are discussed in [26], [218].

The frequency-domain backscattered-based tags are attractive because they can be compact while also allow higher coding capacity than the time domain chipless RFID. Moreover, the hybrid coding techniques are mostly proposed for the frequency domain backscattered-based tags. Another substantial feature for the classification of the frequency domain backscattered-based tags is the presence or absence of a ground plane. The performances achieved by chipless RFID tags with or without ground plane are different. The chipless RFID tags with a ground plane follow the microstrip structures and usually have a high RCS due to reflection from the ground plane. The ground plane isolates the resonators from the object to which they are attached. Thus, chipless RFID tags with a ground plane can be attached to various objects, including metals. However, the presence of the ground plane makes it difficult to manufacture tags using printing techniques on low-cost substrates since there are two conductive layers.

On the contrary, the chipless RFID tags without ground plane generally have weak RCS and less significant resonance peaks/dips. The performance will change depending on the materials of the object on which they are mounted. However, the chipless RFID tags without ground plane are much simpler to design and manufacture [202].

2.6.2 Chipless RFID Sensors

Like the traditional chipped RFID, the sensitivity of chipless RFID tags to their environment makes it possible to use and adapt them for sensing applications [202]. On top of being wireless and passive, chipless RFID sensors can be extremely low-cost, printable, suitable for mass production, and durable in harsh environments. The absence of a chip lowers the cost and so facilitate large-scale deployment [24]. For these reasons, there is a growing interest in the scientific community for chipless RFID sensors [221], [222]. Integrating sensing capabilities with chipless RFID tags will open up many new applications in various fields such as healthcare, agriculture, energy sectors, retails, public transportations, construction, logistics, and supply chain management [27].

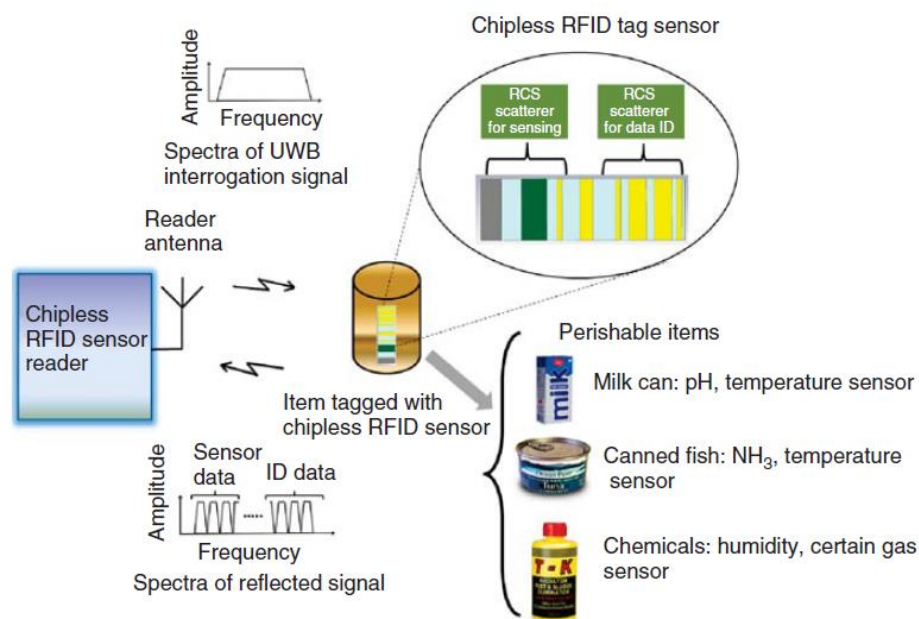


Figure 2.31 Generic principle of a chipless RFID sensor system [27].

Figure 2.31 illustrates the generic principle of a chipless RFID sensor system, mainly the frequency domain-based system. The principle is quite straightforward, similar to that of reading chipless RFID tags. A chipless RFID sensor reader transmits a broadband interrogation signal to the chipless RFID sensor attached to an object. The chipless RFID sensor consists of resonant elements to encode both ID and sensor data. The sensor may incorporate sensing materials sensitive to the measurands, such as temperature, humidity, or certain gas. As a radar target, the chipless RFID sensor will reflect a signal containing the ID data and the sensor data towards the reader. The sensor data will vary due to the resonant elements' sensitivity and the sensing materials to the measurands and can be analyzed at the reader side.

Chipless RFID sensors have been investigated for a significant number of applications, such as physical (pressure, humidity, temperature) sensors, chemical/gas sensors, smart packaging,

structural health sensors, position, displacement, touch sensors, wearables, and implants. Various chipless RFID sensors, as well as smart sensing materials, have been comprehensively reviewed in [24], [221], [222]. By using different types of resonant elements incorporated with sensing materials, many studies have demonstrated the feasibilities and the printability of chipless RFID sensors. Different resonant elements, including antenna structures and various resonators such as LC, dipole, ring, fractal, stepped impedance, spiral, have been reported. Kapton, polyvinyl alcohol (PVA), polydimethylsiloxane (PDMS), PEDOT, carbon nanotubes (CNTs), silicon nanowires (SiNWs), graphene are a few examples of sensing materials used for detecting temperature, humidity, and gas [223]. These sensing materials can be used to compose or modify the resonant elements. The non-conductive sensing materials, e.g., Kapton, PVA, PDMS, PEDOT, can be applied as a substrate or superstrate for the resonant elements to incorporate dielectric change in the resonant property. The conductive and semi-conductive sensing materials, e.g., CNTs, graphene, SiNWs, can be used as a forming material of the resonant elements to exploit conductivity change for sensing. Depending on the sensing principle, some typical sensing features in the signal that can be extracted from chipless RFID sensors include resonance frequency shift, magnitude variation, and group delay variation.

Most works on chipless RFID sensors focused on the frequency domain chipless RFID tags. Many physical variables can be sensed by exploiting the frequency-dependent behavior of resonant structures and materials. Another exciting aspect of chipless RFID sensors is the possibility to implement multi-parameter sensors for simultaneous detection of temperature and humidity [25], thanks to the broadband operation of chipless RFID technology so that multiple features can be incorporated within the sensor's signature. The problems and challenges in implementing chipless RFID sensors include read range, tag/sensor size, ease of fabrication, and sensor performance, such as sensitivity, resolution, and reliability [221].

2.6.3 State-of-the-Art Chipless RFID Sensors and Antenna Sensors for SHM

As for other sensing applications, chipless RFID technology has great potentials to lower the cost of wireless and passive sensors for the IoT-based SHM [221]. Chipless sensors can be mounted or embedded in safety-critical structures at predefined locations or to cover a wide area as a smart coating/skin [224]. Moreover, chipless sensors can work in harsh environments where most electronic components are unable to operate. For instance, sensing on an engineering structure at sub-zero or 200°C temperatures would be challenging tasks with chipped RFID sensors because the chip may face issues at extreme temperatures [203]. Since chipless RFID is relatively new for SHM, the pursuit of chipless RFID sensors for SHM in this section includes antenna sensors. In the literature, antenna sensors are frequently included in

the discussions on chipless RFID sensors for SHM [24], [175], [221], [222]. Although typical antenna sensors use wired excitation, antennas can work as passive resonant structures, wirelessly interrogated, and they can be regarded as building blocks for chipless RFID sensors.

2.6.3.1 Chipless RFID Sensors and Antenna Sensors for Crack Detection and Characterization

Table 2.6 List of chipless RFID sensors and antenna sensors for crack detection and characterization. The highlighted row shows the only chipless RFID sensors for crack detection before 2016. The sensor was proposed for crack detection in concrete and using time-domain chipless RFID.

Ref	Year	Measurand	Sensor design			Measured parameter [feature]	Pros	Cons
			Band	Design	Size			
Mohammad [225]–[227]	2012	Crack in aluminum	5.6-7.7 GHz	Dual-band rectangular patch antenna using optimum feeding position	17.3 mm × 12.7 mm	Reflection coefficient [resonance frequency shift]	Crack length and orientation detection; sensitivity of 48.7 MHz/mm crack	Wired excitation
Cook [228]	2012	Crack in metal	1.8-2 GHz	Rectangular patch antenna on paper and foam	87 mm × 70 mm	Reflection coefficient or time-gated frequency response [resonance frequency shift]	0.5-m reading distance; can detect crack with different length, shapes, and orientation	Crack needs to break the sensor; needs dual-polarization interrogation for wireless reading
Xu [229]	2012	Crack in aluminum	5.5-14 GHz	Rectangular patch antenna array on Kapton	10.4 mm × 8.6 mm and 7.2 mm × 6 mm	Reflection coefficient or time-gated frequency response [resonance frequency shift]	Crack length progression detection; sensitivity of tens MHz/mm crack; sub-mm resolution; 0.84-m reading distance	Needs laser beam illumination and impedance switching for wireless reading
Kalansuriya [230], Dey [231]	2012, 2014	Crack in concrete	1-4 GHz; 2-20 GHz	Planar monopole antenna with the long meandered transmission line (TDR-based chipless RFID)	810-mm length	Signal amplitude in the time domain (echo pulse delay)	can detect crack location and propagation	Crack needs to break the sensor; need a long transmission line or a narrow pulse with massive bandwidth; 150-mm reading distance
Cho [232]	2016	Strain in aluminum and crack on the sensor	2.9 and 5.8 GHz	Two rectangular patch antennas connected via a matching network for frequency doubling mechanism	140 mm × 70 mm × 0.79 mm	Received power [resonance frequency shift]	Able to distinguish sensor signal from environmental reflections; 0.5-m reading distance	Crack needs to break the sensor; needs a diode in the matching network
Ke [233]	2018	Crack in metal	1-3 GHz	Dual-band rectangular patch antenna using optimum feeding position	40 mm × 28 mm × 0.5 mm	Reflection coefficient [resonance frequency shift]	Algorithm to predict crack length for different crack orientation	Wired excitation

A literature survey was attempted to find articles related to chipless RFID sensors and antenna sensors for crack detection and characterization. The list is presented in Table 2.6, providing

extracted information about the sensors' operating frequency band, design geometry, size, measured parameter, and feature, as well as the pros and cons.

Antenna sensors, particularly rectangular patch antennas, have been extensively studied for detecting cracks. Most studies were conducted in the microwave band above 1 GHz and exploited the resonance frequency shift measured via the reflection coefficient to indicate the crack parameters. In 2012, *Mohammad et al.* published several articles demonstrating dual-band rectangular patch antennas for detecting crack length and crack angular orientation by using the shifts of two resonant frequencies [225]–[227]. The optimum asymmetric microstrip line feeding offers dual resonant modes, which were used to distinguish two crack parameters simultaneously. Despite the high sensitivity to crack, the proposed antenna sensors used traditional wired excitation. A rectangular patch antenna printed on the paper substrate was proposed by *Cook et al.* to detect crack length, shape, and orientation. The crack was only emulated by breaking the antenna, but the sensor was able to work as a passive sensor and read wirelessly from a 0.5-m distance. For performing the wireless reading, dual-polarization interrogations and time gating were introduced, and an additional terminating impedance on the antenna sensor was required to delay the antenna backscatter at one of the antenna polarization [228].

Similarly, a rectangular patch antenna array can detect a longer crack progression using the resonance frequency shift, as shown by *Xu et al.* The antenna sensor could also work as a passive sensor and can be interrogated wirelessly. However, at least two readings were required for the impedance switching mechanism on the sensor, along with signal processing for time-gating. An additional laser beam at the reader and electronic components, i.e., photocell, resistor, transistor, were required on the sensor to control the impedance switching [229]. Whereas the feasibility of wireless and passive antenna sensors for crack detection was reported, chipless RFID sensors for crack detection were rarely seen until the publications by *Kalansuriya et al.* [185] and *Dey et al.* in 2012 and 2014, respectively [186]. They proposed TDR chipless RFID sensors to detect the crack location and crack propagation in concrete by exploiting a UWB planar monopole antenna connected to a long-meandered transmission line. The crack was emulated by cutting the transmission line at a specific location and was indicated by the time of arrival of the received echo pulse. Either a long transmission line or a very short pulse with super-wide bandwidth was required to achieve high-resolution crack location detection.

Thenceforward, scientific attention to chipless RFID sensors for crack detection and characterization remained relatively low while several antenna sensors for crack detection were

still reported. In 2016, *Cho et al.* proposed a frequency doubling antenna sensor using two rectangular patch antennas connected via a matching network. The design could distinguish the sensor response from the environmental reflection [232]. However, the sensor was relatively large and incorporated a diode on the matching network. In 2018, *Ke et al.* also reported a dual-band rectangular patch antenna and an algorithm to predict crack length under different crack orientations. There was no wireless reading performed as the antenna sensor used wired excitation [233].

Overall, different configurations and sizes of rectangular patch antennas have been investigated for crack detection. However, only a few articles on chipless RFID sensors for crack detection were found. The rectangular patch antennas operated at higher frequencies tend to be smaller in size than chipped UHF RFID tag antennas. Additionally, sensitivity in the order of tens MHz per mm crack is achievable in the microwave frequency range. With the wired excitation and asymmetric feeding, dual resonant modes can be obtained to distinguish two crack parameters simultaneously. This shows the multi-parameter sensing capability of antenna sensors operated in a broad bandwidth. Several efforts to read the antenna sensors wirelessly have been reported, but electronic components are required on the sensors, opposing the electronic-free characteristic of chipless RFID. There are common issues and challenges related to antenna sensors for crack detection. Some of them are the ability to detect multiple parameters of crack, sensitivity to crack, resolution, reading distance, and separation of the antenna sensor response from environmental reflections in the wireless reading mechanism. Furthermore, the studies are mostly at the level of proof of concept in a laboratory, where VNA is commonly used as the reader platform.

2.6.3.2 Chipless RFID Sensors and Antenna Sensors for Corrosion Detection and Characterization

Corrosion detection and characterization using chipless RFID sensors and antenna sensors received not much attention in the literature, especially before 2016. In Table 2.7, a list of recent chipless RFID sensors and antenna sensors for corrosion detection is presented.

Chipless RFID sensors and antenna sensors for corrosion detection and characterization have been investigated using the frequency domain retransmission-based chipless RFID and planar resonators. Resonance frequency shift from the measured scattering parameters using VNA has been a typical feature to indicate corrosion. In 2016, *Khalifeh et al.* demonstrated the retransmission-based chipless RFID sensor developed based on the microstrip stub resonators [234]. Exposing the resonator's stubs to a constant humidity for a few months resulted in variations in the form of resonance frequency shifts. By connecting the resonator to two UWB

planar monopole antennas, the sensor was readable from a 0.3-m distance using a portable USRP. However, the connection between the resonator and the transceiver antennas was by wire, thus making the sensor troublesome in installation.

Table 2.7 List of chipless RFID sensors and antenna sensors for corrosion detection.

Ref	Year	Measurand	RFID tag antenna sensor			Measured parameter [feature]	Pros	Cons
			Band	Design	Size			
Khalifeh [234]	2016	Corrosion affecting the sensor	0.2-9 GHz	Retransmission-based chipless RFID (microstrip stub resonator connected to UWB monopole transceiver antennas)	Resonator only: ~50 mm × 39 mm	Transmission coefficient [resonance frequency shift]	0.3-m reading distance; reader implemented using a portable USRP	Resonator and the transceiver antennas are connected by wire
Zarifi [235]	2017	Coating lift-off due to water ingress on metal pipe	90-120 MHz	LC resonator (interdigitated capacitor connected to a coil)	130 mm × 100 mm	Reflection coefficient [resonance frequency shift]	Simple and inexpensive structure	Large coil required to communicate with the reader; 10-mm reading distance; not tested with real corrosion
Zarifi [236]	2018	Air breaches and water ingress on metal pipe	1-3 GHz	Microwave ring resonator connected to a bow-tie antenna	Resonator: N/A; antenna: 120 mm × 70 mm	Reflection coefficient [resonance frequency shift]	Simple and inexpensive structure	Large antenna to communicate with the reader; 60-mm reading distance; not tested with real corrosion
Deif [237]	2019	Water ingress on metal pipe	3.1-3.9 GHz	Retransmission-based chipless RFID (planar filter with multiple spiral resonators connected to monopole antennas)	Filter: >120 mm long; Antenna: 48.2 mm × 43 mm	Transmission coefficient [resonance frequency shift]	Multiple location detection using multiple resonators; off-sight detection	Reading distance 70 mm; no quantitative level of water ingress; not tested with real corrosion

A wireless and passive sensor for detecting water ingress and corrosion prediction was proposed by *Zarifi et al.* using an LC resonator that operated around 100 MHz [235]. The resonator integrated an interdigitated capacitor (IDC) structure connected to a coil antenna to communicate with the reader coil. The sensor structure was simple and inexpensive, but the coil was relatively large, and the reading distance was only 10 mm. For operation at the microwave frequency range, *Zarifi et al.* also designed a microwave ring resonator, which can be connected to a bow-tie antenna for wireless reading [236]. The reading distance was only 60 mm and thus not significantly improved than the previous system using a coil at 100 MHz. Another retransmission-based chipless RFID was recently reported by *Deif et al.*, employing an array of spiral resonators connected to planar monopole antennas [237]. The flexible sensor could detect water ingress locations below a pipeline by observing resonance frequency shifts of the spiral resonators. However, the reading distance was only 70 mm, and no quantitative level of water ingress was presented.

Currently, chipless RFID sensors for corrosion detection are still limited to the retransmission-based chipless RFID. In this type of chipless RFID, planar resonators are connected to

transceiver antennas, which makes the overall size of the sensor large. Moreover, instead of detecting real corrosion, the studies offered corrosion prediction by detecting water ingress. This might be because of the difficulty in obtaining corrosion samples and experimenting with corrosion in the laboratory environment. Regarding the reading distance, a study has shown a possibility to read a chipless sensor from 0.3 m using a portable USRP. The studies that mounted the chipless sensor on a metallic pipe, however, appeared to suffer from the limited reading distance, as the maximum achievable reading distance was only 70 mm.

2.7 Research Gap, Problems, and Challenges Identified

This chapter has systematically reviewed several topics related to approaches for defect detection, including NDT&E techniques, SHM technologies, and the trend towards the IoT based SHM, chipped RFID tag antenna-based sensors, chipless RFID sensors, and antenna sensors for SHM. Various NDT&E and SHM techniques, including chipped RFID, have been applied for crack and corrosion detection and characterization. While chipless RFID is a breakthrough in wireless identification and sensor technology, there is a research gap found in the literature that not many chipless RFID sensors have been studied for SHM of defects. In particular, the frequency domain backscattering-based chipless RFID for SHM is insufficiently investigated. Whereas, chipless RFID technology opens opportunities for developing sensors that can be wireless, passive, low-cost, durable in harsh environments, and simple to manufacture. While being operated in the microwave frequency range, chipless RFID sensors potentially have a smaller size and thinner profile than the chipped RFID sensors. Furthermore, the broadband operation of chipless RFID makes it possible to develop multi-parameter sensors.

Based on the review and for the contexts of research carried out in this thesis, relevant problems and challenges related to chipless RFID sensor systems for SHM are categorized and listed in Figure 2.32. The problems and challenges can be associated with the type of metal defects, sensor design and fabrication, sensor performance, reader platform, and signal processing. The type of defects, i.e., crack and/or corrosion, should be regarded as problems, which determine the sensing mechanism. On the aspect of sensor design and fabrication, metal-mountable sensor design and geometry, sensor size and profile, and the ease of manufacturing and printability are challenges. Therefore, the selections of operating frequency, resonant elements and geometry, and substrates/materials are crucial. On the sensor performance, the ability to perform multi-parameter sensing, readability/reading distance, sensitivity, resolution, as well as reliability, and robustness against the wireless channel need to be tackled and evaluated. On the reader and signal processing aspect, approaches for signal measurement, signal processing, and feature extraction are needed for the quantitative evaluation of defects. In addition, unlike the standard

chipped RFID technologies, there is no mature and commercial reader for chipless RFID sensor systems. Therefore, although VNA can be used as a reader platform at the proof of concept levels, the implementation of a portable reader and antennas is a challenge for chipless RFID sensor systems.

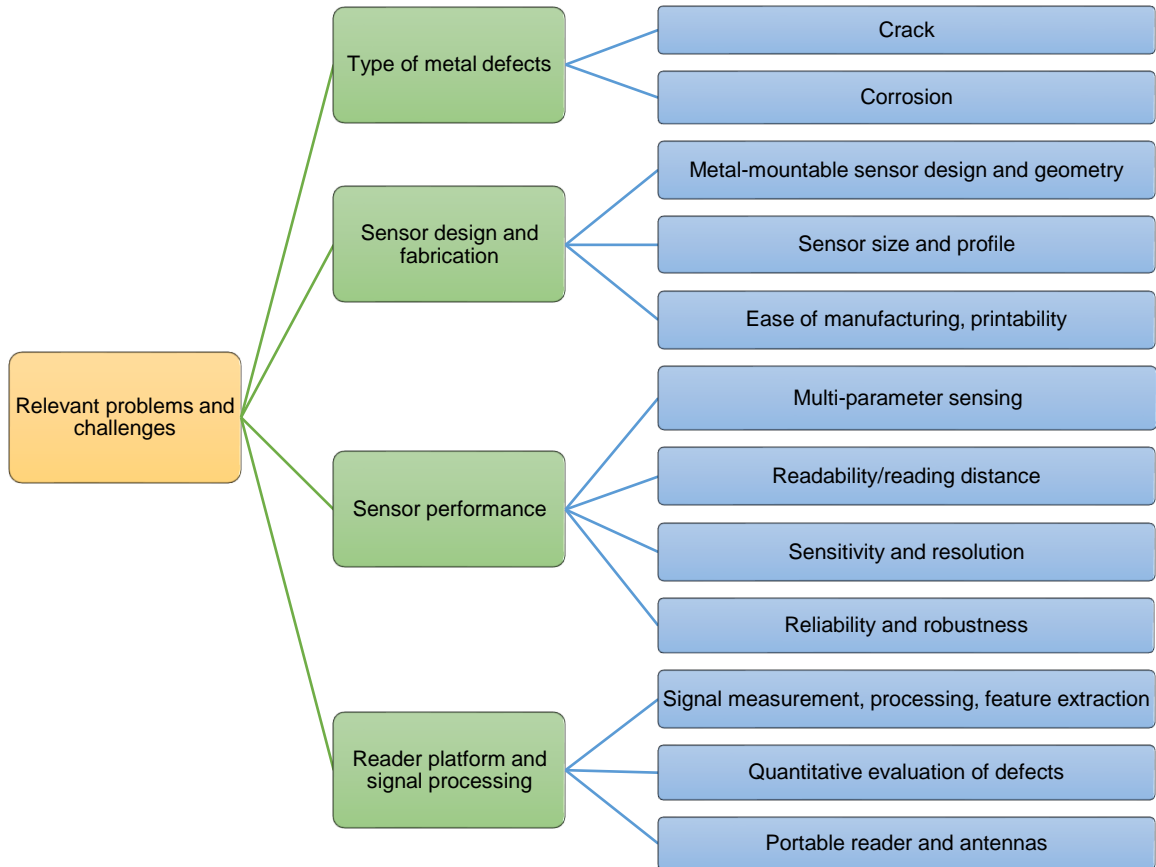


Figure 2.32 Relevant problems and challenges for research on chipless RFID sensor systems for SHM.

Chapter 3 Research Methodology and the Proposed Chipless RFID Sensor System for Defect Detection and Characterization

Following the research gaps, problems, and challenges identified in Chapter 2, the research methodology and background of the proposed chipless RFID sensor system for defect detection are introduced in this chapter. The application of chipless RFID technology for defect detection is relatively new compared to the chipped ones. This chapter proposes a chipless RFID sensor system for defect detection that consists of not only the sensor and reader but also the signal processing subsystem, including feature extraction, selection, and fusion. Problems and challenges related to crack and corrosion detections and robustness against multiple influences are tackled with novel chipless RFID sensor designs, reader configurations, alongside feature extraction, selection, and fusion methods.

In this chapter, the research methodology is outlined in Section 3.1, linking the relevant problems and challenges with three studies carried out in this thesis. Then, the background theories related to the proposed chipless RFID sensor system are described in Section 3.2. Design approaches for metal-mountable chipless RFID sensors are discussed in Section 3.2.1 based on strategies for designing metal-mountable chipless RFID tags, such as microstrip patch antennas, frequency selective surfaces (FSS), and RF encoding particles. As the proposed sensor systems will be demonstrated using different reader platforms, i.e., VNA and portable reader, the chipless RFID reader mechanism based on the radar principle is described in Section 3.2.2. Then, the required signal processing for chipless RFID sensor systems is explained in Section 3.2.3, introducing pre-processing, feature extraction, selection, and fusion. Finally, the chapter is summarized in Section 3.3.

3.1 Research Methodology

The research in this thesis is focused on the design and development of chipless RFID sensor systems to address three sets of problems and challenges related to defect detection and characterization. The research methodology is outlined in a diagram shown in Figure 3.1. The problem and challenges to be addressed include crack detection and characterization with integrated ID encoding and sensing; corrosion characterization with enhanced sensitivity and reliability; and robust characterization of crack and corrosion in a realistic environment using a portable reader. The research methodology involves the design, simulation, and experimental studies of chipless RFID sensor systems using dedicated defect samples. A metal-mountable chipless RFID sensor is a critical component in the sensor system. In the first stage, a metal-

mountable chipless RFID sensor is designed and simulated in an EM modeling software, i.e., CST Microwave Studio. The sensor design is preceded by a theoretical analysis of the defect detection mechanism, which is verified in the simulation. Thus, not only is the sensor modeled, but also the variation of defect parameters is studied in the simulation. Once the sensing capability of the sensor is confirmed, the sensor is fabricated. The second stage is the experimental study incorporating the fabricated chipless RFID sensor, chipless RFID reader configuration, and preparation of dedicated defect samples. Unlike the chipped RFIDs, there is no mature and commercially available chipless RFID reader. In this research, therefore, the reader is configured by the selection and development of measurement platforms for data collection, e.g., VNA or portable reader and the reader antennas. In the third stage, after collecting experimental data, the signal pre-processing, feature extraction, selection, and fusion approaches are developed. Then finally, the defect is quantitatively evaluated and validated against the known status of the dedicated defect samples. Furthermore, the sensor performance from the measurement is evaluated and validated against the simulation results.

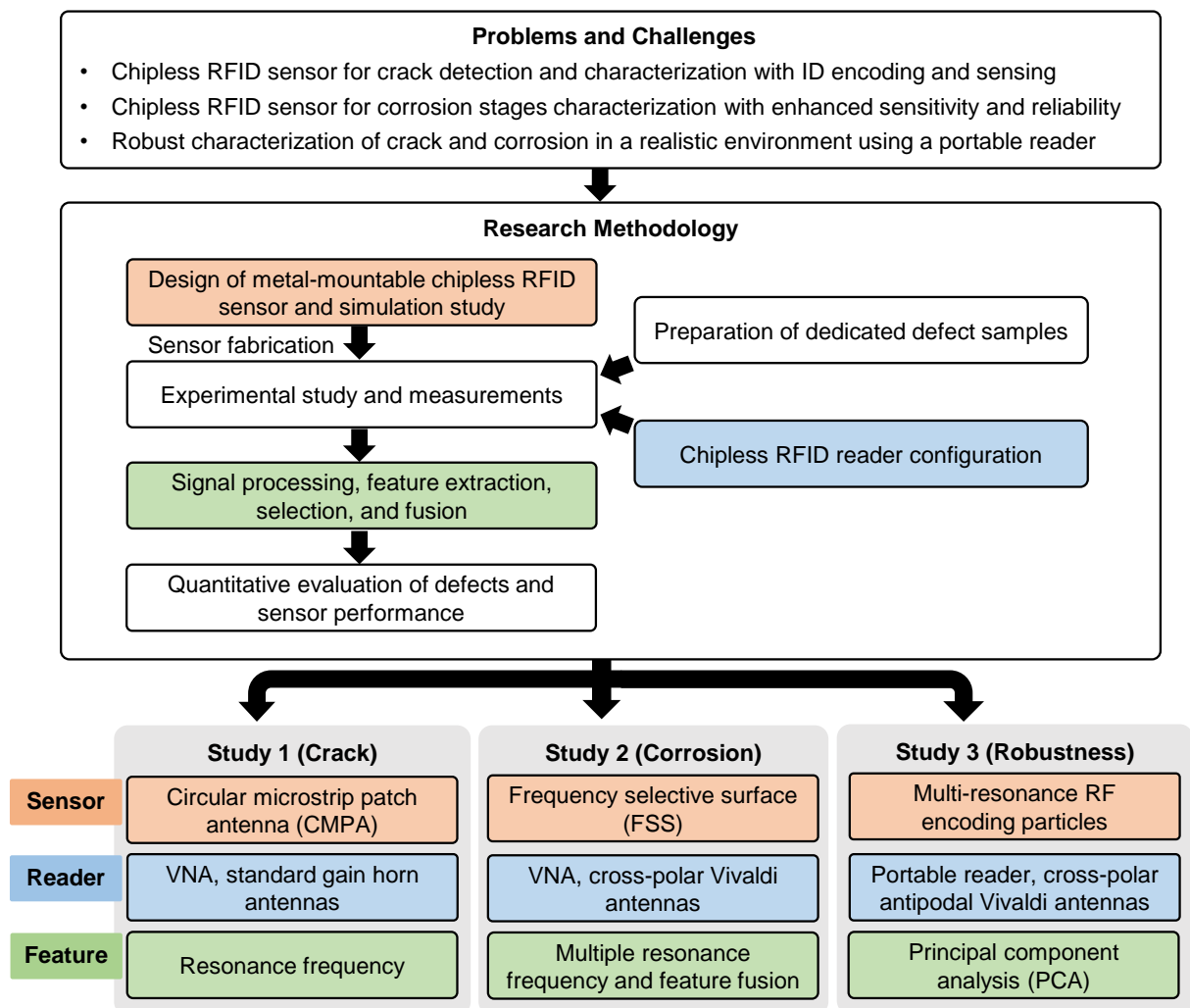


Figure 3.1 Diagram of the research methodology.

Based on the selected problems and challenges, as well as the research methodology, three studies are formulated. Different design approaches for chipless RFID sensors, reader configurations, as well as feature extraction, selection, and fusion methods, are exploited. The three studies are explained as follows.

3.1.1 Study 1: Chipless RFID sensor for crack detection and characterization based on circular microstrip patch antenna (CMPA)

This study proposes a novel use of the frequency-domain backscattering based chipless RFID for metal crack detection and characterization. The study designs a metal-mountable chipless RFID sensor that provides both sensor ID and cracks sensing functionality based on CMPA. Detection and characterization of multiple crack parameters, such as crack width and crack orientation, are studied. Standard laboratory equipment, i.e., VNA and horn antennas, are configured as the chipless RFID reader for RCS measurements and experimental study. The study analyzes relationships between the resonance frequency of the CMPA and the crack parameters in both simulation and experiment. Furthermore, the sensor performance, in terms of sensitivity and resolution, is examined.

3.1.2 Study 2: Chipless RFID sensor for corrosion characterization based on frequency selective surface (FSS) and feature fusion

After investigating crack detection and characterization in Study 1, this study deals with a chipless RFID sensor system for corrosion characterization. The study proposes a novel chipless RFID sensor designed based on FSS for the characterization of corrosion undercoating. Detection of corrosion rust thickness based on the principle of FSS is analyzed and verified in simulation. A VNA and dual-polarized Vivaldi antennas are used in the experimental study replacing the bulky horn antennas in Study 1. The study designs an FSS that generates multiple resonances for corrosion sensing. Therefore, multiple resonance frequency features are extracted, and the sensitivities to corrosion progression are analyzed. Furthermore, this study will apply feature fusion to enhance the sensitivity and reliability of the proposed chipless RFID sensor.

3.1.3 Study 3: Robust characterization of defects in a realistic environment using a portable reader, multi-resonance chipless RFID sensor, and Principal Component Analysis

This study is aimed at tackling the robustness issue against multiple influences in the characterizations of crack and corrosion in a realistic environment using a portable reader. A

novel multi-resonance chipless RFID sensor based on multiple RF encoding particles is designed and simulated. With the high number of resonances, the chipless RFID sensor is expected to convey rich sensing information. Unlike the other two studies that were carried out using a VNA, this study undertakes the experiment using a portable reader. The study eliminates the background subtraction requirement in the chipless RFID sensor system to demonstrate the robustness of the method. Statistical feature extraction based on principal component analysis (PCA) is used for the first time in a chipless RFID sensor system for multi-parameter evaluation of crack and corrosion in a realistic environment.

3.2 Background of the Proposed Chipless RFID Sensor System for Defect Detection and Characterization

The frequency-domain backscattering based chipless RFID is of interest to this thesis because of two reasons. First, its investigation for defect detection and SHM applications is still rare in the literature. Second, backscattering chipless RFID tags and sensors can be designed in a minimum size with multiple resonances for ID encoding and defect sensing. As reviewed in Chapter 2, the TDR chipless RFID and the frequency domain retransmission based chipless RFID have been studied for defect detection. These types of chipless RFID, however, integrate a transmission line or a microwave filter with antennas, thus making the size of tags and sensors relatively large.

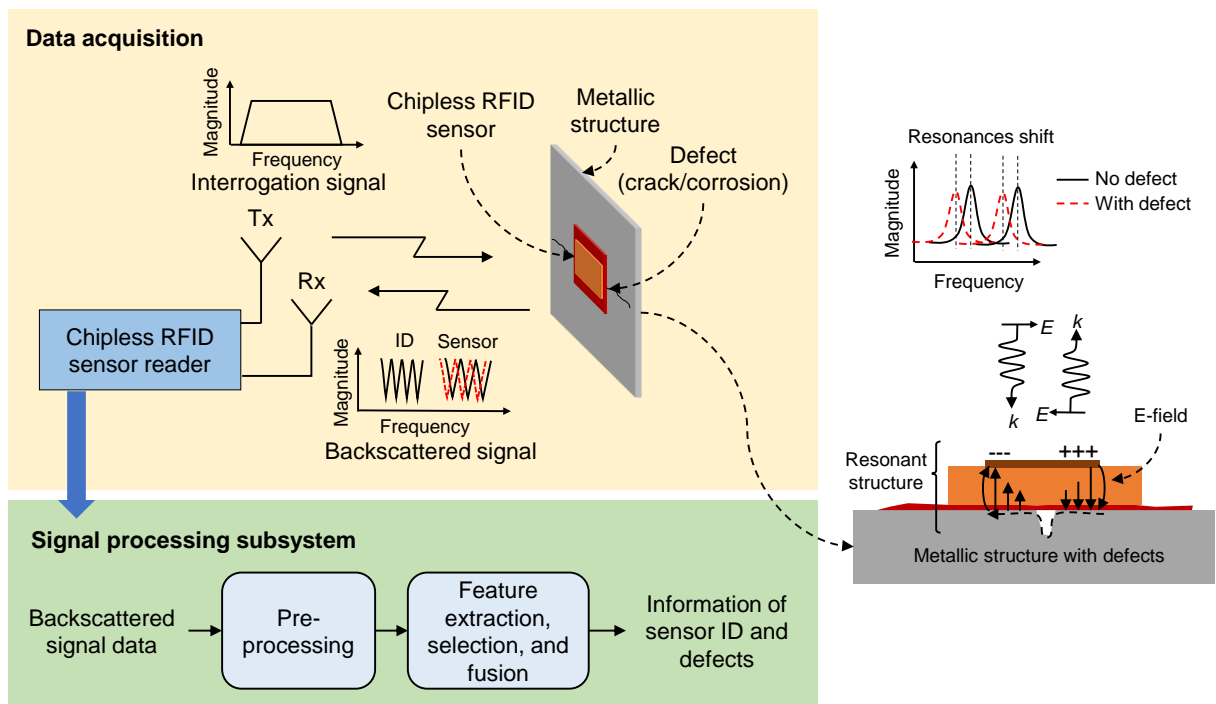


Figure 3.2 Operating principle of a chipless RFID sensor system for defect detection and characterization.

A frequency-domain backscattering based chipless RFID sensor system for defect detection is illustrated in Figure 3.2. It consists of a chipless RFID sensor and a reader for data acquisition and a signal processing subsystem. The chipless RFID sensor is mounted on the monitored metallic structure for defect detection. In operation, the reader first interrogates the sensor by transmitting broadband or sweep frequency signal through the transmitting (Tx) antenna. The interrogation signal is, in turn, reflected by the sensor and its surrounding environment resulting in a backscattered signal, which is then captured by the receiving (Rx) antenna. Since the chipless RFID sensor consists of resonant structures, it forms a multi-resonance signature in the backscattered signal. The ID of the sensor can be represented by the presence and absence of the resonance peaks/dips. The chipless RFID sensor and the monitored metal are designed to form a resonant structure. Due to the electromagnetic interaction, e.g., electric/capacitive coupling, between the chipless RFID sensor and the metal, the defect information can be related to the resonance frequency shifts or other variations in the sensor's electromagnetic signature. Then, the signal processing subsystem is responsible for performing signal pre-processing, feature extraction, selection, and fusion for the backscattered signal data to decode the sensor ID as well as to interpret the defect information. Further theoretical backgrounds related to the elements of a chipless RFID sensor system for defect detection are discussed in the next sections, including design approaches for metal-mountable chipless RFID sensors, chipless RFID readers and the reading mechanism, as well as signal processing, feature extraction, selection, and fusion.

3.2.1 Design Approaches for Metal-mountable Chipless RFID Sensors

Chipless RFID sensors for defect detection in metallic structures require the sensors to be metal-mountable. Metal-mountable chipless RFID tags and sensors have characteristics that do not change significantly in the proximity of metals. In the case of chipped RFID tags, the undesired electromagnetic interaction is a serious issue when tag antennas are mounted on conductive items. If the proximity of conductive material is omitted in the design, the operation of antennas is strongly influenced by metals, causing the tags not to function at all [156]. Likewise, the metal-mountable design is also a specific case for chipless RFID tags. One fundamental feature to classify chipless RFID tags is based on the presence and the absence of a ground plane. Chipless RFID tags designed with the presence of a ground plane are metal-mountable because the ground plane can isolate the resonant structures from the object on which the tag is mounted [202]. Several design approaches for chipless RFID tags with the ground plane are available in the literature: microstrip patch antenna, frequency selective surface (FSS), and RF encoding

particles (REPs). These design approaches can be adapted for metal-mountable chipless RFID sensors.

3.2.1.1 Microstrip Patch Antenna (MPA)-based Design

Microstrip patch antennas have been a well-known subject because of the requirements of low-profile antennas for aircraft, satellite, and wireless communications. Detailed analysis and designs of microstrip patch antennas have been adequately available in the literature [238]. As exhibited in Figure 3.3(a), a microstrip patch antenna comprises a very thin metallic strip/patch placed a small fraction of a wavelength above a ground plane. The strip/patch and the ground plane are separated by a dielectric slab, which is referred to as the substrate. Thick substrates with low dielectric constants provide better efficiency and larger bandwidth, but at the expense of larger element size. Thin substrates with high dielectric constants lead to smaller element sizes but less efficient and have relatively smaller bandwidths due to the more significant losses. Since the antenna size is vital, the miniaturization of microstrip patch antennas was recently studied by introducing a partial ridge or projection of the patch and combinations of multiple substrates [239], [240].

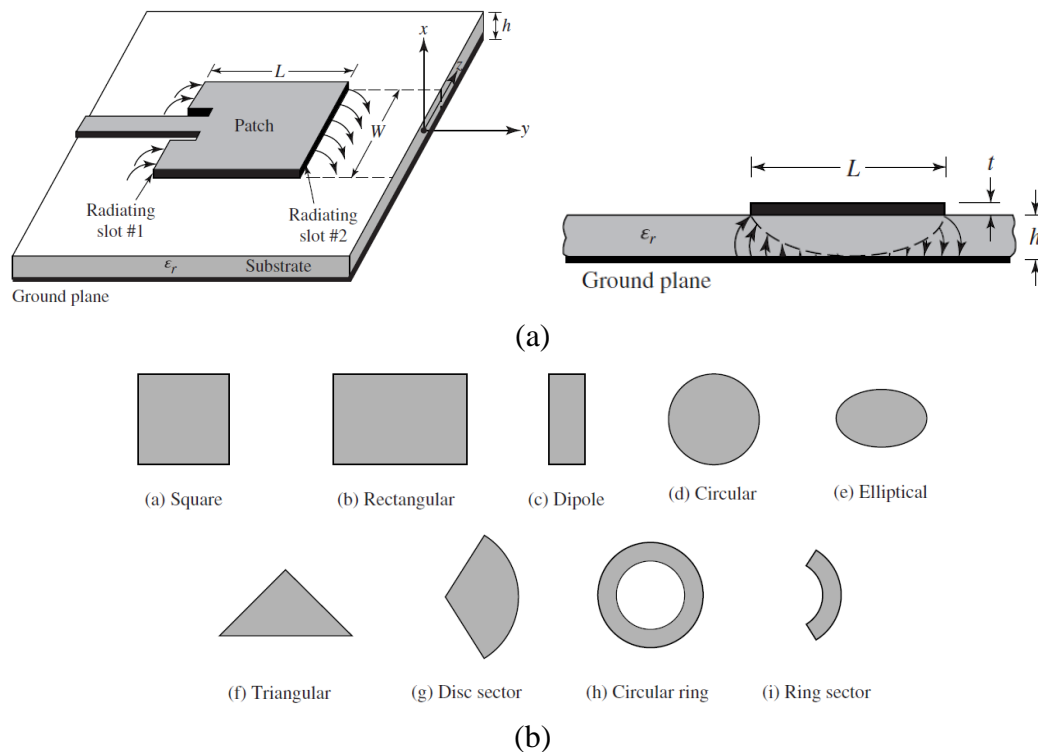


Figure 3.3 Microstrip patch antenna: (a) General geometrical representation. (b) Typical shapes for microstrip patch elements [238].

Typical patch elements for MPA can be square, rectangular, dipole, circular, elliptical, triangular, or any other configuration, as illustrated in Figure 3.3(b). An example of a metal-mountable chipless RFID tag based on square MPA is shown in Figure 3.4. The tag consists of square patches above a ground plane resonating at four distinct frequencies. By tuning the

dimensions of the square patch, four resonance dips can be controlled and used to encode a 4-bit tag ID [241].

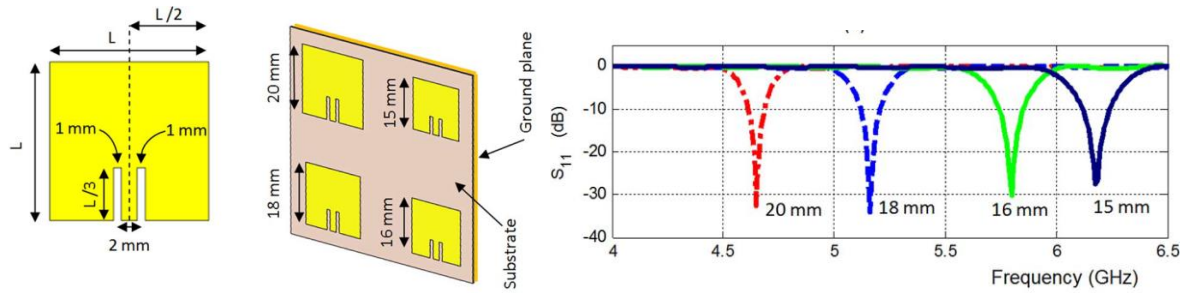


Figure 3.4 A metal-mountable chipless RFID tag based on MPA comprising four inset-fed rectangular patches with distinct sizes on a ground plane [241], [242]. The patch size determines the resonance frequencies used for ID encoding.

3.2.1.2 Frequency Selective Surface (FSS)-based Design

Frequency selective surface (FSS) is two-dimensional periodic structures composed of planar metallic array patches or apertures designed to transmit, reflect, or absorb EM waves [243]. Depending on the design, FSS can pass or block EM waves of certain frequencies in free space, and thus FSS is known as spatial filters in electromagnetics. Filtering characteristics of FSS can be classified into low-pass, high-pass, band-pass, and band-stop. The low-pass and high-pass filtering can be implemented using basic elements such as square patches and the complementary (grid), as shown in Figure 3.5(a). An FSS can be modeled by a series or parallel RLC circuit, where R and L are created by the metal patches, and C is generated by the gaps among the metal patches. The equivalent circuits correspond to the filter responses of the FSS. Simple square metal patches act like a spatial low-pass filter, while the complementary elements (square slot array or square grid) behave like a spatial high-pass filter. The inductive and capacitive surfaces can be combined and tuned to generate the desired filter response. In general, there are four groups of typical FSS elements, as shown in Figure 3.5(b). FSS can be designed by selecting any of these shapes or using a combination and modification of them.

FSS-based design for metal-mountable chipless RFID tags exploits the properties of multi-resonance high impedance surface (HIS) [244]. HIS can be implemented by composing FSS elements over a grounded dielectric slab. The sandwich configuration of FSS elements, a dielectric slab, and a ground plane form a subwavelength resonant cavity denoted by an input impedance approaching infinite and a reflection phase crossing zero at the resonance frequencies. The matching between the high input impedance and the free-space impedance at 377Ω creates absorptions of incident waves at the resonance frequencies. Figure 3.6 illustrates a chipless RFID tag based on FSS, which exploits periodic multiple square ring elements on a dielectric substrate and a ground plane. The RCS and reflection coefficient shows that the FSS

structure generates multiple resonances governed by the dimensions of the square rings. Each square ring corresponds to the presence and absence of each resonance dip used to encode the tag ID.

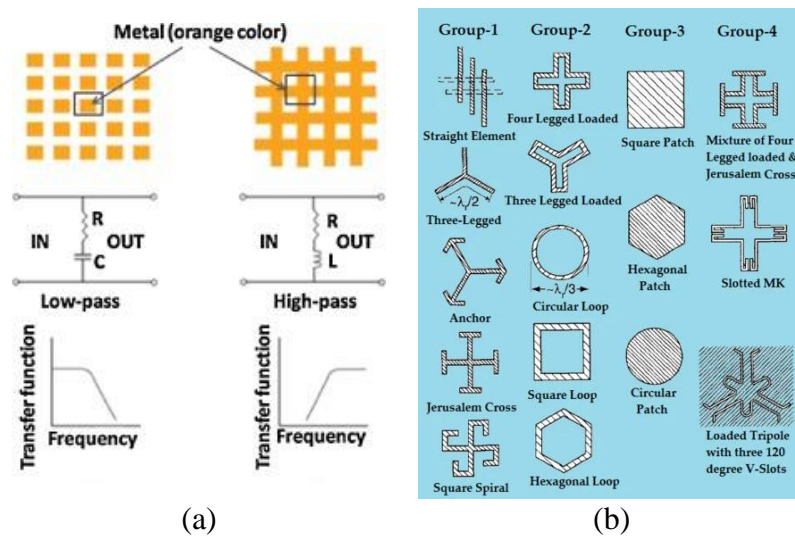


Figure 3.5 FSS: (a) FSS periodic structure consisting of complimentary array elements, their equivalent circuits, and the frequency responses. (b) Various shapes of FSS elements [243], [245], [246].

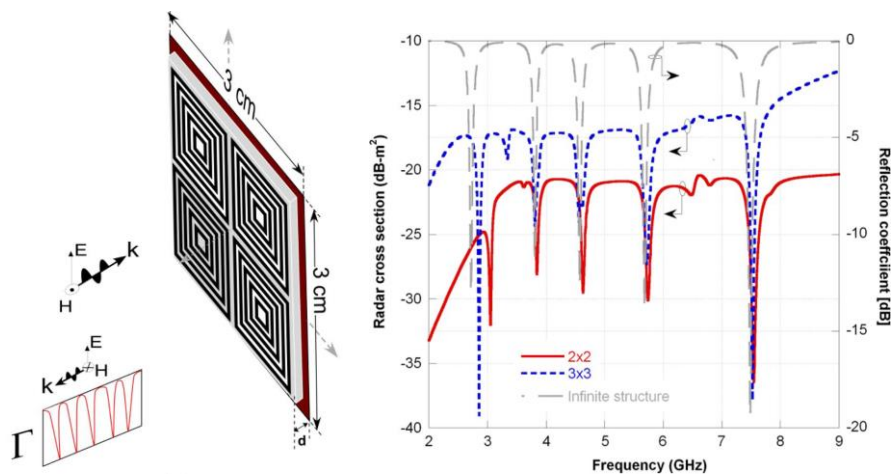


Figure 3.6 A metal-mountable chipless RFID tag based on FSS comprising periodic multiple square ring elements on a dielectric substrate and a ground plane. The RCS and reflection coefficient show multiple resonances for ID encoding [244].

3.2.1.3 RF Encoding Particle (REP)-based Design

The REP design approach is based on the idea of using resonant scatterers, which carry out the function of receiving antenna, filter, and transmitting antenna. A backscattering chipless RFID tag can be composed of a certain number of resonant scatterers depending on the desired amount of resonances and the available surface area. The first and straightforward implementation of a chipless RFID tag based on REP is using dipole resonators, as shown in Figure 3.7 (a). The coding capacity of this tag can correspond to the number of dipoles and the generated resonances. Another example of a REP-based design is using C-shaped resonators, as exhibited

in Figure 3.7(b). C-shaped resonators show a good compromise between the resonance selectivity and size. The structure is suitable for achieving a high coding capacity since many resonances can be occupied within a limited tag area and limited frequency bandwidth. However, C-shaped resonators work without a ground plane, thus unsuitable for metal-mountable chipless RFID tags and sensors. Other shapes such as circular or rectangular ring, split ring resonator (SRR), Z shape, and fractal shapes have been employed for designing chipless RFID tags [217]. The REP-based design approach shows the freedom in designing chipless RFID tags and sensors using any resonant structures without adhering to common shapes of antennas.

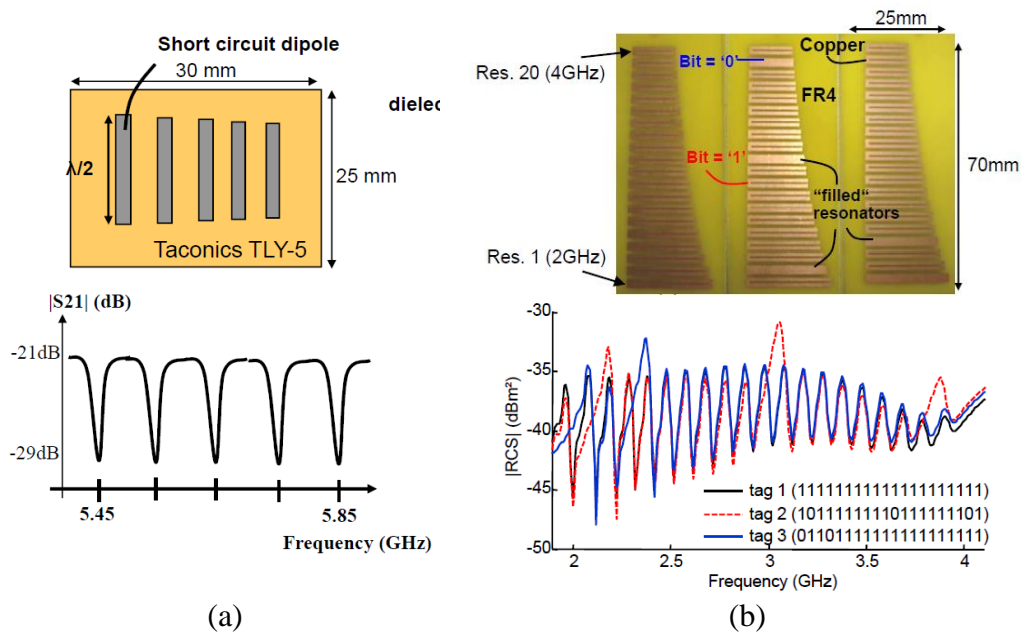


Figure 3.7 Chipless RFID tags based on REP: (a) Dipole resonators. (b) C-shaped resonators [217].

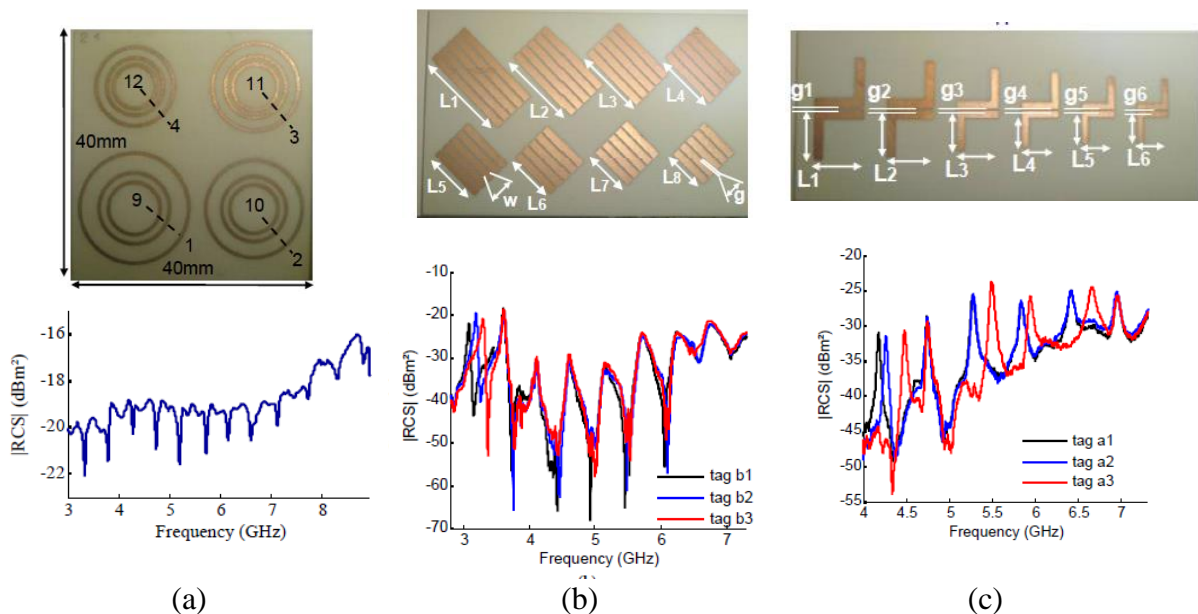


Figure 3.8 Metal-mountable chipless RFID tags based on REP: (a) Circular ring resonators. (b) Dipole resonators. (c) L-shaped resonators [217].

For metal-mountable chipless RFID tags, circular rings, dipoles, and L-shaped resonators can resonate above a ground plane, as shown in Figure 3.8. The nested circular ring tag, shown in Figure 3.8(a), has the advantage of being polarization-independent, meaning that the tag can be detected regardless of the tag's orientation. The diagonal dipole tag and the double L-shaped tag, shown in Figure 3.8(a) and (b), are depolarizing tags. A depolarizing tag is a wave depolarizer that reflects part of its EM signature in the cross-polarization compared to the interrogating signal. If the transmitter antenna is in vertical polarization, the receiver antenna is set in horizontal polarization. By this means, the received signal is isolated from the reflections of nearby objects that are usually in the same polarization as the interrogation signal. By exploiting polarization diversity, depolarizing tags are advantageous in terms of robustness for detection in a realistic environment.

3.2.2 Chipless RFID Reader Mechanism

A chipless RFID reader operates based on the radar principle, which transmits an interrogation signal towards the chipless RFID sensor and to collect the backscattered signal. In the reader's point of view, a chipless RFID tag or sensor is a tiny radar target that has a quantity of radar cross section (RCS) or echo area. RCS of a target is often symbolized as σ and can be expressed as [238]:

$$\sigma = \lim_{R \rightarrow \infty} \left[4\pi R^2 \frac{W_s}{W_i} \right] = \lim_{R \rightarrow \infty} \left[4\pi R^2 \frac{|E_s|^2}{|E_i|^2} \right] = \lim_{R \rightarrow \infty} \left[4\pi R^2 \frac{|H_s|^2}{|H_i|^2} \right] \quad (3.1)$$

where R is reading distance from the target, W_i is incident power density, W_s is scattered power density, E_i and E_s are incident and scattered electric field, H_i and H_s are incident and scattered magnetic field. The expression (3.1) shows that a chipless RFID tag or sensor has RCS, which is proportional to the ratio between the scattered and the incident of either power density, electric field, or magnetic field. Generally, the RCS of a target is a function of the geometrical shape and electrical properties of the target, frequency of operation, the polarization of incident wave, and the angles of incidence and observation [238].

A chipless RFID system can be arranged based on the configuration of a transmitter, a radar target, and a receiver, as shown in Figure 3.9. According to the radar range equation, the ratio of the received and the transmitted power from a target with the RCS of σ can be expressed as [238]:

$$\frac{P_r}{P_t} = \sigma \frac{G_t G_r}{4\pi} \left(\frac{\lambda}{4\pi R_1 R_2} \right)^2 \quad (3.2)$$

where P_r is the received power, P_t is the transmitted power, G_t is the gain of the transmitting antenna, G_r is the gain of the receiving antenna, λ is the wavelength, R_1 is the distance between the transmitting antenna to the target, and R_2 is the distance between the target and the receiving antenna.

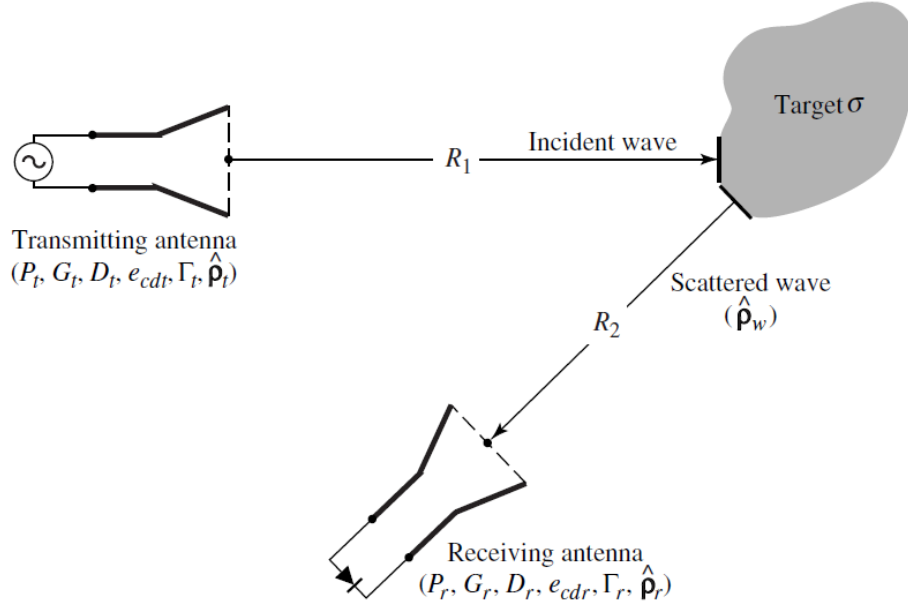


Figure 3.9 Arrangement of transmitter, target, and receiver for the radar range equation. In a chipless RFID system, the target is a chipless RFID tag or sensor [238].

The expression (3.2) is a simplified version of the radar range equation for polarization-matched antennas and maximum directional radiation and reception. Other factors are affecting the received power, such as radiation efficiencies, reflection losses, polarization losses, and directions of the transmitting and receiving antennas. If these factors are included, thus (3.2) can be written as

$$\frac{P_r}{P_t} = e_{cdt}e_{cdr}(1 - |\Gamma_t|^2)(1 - |\Gamma_r|^2)\sigma \frac{D_t(\theta_t, \phi_t)D_r(\theta_r, \phi_r)}{4\pi} \left(\frac{\lambda}{4\pi R_1 R_2}\right)^2 |\hat{\rho}_w \cdot \hat{\rho}_r|^2 \quad (3.3)$$

where e_{cdt} is the radiation efficiency of the transmitting antenna, e_{cdr} is the radiation efficiency of the receiving antenna, Γ_t is the reflection loss of the transmitting antenna, Γ_r is the reflection loss of the receiving antenna, $D_t(\theta_t, \phi_t)$ is the directivity of the transmitting antenna in the direction θ_t, ϕ_t , $D_r(\theta_r, \phi_r)$ is the directivity of the receiving antenna in the direction θ_r, ϕ_r , $\hat{\rho}_w$ is the polarization unit vector of the scattered waves, and $\hat{\rho}_r$ is the polarization unit vector of the receiving antenna.

The radar range equation, both (3.2) and (3.3), illustrates the relationship between the transmitted power (P_t) and the power delivered to the receiver (P_r) after being scattered by a radar target, i.e. a chipless RFID sensor. It represents the reading mechanism of a chipless RFID sensor through its RCS, which is governed by the geometrical shape and the electrical properties of the sensor. The received signal at the reader is directly linked to the RCS of the chipless RFID sensor under the circumstances of the wireless channel and the characteristics of the reader antennas. The (3.2) also allows us to calculate the theoretical maximum read range. Assuming the distances of the transmitting and the receiving antennas from the chipless RFID sensor are the same, the (3.2) can be rewritten as

$$\frac{P_r}{P_t} = \sigma \frac{G_t G_r \lambda^2}{(4\pi)^3 R^4}. \quad (3.4)$$

Since the chipless RFID reading mechanism is two-way traffic, the field power is reduced by $1/R^4$ [204]. Depending on the receiver sensitivity or minimum detectable power at the receiver (P_{\min}), the theoretical read range is given by [217]:

$$R_{\max} = \sqrt[4]{\frac{P_t G_t G_r \lambda^2 \sigma}{(4\pi)^3 P_{\min}}}. \quad (3.5)$$

Practically, a chipless RFID reader can be implemented using a VNA or a portable radar transceiver operated in a broadband frequency range. In laboratory conditions, a bistatic chipless RFID reader system can be implemented by connecting a VNA to the transmitting antenna in its Port 1 and the receiving antenna in its Port 2, as shown in Figure 3.10 (a). Not only the standard gain horn antennas but also other broadband antennas can be used for measurement. The measured scattering parameter S_{21} or the transmission coefficient represents the ratio of waves at Port 1 and Port 2. The magnitude of S_{21} is related to the power budget in the radar range equation as [202]:

$$|S_{21}| = \sqrt{\frac{P_r}{P_t}}. \quad (3.6)$$

It is also possible to apply a portable radar transceiver for a chipless RFID reader, although the dynamic range, power level, and data resolution may be lower than VNA. Figure 3.10 (b) shows a radar module operated in time-domain pulses within 0.9 to 6.5 GHz and is UWB compliant. A similar model has been demonstrated for a chipless RFID reader in [247].

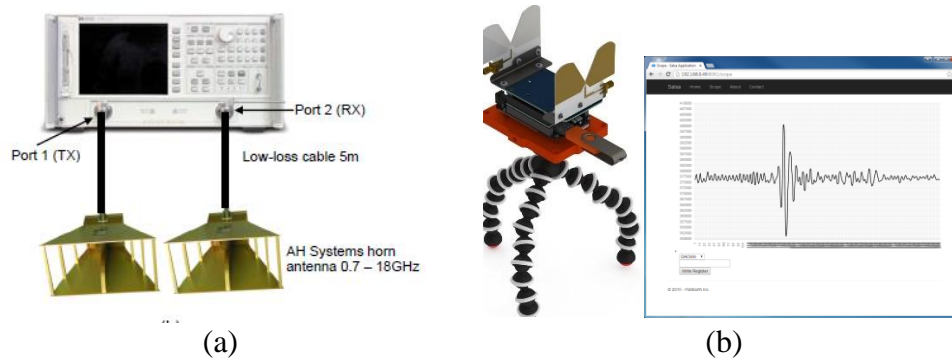


Figure 3.10 Two optional devices to implement a chipless RFID reader: (a) A VNA connected to antennas with bistatic configuration [217]. (b) A commercially available portable radar module [248], a similar radar module was used for a chipless RFID reader in [247].

3.2.3 Signal Pre-processing, Feature Extraction, Selection, and Fusion

The signal processing subsystem is an essential part of the chipless RFID sensor system for defect detection. It is responsible for processing and analyzing the backscattered signal data acquired by the reader to detect and characterize defects automatically. Typically, the signal processing subsystem for NDT&E and SHM consists of the pre-processing stage and feature extraction, selection, and fusion stage.

3.2.3.1 Pre-processing

In a chipless RFID sensor system, pre-processing may involve calibration, filtering, and signal transformation. First, measuring the electromagnetic signature of a chipless RFID sensor may require a rigorous calibration. In the measurement of a chipless RFID sensor, calibration is used to remove the effects of the environment, surrounding objects, and coupling between the reader antennas. Removal of these effects can be done by performing subtraction between the measurements with and without the sensor. The subtraction will isolate the response of the sensor from the other unwanted responses. Calibration can also determine the RCS of the chipless RFID sensor by using background subtraction and a reference RCS [202], [217], [249]. Second, filtering may be required since signals from measurements are often disturbed by noise. Noise is generated by the measurement tools, antennas, and the electronic components inside the measurement equipment. It can be minimized by performing signal filtering methods such as moving average filter or wavelet-based denoising [250]. Third, a signal transformation may be required if the backscattered signal is in the time domain. This is not the case for the measurement using a VNA but is essential for the chipless RFID reader that transmits and receives signals in the time domain. Since the electromagnetic signature of a chipless RFID sensor is in the frequency domain, the signal must be transformed from time to frequency. Fourier Transform is a standard method to convert signals between the time domain and the frequency domain. The overall goal of the pre-processing stage is to obtain the frequency

domain signature of the chipless RFID sensor with the minimized noise to perform feature extraction, selection, and fusion.

3.2.3.2 Feature Extraction, Selection, and Fusion

Feature extraction, selection, and fusion are broad subjects in signal/data processing, pattern recognition, and sensor systems, including SHM. Since the sensing mechanism in a chipless RFID sensor system is based on the analysis of data collected by the reader; therefore, feature extraction, selection, and fusion are essential. Feature extraction is a transformation process of raw sensing data/signals into more informative features relevant to the sensing variables. In SHM, feature extraction refers to the process of transforming the measured data into alternative forms where the correlation with defects can be observed [251]. The properties of data from the signals should be concerned in selecting an appropriate feature extraction method. The typical electromagnetic signature of a chipless RFID sensor is a broadband spectrum in the frequency domain with multiple resonances. For a chipless RFID tag, the presence or absence of the resonances is used to decode the tag ID. For defect detection, feature extraction is needed to obtain the features from the multi-resonance spectra that can indicate the defect.

Since RFID sensors are built upon resonant structures, such as antennas, the sensing feature is usually associated with the resonance frequency shift. This is in accordance with the review in Chapter 2 that most RFID sensors and antenna sensors are based on the resonance frequency shift. The resonance frequency can be extracted by the detection of peaks/dips, i.e., maxima/minima, in the spectra. Another suitable feature extraction method for chipless RFID is based on the statistical feature extraction using PCA. As reviewed in Chapter 2, PCA has been employed for RFID tag-antenna based sensors when robustness against wireless channel or environment is required. Furthermore, PCA can be used as an exploratory tool to evaluate multiple parameters from multivariate data. Since the broadband signature data of a chipless RFID sensor is high-dimensional, PCA is a viable method to reduce the data dimension and to extract the significant contributing parameters in the signals [252], [253].

Feature selection is the process of selecting features that are most relevant to the sensing variables. In SHM, when there are several features extracted from signals or a dataset, one should select features that are sensitive to defects in the structure. The selected features should be insensitive to operational and environmental variability. A common method for feature selection in SHM is based on correlating the available features with dedicated defect samples or engineered flaws similar to ones expected in actual conditions [251]. If multiple types or multiple parameters of defects are available, multiple features may need to be extracted and selected from the signal to identify different defect parameters. There are methods for feature

selection [254], [255], but not to be discussed here since the feature selection in this thesis is mostly by intuitively correlating the features with the dedicated defect samples.

Feature fusion is a process of combining multiple features to enhance sensor performance in comparison to using individual features. Feature fusion is a subset of data fusion, in which the fusion is performed at the feature level. In general, data fusion may integrate data from multiple sensors, multiple features, or many decisions [256]. The aggregation of information obtained from multiple sources is useful for making a reliable and robust decision. Data fusion on different levels has been gaining attention for defect evaluation by different SHM methods to improve assessment accuracy and reliability [257]. In a chipless RFID sensor system, generating multiple features is possible through the broadband and multi-resonance nature of the sensor's signature. With multiple resonance frequency features, feature fusion using simple sum and confidence weighted averaging (CWA) can be used to address the challenge of sensitivity and reliability.

3.3 Chapter Summary

This chapter has described the research methodology and the background of the proposed chipless RFID sensor system for defect detection and characterization. The research in this thesis involves the design and simulation study of novel chipless RFID sensors, experimental study using a configured chipless RFID reader and dedicated samples, and signal processing, feature extraction, selection, and fusion for quantitative evaluation of defects. The theoretical background regarding the proposed system operating principle and system elements have been thoroughly discussed. The research is branched out into three studies to investigate chipless RFID sensor systems dealing with different types of defects, sensor design approaches, reader configurations, and signal processing and feature extraction methods. In the study presented in Chapter 4, a chipless RFID sensor system for crack detection and characterization will be demonstrated with a sensor that integrates ID encoding and sensing based on CMPA. In Chapter 5, corrosion characterization will be investigated using an FSS-based chipless RFID sensor and feature fusion for enhanced sensitivity and reliability. Then, a chipless RFID sensor system that demonstrates a robust characterization of defects is presented in Chapter 6 using a multi-resonance chipless RFID sensor, a portable reader, and PCA.

Chapter 4 Chipless RFID Sensor for Crack Detection and Characterization Based on Circular Microstrip Patch Antenna (CMPA)

In the previous chapter, the working principle and theoretical background of chipless RFID sensor systems for defect detection and characterization were discussed. It was highlighted that microstrip patch antennas could be used to design metal-mountable chipless RFID tags. This chapter presents a novel chipless RFID sensor for crack detection and characterization based on the circular microstrip patch antenna (CMPA). Chapter 2 has reviewed that antennas, especially microstrip patch antennas, can be used as sensors for detecting various measurands, including dielectric constant, temperature, strain, and surface-breaking cracks [175]. The circular-shaped patch is attractive among microstrip patch antenna designs because a study has revealed its good performance for multi-directional strain detection [258]. In [258], the CMPA sensor has shown the capability of detecting the magnitude of strain while also distinguishing 0° and 90° strain orientations by using its resonance frequency shift. The multi-parameter strain sensing capability becomes the motivation for using CMPA as an element for a chipless RFID sensor.

The research in this chapter is an initial study that investigates the feasibility of a chipless RFID sensor system for defect detection using the antenna principle. Therefore, the crack detection approach using CMPA is outlined in Section 4.1. The geometry of the proposed chipless RFID sensor is then described in Section 4.2, followed by simulation studies of CMPA for crack characterization in Section 4.3. By performing parametric studies in the simulation, the relationships between the resonance frequency of CMPA and the changes of crack parameters are observed. In Section 4.4, the simulation results are validated by experimental studies using man-made and natural fatigue crack samples in the anechoic chamber. The sensor's readability, the characterization results for different samples, and measurement in the multipath environment are discussed. Comparisons with chipped RFID sensors are provided in the discussion in Section 4.5. Lastly, the conclusion of the study in this chapter is summarized in Section 4.6.

4.1 Chipless RFID Sensor System and Crack Detection Approach Using CMPA

The operating principle of a chipless RFID sensor system for crack detection and characterization is illustrated in Figure 4.1(a). It works similarly to the operating principle explained in Chapter 3. The reader transmits a broadband signal and then acquires the backscattered signal from the sensor mounted on a metallic structure. The collected

backscattered signal data is calibrated with the response from the environment to derive the RCS of the sensor. Then, the resonance frequency is extracted to obtain the sensor ID and to characterize the crack parameters, e.g., crack width and crack orientation.

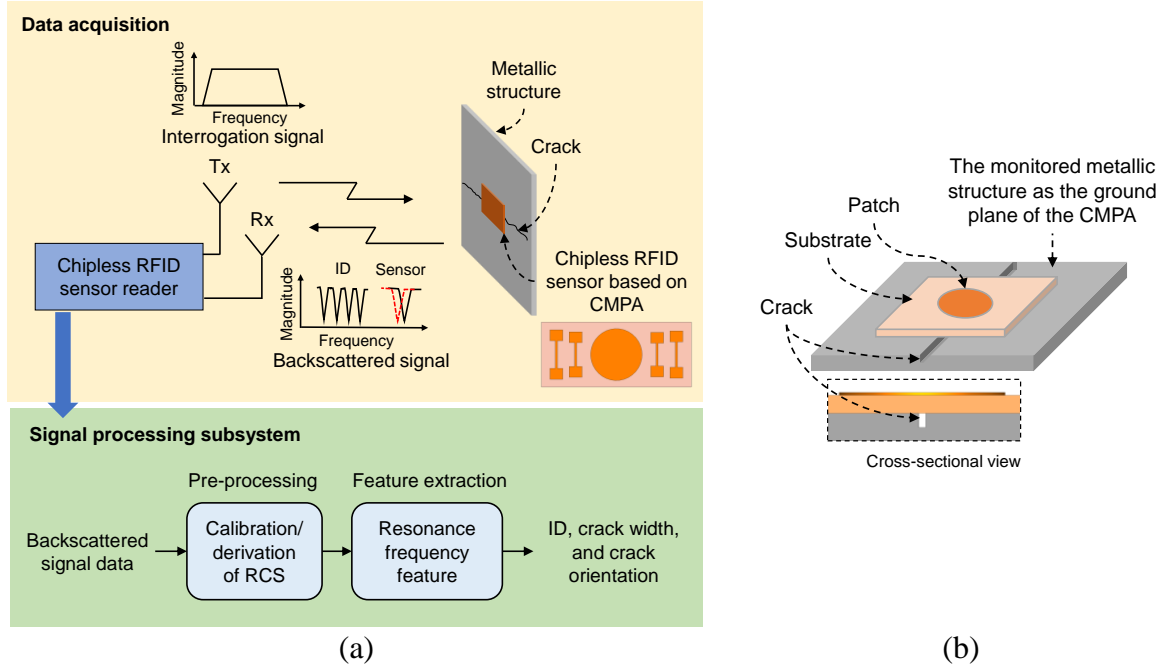


Figure 4.1 (a) Illustration diagram of a chipless RFID sensor system for crack detection and characterization using CMPA. (b) The structural configuration of CMPA when applied for crack sensing on a metallic structure.

The chipless RFID sensor in this study is designed to generate several resonances for ID encoding and crack sensing. More specifically, the sensor contains patches, one of which is a CMPA that is assigned for crack sensing. The structural configuration of CMPA, when applied as a crack sensor, is shown in Figure 4.1(b). In theory, the supported modes and the resonance frequency of a CMPA are defined by treating the patch, substrate, and the ground plane as a circular cavity [238]. It is noteworthy that the fundamental resonance frequency of a CMPA is not different when using a wired or transmission line excitation and using an external wireless excitation [229]. The fundamental resonance of a circular microstrip patch antenna with the radius of a , substrate thickness of h , and relative permittivity of ϵ_r in its dominant mode (TM_{110}) is given by [238]:

$$f_r = \frac{1.8412c}{2\pi a_e \sqrt{\epsilon_r}} \quad (4.1)$$

where c is the speed of light in free space, and a_e is the effective radius of the antenna, which can be calculated using the following equation:

$$a_e = a \left\{ 1 + \frac{2h}{\pi a \epsilon_r} \left[\ln \left(\frac{\pi a}{2h} \right) \right] + 1.7726 \right\}^{\frac{1}{2}}. \quad (4.2)$$

When a CMPA is applied as a crack sensor on metal, the surface of the monitored metallic structure is treated as the ground plane. Consequently, the electrical properties and physical condition of the metal, such as the presence of discontinuity due to crack, will affect the characteristics of the CMPA. A crack on the ground plane will not alter the actual radius of the circular patch if the crack does not break the patch. However, since the crack creates an air gap in the ground plane, it will modify the formed circular cavity of CMPA and thus its effective antenna radius. As in (4.2), the effective antenna radius must consider the substrate thickness and permittivity, which change partially due to the presence of a crack. Since the resonance frequency of CMPA is dependent on the antenna effective radius, it can be expected that the presence of a crack will shift the resonance of the CMPA.

4.2 Design of the Chipless RFID Sensor based on CMPA

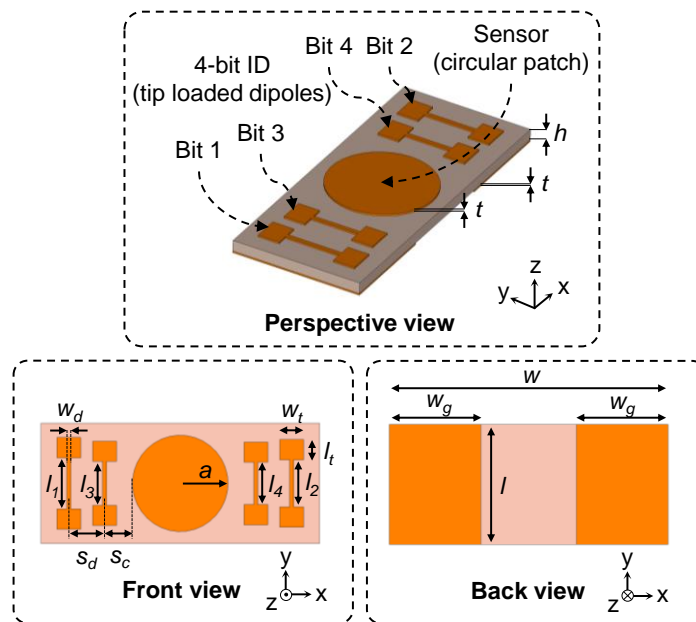


Figure 4.2 Geometry of the proposed chipless RFID sensor consisting of tip loaded dipoles for ID encoding and CMPA for crack sensing. The sensor has a partial ground plane on the backside to protect the ID signature from changes due to a crack.

Table 4.1 Dimensions of the proposed chipless RFID sensor (in mm).

a	h	l	l_1	l_2	l_3	l_4	l_t	s_c	s_d	t	w	w_d	w_g	w_t
6	1.27	15	6.4	5.9	5.5	5.3	2.5	3.5	4.5	0.035	35	0.5	11.5	3

The geometry and dimension of the proposed chipless RFID sensor are presented in Figure 4.2 and Table 4.1, respectively. The sensor was designed on Taconic CER-10-0500 laminate with a dielectric constant of 10, a loss tangent of 0.0035, and a thickness of 1.27 mm. A substrate with a high dielectric constant was chosen to minimize the sensor's size and maximize the quality factor. The chipless RFID sensor has an overall size of 35 mm \times 15 mm and consists of

two parts: sensor and ID encoder. The sensor part uses CMPA as described in Section 4.1, while the ID encoder is four tip-loaded dipoles positioned on the sides of the CMPA. These four tip-loaded dipoles are to generate a binary ID of “1111”. On the backside of the sensor, a partial ground plane is created only at the back of the tip-loaded dipoles. The partial ground plane is to protect the ID signature not to be affected by a crack on the metallic structure. Meanwhile, the backside of the circular patch is made without a ground plane to sense a crack on the metallic structure.

For ID encoding, dipole shaped patch was chosen because of its simple geometry and its ability to resonate on a ground plane. A dipole on a ground plane operates as a half-wavelength resonator, and thus the resonance frequency can be tuned by varying its length. In the proposed sensor design, both tips of each dipole patch are enlarged, forming a dumbbell shape. This capacitive tip loading technique shortens the physical dipole length and reduces the mutual coupling among the dipoles [259]. The benefit of this shape is the dipole patches can be placed close together and thus minimizing the sensor size. Nonetheless, dipole patches that have slightly different lengths should not be placed near to each other as they generate adjacent resonances. Two dipole patches with lengths of $l_1 = 6.4$ mm and $l_3 = 5.5$ mm were positioned on the left side, while the other two with lengths of $l_2 = 5.9$ mm and $l_4 = 5.3$ mm were placed on the other side of the CMPA.

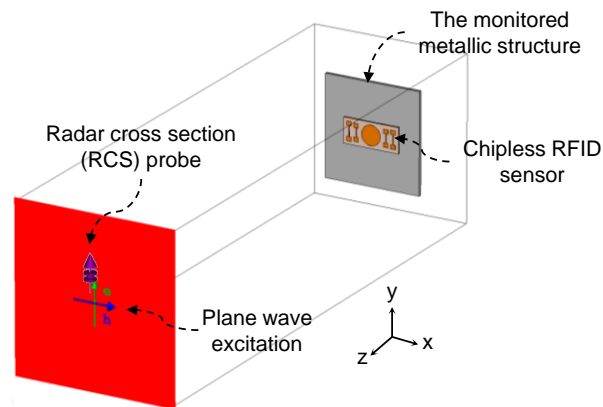


Figure 4.3 Simulation setup of the chipless RFID sensor in CST Microwave Studio.

The chipless RFID sensor was simulated in CST Microwave Studio, as exhibited in Figure 4.3. The sensor was modeled on a metallic plate, i.e., aluminum, with a dimension of 60 mm \times 60 mm \times 2 mm and electrical conductivity of 3.56×10^7 S/m. A plane wave excitation and an RCS probe were positioned 30 cm away from the sensor. The purpose of the plane wave excitation is to transmit linearly polarized signals with its E -plane parallel to the y -axis. It propagates along the $-z$ -axis or towards the chipless RFID sensor. The simulation was performed for a frequency range from 2 to 6 GHz. As a result, the simulated RCS spectrum of the chipless RFID sensor is

shown in Figure 4.4. When a plane wave excites the chipless RFID sensor, RCS shows a frequency selective behavior of the sensor represented by notches at several frequencies. The notches appear because the conductive patterns on the sensor resonate with the signal leading to EM energy absorptions at the resonant frequencies. The sensor generates two sets of resonance within the frequency range. One set of resonance is the ID encoding signature consisting of four notches at 3.29, 3.41, 3.52, and 3.59 GHz, while another set of resonance is the sensor signature generated by the CMPA at 4.93 GHz. The ID of this sensor structure is “1111” associated with the presence of four resonance notches. Modification of the tag ID can be done either through eliminating the corresponding dipole/s structure or equalizing the length to the dipole/s that have an ID bit of “1”. For instance, a tag ID of “1011” can be acquired by eliminating the dipole bit 2, making the second resonance notch absent in the ID encoding signature.

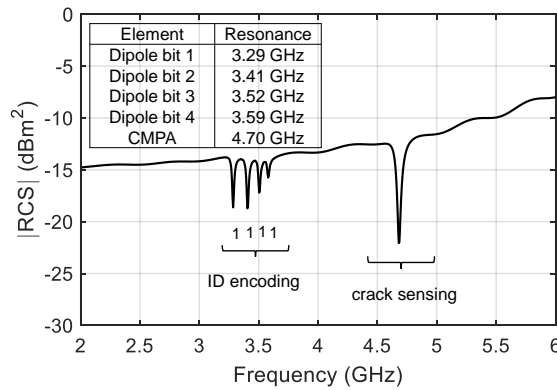


Figure 4.4 Simulated RCS spectrum of the chipless RFID sensor showing two sets of resonance frequency for ID encoding and crack sensing.

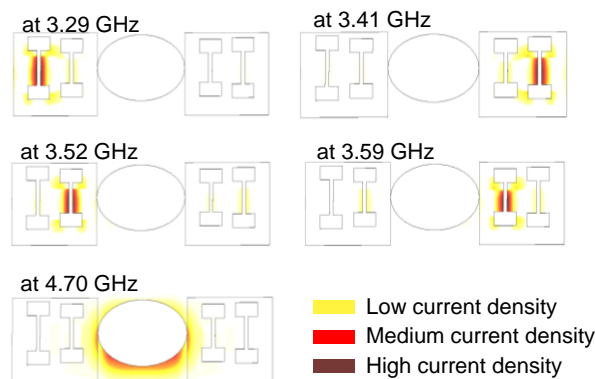


Figure 4.5 Simulated surface current distributions of the chipless RFID sensor showing the concentration of current at each resonance on the backing metal slab.

In order to associate the resulting resonances with the physical structure of the sensor, surface current distributions at the resonant frequencies were collected from simulation and illustrated in Figure 4.5. Each resonating structure manifests a concentrated surface current at a certain

resonance frequency. It can be verified that the resonances are contributions from individual dipole and CMPA structure. It is noticeable that the currents are distributed on the backing metal slab underneath the dipole and CMPA. Hereinafter, particularly for the CMPA, any change in the RCS spectrum due to a crack on the metallic structure can be analyzed using surface current distribution.

4.3 Simulation Studies of CMPA for Crack Characterization

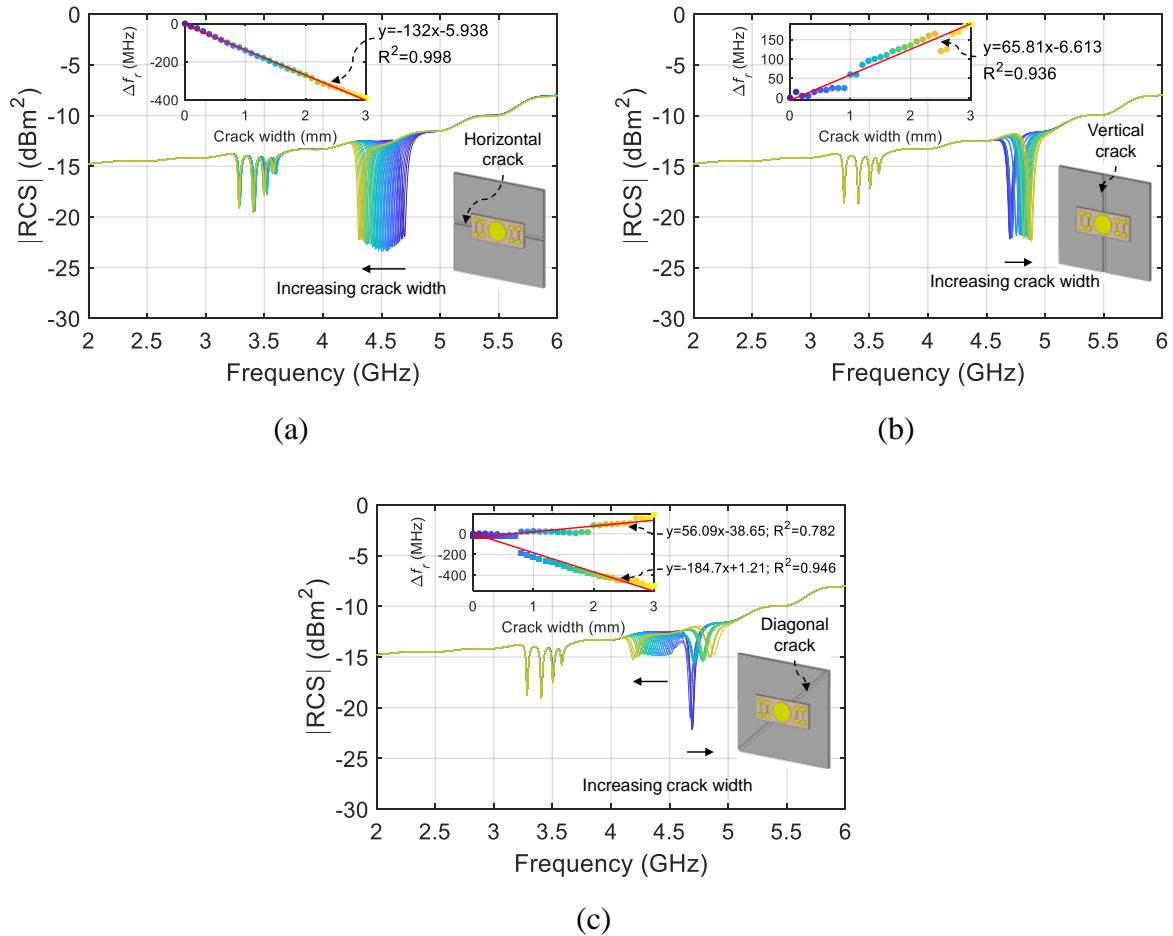


Figure 4.6 Simulated RCS spectra of the chipless RFID sensor showing the resonance frequency shift for different crack orientations and widths. (a) Horizontal crack. (b) Vertical crack. (c) Diagonal crack. The insets show the amount of resonance frequency shifts and linear fitting lines.

In order to examine the effects of cracks on the RCS of the sensor, simulation studies were performed for different crack orientations and crack widths. In the simulation, the sensor was placed at the center of a metallic surface. The crack creates a cavity in the metallic structure passing through the backside of the CMPA. Different widths of crack with 0° (horizontal), 90° (vertical), and 45° (diagonal) orientations were investigated. For different crack orientations, parametric sweeps were performed with the crack width varied from 0 to 3 mm in a 0.1-mm

step. The crack depth was fixed at 1 mm. The resonance frequency of CMPA can be expected to change with the orientation and width of the crack.

The simulated RCS spectra of the chipless RFID sensor for different crack orientations and widths are given in Figure 4.6. It is evident that the crack shifts the resonance frequency of the CMPA without affecting the ID signature. The resonance of CMPA is shifted to different directions and amounts depending on the crack orientation and the crack width. The normalized amount of resonance shift Δf_r can be written as

$$\Delta f_r = f_r^{\text{crack}} - f_r^{\text{initial}} \quad (4.3)$$

where f_r^{crack} is the resonance frequency of CMPA after the presence of crack and f_r^{initial} is the initial resonance frequency of CMPA without crack. The numerical sign of Δf_r denotes the direction of the resonance shift. It is negative for the shifts towards a lower frequency and positive for the shifts towards a higher frequency. Figure 4.6 (a) shows that a horizontal crack shifts the resonance to lower frequencies linearly as the crack width increases. The detection sensitivity is roughly -134.3 MHz/mm or -13.43 MHz shift per 0.1 mm increase of the crack width. Oppositely, a vertical crack tends to shift the resonance to higher frequencies, as shown in Figure 4.6(b). In general, the trend of resonance shift for the vertical crack is linear, with the detection sensitivity of averagely +66.7 MHz/mm. Different from the horizontal and vertical cracks, a diagonal crack, to some extent, splits the resonance of CMPA into two resonances. The two resonances after splitting have more shallow resonance notches. As the crack width increases, one resonance shifts to lower frequencies, while another resonance shifts to higher frequencies. When the crack width is lower than 0.5 mm, however, the presence of a diagonal crack is hard to detect because the resonance frequency shift is insignificant. When the crack width is above 0.6 mm, the resonance shift is detectable, especially the one that shifts towards lower frequencies. Both resonances shift simultaneously as the crack width increases, one to lower frequencies and another to higher frequencies. Hence, a diagonal crack can be detected and characterized by using these two resonances.

In order to observe how different types of cracks shift the resonance of CMPA to different directions, the surface current distributions for different crack orientations are evaluated, as shown in Figure 4.7. As seen in Figure 4.7(a), most current paths flowing on the healthy metallic structure are in a parallel direction to the E -plane. While the outer side current paths are curved in accordance with the shape of CMPA, which is circular. When a horizontal crack presents in the metallic structure, as shown in Figure 4.7(b), the current is forced to flow across the crack cavity. Consequently, the horizontal crack lengthens the current paths and increases the electrical length of the CMPA. The wider or deeper the horizontal crack, the longer the

electrical length of CMPA. Since the resonance frequency of an antenna is inversely proportional to the effective aperture of the CMPA, a horizontal crack will shift the resonance towards a lower frequency. In Figure 4.7(c), a vertical crack displaces some current paths to the bottom surface of the crack. A portion of currents that flow on the crack bottom is disregarded in determining the CMPA effective radius. Thus, because of the current displacements, a vertical crack decreases the electrical length of the CMPA and subsequently shifts the resonance to a higher frequency. Interestingly, a diagonal crack combines both phenomena of horizontal and vertical cracks. When a sizeable diagonal crack presents, the CMPA resonates at two current propagation modes, as depicted in Figure 4.7(d). The first mode at the lower frequency occurs due to the current that flows diagonally across the crack; thus, the length of current paths increases as the crack width increases. It is the same as the phenomenon that happens with the horizontal crack. Another resonance mode at the higher frequency occurs due to the current that propagates in parallel to the crack. The direction of current paths in this mode is orthogonal to the mode at the lower frequency. The propagating currents are displaced to the crack bottom, and there is also a small amount of current flowing across the crack. Therefore, the trend of the resonance frequency shifts of the diagonal crack for different crack widths is less linear.

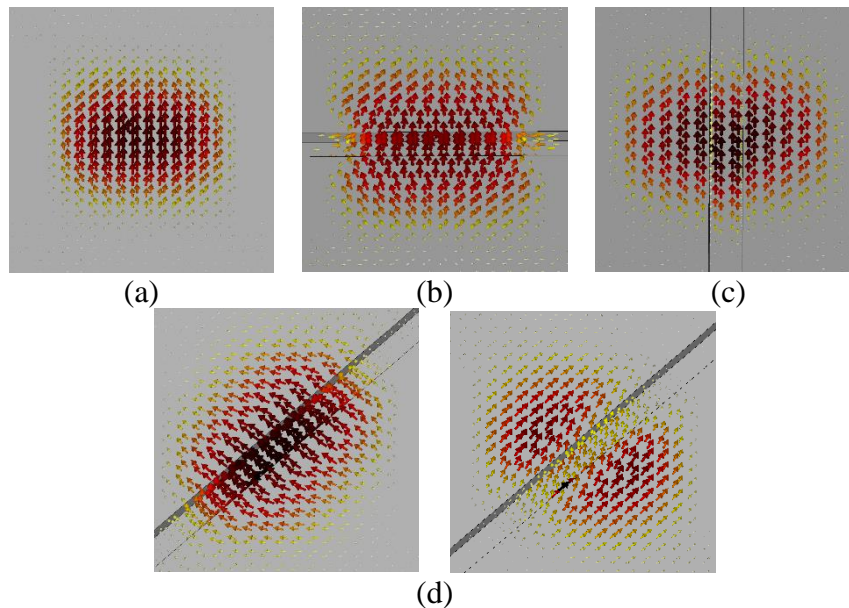


Figure 4.7 Simulated surface current distribution on the metallic structure under the CMPA, showing the current flows for different crack orientations. (a) Without crack: at 4.70 GHz. (b) With a 2-mm horizontal crack: at 4.43 GHz. (c) With a 2-mm vertical crack: at 4.84 GHz. (d) With a 2-mm diagonal crack: at 4.30 GHz (left) and 4.77 GHz (right).

4.3.1 Effects of Substrate's Thickness on RCS and Sensitivity

According to (4.2), the effective antenna radius, which determines the resonance frequency of CMPA, is a function of the substrate's thickness. It is interesting to study the effects of the substrate's thickness on the RCS spectrum and the sensitivity of CMPA to crack. Figure 4.8

shows a parametric sweep for different substrate thicknesses, i.e., 0.64 mm, 1.27 mm, and 2.54 mm. The substrate's thickness used in this work is 1.27 mm. When the substrate's thickness was doubled to 2.54 mm, the resonance frequency of CMPA shifted to a lower frequency, as shown in Figure 4.8(a). Unfortunately, as denoted in Figure 4.8(b), a thick substrate degrades the sensitivity to crack. The crack simulated in this parametric sweep is a horizontal crack with a fixed depth of 1 mm, and the width varied from 0 mm to 3 mm. With a thin substrate of 0.64 mm, the resonance of CMPA is located at a higher frequency. A thin substrate will increase the sensitivity to crack, as suggested in Figure 4.8(b). However, it tends to generate shallow resonance dips, making the sensor challenging to read. Therefore, the substrate's thickness of 1.27 mm was a thoughtful choice to balance between the sensitivity to crack and the readability of the resonances.

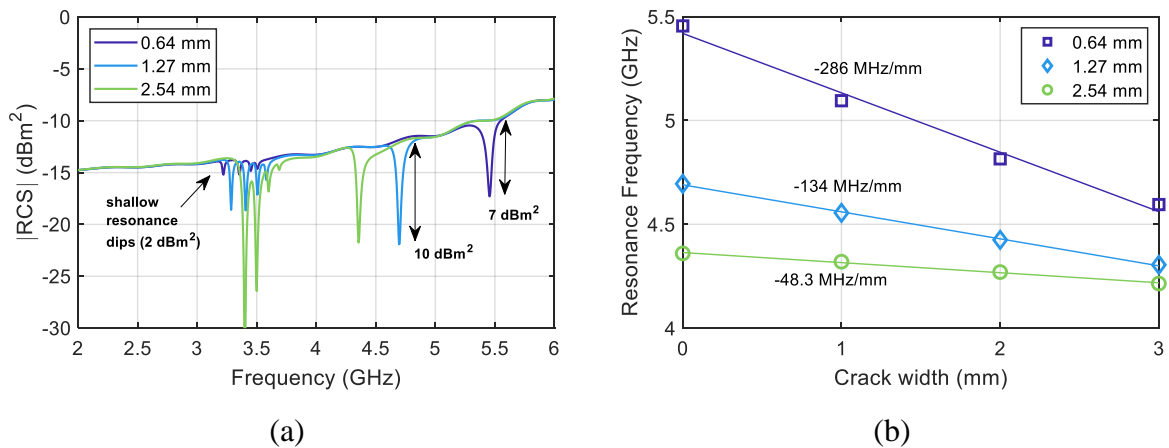


Figure 4.8 Effects of the substrate's thickness on: (a) RCS of the chipless RFID sensor, showing that the resonance of CMPA moves towards a higher frequency with a shallow resonance when the substrate thickness decreases. (b) The sensitivity of CMPA to crack, showing that the sensitivity increases when the substrate thickness decreases.

4.3.2 Effects of Substrate's Dielectric Constant on RCS and Sensitivity

Apart from the thickness, it is important to study the effects of the substrate's dielectric constant to the RCS of the sensor and the sensitivity of CMPA to crack. According to (4.1), the substrate's dielectric constant and the antenna radius are inversely proportional to the resonance frequency. That means, by using high dielectric constant substrates, the antenna radius can be smaller than using the low ones to achieve the same resonance frequency. Figure 4.9 depicts the results of a parametric sweep for different dielectric constants and antenna radius. Without altering the antenna radius, it is theoretically known that lowering the dielectric constant will shift the resonance frequency to a higher frequency and vice versa. In this simulation study, the antenna radius was adjusted so that the CMPA generated a similar resonance frequency. In Figure 4.9(a), it can be seen that a substrate with a low dielectric constant allows for a deep

resonance notch of the CMPA. The deep resonance is likely a result of the large antenna radius, which has more absorptive characteristics. A substrate with a high dielectric constant, as used in this work, generates a shallower resonance, but it allows for a small antenna radius. Figure 4.9(b) suggests that the dielectric constant has insignificant effects on the sensitivity of CMPA to crack. The resonance frequency was maintained to be the same by adjusting the antenna radius, but the sensitivity to crack remains similar for different values of dielectric constant.

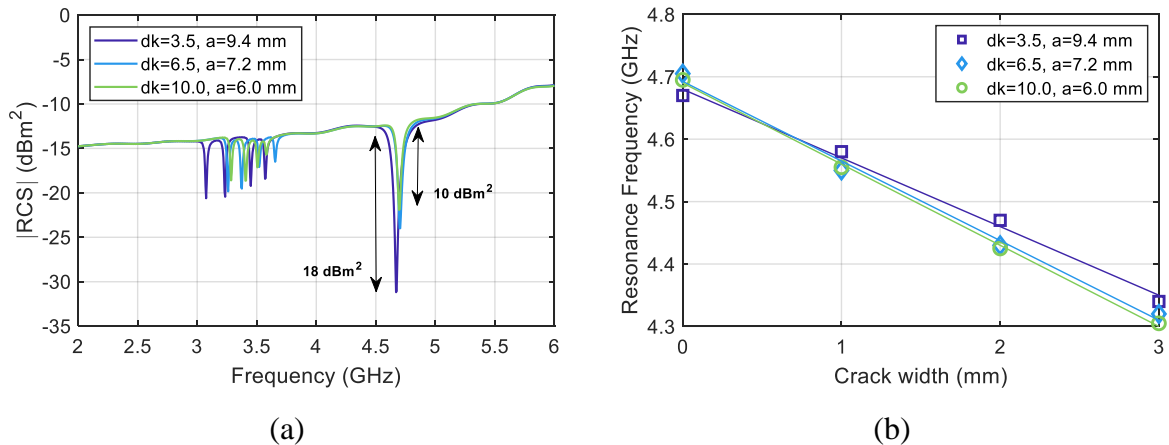


Figure 4.9 Effects of the substrate's dielectric constant on: (a) RCS of the chipless RFID sensor, showing that the substrate with a high dielectric constant generates a shallow resonance magnitude and vice versa. (b) The sensitivity of CMPA to crack, showing that the sensitivity to crack remains similar for different substrate's dielectric constants.

4.4 Experimental Studies and Results

The chipless RFID sensor was fabricated through the photochemical etching process, which is a common method of etching PCB. The process consists of lamination, exposure, developing, etching, and stripping. The material, i.e., Taconic CER-10-0500, is cleaned to remove all surface contamination and then laminated with a UV sensitive photoresist film. A photo tool containing the design layout exported from the CST microwave studio is placed on top of the laminated material. It is exposed to UV light, which passes through the clear areas of the photo tool and hardens the laminated film. Then, resist film on non-UV-exposed areas is chemically developed to reveal the desired layout image. The resist coated area is heated to improve acid resistance before etching. Next, in the etching machine, the material is sprayed with a high-pressure and temperature-regulated Ferric Chloride solution. The solution etches the unprotected parts of the material away to produce the desired layout.

The fabricated chipless RFID sensor was used to validate the simulation results with experimental studies. Nine man-made crack samples and a natural fatigue crack sample were prepared for the experiments, as shown in Figure 4.10. The man-made samples are artificial slots in aluminum plates with three different crack orientations, i.e., horizontal, vertical, and

diagonal, and three different crack widths, i.e., 1, 2, and 3 mm. The crack depth of all man-made crack samples is 1 mm. The natural fatigue crack sample is a submillimeter crack on a steel bar with a dimension of 170 mm × 50 mm × 20 mm. The fatigue crack is a tiny surface crack located at the center of the steel bar.

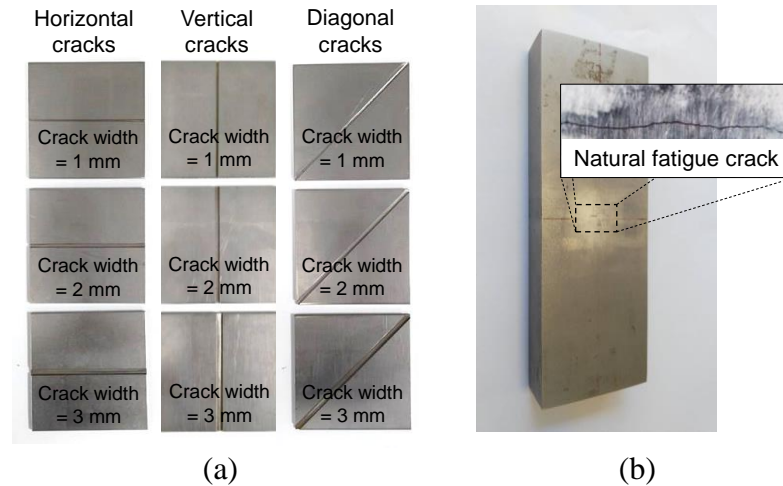


Figure 4.10 Crack samples. (a) Man-made crack samples. (b) Natural fatigue crack sample.

The experimental setup using bistatic radar configuration in an anechoic chamber is illustrated in Figure 4.11. A vector network analyzer (VNA) was connected to two identical standard gain horn antennas separated by 5 cm. The chipless RFID sensor was attached to a crack sample using a thin transparent tape. The sensor and the sample were put upright on the sample holder and positioned 30 cm away from the horn antennas. The power of the VNA was set as 0 dBm with the averaging activated for 100 measurements to enhance the signal to noise ratio.

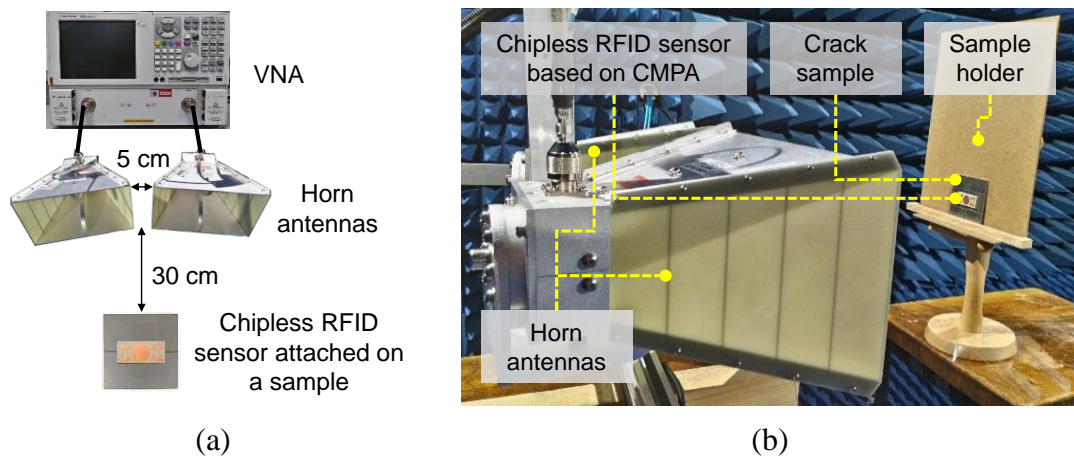


Figure 4.11 Experimental setup using the bistatic radar configuration. (a) Schematic diagram of the experimental setup. (b) Photograph of the experimental setup in the anechoic chamber.

In order to obtain the RCS response of the sensor and the sample, it is necessary to perform subtraction with the measurement background and then to scale the subtracted results with a reference RCS. This subtraction and scaling process can also be referred to as calibration. For this calibration purpose, three S_{21} measurements are needed to derive the RCS of the sensor

and the sample. The measured RCS of the sensor and the sample can be calculated as follows [217], [249]:

$$\text{RCS}_{\text{sensor+sample}} = \left(\frac{S_{21}^{\text{sensor+sample}} - S_{21}^{\text{background}}}{S_{21}^{\text{ref}} - S_{21}^{\text{background}}} \right)^2 \cdot \text{RCS}_{\text{ref}}. \quad (4.4)$$

In (4.4) above, the $S_{21}^{\text{sensor+sample}}$ is the measurement with the sensor and the sample included in the scene. The $S_{21}^{\text{background}}$ is the measurement of background with the sample holder included while both the sensor and the sample are excluded. The S_{21}^{ref} is the measurement of a reference object with a known RCS, i.e. RCS_{ref} . As an example, this study used a 50 mm × 50 mm × 2 mm aluminum plate as the reference object, which can be easily modeled in the simulation. Therefore, the RCS_{ref} can be obtained through a simulation in CST Microwave Studio.

It should be noted that all metallic materials have dominant contributions in forming RCS due to its reflective behavior in microwaves. When the size of the metal sample is large, the signal absorption due to the sensor can be too low in comparison to the reflection of the sample. This may lead to unreadable resonances of the sensor. That is to say, $\text{RCS}_{\text{sensor+sample}}$ in (4.4) is dependent on the size of the sample. Nevertheless, the RCS due to the reflection of the metal sample can be isolated, and thus leaving only the reflection characteristics of the chipless RFID sensor, i.e. $\text{RCS}_{\text{sensor}}$. Derivation of $\text{RCS}_{\text{sensor}}$ requires subtraction with the S_{21} measurement of the sample in addition to S_{21} of background. $\text{RCS}_{\text{sensor}}$ can be expressed as follows:

$$\text{RCS}_{\text{sensor}} = \left(\frac{S_{21}^{\text{sensor+sample}} - S_{21}^{\text{sample}}}{S_{21}^{\text{ref}} - S_{21}^{\text{background}}} \right)^2 \cdot \text{RCS}_{\text{ref}}. \quad (4.5)$$

Although $\text{RCS}_{\text{sensor}}$ disregards the reflection from the metal sample by subtraction, information of the presence of crack on the sample will be still conveyed by the $\text{RCS}_{\text{sensor}}$ because the crack anyhow affects the resonance of the CMPA. By using the formulae above, the following sections will discuss the readability of the chipless RFID sensor and experimental studies under different conditions and samples.

4.4.1 Readability of the Chipless RFID Sensor

RCS of the chipless RFID sensor, when placed on a 60 mm x 60 mm aluminum plate, was measured with a 30-cm reading distance. It can be seen from Figure 4.12 that the measured RCS of the sensor agrees very well with the simulated one. This means that the chipless RFID sensor is readable from a 30-cm reading distance. Next, the readability of the sensor was tested

for longer reading distances. RCS spectra of the sensor for reading distances of 30, 60, 90, and 120 cm are presented in Figure 4.13. Apparently, the sensor with all its resonances is readable over any distance up to 120 cm. Reading the sensor from even up to 120 cm is possible because the measurement is done in the anechoic chamber while the derivation of the RCS involves calibration, i.e., subtraction with the background. The RCS shows the ability of the sensor and sample to reflect waves, which is less dependent on reading distance. Here, the $S_{21}^{\text{background}}$ used for calibration is re-measured when changing the reading distance. The derived RCS is a parameter showing the ability of the sensor and sample in reflecting waves and therefore is less dependent on reading distance. It can be observed in Figure 4.13 that increasing the reading distance can lower the SNR as more ripples present at 120-cm reading distance, although insignificant. Such a calibration procedure in the derivation of RCS makes the readability limited by the gain of the horn antennas and the dynamic range of the VNA. When the reflection from the sensor is weak, thus the SNR will be lower, leading to difficulties in observing the resonance notches due to ripples.

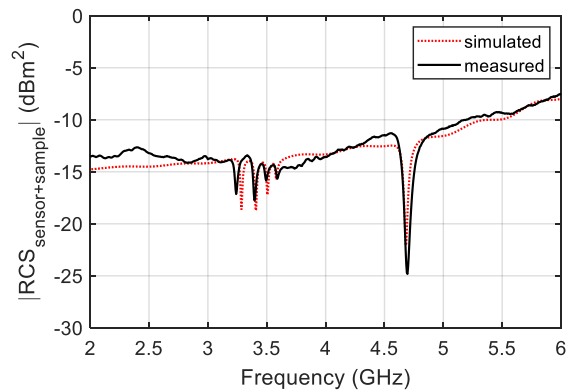


Figure 4.12 Comparison between the simulated and measured RCS spectra of the chipless RFID sensor.

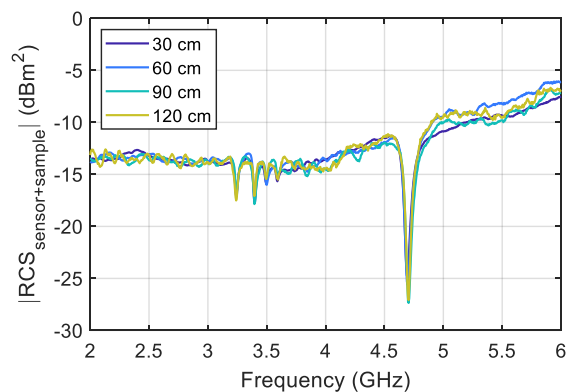


Figure 4.13 Measured RCS spectra with different reading distances.

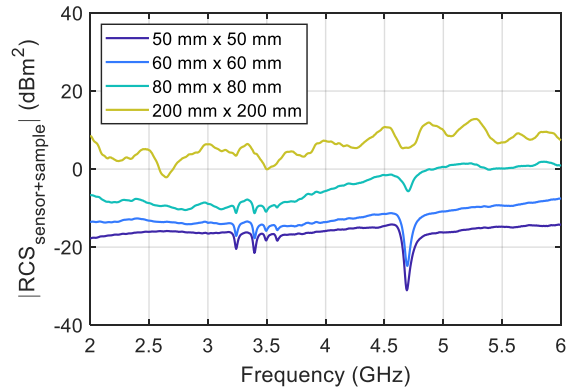


Figure 4.14 Measured RCS spectra of the chipless RFID sensor placed on different sizes of metal plate samples showing an unreadable sensor when the metal size is large.

Apart from the readability over different distances, it is also essential to observe the readability with different sizes of metal samples. In SHM applications, the size of the monitored metallic structure can be much larger than the samples used in this study. The measured RCS spectra of the chipless RFID sensor when placed on different sizes of metal plate samples are displayed in Figure 4.14. The measurements are taken from a 30-cm distance. Larger metal samples increase the overall RCS spectra because of the increasing amount of reflection over the entire frequency range. With the increasing reflection due to the metal size, the signature of the chipless RFID sensor becomes less visible. Resonances of the sensor are unseen when the size of the metal plate is 200 mm \times 200 mm. It is because a considerable amount of reflection from the large metal surfaces conceals the absorption notches generated by the sensor.

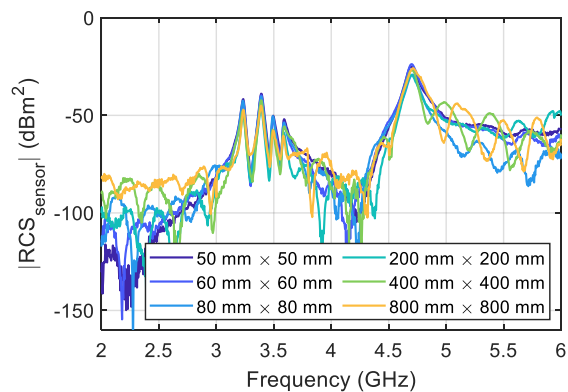


Figure 4.15 Measured RCS of the chipless RFID sensor placed on metal plate samples of different sizes. The RCS is calibrated with the response of each metal plate sample.

When the metal sample or the monitored metallic structure is large, the RCS measurement procedure should involve subtraction with the response of the sample following the (4.5). As stated earlier, the reflection of the metal sample can be calibrated by recording its S_{21} response

and to be subtracted from the S_{21} measuring both the sensor and the metal sample. The measured RCS_{tag} for different sizes of the sample are presented in Figure 4.15. By applying (4.5), the resonances of the sensor can be revealed for all sizes of metal samples. The resonances obtained using (4.5) are at the same frequencies as the resonances acquired using (4.4). The only difference is that the resonances are in the form of peaks instead of notches. This is because the RCS_{tag} represents the reflection behavior of the sensor instead of its absorption with respect to the reflection of the metal sample. It is worth noting that although the calibration procedure can remove the influence of sample size, it is harder to perform than the calibration with the background in (4.4). Subtraction with the response of the metal sample is sensitive to any movement of the metal sample and the reader antennas during the measurement. Large metal samples and metallic objects, e.g., the horn antennas, produces multipath, and thus the response near noise levels fluctuates during the measurement. This necessitates the RCS measurements using (4.5) to be done precisely by avoiding any significant changes in the setup.

4.4.2 Experimental Studies Using Man-made Crack and Natural Fatigue Crack Samples

Experimental studies using man-made and natural fatigue crack samples were undertaken to examine the chipless RFID sensor for crack detection and characterization. Particularly, experimental studies using the man-made crack samples are to validate the simulation results. With the reading distance of 30 cm, RCS for different crack orientations and widths were measured and exhibited in Figure 4.16. Results from the simulations are plotted in the same graphs with dotted lines for comparisons. It is obvious that the measured and simulated results show good agreement in trend for horizontal, vertical, and diagonal cracks. Therefore, it is validated that the orientation and the width of the crack can be differentiated by using the direction and the amount of resonance shift. The measured RCS for the samples with horizontal cracks in Figure 4.16(a) shows that the resonance of CMPA shifts to lower frequencies as the crack width increases. In Figure 4.16(b), vertical cracks shift the resonance of CMPA to higher frequencies, and the amount of shift grows with the increase of the crack width. Furthermore, the measured RCS for diagonal cracks provides a good validation for the simulated results, as shown in Figure 4.16(b). The resonance of CMPA splits into two resonances as the crack width increases.

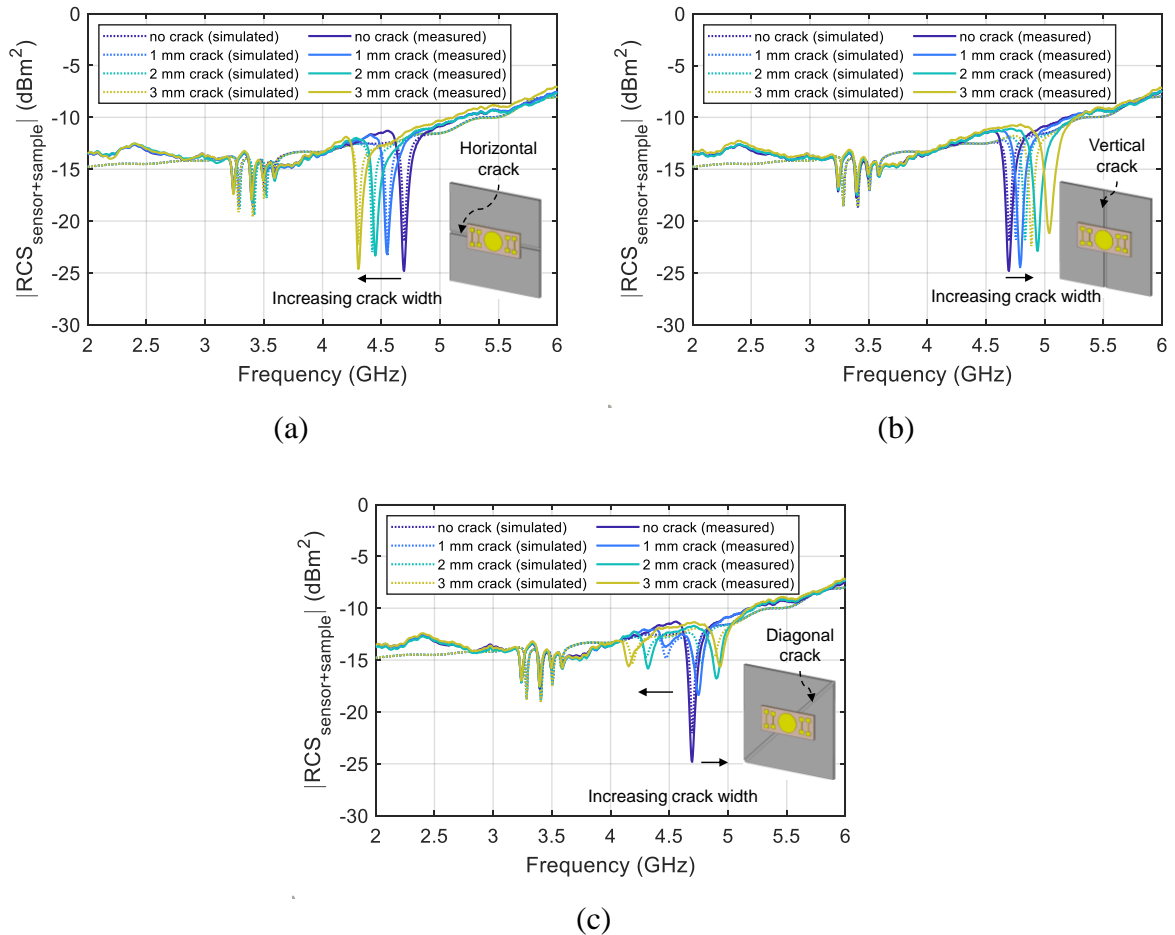


Figure 4.16 Measured RCS spectra of the chipless RFID sensor for different crack orientations and widths, showing good agreement between simulations and measurements. (a) Horizontal crack. (b) Vertical crack. (c) Diagonal crack.

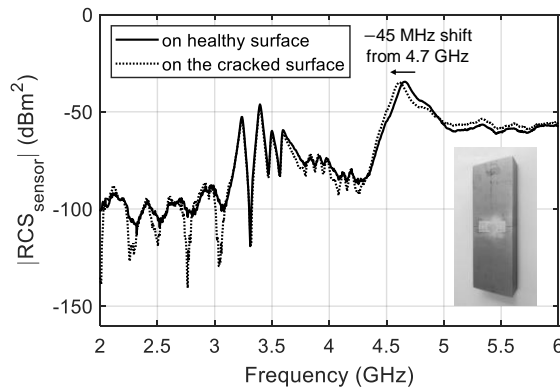


Figure 4.17 Measured RCS spectra of the chipless RFID sensor when placed on a natural fatigue crack sample showing detection of a submillimeter crack using the resonance frequency shift.

In order to demonstrate the sensitivity and resolution of the chipless RFID sensor, an experiment using a natural fatigue crack sample was conducted. The steel bar, which has a natural crack as its center, is quite significant in comparison to the sensor; therefore, calibration

with the sample without the sensor as in (4.5) was applied to obtain the RCS. The natural fatigue crack sample was placed upright at the sample holder so that the orientation of the natural crack is horizontal. The RCS spectra of the sensor placed on a healthy non-cracked surface and on the cracked surface were measured and shown in Figure 4.17. The measurement on the healthy surface was done by attaching the sensor on the opposite side of the sample. Placing the sensor on the cracked region shifts the resonance -45 MHz from the resonance obtained on the healthy surface. With the detection sensitivity for horizontal cracks is -134.2 MHz/mm, -45 MHz shift is equivalent to ~0.3-mm horizontal crack. Hence, the high sensitivity allows the sensor to have a submillimeter resolution and thus capable of detecting a submillimeter fatigue crack.

4.4.3 Experimental Study in Multipath Environment

The experimental studies conducted in the anechoic chamber have shown good results validating the simulation. In the anechoic chamber, interferences and multipath effects are suppressed by RF absorbers and, therefore, impractical. A realistic environment, however, is a multipath environment where the system may not perform as well as in the anechoic chamber. An experimental study outside the anechoic chamber was conducted to test the chipless RFID sensor system in a multipath environment, as shown in Figure 4.18. The setup was modified to be more challenging by placing the samples on a large metallic surface (0.8 m × 0.8 m). Moreover, the environment was surrounded by metallic objects such as a large metallic cabinet, VNA, computers, chairs, etc. The horn antennas were placed 30 cm away from the sample. RCS spectra of the chipless RFID sensor on three horizontal crack samples with different widths were measured.

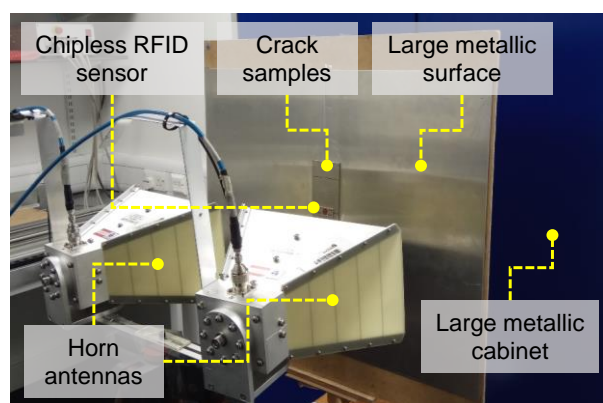


Figure 4.18 Experimental setup outside the anechoic chamber to represent a multipath environment.

The measurement results in the multipath environment are shown in Figure 4.19. The RCS was derived using (4.5) considering the sizeable metallic surface behind the sample, which obviously conceals the absorption by the sensor. The calibration by subtraction was challenging

because the noise floor was found changing when recording the S_{21} data. In the multipath environment, the measured RCS suffers from a high noise level within the entire measurement frequency band. As a result, the resonance peaks, especially the ones generated for ID encoding, are obscured by noise as the levels are almost comparable. The resonances for ID are slightly noticeable at the corresponding frequencies but are noisier compared to the measurements in the anechoic chamber. The resonance of CMPA, however, stands out and is easy to observe from the RCS. This is because the circular patch gives a prominent resonance compared to the dipole patches. Furthermore, the resonance shifts due to the crack width variation are noticeable, giving apparent differences from the sample without a crack to the one with a 3-mm crack. The result suggests that the sensor and system are usable in the multipath environment but suffer from noise, which makes the sensor ID challenging to read.

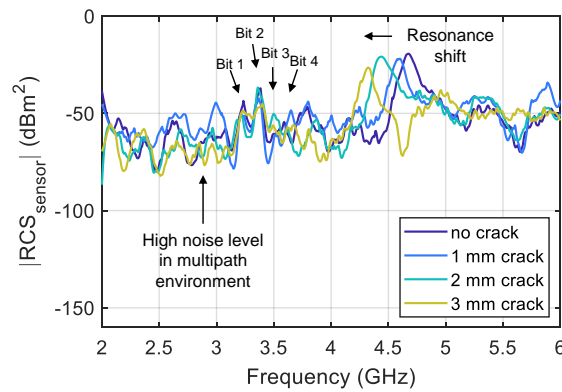


Figure 4.19 Measured RCS spectra of the chipless RFID sensor on horizontal crack samples of different widths in a multipath environment. The resonances for ID signature are hard to detect due to the high noise level.

4.5 Discussions

The chipless RFID sensor in this work has several advantages compared to chipped RFID tag-antenna based sensors for crack detection and characterization. A comparison is provided in Table 4.2, which highlights several aspects, including the sensor size, sensitivity, and reading distance. Table 4.2 lists only the chipped RFID tag antenna-based sensors that use resonance frequency shift for crack sensing on metal so that the sensitivity can be compared. The chipped RFID in the UHF band has a limited bandwidth and is operated in the sub-GHz frequency range. Therefore, multi-parameter sensing is hardly attainable, the antenna design is relatively large or thick in profile, and the sensitivity is limited. Nevertheless, the proposed chipless RFID tag in this work is multi-parameter, small, low-profile, and has a high sensitivity, thanks to the broadband operation in the microwave.

Table 4.2 Comparison of this work with chipped RFID tag antenna-based sensors for crack detection and characterization.

Ref	Year	Measurand	Chipped/chipless	Sensor size	Sensitivity	Reading distance
Yi [176]	2013	Crack length in aluminum	Chipped (UHF)	60 mm × 69 mm	0.08 MHz/mm	210 cm
Zhang J. [178]	2017	Crack depth in aluminum	Chipped (UHF)	20 mm × 20 mm × 16 mm	~1.8 MHz/mm	100 cm
Zhang J. [183]	2018	Crack depth in aluminum	Chipped (UHF)	67-mm diameter × 2mm	7 MHz/mm	100 cm
Sunny [184]	2018	Crack depth in aluminum	Chipped (LF)	26-mm diameter	0.39 kHz/mm	4 cm
This work [28]	2018	Crack width and orientation in aluminum	Chipless	35 mm × 15 mm × 1.27 mm	134.2 MHz/mm	30 cm

Despite the mentioned advantages, the proposed chipless RFID sensor also has disadvantages and limitations. First, the reading distance is moderate and relatively shorter than the chipped UHF RFID systems. Although a more extended reading distance, e.g., 1.2 m, is possible, the chipless RFID sensor system in this study requires calibrations with the sample as well as the background environment. Not only increasing the level of complexity, but the subtraction procedure for calibration also encounters robustness issues in a multipath and dynamic environment. Since the background would be practically different in different places, this sensor system should be used in a controlled environment where calibration with the background can be performed before measurements. Second, the number of ID bits encoded in the sensor is limited by the sensor's surface area and bandwidth. The 4-bit ID in this work shows the viability of having both ID encoding and sensing functionality within a chipless tag. However, a greater number of ID bits is expected to differentiate many sensors. Third, the sensing functionality by using CMPA relies on a single resonance. In this study, it has been seen that the number of resonances affects the capability of the sensor. A greater number of resonances for sensing are desirable for detecting more parameters. For instance, two resonances were required in detecting diagonal cracks. Fourth, the sensor sensitivity to crack depends on the crack position with respect to the sensor. The sensitivity is high when the crack passes the center of the CMPA, where the currents are highly concentrated. As the current distribution gets lower around the edges of the CMPA, the sensitivity to crack becomes low. Fifth, the demonstrated sensor system is limited at the proof of concept level since it is built based on laboratory equipment, i.e., VNA and bulky horn antennas. Moreover, the measurements were mostly done in an anechoic chamber. Therefore, the applicability of chipless RFID sensor systems for SHM remains a practical challenge.

4.6 Chapter Summary

In this chapter, the application of the frequency signature-based chipless RFID for crack detection and characterization has been demonstrated through simulation and experimental studies. A chipless RFID sensor design integrating dipole patches and a CMPA is proposed. The resonances of dipole patches are functionalized for ID encoding, while the resonance of CMPA is used for crack sensing. The crack sensing approach is based on the principle that the crack will change the geometry of the ground plane of the CMPA, which alters its resonance frequency. The simulated and measured RCS have shown that the resonance frequency shift of CMPA can be used as a feature to indicate two crack parameters simultaneously, i.e., crack orientation and crack width. The direction of the resonance shift indicates the crack orientation, while the value of the resonance frequency shift is proportional to the increase of the crack width. Horizontal cracks shift the resonance of CMPA towards lower frequencies, while vertical cracks result in resonance shifts towards higher frequencies. Meanwhile, diagonal cracks split the resonance of CMPA into two, where the shift of one of them has a linear relationship with the crack width. With the sensitivity of 134.3 MHz/mm, the proposed sensor has demonstrated its submillimeter resolution by detecting a natural fatigue crack. Validation of the chipless RFID sensor system was done through experiments using a VNA and horn antennas with a reading distance of 30 cm. Compared to the chipped RFID tag-antenna sensors, the proposed chipless RFID sensor is multi-parameter, small, low-profile, has high sensitivity and submillimeter resolution.

Chapter 5 Chipless RFID Sensor for Corrosion Characterization Based on Frequency Selective Surface (FSS) and Feature Fusion

In the previous chapter, a chipless RFID sensor system for crack detection and characterization was developed and studied based on CMPA. This chapter deals with a chipless RFID sensor system for corrosion characterization based on frequency selective surface (FSS). As highlighted in Chapter 3, one design approach for the implementation of metal-mountable chipless RFID tags is using FSS [245], [246]. FSS has the potential for developing compact, low-profile, and highly sensitive sensors [260]. Classical FSS geometries, such as the cross, rectangular loop, and circular loop, has inspired researchers in designing functional smart materials so that strain or cracks within the material can be detected remotely [261], [262]. Also, chipless dielectric constant sensors based on tilted dipole FSS and Z-shaped FSS have been reported for civil materials [263], [264].

This chapter introduces a novel chipless RFID sensor design based on FSS with the ability to generate three resonances for corrosion sensing. In addition to the sensor design, feature fusion is applied to consolidate multiple features for improving the sensitivity and reliability of the sensor. It is known that the aggregation of information obtained from multiple features is useful to make robust and reliable decisions [256]. Although feature fusion is a common practice in NDT&E and SHM [257], its application for chipless RFID sensors is rarely found. In Section 5.1, the principle of a chipless RFID sensor system for corrosion characterization, including the corrosion sensing approach using FSS and feature fusion using simple sum and confidence weighted averaging (CWA), is explained. Next, the design of the proposed sensor and a simulation study on corrosion sensing are presented in Section 5.2 and 5.3, respectively. Then, the experimental study and results using dedicated corrosion undercoating samples are elaborated in Section 5.4, followed by further discussions in Section 5.5. Finally, the overall conclusion of the study is summarized in Section 5.6.

5.1 Chipless RFID Sensor System, Corrosion Detection Approach Using FSS, and Feature Fusion

In corrosion characterization, sensitivity and reliability are important issues due to the complicated corrosion morphology and inevitable measurement uncertainties. Therefore, the chipless RFID sensor system proposed in this study employs an FSS-based sensor and feature fusion, as illustrated in Figure 5.1. The system consists of an FSS-based chipless RFID sensor and a reader for data acquisition and a signal processing subsystem. As the typical operating

principle of a chipless RFID sensor system, the reader sends a broadband sweep-frequency signal through the transmitting antenna and, in turn, captures the backscattered signal at the receiving antenna. However, the reader in this study uses the cross-polarization reading technique to allow robust measurement in the multipath environment [265]. The orientations of the reader antennas are orthogonal; one is with vertical polarization, and another one is with horizontal polarization. With this principle, the receiving antenna picks up the cross-polar component of the backscattered signal to be recorded in the reader. Since the FSS-based sensor has a frequency selective behavior, the FSS signature contains resonances that can be used as the corrosion indicators.

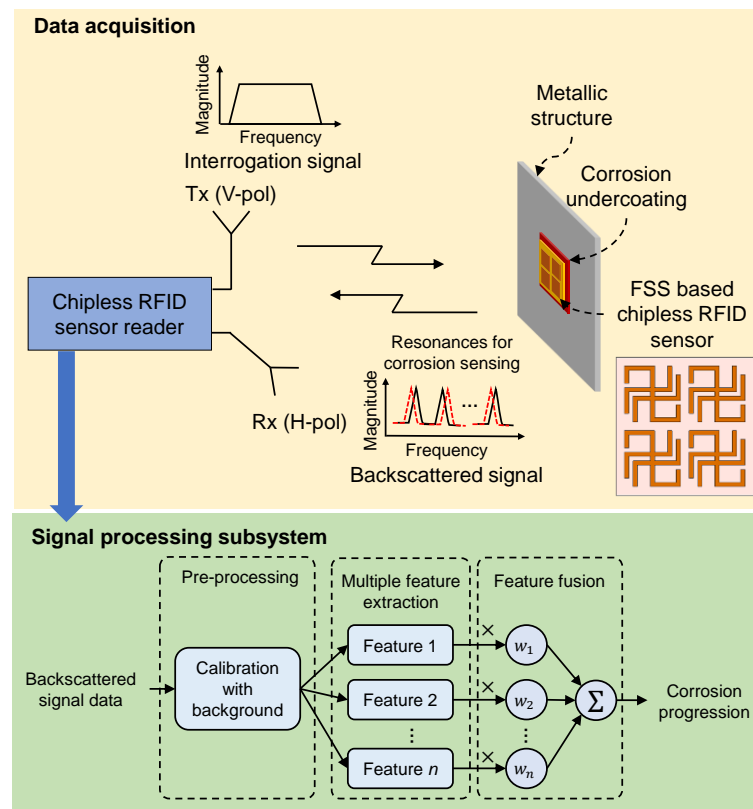


Figure 5.1 Illustration diagram of a chipless RFID sensor system for corrosion characterization using FSS and feature fusion.

The backscattered signal data is processed in the signal processing subsystem, which includes pre-processing, feature extraction, and feature fusion. The pre-processing is a calibration to compensate for the effects of unwanted influences, such as the measurement background and mutual coupling between the Tx and Rx antennas. Then, multiple feature extraction is performed to the signature of the chipless RFID sensor, which contains multiple resonances for corrosion sensing. The multiple features are consolidated by summing the features with or without weightings. In the following subsections, the corrosion sensing approach using FSS and the feature fusion method using simple sum and CWA are described.

5.1.1 Corrosion Detection Approach Using FSS

As reviewed in Chapter 2, corrosion in steel is composed of oxides and hydroxides compounds. These compounds mainly consist of FeOOH (hydroxides), Fe₂O₃ (hematite and maghemite), and Fe₃O₄ (magnetite). According to [40], [41], the dielectric constant of α -FeOOH, γ -FeOOH, α -Fe₂O₃, amorphous Fe₂O₃ and Fe₃O₄ measured at ambient temperature within 10 kHz to 10 MHz are 11, 2.6, 12, and 20, 4.5, and 20, respectively. With such an anisotropic morphology, therefore, it is hard to have an exact model of corrosion. Nevertheless, according to [266], corrosion rust can be modeled as a dielectric material layer formed over a metal.

In the long-term exposure to the atmosphere, metals such as steel will continue to corrode over time. Corrosion progression involves two general stages, early-stage and later stage. In the early stage, corrosion thickness (t) increases as corrosion progresses [86]. While only the proportions of the corrosion rust compounds increase in volume, the properties of compounds are less affected. In addition, as the corrosion progresses, the increase in rust thickness is irregular and thus affects the surface roughness and texture of the steel [267]. In the later stage, the metal loss is dominant, and the corrosion tends to spread rather than to increase in thickness.

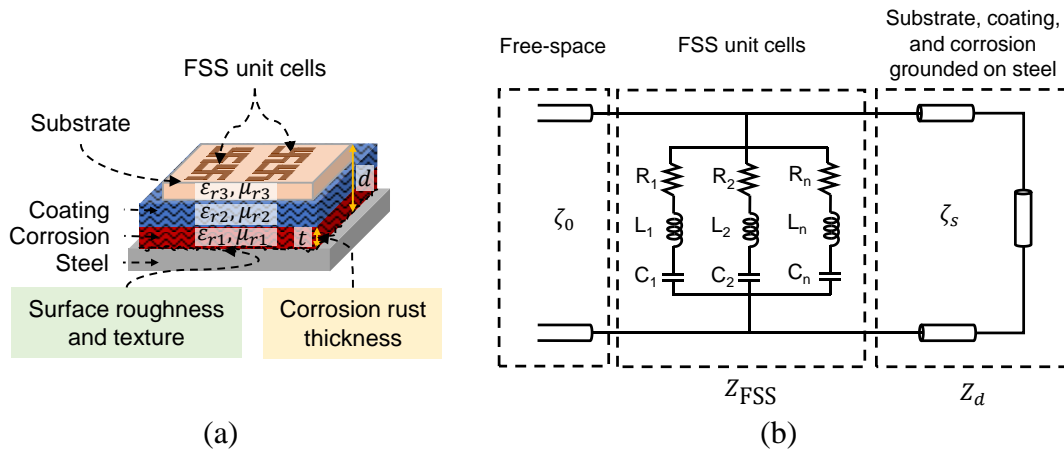


Figure 5.2 Corrosion sensing approach: (a) Simplified model of a corrosion undercoating with FSS-based chipless RFID sensor on corroded steel covered by a paint coating, (b) Equivalent-circuit model of FSS grounded on a corroded and coated steel.

An FSS placed over a grounded slab is a subwavelength resonant cavity with an input impedance approaching infinite and a reflection phase crossing zero at the resonances; it is designated as a high-impedance surface (HIS) [244]. As in Figure 5.2(a), when FSS is grounded over a corroded and coated steel, multiple dielectric slabs exist between them. An equivalent circuit model for the grounded FSS is drawn in Figure 5.2(b). It involves the characteristic impedance of free space (ζ_0), the impedance of multi-resonance FSS (Z_{FSS}), and the impedance of the substrate (ζ_s), coating, and corrosion grounded on steel (Z_d). The resonances of the FSS are obtained for the frequencies at which the surface impedance Z_R approaches or equals to the

free space impedance. The surface impedance Z_R is the parallel relation between Z_{FSS} and Z_d as [244]:

$$Z_R = \frac{Z_d Z_{\text{FSS}}}{(Z_d + Z_{\text{FSS}})}. \quad (5.1)$$

For multi-resonance FSS, the FSS impedance Z_{FSS} is represented by parallel RLC circuits depending on the number of resonances generated by the FSS elements. Meanwhile, the impedance of the grounded dielectric materials underneath the FSS elements (Z_d) can be expressed as [268], [269]:

$$Z_d = j \frac{\zeta_0}{\sqrt{\varepsilon_r' + j\varepsilon_r''}} \tan(k_0 \sqrt{\varepsilon_r' + j\varepsilon_r''} d) \quad (5.2)$$

where d is the thickness of dielectric materials between the FSS unit cells and the steel and k_0 is the free space wavenumber. The thickness of corrosion rust is a part of d , and its relation is proportional to Z_d . The increase in corrosion thickness, therefore, increases the impedance Z_d and subsequently increases Z_R . As the Z_R increases, the resonances are shifted towards lower frequencies proportionally to the square root of the total inductance of the dielectric materials between the FSS unit cells and the steel. Hence, the corrosion progression can be reflected by the systematic change of the corrosion thickness, which affects the resonances of the prototype FSS-based sensor.

5.1.2 Feature Fusion Using Simple Sum and Confidence Weighted Averaging (CWA)

A chipless RFID sensor with multiple resonances conveys multiple sensing information represented by features. If these features provide consistent measures of the same measurand, feature fusion can be applied to improve the sensitivity and reliability of the sensor. Assuming there are n features from n number of resonances, the fused feature value using the simple sum rule is a non-weighted summation of all feature values x_i :

$$x_{\text{fused-sum}} = \sum_{i=1}^n x_i. \quad (5.3)$$

Another way of feature fusion is by using CWA. It is a data fusion method for combining multiple measurement data with respect to their variance into a more reliable estimation of the measurand. It has been used for enhancing accuracy in using multiple sensors [270]. In NDT&E and SHM, it has been applied for mitigating noisy measurements in pulsed eddy current systems

[271]. The fused feature value using CWA is calculated as the weighted average of all feature values x_i , thus can be calculated as

$$x_{\text{fused-CWA}} = \sum_{i=1}^n x_i w_i \quad (5.4)$$

with the weighting coefficient w_i is determined by the variance of each feature F_i as follows

$$w_i = \frac{1}{\mathbb{V}(F_i) \sum_{j=1}^n \frac{1}{\mathbb{V}(F_j)}} \quad (5.5)$$

where n is the number of features, x_i represents a value obtained from the feature F_i and $\mathbb{V}(F_i)$ is the approximate variance associated with the corresponding feature. The approximated variance $\mathbb{V}(F_j)$ is the average variances from multiple measurements and different samples. Under the assumption that the uncertainties between features are independent, the method minimizes the variance of the fused feature value. CWA finds the optimal averaging weights that minimize uncertainties in sensor systems where multiple measurements from sensors or features are applicable.

5.2 Design of the Chipless RFID Sensor based on FSS

The FSS-based chipless RFID sensor proposed in this work follows several main design criteria. First, the FSS is designed to be metal-mountable and has multiple resonances in the reflection mode, following the nature of the backscattering chipless RFID tags. The traditional FSS elements, i.e., N-poles, loop shapes, solid patch shapes, and combinations of them [245], [246], usually have single narrowband resonance and operated for spatial filtering applications in the transmission mode. Thus, the finite-size FSS structures that have a ground plane and act as multi-resonance absorbers are desired. Second, the FSS is designed to be depolarizing since the reader is operated in cross-polarization for robustness reading. In order to act as a wave depolarizer, the FSS unit cell geometry should be made asymmetric [30], [247], [264]. Third, the FSS is designed to be sensitive to the variation of corrosion. In EM simulation, corrosion progression can be modeled as a dielectric layer with a varied thickness between the FSS and a steel slab. The simulation of the proposed FSS against corrosion using CST Microwave Studio will be shown later in the next section.

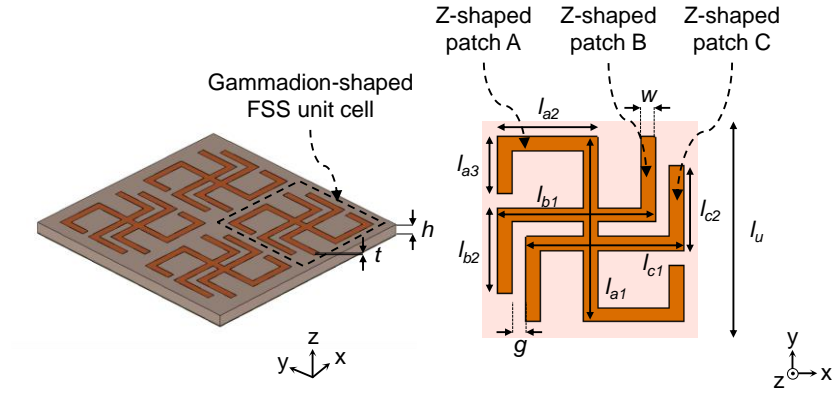


Figure 5.3 Design and geometry of the multi-resonance FSS-based chipless RFID sensor with periodically arranged 2×2 unit cells. Each unit cell comprises three Z-shaped patches; one of them (Z-shaped patch A) is the longest, and the other two (Z-shaped patch B and C) are of the same lengths.

Table 5.1 Dimensions of the FSS-based chipless RFID sensor with 2×2 unit cells (in mm).

g	h	l_{a1}	l_{a2}	l_{a3}	l_{b1}	l_{b2}	l_{c1}	l_{c2}	l_u	t	w
1	1.52	13	7	4	11	6	11	6	15	0.035	1

The geometry of the FSS-based chipless RFID sensor is exhibited in Figure 5.3, with the detailed dimensions listed in Table 5.1. The sensor comprises periodically arranged 2×2 FSS unit cells with a modified gammadion shape, which is a combination of three Z-shaped patches. Gammadion shape is an FSS pattern that has been used to produce a wave depolarizing behavior and chiral metasurfaces/metamaterials [272], [273]. FSSs with gammadion shaped unit cells typically work at a single frequency and produce a resonance. In this chipless RFID sensor design, therefore, the gammadion shape was modified to generate multiple resonances for sensing. In Figure 5.3, one of the Z-shaped patches (Z-shaped patch A) was made to be the longest to generate a resonance at the lowest frequency. The other two Z-shaped patches (Z-shaped patch B and C) are of the same lengths. Although having the same lengths, the positioning of the two Z-shaped patches allows for different lengths of current paths that generate two resonances. The FSS elements were designed on Rogers RO-3035 with a dielectric constant of 3.5, loss tangent of 0.0015, and a thickness of 1.52 mm. The design and simulation were performed in CST microwave Studio with a steel slab placed at the backside of the FSS as a ground plane.

The simulated RCS of the FSS for a different number of unit cells are shown in Figure 5.4. It is apparent that the FSS generates three resonances within 2-6 GHz for 1×1 to 4×4 unit cell configurations. FSS allows the sensor size to be scalable so that it is conformable with the area of the monitored corrosion. A greater number of the unit cell leads to a larger periodic surface and thus increases the RCS magnitude. The FSS unit cell has the dimensions of $15 \text{ mm} \times 15$

mm, which is approximately $\lambda/5 \times \lambda/5$ at 4 GHz. An FSS design with 2×2 unit cells is used in this paper to suit the size of corrosion on the dedicated samples shown later in the experimental section. The overall size of the sensor is, therefore, $30 \text{ mm} \times 30 \text{ mm} \times 1.52 \text{ mm}$ and generates three resonances at 3.06, 3.85, and 4.88 GHz. The generated resonances can be associated with the three Z-shaped patch structures, as shown in Figure 5.5. The Z-shaped patch A, which is the longest one, contributes to the first resonance at 3.06 GHz. The Z-shaped patch B and C create two mutual current propagating modes on the ground. One of which propagates along the outer part of the patches creating a long path of currents. This forms the second resonance at 3.85 GHz. Another mode follows the inner part of Z-shaped patch B and C, resulting in the third resonance at 4.88 GHz.

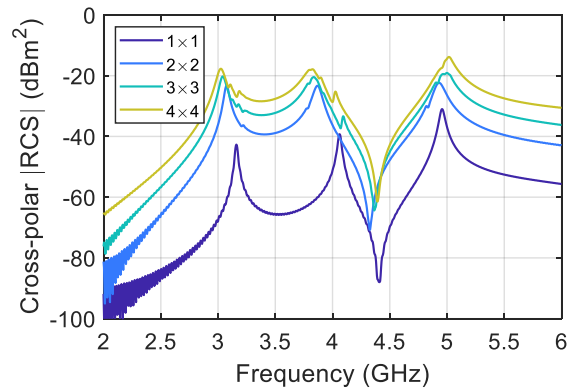


Figure 5.4 Simulated cross-polar RCS of the FSS-based chipless RFID sensor for the different number of unit cells. The greater number of unit cells exhibits higher resonance magnitudes.

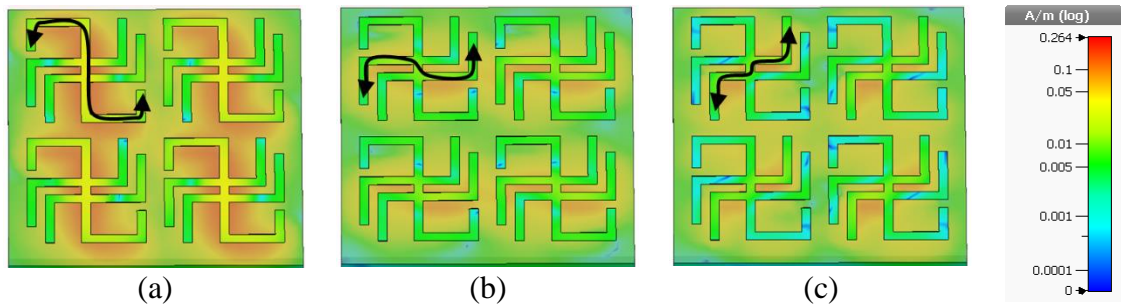


Figure 5.5 Simulated surface current distributions of the FSS-based chipless RFID sensor: (a) at 3.06 GHz. (b) at 3.85 GHz. (c) at 4.88 GHz.

5.3 Simulation Studies of FSS for Corrosion Characterization

In order to observe the FSS structure as a corrosion sensor, a simulation study was performed. In the simulation setup shown in Figure 5.7, two dielectric layers were presented in between the FSS substrate and the metal slab. A dielectric layer below the FSS's substrate is a paint coating layer with a dielectric constant taken to be 3 [266]. The thickness of the coating layer was fixed at $100 \mu\text{m}$, with a loss tangent of 0.0045. Another dielectric layer between the steel

and coating is corrosion rust, with the dielectric constant taken to be 11, which approximates the dielectric property of the α -FeOOH and α -Fe₂O₃. In the simulation study, the corrosion rust thickness was varied from 0 μ m to 200 μ m with 40 μ m steps, while other parameters were fixed. The loss tangent of corrosion rust was fixed at 0.0045. The simulation results, as shown in Figure 5.7, indicate that all three resonances were shifted to lower resonances as the corrosion thickness increased. The sensitivity of the resonances from the lowest frequency to the highest frequency is 0.22 MHz/ μ m, 0.30 MHz/ μ m, and 0.24 MHz/ μ m, respectively.

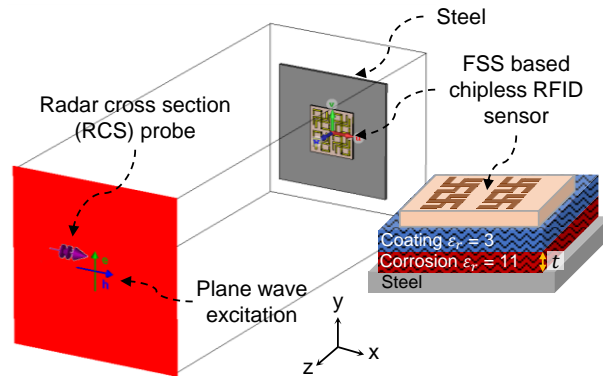


Figure 5.6 Simulation setup of the FSS-based chipless RFID sensor for corrosion characterization in CST Microwave Studio.

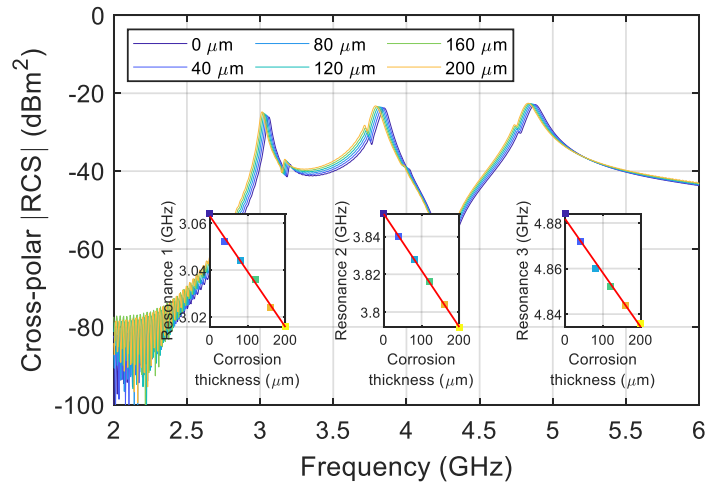


Figure 5.7 Simulated cross-polar RCS of the FSS-based chipless RFID sensor against variations of corrosion rust thickness showing three resonance shifts. Three resonance shift features allow for feature fusion to enhance the sensitivity and reliability of the sensor. The insets show the resonance frequency shifts and linear fitting lines.

Apart from the effects of corrosion thickness, it is interesting to observe how the dimension of FSS, particularly the substrate thickness, affects the RCS magnitude and sensitivity. The substrate thickness used in this work is 1.52 mm, thus for the sake of comparison, the simulated results with the thicknesses of 0.76 mm, 1.52 mm, and 3.04 mm are presented in Figure 5.8(a).

The FSS with the 0.76-mm substrate thickness generates resonances with low magnitudes of RCS around -30 dBm^2 , while the one with 3.04 mm tends to generate prominent resonances with higher magnitudes approaching -20 dBm^2 . In Figure 5.8(b), the simulated resonance frequencies for different FSS substrate thicknesses and with the variation of corrosion thickness are presented. By looking at the steepness of the changes of resonance frequencies against the variation of corrosion thickness, the FSS with the 0.76-mm substrate poses a higher sensitivity to corrosion. Conversely, FSS with the 3.04-mm thick substrate tends to have lower sensitivity. For instance, the FSS with 0.76-mm thickness poses a sensitivity of $0.52 \text{ MHz}/\mu\text{m}$, while increasing the thickness of the substrate to 3.04-mm significantly reduced the sensitivity to $0.08 \text{ MHz}/\mu\text{m}$. Hence, the substrate thickness of 1.52 mm was chosen in this study to compromise between having prominent resonances and reasonable sensitivity.

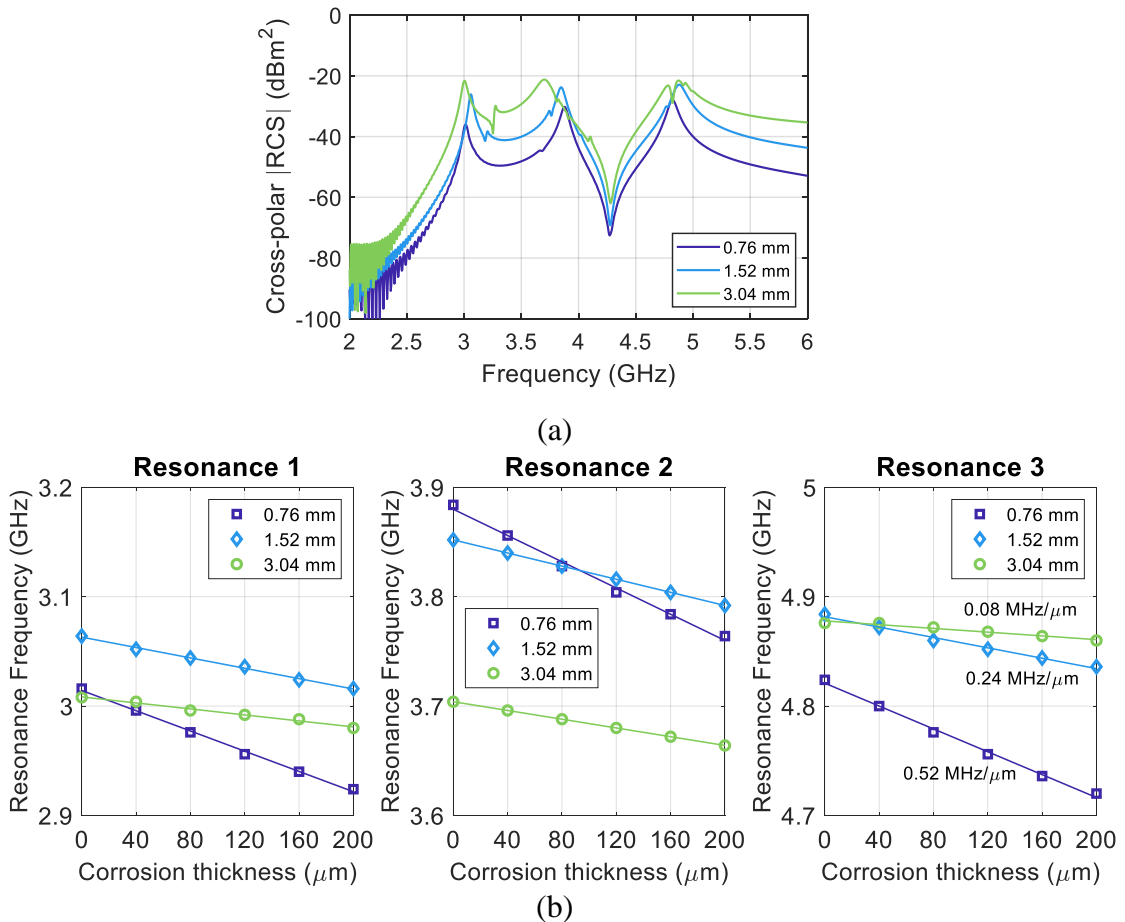


Figure 5.8 Effects of the substrate thickness on: (a) RCS of the FSS, showing that the resonance magnitudes decrease with the decrease of substrate thickness. (b) The sensitivity to corrosion thickness, showing that the sensitivity increases when the substrate thickness decreases.

5.4 Experimental Study and Results

The chipless RFID sensor was fabricated using a Rogers RO-3035 laminate and with the same photochemical etching method explained in Chapter 4 Section 4.4. In order to validate the

simulation results and examine the FSS-based chipless RFID sensor, an experimental study was carried out using the fabricated sensor and dedicated corrosion undercoating samples. The corrosion undercoating samples are on mild steel S275 with the dimensions of 300 mm × 150 mm × 3 mm, as depicted in Figure 5.9. The center part of each sample was exposed to a marine atmosphere for different periods. Then, the entire surface of the sample was coated using nonconductive paint with a thickness of ~0.1 mm. The corroded area has dimensions of 30 mm × 30 and different corrosion progressions according to the exposure period. The corrosion progression samples include the early-stage corrosion samples: i.e., non-corroded sample (M0), 1 month (M1), 3 months (M3), 6 months (M6); and later-stage corrosion samples: i.e., 10 months (M10), and 12 months (M12). For the sake of simplicity, the corrosion samples are abbreviated as M0, M1, M3, M6, M10, and M12 in the rest of this paper. The samples have been tested using different EM NDT&E techniques [86], [98], [193], [195], [196].

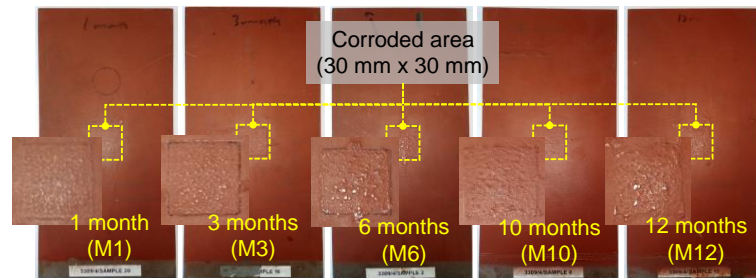


Figure 5.9 Corrosion undercoating samples with different exposure periods to a marine atmosphere.

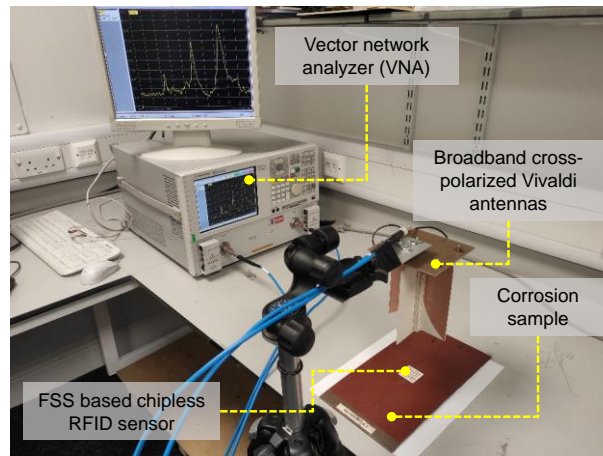


Figure 5.10 Experimental setup in a laboratory environment using VNA and dual-polarized Vivaldi antennas.

Figure 5.10 exhibits a photograph of the experimental setup in a laboratory environment. The fabricated FSS-based chipless RFID sensor was placed on the corroded area of the corrosion. Dual-polarized broadband Vivaldi antennas were employed as the reader antennas and mounted at a 15-cm reading distance above the sensor and the corrosion sample. The design of the reader antennas is inspired by [274] (see Appendix A), which intersects two orthogonally oriented

identical broadband Vivaldi antennas. The transmitting and receiving antennas, therefore, are compactly integrated and have the same phase center. The radiation pattern of the antennas is unidirectional, with a gain of 7 to 11.5 dBi over 2-6 GHz. For measurements, the antennas were connected to the Port-1 and Port-2 of a VNA. Then, the measured transmission coefficient ($|S_{21}|$) responses for the sensor mounted on different samples were acquired. Ten sequential $|S_{21}|$ measurements were performed in this setup for each corrosion sample to consider measurement uncertainties. The $|S_{21}|$ response of each corrosion sample without the sensor was also recorded for calibration.

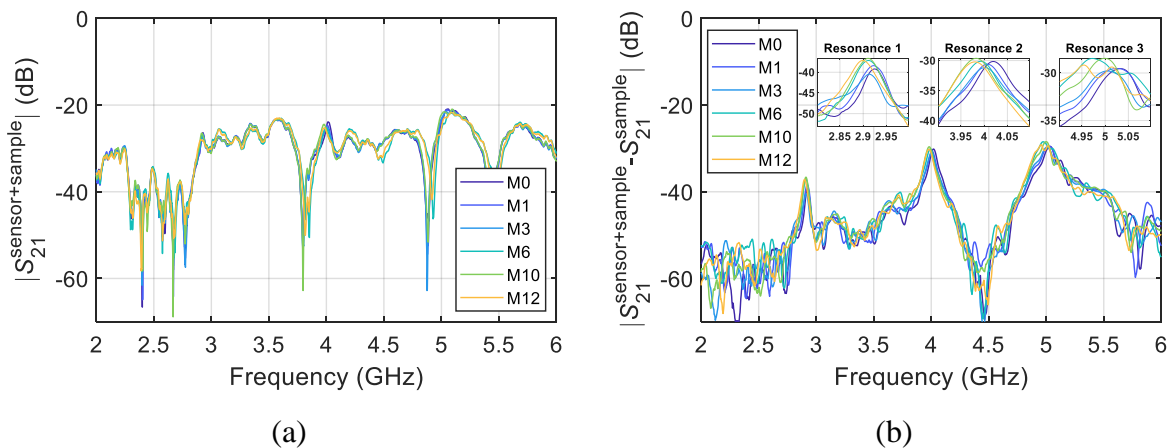
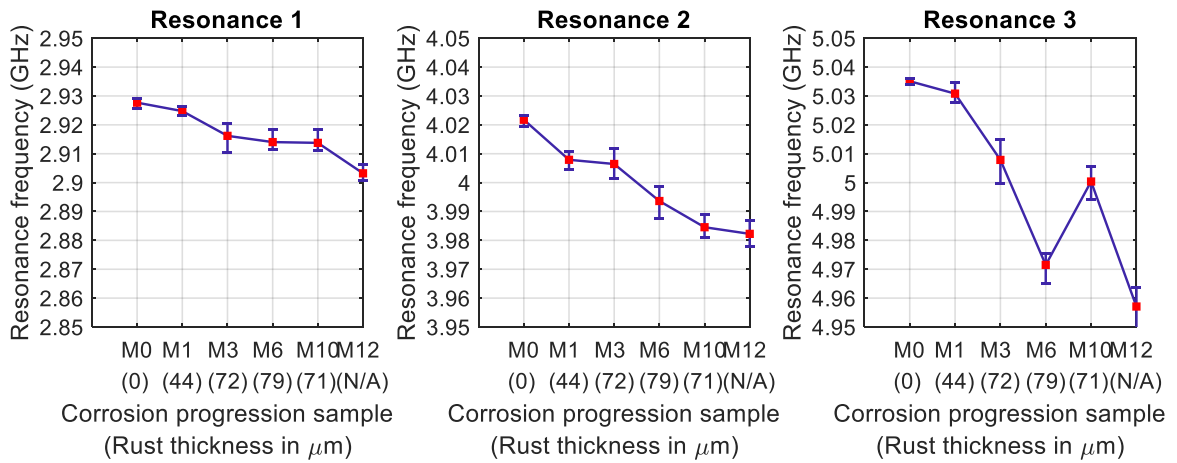
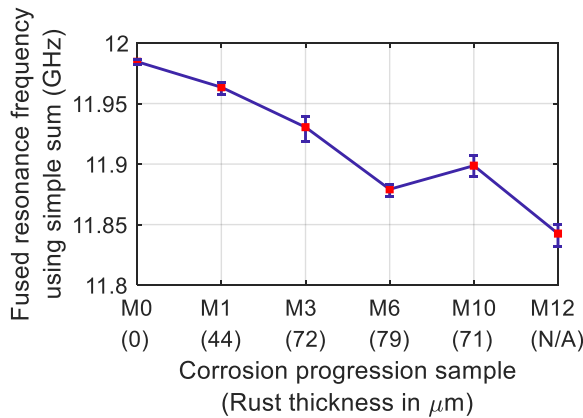


Figure 5.11 Measured transmission coefficient ($|S_{21}|$) averaged from 10 repeated measurements of the FSS-based chipless RFID sensor for different corrosion undercoating samples: (a) Raw (uncalibrated) $|S_{21}|$. (b) Calibrated $|S_{21}|$ by subtracting the raw $|S_{21}|$ with the $|S_{21}|$ response of the sample.

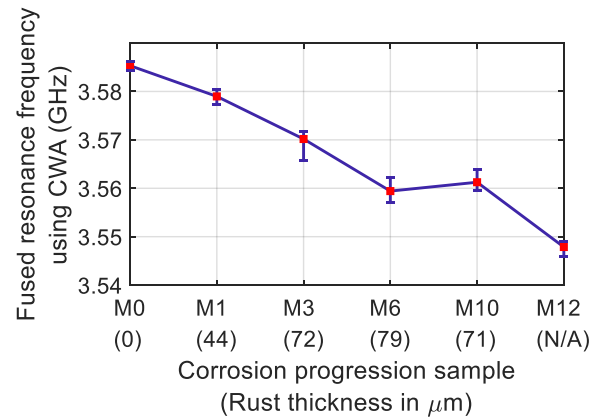
The raw (uncalibrated) $|S_{21}|$ responses for different corrosion undercoating samples, as shown in Figure 5.11(a), indicated that the resonances of the FSS-based chipless RFID sensor are hardly noticed. The resonances are obscured by the polarization leakage between the Tx and Rx antennas. The low echo signal from the sensor poses the requirement of high isolation between the Tx and Rx antennas. The $|S_{21}|$ response of each corrosion sample without the sensor was recorded earlier for calibration. To eliminate the leakage between antennas and other unwanted background influences, calibration was performed by subtracting the raw $|S_{21}|$ response with the $|S_{21}|$ response of the corrosion sample without the sensor in place. As shown in Figure 5.11(b), the calibrated $|S_{21}|$ responses result in the signatures of the sensor, which contain three resonances at around 2.9 GHz, 4 GHz, and 5 GHz. The resulting resonance frequencies are close to the simulated ones in Figure 5.4. It signifies a good agreement between the simulation and measurement. Furthermore, it is noticeable in Figure 5.11(b) that the changes in corrosion samples, as expected, lead to the variation of the three resonances of the FSS.



(a)



(b)



(c)

Figure 5.12 Characterized corrosion progression indicated by: (a) Resonance frequency features. (b) Fused resonance frequency feature using simple sum. (c) Fused resonance frequency feature using CWA. The fused features show less overlapped and smaller error bars than individual features.

From the calibrated $|S_{21}|$, three resonance frequency features were extracted to characterize the corrosion progression. In Figure 5.12, the values of resonance frequency features are plotted against the corrosion samples. The plotted dots indicate the average feature values while the error bars show the range of feature values, i.e., minimum and maximum values taken from ten measurements. In general, the increase of corrosion progression manifests declining trends of the resonance frequencies. As shown in Figure 5.12(a), the trends for three resonance frequency features are relatively consistent but with different rates and characteristics. Resonance frequency 1, i.e., the one around 2.9 GHz, decreases less sharply, with indistinguishable corrosion progressions for M6 and M10. Resonance frequency 2 decreases moderately and shows the monotonic trend of corrosion progression. Meanwhile, Resonance frequency 3, which is at the highest frequency, declines most rapidly against the corrosion progression but with the stage of M10 deviates from the overall trend. Hence, the three resonances exhibit different sensitivity and characterization results, thanks to the multi-resonance characteristic of the chipless RFID sensor so that multiple interpretations of corrosion progression can be

acquired at once. The idea of having multiple features to interpret corrosion progression makes it possible to fuse the sensing information and to enhance the sensitivity and reliability of the sensor.

Feature fusion using simple sum and CWA were applied to find the final interpretation of the corrosion progression. By using (5.5), the fusion weights for CWA $w_i = [0.55; 0.29; 0.16]$ were assigned to the three resonance frequency features, respectively. The fused resonance frequency features using simple sum and using CWA are depicted in Figure 5.12(b) and Figure 5.12(c), respectively. The fused features using both simple sum and CWA show similar results with monotonic trends of corrosion progression for early-stage corrosions (M0 to M6). In the early stage, the values of fused resonance frequency features decrease monotonically as the corrosion stage increases. However, the trend is anomalous at month 10, which is because of the abnormality of the M10 sample. According to previous studies [86], [98], [193], [195], [196], the M10 and M12 samples are later-stage corrosions, in which corrosion tends to spread rather than to increase in thickness [275]. Therefore, the characterization results, shown in Figure 5.12(b) and Figure 5.12(c), are reasonable and correspond to the results of the previous studies that used the same corrosion samples.

Table 5.2 Sensitivity and standard deviation of individual resonance frequency features and the fused features.

Feature	Sensitivity	% average standard deviation
Resonance frequency 1	2.3 MHz/month; 0.17 MHz/ μm	0.062%
Resonance frequency 2	4.7 MHz/month; 0.36 MHz/ μm	0.063%
Resonance frequency 3	10.6 MHz/month; 0.81 MHz/ μm	0.066%
Fused resonance frequency using simple sum	17.6 MHz/month; 1.34 MHz/μm	0.037%
Fused resonance frequency using CWA	4.3 MHz/month; 0.33 MHz/ μm	0.036%

Measured using laser profilometry, the average thickness of corrosion rust for M1, M3, M6, and M10 are 43.86 μm , 71.72 μm , and 79.09 μm , and 70.99 μm , respectively [276]. The thickness of rust for M12 is not available in [276]. The measured thickness of corrosion rust for the M10 sample is indeed less than the M6, which validates the characterization result in this work. The sensitivity and standard deviation of individual resonance frequency features and the fused features are calculated and summarized in Table 5.2. The sensitivity is calculated based on the change of feature during the early-stage (M0-M6) against the sample's exposure period (6 months) and against corrosion thickness at month 6 (79.09 μm). The sensitivity against the exposure period is in MHz/month, while the one against corrosion thickness is in MHz/ μm . It can be seen that the resonances generated by the FSS-based chipless RFID sensor at different frequencies provide different sensitivities to corrosion. Resonance 3 of the proposed sensor,

which is at 5 GHz, provides the highest sensitivity of 10.6 MHz/month or 0.81 MHz/ μm . The sensitivity of the fused feature using the simple sum, which is 17.6 MHz/month or 1.34 MHz/ μm , is equivalent to the sum of sensitivities of the individual features. Furthermore, it is revealed that the fused feature has a low average standard deviation in comparison with individual resonance frequency features. The percentage average standard deviation of the individual resonance frequency features are higher than 0.062%, while feature fusion can reduce it to roughly 0.036%. The low standard deviation indicates a low degree of uncertainties/errors in the measurements, thus also represents the high reliability of the sensor. In the characterization result, the high reliability is shown by the less-overlapping error bars, as in Figure 5.12(b) and Figure 5.12(c). Hence, the results have proven that feature fusion can enhance the sensitivity and reliability of the FSS-based chipless RFID sensor.

5.5 Discussions

In order to compare this work with other RFID sensors, a summary of RFID sensors that used the same corrosion samples is presented in Table 5.3. Different RFID frequency bands, sensor designs, and features have been investigated for corrosion characterization. Information on sensor size, sensitivity, and reading distance is extracted for quantitative comparisons.

Table 5.3 Summary of several RFID sensors for corrosion characterization.

Ref.	Year	Sensor system	Sensor design	Sensor size	Feature	Sensitivity	Reading distance
Sunny [193]	2016	Chipped LF RFID (125 kHz)	Off-the-shelf coil tag	26 mm diameter	Transient response	0.32×10^{-3} V/month; 0.24×10^{-4} V/ μm	30 mm
Zhang H. [194]	2016	Chipped HF RFID (10-20 MHz)	Off-the-shelf coil tag	50 mm diameter	Impedance	15.33 Ω /month; 1.16 Ω / μm	25 mm
Zhang J. [195]	2016	Chipped UHF RFID (902-928 MHz)	3D folded dipole	20 mm \times 20 mm 16 mm	Analog identifier (AID) and PCA feature	0.583/month; 0.044/ μm	1000 mm
Zhao [196]	2017	Chipped UHF RFID (900-925 MHz)	Meandered dipole patch	48 mm \times 20 mm \times 5 mm	Resonance frequency	0.51 MHz/month; 0.039 MHz/ μm	660 mm
This work		Chipless RFID (2-6 GHz)	FSS	30 mm \times 30 mm 1.52 mm	Multiple resonance frequency features and feature fusion	17.6 MHz/month; 1.34 MHz/μm	150 mm

In terms of size, the FSS-based chipless RFID sensor in this work is small and low-profile in comparison with the chipped HF and UHF RFID sensors [194]–[196]. Due to the lower

operating frequencies and in order to work on metal, HF and UHF RFID sensors have a relatively large size and a thick profile. Regarding the sensitivity, the FSS-based chipless RFID sensor in this work gives a high sensitivity, especially compared to the UHF RFID sensor in [196]. The UHF RFID sensor in [196] has a sensitivity of 0.51 MHz/month or 0.039 MHz/ μm , while the proposed sensor has a sensitivity of 17.6 MHz/month or 1.34 MHz/ μm . The high sensitivity of the chipless RFID sensor can be attributed to its operation at a higher microwave frequency range and the applied feature fusion. In this study, it is demonstrated that the FSS-based chipless RFID sensor can characterize corrosion progression from a 15-cm reading distance. This distance is five times longer than the capability of the LF and HF RFID sensor systems but shorter than the reading distance demonstrated by UHF RFID sensor systems. Overall, the chipless RFID sensor in this work offers a moderate reading distance with high sensitivity and reliability compared to the RFID sensors that shared the same corrosion samples.

The above advantages in terms of size, sensitivity, and reliability come with the costs of the high operating frequency range and the broad bandwidth to occupy multiple resonances. The high sensitivity in microwaves applies not only to corrosion but also to other parameters. The cross-polarization reading may improve the robustness of the measurements but necessitates the reader antennas to have high isolation. Therefore, when the detection of the measurand demands high sensitivity, prior calibration with the background environment is still required to remove unwanted influences. Also, the reliability enhancement using CWA-based feature fusion needs prior measurements to study the sensor's characteristics and find the proper weightings for the features. Furthermore, an obvious limitation with corrosion characterization using a chipless RFID sensor is the incapability of localization. Since the chipless RFID sensor can only characterize corrosion located at the sensor position, this technique is limited to the characterization and monitoring of localized corrosion.

Reading range, the bulkiness of reader antennas, and temperature influence are among the further practical issues. The 15-cm reading distance demonstrated in this work may not be the best for real applications. Thus, the reading range could be improved by increasing the gain and directivity of the reader antennas, such as using reflectarray antennas [277]. Nevertheless, the bulkiness of reader antennas should also be considered to improve the reading range. The dual-polarized Vivaldi antennas used in this work is good enough for a proof of concept in a laboratory. The compactness of reader antennas should be improved in the later stage for real applications [278]. Furthermore, in a hostile environment, temperature variations could influence the sensor's reliability. Sensor protection and temperature compensation, therefore, may be required in practical situations. By observing the effects of temperature variation in the

signal, feature selection and fusion could be used to achieve temperature-independent corrosion monitoring [197].

5.6 Chapter Summary

In this chapter, a chipless RFID sensor design based on FSS and feature fusion for characterization of corrosion undercoating has been presented. The sensor has an overall size of $30\text{ mm} \times 30\text{ mm} \times 1.52\text{ mm}$ and is composed of 2×2 gammadion shaped unit cells formed using three Z-shaped patches on a substrate. The FSS-based chipless RFID sensor generates three resonances, which shift to lower frequencies with the increase of corrosion thickness. The sensor was designed with simulation studies and validated through an experimental study using a VNA and dual-polarized Vivaldi antennas as the chipless RFID reader. The experiment using dedicated corrosion samples has shown that the proposed sensor can be used to characterize corrosion progression. Moreover, the fusion of multiple resonance frequency features using simple sum and confidence weighted averaging (CWA) can enhance the sensitivity and reliability of the sensor. The sensitivity of the fused feature is up to 17.6 MHz/month or $1.34\text{ MHz}/\mu\text{m}$, which is a higher sensitivity compared to the chipped RFID counterpart. The improvement of reliability using feature fusion is indicated by the reduction of measurement errors by half of that using individual resonance frequency features.

Chapter 6 Robust Characterization of Defects in Realistic Environment Using Multi-resonance Chipless RFID Sensor, Portable Reader, and Principal Component Analysis

The previous chapters have shown the capability of chipless RFID sensors for the characterization of crack and corrosion progression with good performance in terms of sensitivity. However, the systems were demonstrated using a big-sized VNA and horn antennas while subtraction with the background or the sample for calibration was necessary. Such bulky equipment and calibration are insufficiently practical for a real scenario. In practice, defects can occur with multiple parameters, while the signal from the chipless RFID sensor is entangled with multiple influences from the reader system and the surrounding environment. In Chapter 4, a chipless RFID sensor with a single resonance can only indicate the crack width and two types of crack orientations, i.e., horizontal and vertical cracks. A diagonal crack needs two resonances as indicators, and in general, defects can occur with multiple parameters to recognize. In Chapter 5, the sensitivity of a single resonance to corrosion is relatively limited, but three resonances can be fused to achieve high sensitivity. Furthermore, interferences and noise in a realistic environment can cause variations in the signal, which may affect detection sensitivity to defects.

The above cases highlight the importance of having multiple resonances for multi-parameter sensing and robustness. Essentially, the detection of multiple variables would need a great number of features as the sensing indicators. The principles of multi-frequency eddy-current and pulsed eddy current are particular examples in NDT&E and SHM. Detection of multiple defect parameters is made possible because of the richness of spectral components for sensing [15], [279]. Fortunately, since a chipless RFID sensor system is operated in broadband, the spectral component can be made rich by incorporating multiple resonances. As highlighted in Chapter 3, RF encoding particles can be used to design metal-mountable and multi-resonance chipless RFID tags and sensors. With the presence of multiple resonances, however, interpretation by observation of resonance peaks/notches is troublesome, especially for resonances having non-uniform characteristics [280]. Therefore, a statistical feature extraction technique, such as principal component analysis (PCA), is desirable to analyze the significant contributing parameters in signals. PCA has been proven as a powerful tool to analyze multivariate spectral data of various electromagnetic sensor systems, including eddy current testing, microwave NDT, and UHF RFID sensor [98], [195], [281].

This chapter addresses the challenge associated with the robustness of the characterization of defects in a realistic environment. Accordingly, a multi-resonance chipless RFID sensor, portable reader, and feature extraction and selection using PCA are investigated. Section 6.1 describes the principle of a chipless RFID sensor system using a multi-resonance chipless RFID sensor and PCA. The multi-resonance chipless RFID sensor is designed based on RF encoding particles, which mainly exploits a combination of dipole patch structures. Then, the crack and corrosion sensing approach based on RF encoding particles is explained in Section 6.1.1. the implementation of a portable chipless RFID sensor reader using an off-the-shelf UWB radar module is elaborated in Section 6.1.2. Next, multiparameter analysis using PCA is explained in Section 6.1.3. Afterward, the proposed design of a multi-resonance chipless RFID sensor is exhibited in Section 6.2, followed by simulation studies in Section 6.3. The experimental study and results using crack and corrosion samples are discussed in Section 6.4. After further discussions in Section 6.5, the conclusion of this study is summarized in Section 6.6.

6.1 Chipless RFID Sensor System Using Multi-resonance Sensor, Portable Reader, and PCA

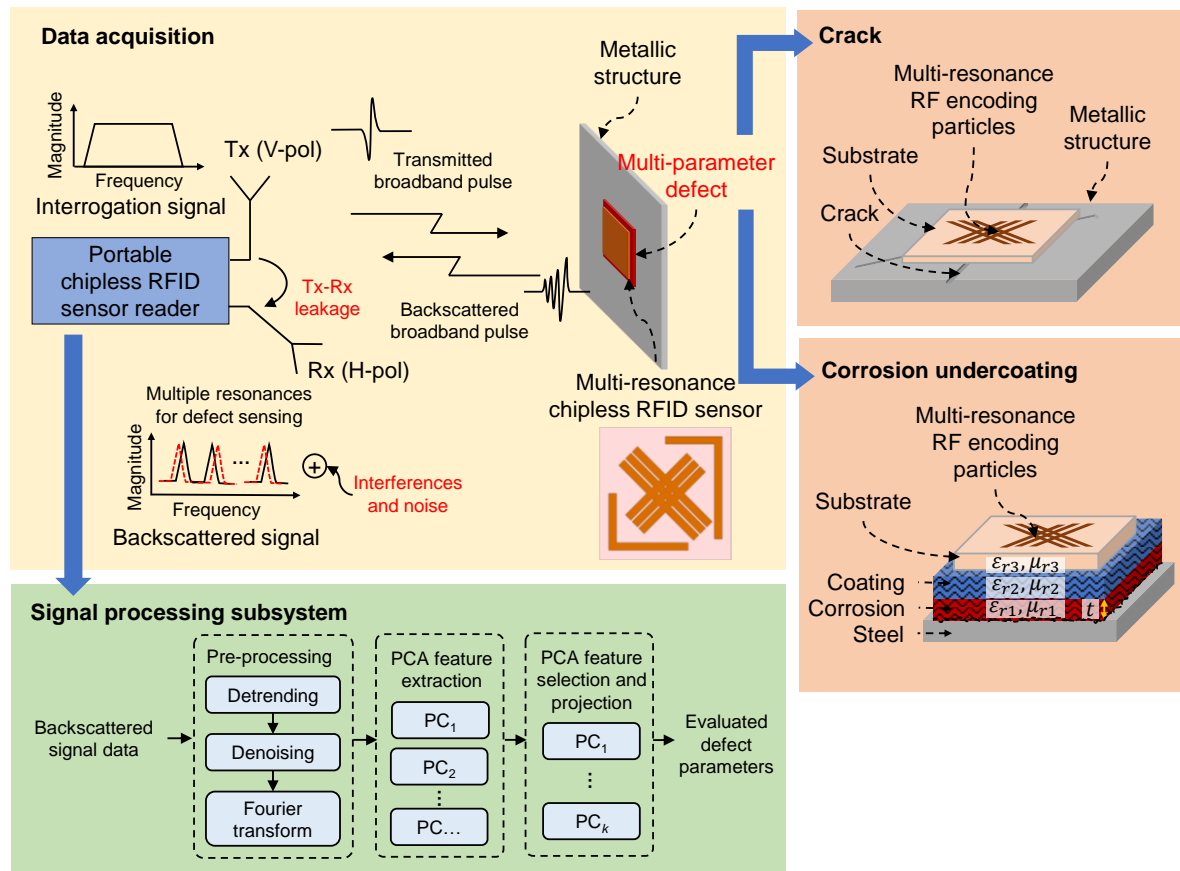


Figure 6.1 Illustration diagram of a chipless RFID sensor system using a multi-resonance sensor, portable reader, and principal component analysis (PCA). Principal components (PCs) represent the extracted features used for evaluating the most contributing physical parameters contained in signal data.

In order to demonstrate a robust characterization of defects in a realistic environment, the chipless RFID sensor system in this study exploits a multi-resonance sensor, portable reader, and PCA, as illustrated in Figure 6.1. The portable chipless RFID sensor reader uses the cross-polarization reading as it is desirable for robust chipless RFID tag and sensor detection on metal [247], [282]. Being operated in the time-domain, the portable reader transmits a broadband interrogation signal in the form of a pulse to the multi-resonance chipless RFID sensor. The broadband pulse is transmitted by the Tx antenna in vertical polarization. Then, the pulse is depolarized and scattered back by the multi-resonance chipless RFID sensor, which is later picked up by the Rx antenna in horizontal polarization. The backscattered signal, however, is affected by several factors, including Tx-Rx coupling/leakage, multiple parameters of the defect, and may get interfered with noise along the transmission path.

The backscattered signal data collected by the portable reader requires pre-processing, which includes detrending, denoising, and transformation into the frequency domain. Detrending is meant to remove the trend, which refers to a change in the mean over time, from the backscattered UWB pulse in the time domain. Denoising aims to remove noises in the signal. Then, the Fourier transform is required to transform the time series signal into the sensor signature in the frequency domain. In the frequency domain, the backscattered signal contains multiple resonances as shaped by the multi-resonance chipless RFID sensor. Since the backscattered signal contains multiple influences, feature extraction and selection using PCA is employed to analyze multiple parameters, and ultimately, to reveal the defect parameters. Details of the defect sensing approach, the portable reader, and multi-parameter analysis using PCA are described in the following subsections.

6.1.1 Defect Sensing Approach Using RF Encoding Particles

A multi-resonance chipless RFID sensor for defect sensing can be constructed via RF encoding particles [217], [247]. The term “particle” was introduced by Perret [217], [247], referring to the resonant scatterers that can compose a chipless RFID tag or sensor with minimum size and a high number of resonances. RF encoding particles, such as multiple dipole patches with different lengths, create several current propagating modes on a ground plane and thus creating resonances. When the dipole patches are placed over a defected metal, the defect causes variations to the resonances, which are detectable remotely by a reader through the backscattered signal. The geometry of a dipole patch is similar to the rectangular patch antenna by the case that the width is relatively small compared to the length. A rectangular microstrip patch on a dielectric substrate and a ground plane has a fundamental resonance frequency that can be estimated as [238]:

$$f_r = \frac{c}{2L_{eff}\sqrt{\epsilon_{reff}}} \quad (6.1)$$

where c is the speed of light in a vacuum, L_{eff} is the effective length of the patch, and ϵ_{reff} is the effective relative permittivity of the substrate. L_{eff} considers both physical length and fringing fields at the tips of the patch and thus:

$$L_{eff} = L + 2\Delta L \quad (6.2)$$

where L is the physical length of the patch, and ΔL is the fringing extension added to the L . ΔL can be further elaborated as:

$$\Delta L = 0.412h \frac{(\epsilon_{eff} + 0.3) \left(\frac{W}{h} + 0.264\right)}{(\epsilon_{eff} - 0.258) \left(\frac{W}{h} + 0.8\right)} \quad (6.3)$$

where W is the width of the patch, and h is the thickness of the substrate below the patch. In both (6.1) and (6.3), ϵ_{reff} is related to the substrate's relative permittivity (ϵ_r), W , and h , thus can be written as:

$$\epsilon_{reff} = \frac{\epsilon_r + 1}{2} + \frac{\epsilon_r - 1}{2} \left[1 + 12 \frac{h}{W} \right]^{-\frac{1}{2}} \quad (6.4)$$

The (6.1) to (6.4) express the relationships between the resonance of a dipole patch and several parameters, including the length and width of the patch, the substrate thickness, and the substrate's dielectric constant. These estimation formulae hold true for a dipole patch designed on a perfect ground plane.

When a metallic structure is treated as a ground plane for multiple dipole patches, the occurrence of defects leads to structural changes. A surface crack is intrinsically a slot on a metal surface, which creates discontinuities and displacements of currents, as discussed in Chapter 4. The currents propagating on the ground plane affect the effective length of the dipole patch, and so as the resonance. Therefore, resonance frequency shifts can be expected depending on the crack geometry and parameters. When multiple dipole patches are placed on corroded steel, the steel becomes a ground plane, and the corrosion rust and coating become additional inhomogeneous substrates for the patches. Consequently, multiple parameters are responsible for the resonances of the patches, such as relative permittivity, thickness, and surface roughness of both corrosion and the coating layer. In accordance with expressions in (6.3) and (6.4), alterations in the substrate's thickness can shift the resonance frequencies of dipole patches, which can be used to indicate the corrosion progression.

6.1.2 Portable Chipless RFID Sensor Reader Implemented Using a UWB Radar Module

In this study, a portable chipless RFID sensor reader was implemented using a commercially available UWB radar module, i.e., the Salsa Cayenne radar module by Novelda [248]. The radar module costs \$3500 and is commercialized as a research and development platform for high-precision human presence and tracking applications. The specifications related to electrical characteristics, radar transmitter, transceiver antennas, and the receiver are summarized in Table 6.1. Other specifications from the manufacturer are provided in Appendix C.

Table 6.1 Specification of UWB radar module for chipless RFID sensor reader.

Electrical specifications	Details
Input voltage	+5V _{DC}
Power consumption	70 mA @ 5V _{DC} in continuous reading mode
Transmitter specifications	
Transceiver chip	Xethru X1, IPG0 medium-band UWB pulse generator
Average Tx power	-19 dBm (0.0126 mW)
Operating bandwidth	0.9 – 6.5 GHz (-10dB)
Sampling rate	~34 Gs/s
Pulse repetition frequency (PRF)	Up to 100 MHz
Antenna specifications	
Type of Tx and Rx antennas	Antipodal Vivaldi antennas
Radiation pattern	Unidirectional
Gain at boresight	7 to 10.2 dBi over 2 to 6 GHz
Receiver specifications	
Receiver sensitivity	-95 dBm
ADC settings (adjustable)	min=0, max=8191, step=4
Pulses per steps (adjustable)	64
Samplers per data frame	512 parallel samplers
Frame stitching mode (adjustable)	8 frames
Data resolution of a time-domain pulse	8 frames × 512 data points per frame
Data resolution of frequency-domain spectrum	480 data points for 2 to 6 GHz

The radar module operates at 5V and can be interfaced with a computer via a USB connector. An external power supply is not required as the radar module draws only 70 mA current in continuous reading mode. The radar module employs a UWB pulse generator with an average power of -19 dBm. It is fully compliant with the FCC UWB regulation, which states the power spectral density of transmitted UWB pulses must be restricted under -41.3 dBm/MHz. The radar module operates within 0.9 to 6.5 GHz frequency with a high-speed sampling rate up to ~39 Gs/s and PRF of up to 100 MHz. The transmitted waveform was captured using a high-sampling oscilloscope and depicted in Figure 6.2(a). It is the 1st order monocycle Gaussian pulse, and the normalized power spectral density (PSD) can be seen in Figure 6.2(b). The PSD shows that the 10-dB bandwidth of the pulse lies within 0.8 and 7 GHz, which covers the operating bandwidth stated by the specification. In this study, the chipless RFID sensor reader applies a frequency

range of 2 to 6 GHz, which is within the operating range of the radar module and in accordance with the chipless RFID sensor design.

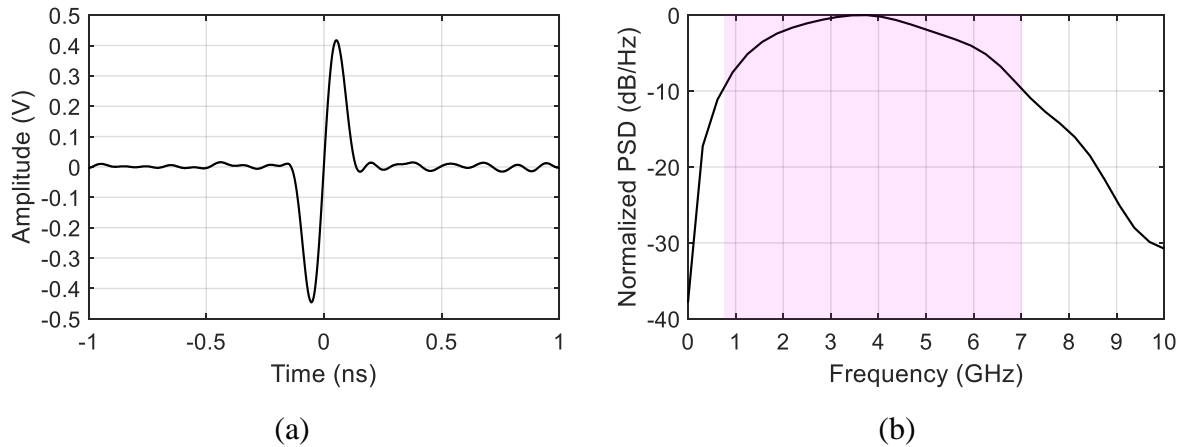


Figure 6.2 Monocycle Gaussian UWB pulse generated by the Xethru1 chip of the Salsa Cayenne radar module. (a) Time-domain pulse waveform. (b) Normalized power spectral density (PSD).

As the front end of the UWB signal transmission and reception, a pair of antipodal Vivaldi antennas are used with the radar module (see Appendix B). The radiation pattern of the antennas is unidirectional. The antipodal Vivaldi antennas are designed to have a high gain, i.e., 7 to 10.2 dBi over the frequency range of 2 to 6 GHz. This is to compensate for the low average power of the transmitted pulse and to maximize the received signal at the receiver. The receiver circuit of the radar module contains high-speed parallel samplers and analog-to-digital converters (ADC). The amplitude of a single ADC step is calculated from a number of pulses, which is defined by pulses per step in the settings. The ADC step and pulses per step settings are adjustable, which both affect the frame rate. A low ADC step and a high number of pulses per step cause a slow frame rate and vice versa. With the default settings, a frame of the received signal contains 512 data points from the parallel samplers. It is considerably low in resolution, but the frame stitching can be applied to improve the number of data points per frame. The default frame stitching value is 1, and the radar span can be increased by setting the frame stitching to a higher value. With the frame stitching, multiple frames are captured in a sequence where the offset time is adjusted to the next frame after the end of the previous frame. In this study, the frame stitching is set to 8 so that the backscattered/received signal in the time domain contains $8 \times 512 = 4096$ data points per frame.

The received pulse signal collected from the reader is a discrete time-domain signal with 4096 data points per reading. The sampled raw signals contain DC offsets and additive noise. Thus, signal pre-processing is required to detrend and to denoise the signals. The signal detrending is done by subtracting the signals with the mean so that each signal has a zero mean. Denoising

using the discrete wavelet transform (DWT) can remove noise while preserves the signal information [250]. The symlet8 mother wavelet with soft thresholding can be applied to obtain smooth denoised signals. Since the chipless RFID sensor works in the frequency domain, the signals need to be converted to the frequency domain using the Fourier Transform. With the sampling rate of ~ 34 Gs/s, the signal spectrum in the frequency domain is from DC to half of the sampling rate, i.e., ~ 17 GHz. The conversion to the frequency domain decreases the number of data points by half to 2048, as only the positive side of spectra should be taken. Furthermore, trimming the frequency spectrum into 2 to 6 GHz limits the frequency spectrum to 480 data points. The data sampling resolution is limited compared to VNA since having 480 data points for 2 to 6 GHz is already maximized for this portable reader. With VNA, the data sampling resolution setting can be set to 1600 data points and even more within the band. The limited data sampling resolution of the portable chipless RFID reader is critical because signals will be represented in fewer details. It limits how small variations, specifically resonance shifts, in signals can be recognized for sensing and demands the chipless RFID sensor to have a high sensitivity.

6.1.3 Multi-parameter Analysis Using Principal Component Analysis (PCA)

In a realistic environment, the interrogation signal transmitted by the reader encounters various effects before being scattered to the receiver antenna. Therefore, the acquired frequency signature of a chipless RFID sensor at the reader contains a mixture of multiple parameters from various sources. Supposed the received signal at the sensor reader is represented by $V_r(f)$ in the frequency domain, it can be mathematically expressed as:

$$V_r(f) = M(f) + \sum_{i=1}^P w_i C_i(f) + O(f) + N(f) \quad (6.5)$$

where $M(f)$ is the mutual coupling between the transmitter and the receiver antennas. In the case of cross-polarization reading, $M(f)$ is equivalent to polarization leakage or self-interference between the transmitter and the receiver antennas [283]. $C_i(f)$ is the backscattered response of the chipless RFID sensor, which is contributed from i number of parameters including the inherent frequency selective behavior of the sensor, defect properties, and other unknown parameters. The defect properties may include different parameters of crack or corrosion, e.g., corrosion thickness, permittivity, surface roughness. P denotes the number of parameters that affect $C_i(f)$ while w_i is a mixing weight. The weighting w_i indicates that some parameters may be dominating or less contributing to $C(f)$ than the others. $O(f)$ represents the influence of nearby objects including the effect of nearby metallic structures or samples that

can affect the characteristics of the reader antennas. $N(f)$ refers to measurement noise, such as noise from the internal circuitry of the reader and from the environment.

PCA can be applied to extract the dominant features to estimate the major contributing parameters in the signals [252]. Since the chipless RFID sensor system operates in broadband, the received signal $V_r(f)$ at the reader contains multi-frequency variables and thus can be treated as multivariate data. The reader collects the sensor frequency signatures from M measurements of distinct defect samples and N frequency points. All measurement data is concatenated in order so that the dataset can be organized as $M \times N$ matrix as a dataset \mathbf{X} . Then, PCA is applied to the dataset \mathbf{X} through *data standardization, principal components (PCs) decomposition, feature reduction, and projection* [253]. For data standardization, the dataset \mathbf{X} is normalized to have zero mean and unity variance. The mean of dataset \mathbf{X} is calculated by

$$\bar{X} = \frac{1}{M} \sum_{m=1}^M X_m \quad (6.6)$$

where X_m is the N -dimensional vector of the m -th measurement. The data standardization is done by subtracting the data with the mean as

$$A = [(X_1 - \bar{X}), (X_2 - \bar{X}), \dots, (X_m - \bar{X})]. \quad (6.7)$$

The principal components (PCs) decomposition is performed by calculating eigenvectors-eigenvalues of the covariance matrix. The covariance matrix can be computed as

$$C = \frac{1}{M} \sum_{m=1}^M [(X_m - \bar{X}) \cdot (X_m - \bar{X})^T] = \frac{1}{M} A \cdot A^T. \quad (6.8)$$

Since the data has N dimensions due to the number of frequency points, the covariance matrix will be $N \times N$. The covariance matrix is decomposed to retrieve a matrix of eigenvectors, which is a set of principal components (PCs) by

$$e_i = A\lambda_i \quad (6.9)$$

Once the eigenvectors are obtained, they are sorted by the eigenvalues in descending order. The first few eigenvectors or k principal components (PCs), i.e., PC_1 to PC_k , are selected as PC features to analyze the major contributed parameters in the dataset. The low-rank principal components are less significant contributing factors and can be ignored. Finally, the original dataset \mathbf{X} is projected to the selected first few PCs by applying dot product multiplication to the selected PC features. The trend of projected values for each PC is observed, and a few of which should represent changes related to the physical condition of the defect samples. In other words, the projection of the original dataset \mathbf{X} onto the PCA feature subspaces extracts the dominant

variances within the measurement data. Since the variability in the data is most likely related to physical parameters, projection to several PC features can help one to evaluate the defects. The projected values to PC features that are noticeably related to defect parameters are then selected for characterization, while the many unrelated ones are ignored. By extracting multiple features, PCA is not only useful in estimating the multi-parameter properties of the defect but also powerful in mitigating unwanted influences from objects and noise.

6.2 Design of Multi-resonance Chipless RFID Sensor Based on RF Encoding Particles

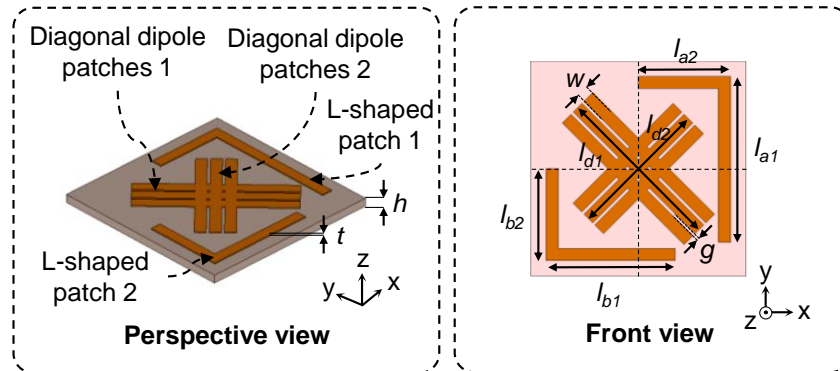


Figure 6.3 Geometry of the multi-resonance chipless RFID sensor.

Table 6.2 Dimensions of the multi-resonance chipless RFID sensor (in mm).

g	h	l_{a1}	l_{a2}	l_{b1}	l_{b2}	l_{d1}	l_{d2}	t	w
0.5	1.52	27	15	21	15	28	23	0.035	2

The design composition of the multi-resonance chipless RFID sensor in this study is inspired by depolarizing RF encoding particles [247]. Diagonal dipole and L-shaped resonators have been studied as two elementary shapes to implement depolarizing chipless RFID tags. In this study, the diagonal dipole and L-shaped resonator were combined in a compact design to form a multi-resonance sensor for defect sensing. The geometry and dimensions of the proposed sensor are presented in Figure 6.3 and Table 6.2, respectively. The sensor has an overall size of 35 mm \times 35 mm. It comprises of crossed two sets of diagonal dipole patches and two L-shaped patches with different lengths. Two sets of three parallel diagonal dipole patches were placed with the orientations orthogonal to each other. The two L-shaped patches were located on the edge sides of dipole patches. The sensor was designed using Rogers RO-3035 laminate with a substrate thickness of 1.52 mm, the dielectric constant of 3.5, and the loss tangent of 0.0015. In comparison to the sensor designs in Chapters 4 and 5, this chipless RFID sensor was designed to generate a higher number of resonances. While the CMPA (design in Chapter 4) and gammadion shape FSS (design in Chapter 5) generates one and three resonances, respectively, the RF encoding particles-based design in this chapter generates six resonances for sensing.

The selection of the dielectric constant, loss tangent, and thickness of the substrate in the sensor design was mainly based on the aim to maximize the RCS magnitude of the resonances. High RCS magnitude at the resonances ensures the sensor to be readable by the reader. According to the read range equation [204], the received power in the reader is directly proportional to the RCS. Substrates with a low dielectric constant tend to force the size of patches large and thus result in high RCS at its resonances [284]. Additionally, the substrate must be sufficiently thick to get high RCS at the resonances because patches on a thin substrate will have limited resonant cavities and cannot generate high-magnitude resonances. Meanwhile, the arrangement and length of the patches were tuned carefully to produce multiple resonances at distinct frequencies with adequate bandwidth separations between the resonances.

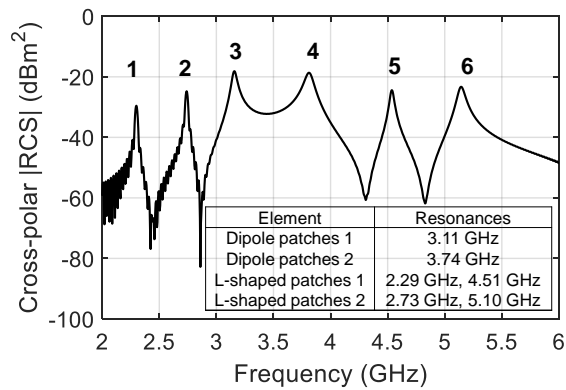


Figure 6.4 Simulated cross-polar RCS spectrum of the multi-resonance chipless RFID sensor placed on metal.

In the simulation, the RCS probe was set to the orientation that is orthogonal to the polarization of the plane wave excitation. The simulated RCS of the multi-resonance chipless RFID sensor is shown in Figure 6.4. The sensor generates six resonances within 2 to 6 GHz; the resonance peaks are at 2.29 GHz, 2.73 GHz, 3.11 GHz, 3.74 GHz, 4.51 GHz, and 5.1 GHz. ID encoding function is disregarded in this sensor as all the generated resonances are intended for defect sensing. To further explain how the sensor generates the six resonances, surface current distributions at the resonant frequencies are depicted in Figure 6.5. It can be seen in Figure 6.5 (a) and (b) that the first two resonances at 2.29 GHz and 2.73 GHz are generated by the L-shaped patches. The resonances occur conforming to the total length of the L-shaped patches, in which the longer L-shaped patch, i.e., L-shaped patch 1, contributes to the lower resonance frequency than the shorter one. The crossed diagonal dipole patches can be associated with the two resonances at 3.11 GHz and 3.74 GHz, as exposed in Figure 6.5 (c) and (d). The last two resonances at 4.51 GHz and 5.1 GHz are harmonics generated by the L-shaped patches. Since the L-shaped patches are electrically long, higher modes occur due to the partial section of the

patches. It is therefore understood that all six resonances are the product of patches and resulting in surface current distributions on the backing metal slab.

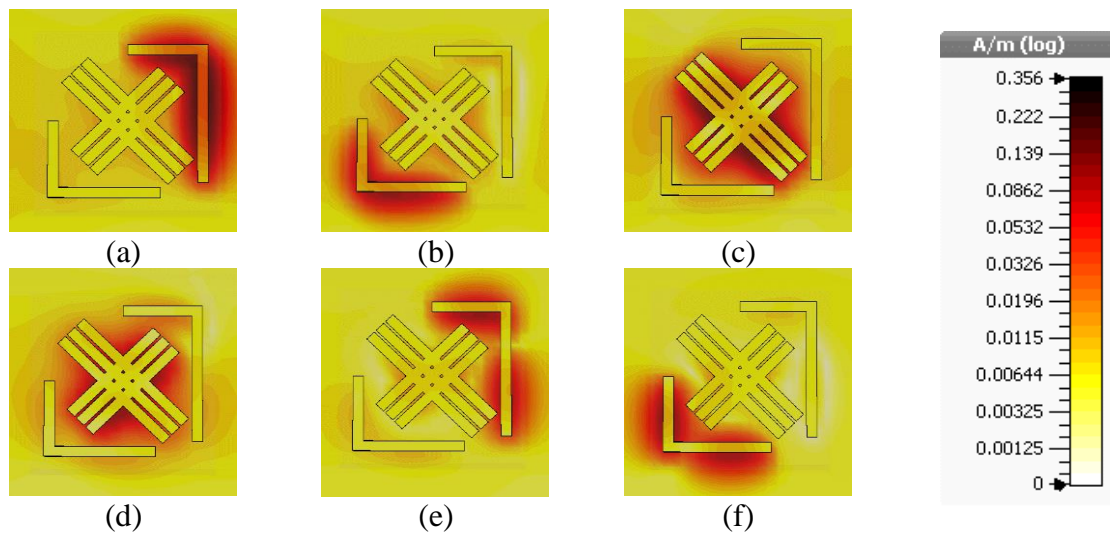


Figure 6.5 Simulated surface current distributions of the multi-resonance chipless RFID sensor showing the concentration of currents on the backing metal slab formed by the diagonal dipole and L-shaped patches: (a) at 2.29 GHz. (b) at 2.73 GHz. (c) at 3.11 GHz. (d) at 3.74 GHz. (e) at 4.51 GHz. (f) at 5.1 GHz.

6.3 Simulation Studies of Multi-resonance Chipless RFID Sensor for Crack and Corrosion Characterization

This section presents simulation studies to examine the multi-resonance chipless RFID sensor for crack and corrosion characterization. The simulation setup was similar to those explained in Chapter 4 and Chapter 5. First, the multi-resonance sensor was simulated against different crack orientations and widths to investigate the behavior of the resonances. Then, the sensor was simulated for different corrosion rust thicknesses to investigate its capability to characterize corrosion progression. Next, the effects of design parameters, i.e., substrate thickness and patch width, to RCS and sensitivity, will also be discussed in this section.

6.3.1 Simulation Study of Crack Characterization

In the simulation, a parametric sweep was performed for cracks with four different orientations and widths. The orientation of the crack was varied with 0° , 45° , 90° , and 135° , while the crack width was varied from 0 mm to 3 mm. The simulated cross-polar RCS spectra for different parameters of crack are exhibited in Figure 6.6. It can be noticed that the crack will shift the resonances towards different directions depending on the crack orientation. Some resonances shift towards the lower frequencies, while the others shift towards higher frequencies. Unlike the other crack orientations, the 135° crack in Figure 6.6(d) only affects resonances 3 and 4 because the 135° crack does not pass on the back of the L-shaped patches that contribute to resonances 1, 2, 5, and 6. It is indeed tedious to describe all the behavior of the resonances

against the crack orientation. The critical point here is that, due to different shift directions of the six available resonances, it is possible to use them as features to classify crack orientation and crack width. Moreover, the resonance frequency shifts are generally proportional to the crack width, making it possible to quantify the crack. The sensitivity to crack is up to 54 MHz/mm for 135° that shifts the resonance 4, as shown in Figure 6.6(d). With multiple resonances, it can be expected that crack will induce resonance frequency shifts and signal variations at many frequencies.

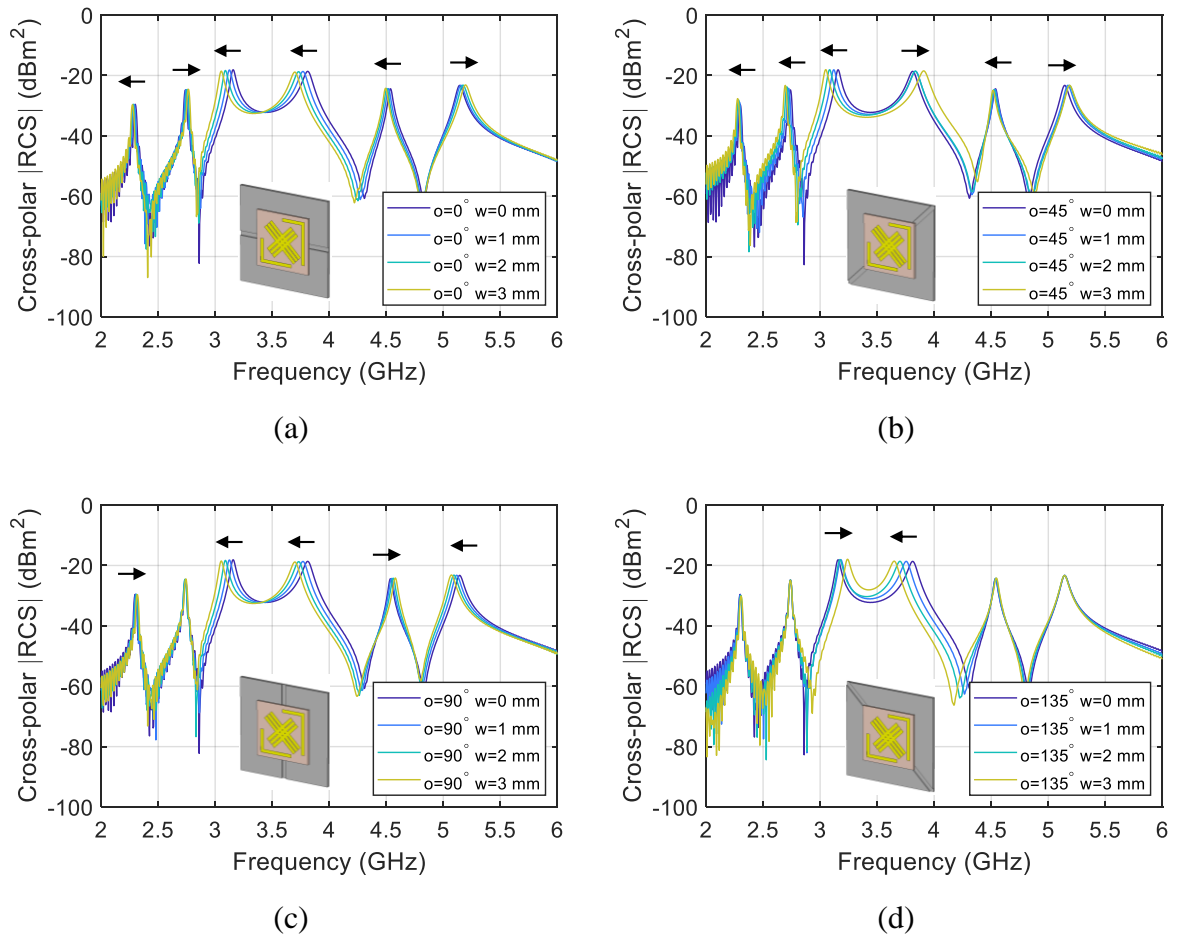


Figure 6.6 Simulated cross-polar RCS of the multi-resonance chipless RFID sensor for different crack orientations and crack widths (o = orientation, w = width): (a) 0° crack orientation. (b) 45° crack orientation. (c) 90° crack orientation. (d) 135° crack orientation.

6.3.2 Simulation Study of Corrosion Characterization

The simulation study for corrosion characterization applied the simulation setup introduced in Chapter 5. Dielectric layers representing corrosion rust and coating layer were presented between steel and the multi-resonance chipless RFID sensor. Then, a parametric sweep was performed by varying the corrosion thickness from 0 to 200 μm with a 40 μm step. The simulated cross-polar RCS spectra for different corrosion thicknesses are presented in Figure 6.7. It is obvious that the increase in corrosion thickness shifts all resonances towards the lower

frequencies. The greatest resonance frequency shift is achieved by resonance 4 with a sensitivity of 0.58 MHz/ μm . This simulation study indicates that the multi-resonance chipless RFID sensor can be used to characterize corrosion progression. Moreover, all six resonances are affected by corrosion thickness changes, and thus the sensor can be expected to be highly sensitive to corrosion progression.

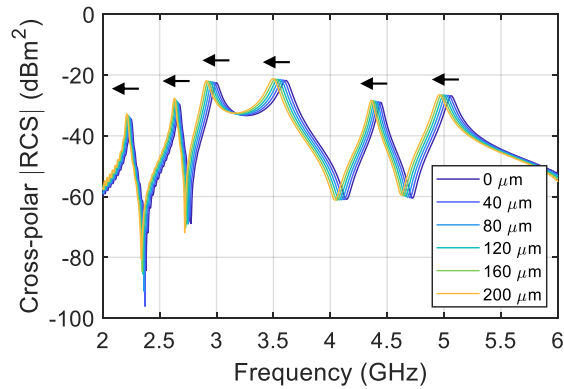
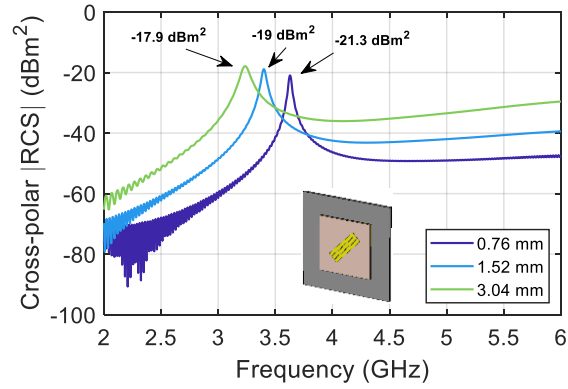


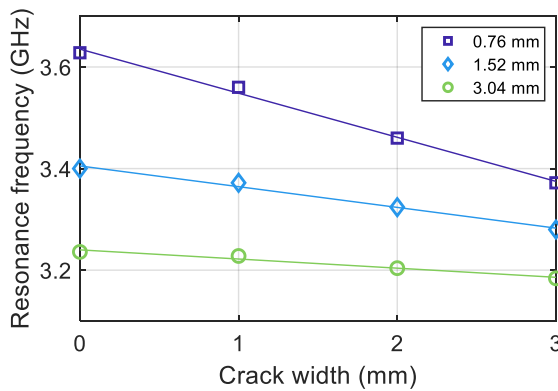
Figure 6.7 Simulated cross-polar RCS of the multi-resonance chipless RFID sensor showing that all six resonances shifted to lower frequencies with the increase of corrosion thickness.

6.3.3 Effects of Substrate Thickness on RCS and Sensitivity

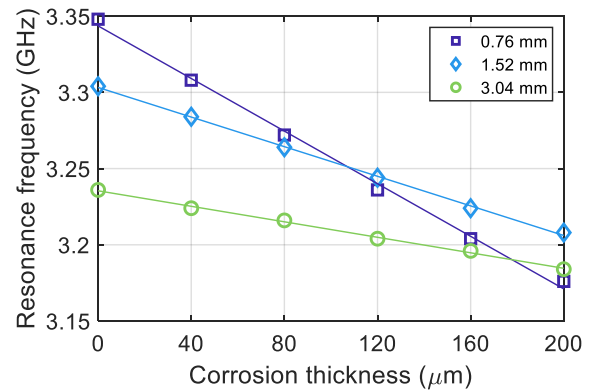
The effects of substrate thickness were studied against the RCS magnitude and the sensor's sensitivity to crack and corrosion. In order to simplify the simulation study, not the full design of the sensor was simulated, but only with diagonal dipole patches of the same lengths as representative resonant elements. As a representation of RF encoding particles used in the design, the diagonal dipole patches that generate resonance 4 were simulated for different substrate thicknesses. There are three collateral dipole patches with a 23-mm length and 2-mm width each, separated by a 0.5-mm gap. As seen in Figure 6.8(a), thickening the substrate leads to a prominent resonance, while reducing the thickness into half degrades the RCS magnitude of the resonance. The simulation results regarding the sensitivity to crack and corrosion are shown in Figure 6.8(a) and (b), respectively. For both sensitivities to crack and corrosion, the thinner substrate owns the highest sensitivities denoted by the step changes against the increase of crack width and corrosion thickness. However, the degradation of RCS of the resonances makes the thin substrate undesirable.



(a)



(b)

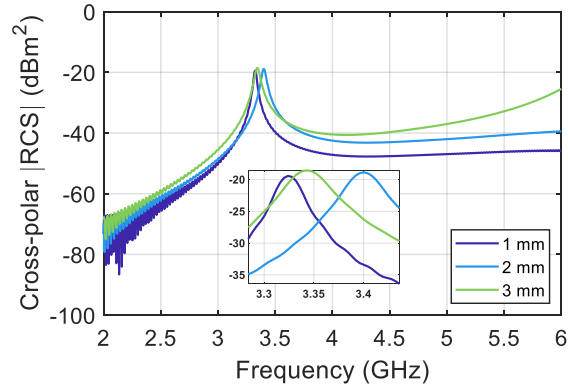


(c)

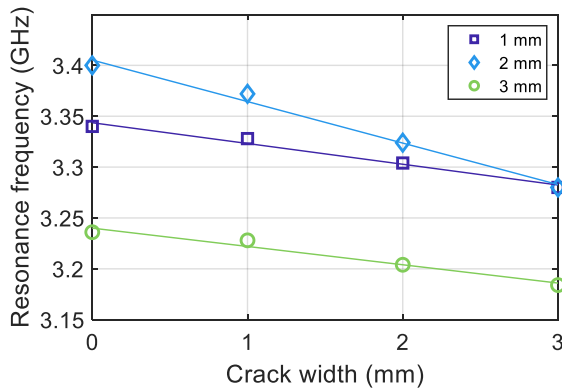
Figure 6.8 Effect of substrate thickness on: (a) RCS. (b) Sensitivity to crack. (b) Sensitivity to corrosion. Instead of using the full design with six resonances, the simulations were performed with diagonal dipole patches of the same length as representative resonant elements for the chipless RFID sensor.

6.3.4 Effects of Patch Width on RCS and Sensitivity

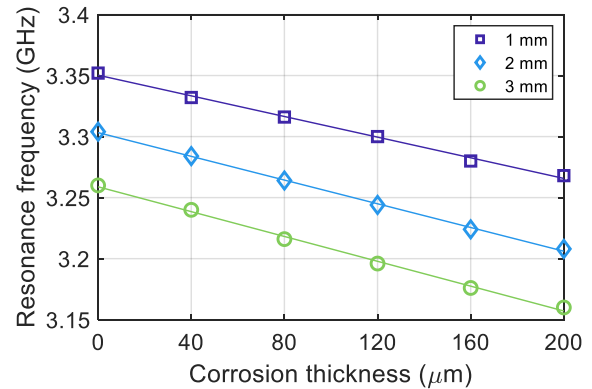
A parametric sweep with patch widths of 1 mm, 2 mm, and 3 mm was attempted to study its effects on the sensor's RCS and sensitivity. The gap between dipole patches was fixed to 0.5 mm, and the substrate thickness was fixed to 1.52 mm. As can be seen in Figure 6.9(a), the effect of patch width on the RCS of resonance is insignificant. The wider patches result in a slightly higher resonance than the narrower patches. Similarly, the sensitivity is not much affected by the patch width. With a 2-mm patch width, the sensitivity to crack is slightly higher than applying a 1-mm patch width (Figure 6.9(b)). However, increasing the patch width to 3 mm does not indicate any significant change to sensitivity and occupy a larger surface area. Moreover, changing the patch width does not affect the sensitivity to corrosion (Figure 6.9(c)). Therefore, the patch width of 2 mm was chosen in the design, taking into account of RCS level of the resonance, sensitivity to crack, and sensor size.



(a)



(b)



(c)

Figure 6.9 Effect of patch width on: (a) RCS. (b) Sensitivity to crack, showing that 2-mm patch width results in an optimum sensitivity. (c) Sensitivity to corrosion, showing that the patch width does not affect the sensitivity.

6.4 Experimental Studies and Results

Experimental studies were undertaken to examine the multi-resonance chipless RFID sensor, the portable reader, and feature extraction using PCA. The proposed multi-resonance chipless RFID sensor was manufactured using a Rogers RO-3035 laminate through the photochemical etching method elaborated in Chapter 4 Section 4.4. Man-made crack samples and corrosion samples were prepared, as shown in Figure 6.10 and Figure 6.11, respectively. Crack samples with four different orientations, i.e., 0° , 45° , 90° , and 135° , and three different widths, i.e., 1 mm, 2 mm, and 3 mm, were used. There were 13 different crack samples in total, including the healthy sample without crack. The crack depth is the same for all samples, i.e., 1 mm. The experimental study using crack samples was attempted to prove the ability of the multi-resonance sensor and PCA in characterizing multi-parameter defects. Corrosion samples were the corrosion undercoating samples with different exposure periods, i.e., from no corrosion (M0) to 12 months (M12), as used in Chapter 5.

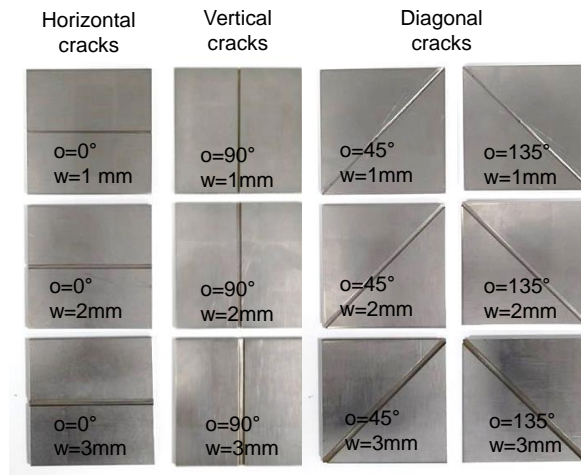


Figure 6.10 Man-made crack samples with three different widths and four different orientations.

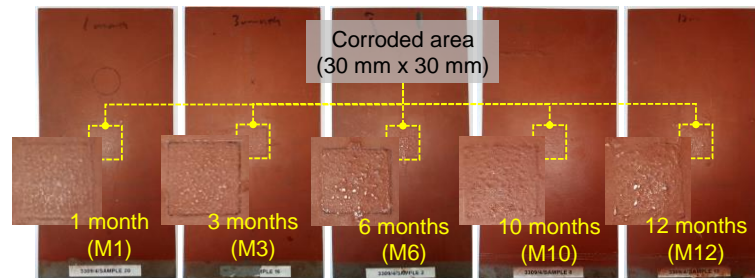


Figure 6.11 Corrosion undercoating samples with different exposure periods to a marine atmosphere.

The experimental setup is illustrated in Figure 6.12. The fabricated multi-resonance chipless RFID sensor was mounted on the crack or corrosion sample. The portable reader was placed 15 cm away from the sensor and sample, and it was connected to a computer for signal collection. The reader was programmed to record a hundred repeated measurements of received signals from the multi-resonance chipless RFID sensor. With 13 crack samples and a hundred measurements for each sample, 1300 signals were collected as a dataset. The experiment with corrosion samples was conducted with repeated experiments for the corrosion samples oriented horizontally and vertically. Nevertheless, the corrosion progression should be independent of the sample orientation, and the resulting corrosion progression is predictably the same for different sample orientations. Therefore, measuring the corrosion samples with different sample orientations is useful for validating the characterization results. Since the portable reader recorded a hundred received signals for each sample, there were 1200 signals in total collected from 6 corrosion samples and two different sample orientations.

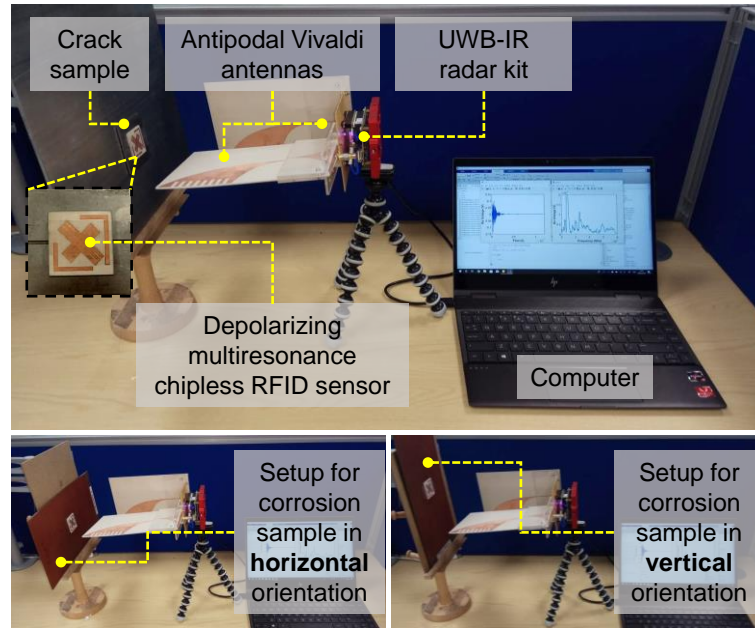


Figure 6.12 Experimental setup of a chipless RFID sensor system for characterization of crack and corrosion. Experiments for corrosion were repeated for different orientations corrosion samples.

6.4.1 Experimental Study Using the Crack Samples

The signature of the multi-resonance chipless RFID sensor, when attached to different crack samples, are exhibited in Figure 6.13. The sensor signature can be noticed by the presence of resonance peaks at the six frequencies denoted in Figure 6.4. The resonances 2, 5, and 6 from the measurements are less clear and noisy; thus, the positions are hard to determine precisely. The signals in Figure 6.13 are grouped based on crack orientations, and each graph shows the impact of different crack widths. Apparently, variations due to the crack are mostly seen at resonance 3 and 4. By careful observation, it can be noticed that different crack orientations and widths shift the resonance 3 and 4 in different directions. For 0° cracks (see Figure 6.13(a)), both resonance 3 and 4 shift to lower frequencies as the crack width increases. For 45° cracks (see Figure 6.13(b)), resonance 3 shifts to lower frequencies while resonance 4 shifts to higher frequencies with the increase of crack width. Next, for 90° cracks (see Figure 6.13(c)), both resonances 3 and 4 shift to lower frequencies as for 0° cracks, but in 90° crack orientation, resonance 1 and 5 shift to higher frequencies. For 135° cracks (see Figure 6.13(c)), resonance 3 and 4 are approaching each other as the crack width increases.

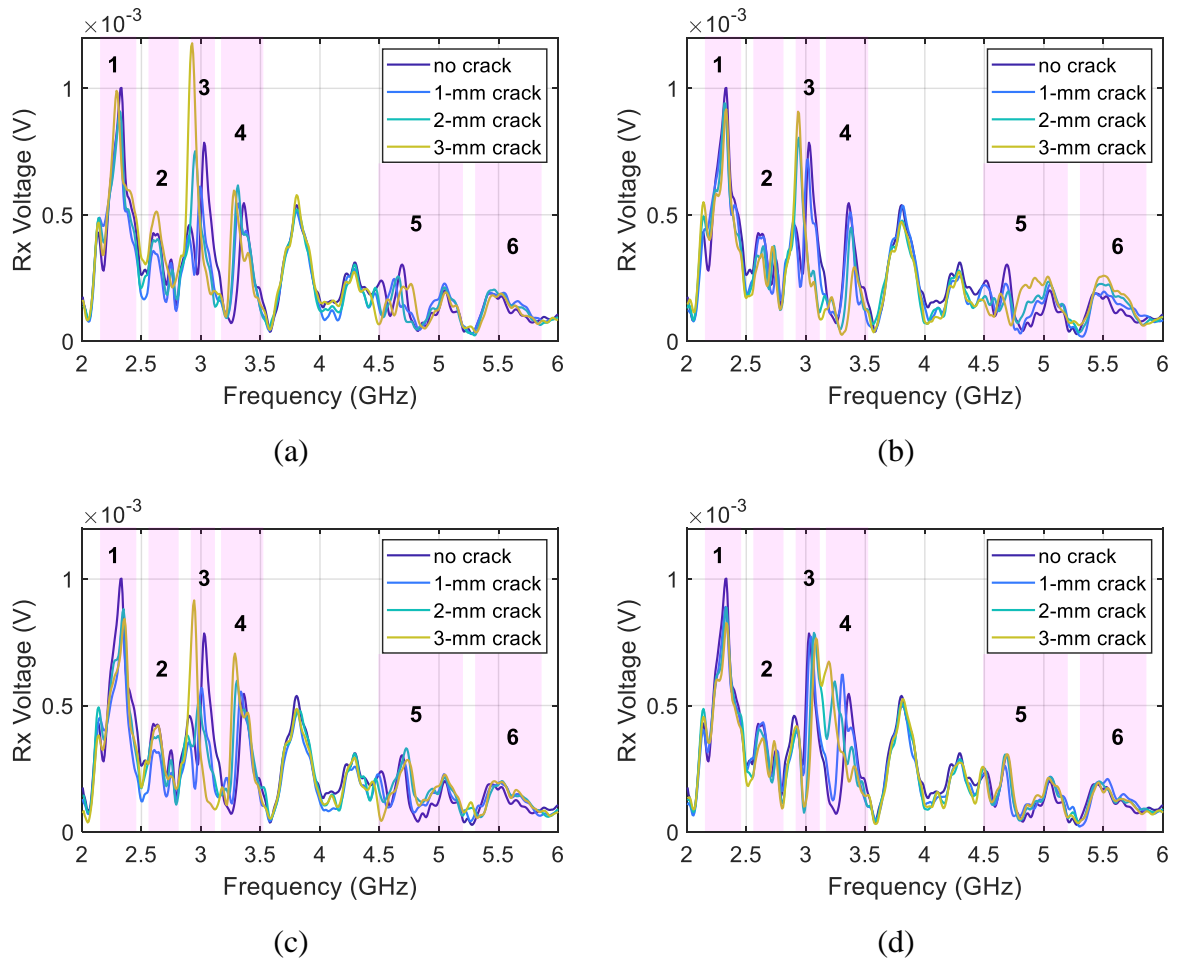


Figure 6.13 The measured received signals after pre-processing from the multi-resonance chipless RFID sensor mounted on crack samples with different crack orientations and crack widths: (a) 0° crack orientation. (b) 45° crack orientation. (c) 90° crack orientation. (d) 135° crack orientation. The signals were taken without calibration (background subtraction). The pink boxes with numbers mean to highlight the resonances generated by the chipless RFID sensor.

Resonance frequencies or resonance peak locations indeed can be used to characterize crack orientation and widths. In this case, however, the detection of multiple peaks is troublesome due to the different characteristics of the peaks and noisy data. It is noticeable from Figure 6.13 that the signals contain peaks with non-uniform characteristics, i.e., peak height, peak width, and peak prominence. Resonance 3 and 4 are high in amplitude since the dipole patches, which generate these resonances, are relatively large and at the center of the tag. The resonances 3 and 4 due to dipole patches are higher than those generated by L-shaped patches. Conversely, resonances 5 and 6 have low amplitudes, and thus the resonance peaks and the shifts are hard to observe. This can be attributed to the lower PSD of the transmitted power at above 4 GHz and the low RCS peaks for the resonances 5 and 6. Still, the shifts of resonance 5 and 6 are noticeable for 45° cracks (see Figure 6.13(b)). Furthermore, there are peaks that unrelated to the resonances of the sensor, such as the peak at around 3.8 GHz. As the peak at 3.8 GHz exists throughout all measurements and unaffected by defect, it is likely originated from the leakage

between transmitter and receiver antennas. Meanwhile, the other unexpected peaks come from multiple sources and contribute to some variations in the data. With such kind of signal data, therefore, PCA is required for robust feature extraction.

All measurements from different crack samples were arranged as a dataset for feature extraction using PCA. Since there were 13 crack samples measured a hundred times each and 480 frequency points, the dataset matrix dimension was 1300×480 . As explained in Section 6.1.3, the process of PCA consists of data standardization, principal components (PCs) decomposition, feature reduction, and projection of data to the selected PC features. The process of PCA is illustrated as a block diagram in Figure 6.14 A block diagram illustrating the process of principal component analysis (PCA). In Matlab, the process from data standardization to PCs decomposition is represented by a single function, i.e., the “pca” function. For a dataset \mathbf{X} , the PCs and other properties can be obtained by command “[coeff,score,latent,tsquared,explained,mu] = pca(X)” [285]. PC coefficients are stored in “coeff”, while the percentage variance explained by each PC can be seen in the vector in “explained”. The original dataset is then projected to first PCs by using the dot product. For analysis, the projected values can be plotted and observed against the defect parameters.

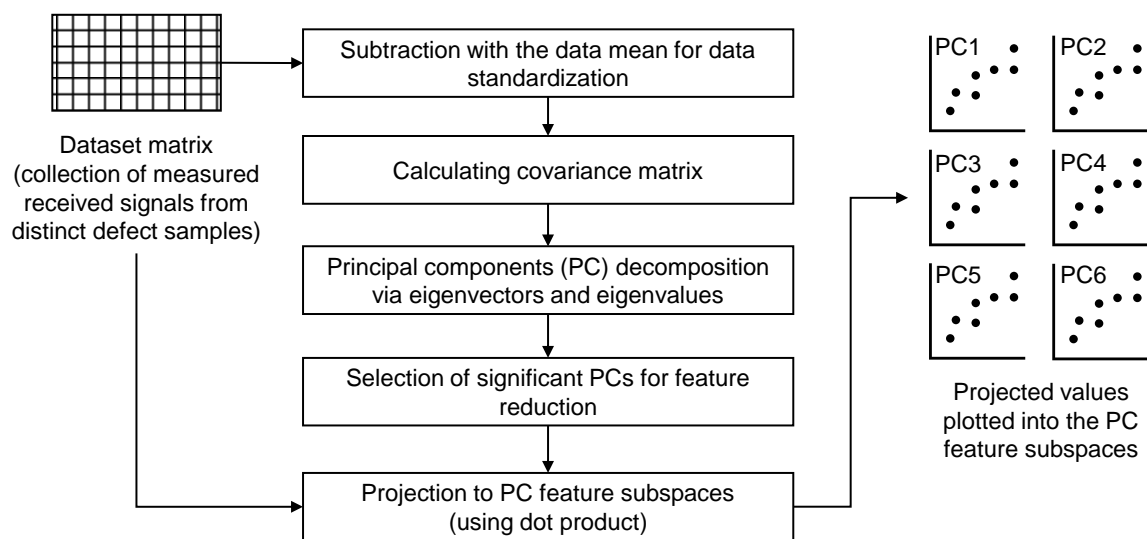


Figure 6.14 A block diagram illustrating the process of principal component analysis (PCA) after collecting the measured signals.

After applying PCA, it was found that 91.8% of the variance in the dataset is in the first six PCs. Figure 6.15 presents the six PCA features plotted according to crack width and crack orientation. The plotted PC values are the average projection value, while the error bars show the maximum and minimum from a hundred times measurements for every sample. Firstly, it can be noticed that the PC1 feature, as shown in Figure 6.15(a), has a strong relationship with crack width. For 0° cracks, 45° cracks, and 90° cracks, the projection value to PC1 increased

linearly against the increasing crack width. For 135° cracks, however, the PC1 decreased monotonically as the crack width increased. Therefore, the PC1 feature can be used to evaluate the crack width of 0° cracks, 45° cracks, and 90° cracks based on the increasing PC1 value. The sensitivity of PC1 to the crack width is $0.696 \times 10^{-3} \text{V/mm}$. Also, PC1 can be used to uniquely indicate 135° cracks and the width using the decreasing value of PC1. Secondly, PC5 was found to be a feature that can indicate the crack orientation. PC5 values for the cracks that have the same orientation were relatively invariant to the crack width. Even though 45° cracks and 135° cracks had only small differences and thus hardly distinguishable using PC5, they were distinguishable using PC1. Hence, PC1 and PC5 features can be applied for the characterization of cracks with different orientation and width.

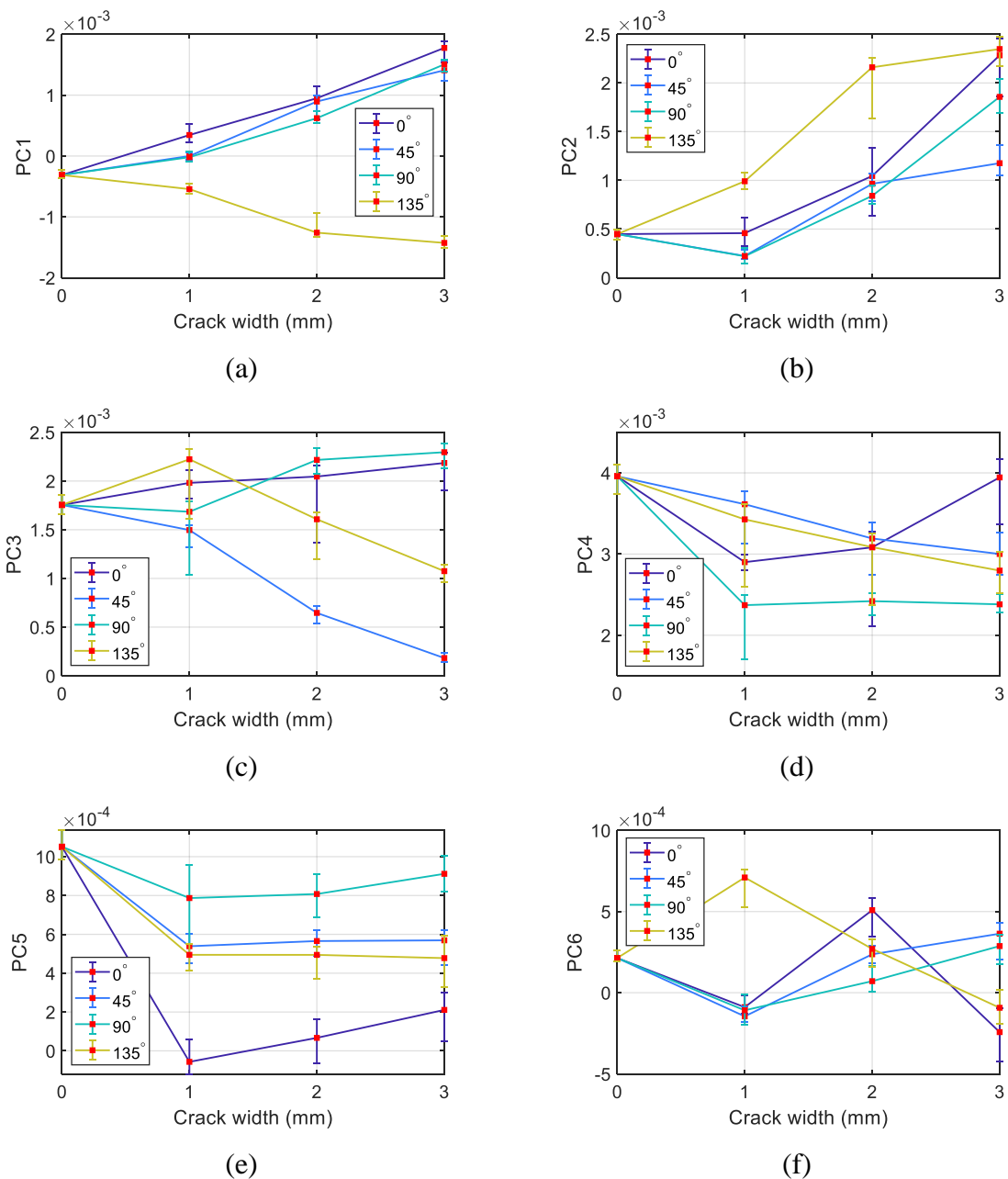


Figure 6.15 PCA features for different crack samples: (a) PC1. (b) PC2. (c) PC3. (d) PC4. (e) PC5. (f) PC6.

6.4.2 Experimental Study Using the Corrosion Samples

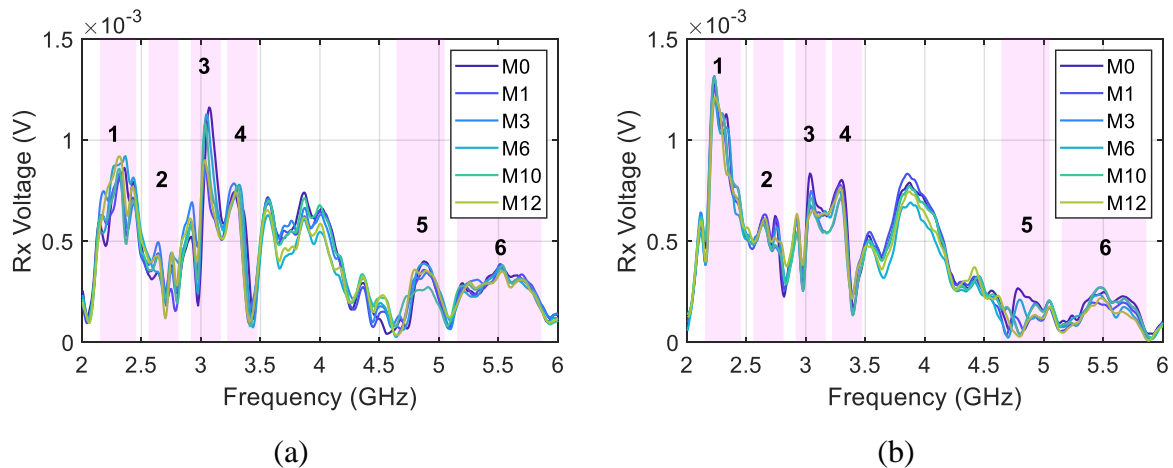


Figure 6.16 The measured received signals after pre-processing from the multi-resonance chipless RFID sensor mounted on different corrosion progression samples: (a) with the samples oriented horizontally. (b) with the samples oriented vertically. The signals were taken without calibration (background subtraction). The pink boxes with numbers mean to highlight the resonances generated by the chipless RFID sensor.

Figure 6.16 shows the pre-processed received signals from the multi-resonance chipless RFID sensor when mounted on different corrosion samples. The frequency signature of the sensor was noticeable with unexpected peaks and the fact that resonance 2, 5, and 6 were not as obvious as resonance 3 and 4. Changing the orientation of corrosion samples in the measurements (compare Figure 6.16 (a) and (b)) did not significantly alter the resonance peak positions but modified the amplitudes. The amplitude changes can be attributed to the different effects of the sample orientation to the transmitting and the receiving antennas. In addition, variations in the sensor signature due to the different corrosion samples were evident. Amplitudes at most frequencies were affected by the change of the corrosion sample. Resonance shifts can be observed for resonance 3 in Figure 6.16(a). Resonance 3 shifted to lower frequencies with the increasing corrosion stage. The resonance shift at other resonances and frequencies are scarcely seen. It is, therefore, unwise to evaluate the corrosion stage by considering only single resonance shifts or amplitude changes at a specific frequency. PCA is required to extract the major contributing parameters in the entire signal.

After feature extraction using PCA, it was revealed that the sum of the percentage of variance contained in the first four PCs is higher than 91.9%. Thus, only PC1 to PC4 features were extracted, as shown in Figure 6.17. Interestingly, the trends of PC2 and PC4 features were independent of the orientation of corrosion samples. The similarity of the trend of PC2 and PC4 implies that these features may be more related to the corrosion rather than other parameters. Regardless of the sample orientation, the trend of the PC2 feature indicates the corrosion progression in accordance with the results in previous studies using microwave NDT [98],

[275], and UHF RFID [195], [196]. In the early stage, i.e., M0 to M6, the PC2 feature decreased with the increase of the corrosion stage. Derived from the PC2, the sensitivity to corrosion with horizontal and vertical orientations are 0.254×10^{-3} V/month and 0.152×10^{-3} V/month, respectively. In the later stage, however, the corrosion area tends to spread rather than to increase in thickness [275]. This causes an anomalous trend for M10 and M12 samples. The characterization results in this study agree well with the results in Chapter 5 and the results using other methods using the same dedicated corrosion samples. Furthermore, the work demonstrates the robustness of the chipless RFID sensor system for crack and corrosion characterization.

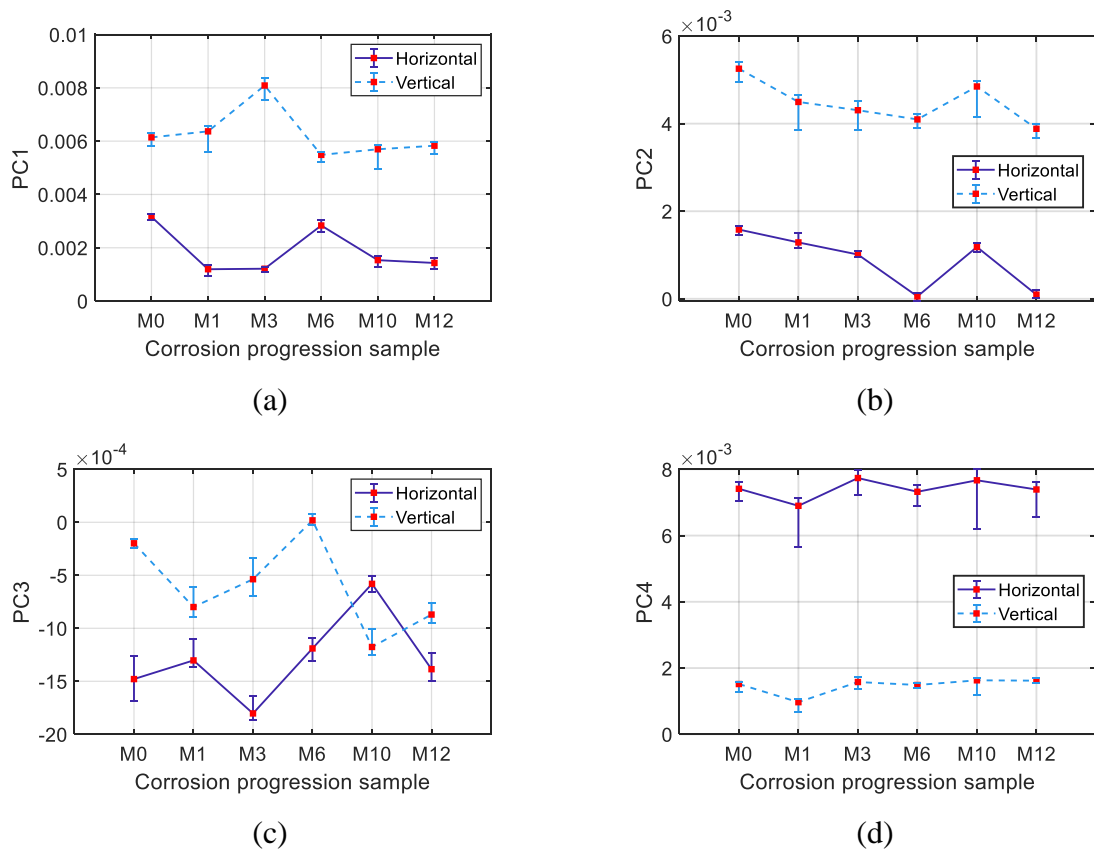


Figure 6.17 PCA features from different coated corrosion samples and different sample orientations: (a) PC1. (b) PC2. (c) PC3. (d) PC4.

6.5 Discussions

This section provides further discussions related to the multi-resonance chipless RFID sensor, portable reader, and PCA. Although they demonstrate a practical and robust chipless RFID system, their applications still pose challenges. The multi-resonance chipless RFID sensor can enrich the sensing information conveyed to the reader. However, having all resonances to be prominent in the received signal is an uneasy design task. Since the sensor size is limited, it is challenging to make all resonances have high RCS magnitudes. Also, when the PSD of the transmitted signal is low at particular frequency ranges, the resonances at those ranges can be

attenuated in the received signal. RCS at the resonances should be designed high so that the resonances, even if without background calibration, can predominate among other non-informative variations in the received signal. RCS synthesis for the design of chipless RFID tags and the inverse problem of electromagnetic signature is discussed in [202].

Regarding the chipless RFID sensor reader, this work shows the potential of using a portable reader instead of using the VNA and bulky antennas. The UWB radar module is operated in the time domain and used to read a frequency domain sensor. It provides a fast reading speed and is compatible with UWB regulations, but it is expensive and sensitive to changes in the setup [286]. In this study, the experimental setup must be fixed, and the read range is limited to 15 cm. The reading distance of 15 cm is the distance at which the multiple resonance peaks are mostly observable. The resonance peaks are less clear and unobtainable when the reader is placed farther than 15 cm or too close to the sample. When the distance between the reader and sensor is longer than 15 cm, the resonance peaks diminish because of the low transmitted power from the radar module. On the other hand, when the distance is too close, the resonance peaks are profoundly affected by interactions between the metal sample and the reader antennas. Although the distance is constrained, it is relatively sufficient for practical applications since the characterization of defects is feasible. Other portable readers, such as frequency domain readers, could be considered for a low-cost alternative and comparison [287], [288].

The feature extraction using PCA takes into account the entire amplitude variations in a signal. It extracts dominant information contained in the signal. That is to say, PCA is only applicable under certain circumstances when the variations in the signal are dominantly caused by the defect, not due to the different measurement scenarios. For instance, when the reader and the sensor positions are not fixed, the variations due to the distance and misalignment may be dominant. In such a case, PCA may not find the important patterns caused by the defect. Furthermore, the repeatability of PCA is a concern since the resulting PCs and their projected values depend on the collected dataset. In this work, dedicated samples with known defects were used to simplify the validation. Repeating the measurement with different sets of samples or scenarios will result in different PCs and projections, which need different interpretations. While PCA is useful for data exploration and evaluation, its application for real-time monitoring would require further investigations.

6.6 Chapter Summary

This chapter has demonstrated robust detection and characterization of defects in a realistic environment using a multi-resonance chipless RFID sensor, portable reader, and feature extraction and selection using PCA. The multi-resonance chipless RFID sensor is composed of

depolarizing RF encoding particles, including dipole patches and L-shaped patches, making it robust and generates six resonances for sensing. In the sensor design, the substrate thickness was carefully selected to have adequately high resonance magnitudes and reasonable sensitivity. In comparison to the CMPA-based and FSS-based designs in Chapter 4 and Chapter 5, respectively, the chipless RFID sensor proposed in this chapter has an increased number of resonances. The CMPA and gammadion shape FSS generate one and three resonances, while the REP-based design in this chapter generates six resonances. By having multiple resonances, the sensor signature becomes rich in sensing information, sensitive, and able to sense multiple parameters. The portable reader was implemented using an FCC compliant UWB radar transceiver with the requirement of signal pre-processing such as detrending, denoising using DWT, and signal transformation using FT. This work has shown that using the multi-resonance chipless RFID sensor and the selected PC features from PCA, multiple parameters of metal cracks, i.e., the crack orientation and crack width, can be characterized quantitatively. In another experimental study, PCA can be used to find a robust feature, i.e., PC2, that indicates the corrosion progression regardless of the sample orientation. The proposed sensor system is robust since the measurements were performed using a portable reader in a realistic environment without any calibration or background subtraction.

Chapter 7 Conclusions and Future Works

In this final chapter, conclusions are drawn to summarize the research findings and contributions from the chipless RFID sensor systems for SHM developed in this thesis. Limitations of the research and recommendations for future works are highlighted.

7.1 Conclusions

For SHM applications such as defect detection and characterization, RFID is an emerging technique and has attracted attention in recent years. State of the art surveys in chipped RFID tag antenna-based sensors and chipless RFID sensors have indicated that the application of chipless RFID in this field is still limited. This thesis has presented the design and development of novel chipless RFID sensors and systems for SHM operating at 2-6 GHz. Three novel metal-mountable chipless RFID sensors for crack and corrosion characterization have been demonstrated through simulation and experimental studies applying different reader configurations, feature extraction, selection, and fusion.

To recap briefly, Chapter 4 has demonstrated a chipless RFID sensor based on CMPA for crack detection and characterization. The sensor incorporates a 4-bit ID and is able to characterize the crack orientation and crack width simultaneously using the resonance frequency shift. The sensor has an overall size of $35 \text{ mm} \times 15 \text{ mm} \times 1.27 \text{ mm}$ and a sensitivity of 134.2 MHz/mm crack, thus able to detect crack with a sub-millimeter resolution. In Chapter 5, a chipless RFID sensor based on FSS has been presented along with feature fusion for corrosion characterization. Three resonances generated by the FSS shift to lower frequencies with the increase of corrosion thickness and thus can be used as features to indicate corrosion progression. Feature fusion of the multiple resonance frequency features using simple sum and CWA is found useful to enhance sensitivity and reliability. The sensor has an overall size of $30 \text{ mm} \times 30 \text{ mm} \times 1.52 \text{ mm}$ and a sensitivity of 17.6 MHz/month or $1.34 \text{ MHz}/\mu\text{m}$. Driven by the use of bulky VNA and the requirement of background calibration in Chapter 4 and Chapter 5, Chapter 6 addresses the robustness issue. In Chapter 6, the robust characterization of crack and corrosion in a realistic environment is demonstrated using a multi-resonance chipless RFID sensor, portable reader, and PCA. The sensor is designed based on RF encoding particles, which consist of depolarizing dipole and L-shaped patches. It has an overall size of $35 \text{ mm} \times 35 \text{ mm} \times 1.52 \text{ mm}$, and generates six resonances for sensing. The multi-resonance chipless RFID sensor, in conjunction with feature extraction and selection using PCA, can be used for multi-parameter evaluation of crack and finding a robust feature that indicates the corrosion progression.

Table 7.1 Comparisons of chipless RFID sensor systems and results in Chapters 4, 5, and 6

System elements	Parameter	Chapter 4	Chapter 5	Chapter 6
Chipless RFID sensor	Sensing variables	Crack (orientation and width)	Corrosion progression	Crack (orientation and width) and corrosion progression
	Design approach	Circular microstrip patch antenna (CMPA)	Frequency selective surface (FSS) with 2×2 gammadion-shaped unit cells	Multi-resonance RF encoding particles integrating dipole and L-shaped patches
	Sensor size	35 mm × 15 mm × 1.27 mm	30 mm × 30 mm × 1.52 mm	35 mm × 35 mm × 1.52 mm
	Operating frequency range	2-6 GHz	2-6 GHz	2-6 GHz
	Number of resonances for sensing	1	3	6
	Sensitivity	Simulation and experiment: 133.2 MHz/mm	From simulation: • 0.3 MHz/μm From experiments: • Without feature fusion: up to 0.81 MHz/μm • With feature fusion: 1.34 MHz/μm	From simulation (resonance frequency shift features): • Crack: 54 MHz/mm • Corrosion: 0.58 MHz/μm From experiment (PCA features): • Crack: 0.696×10 ⁻³ V/mm • Corrosion: 0.254×10 ⁻³ V/month
Reader	Reader platform	VNA	VNA	Portable reader (UWB radar)
	Reader antennas	Horn antennas	Dual-polarized Vivaldi antennas	Antipodal Vivaldi antennas
	Demonstrated reading distance	30 cm	15 cm	15 cm
Signal processing subsystem	Signal pre-processing	Calibration with the environment and a reference object for deriving RCS	Calibration with the environment	Detrending, denoising using discrete wavelet transform (DWT), and Fourier Transform (FT)
	Feature extraction, selection, and fusion	Resonance frequency shift feature	Multiple resonance frequency features and feature fusion	Feature extraction and selection using principal component analysis (PCA)
	Advantages	4-bit ID incorporated in the sensor; high sensitivity to crack; moderate reading distance	Enhanced sensitivity and reliability using feature fusion	No calibration and background subtraction; portable reader; multi-parameter evaluation
	Disadvantages	Bulky VNA and horn antennas; requirement of calibration with the environment and reference object	Bulky VNA; requirement of calibration with the environment; short reading distance	The reader must be at a fixed position; short reading distance; requirement of prior offline training for PCA feature extraction

Table 7.1 compares the chipless RFID sensor systems and results in Chapters 4, 5, and 6. The noticeable differences among the proposed chipless RFID sensors are in the design approaches and the number of resonances for sensing. It is increased from one resonance in Chapter 4, three resonances in Chapter 5, to six resonances in Chapter 6. Increasing the number of resonances in chipless RFID sensors allows for feature fusion to enhance the sensitivity and reliability as well as for multi-parameter evaluation. However, due to the limited bandwidth, increasing the number of resonances for sensing makes it challenging to incorporate sensor ID. The chipless RFID sensors in Chapters 5 and 6 do not have ID as in Chapter 4, but the sensitivity and reliability can be enhanced and can have multi-parameter sensing capability. The reader platform and antennas have been varied, attempting to demonstrate the systems from the proof-of-concept level in the anechoic chamber to more realistic scenarios. Also, the complexity of

calibration was reduced gradually from Chapter 4 to Chapter 6. As the reader becomes portable with the requirement for calibration eliminated in Chapter 6, not only that the reading distance remains a challenge but also, more signal processing is required. Like in Chapter 6, the discrete wavelet transform (DWT) and the Fourier Transform (FT) were necessary for pre-processing, while principal component analysis (PCA) was required to analyze multiple influences.

In terms of the sensor design and sensing mechanism, chipless RFID sensors for defect detection and characterization can benefit from combinations of resonant microstrip structures, such as patch antennas, FSS, and RF encoding particles. The chipless RFID sensor and the defected metal resemble the microstrip structure, which comprises resonant conductive patches on the top of a dielectric substrate placed on the defected metal acting as the ground plane. The sensitivity of chipless RFID sensors to defects can be expected because crack and corrosion can be treated as changes in the ground plane and the substrate thickness of a microstrip structure. Due to the adoption of microstrip structure and being operated in the microwave frequencies, chipless RFID sensors are small, low-profile, and highly sensitive to crack and corrosion compared to the chipped UHF RFID sensors. The sensitivity can be controlled mainly by adjusting the substrate thickness. However, a good compromise between sensitivity and prominence of the resonances should be considered. Increasing sensitivity by reducing substrate thickness degrades the prominence of the resonances, which potentially makes the sensor hardly readable. Furthermore, the substrate dielectric constant and patch size should be carefully selected in the design. Substrates with a high dielectric constant tend to make the sensor size electrically small but will reduce the echo area, which leads to less prominent resonances. The patch size, such as the width, should be optimally selected in simulation to obtain a proper sensitivity. Hence, it is crucial to aid the sensor design with simulation studies to examine the RCS and sensitivity.

A unique characteristic of chipless RFID sensors for SHM is the ability to occupy multiple resonances within a broad operating bandwidth. It can be achieved by combining multiple resonant patch structures with different resonant modes onto the sensor design. With the multi-resonance characteristic of chipless RFID sensors, it is possible to integrate ID and sensing functionalities, to enhance sensitivity and reliability, and to perform robust and multi-parameter analysis of defects. Intrinsically, a multi-resonance signal is rich in sensing information because multiple sensing features can be occupied in the signal. It is hard to achieve using the conventional chipped RFID tag antenna-based sensors because not only is the bandwidth limited, but also the antenna sensors are typically designed to match with the chip impedance and resonate at a single frequency. However, it should be considered that the multi-resonance

characteristic of chipless RFID sensors come with the cost of huge occupancy of the frequency spectrum.

On the reader configuration, the use of VNA, portable reader, and different antennas have been demonstrated in this thesis. VNA is ideal for laboratory purposes, but its bulky aspect makes it impractical for real applications. In this thesis, the portable reader is implemented using a UWB radar module and is evidently feasible for a 15-cm reading distance. Its operation in the time domain makes the signal acquisition fast, but it poses the need for additional signal pre-processing. The data resolution in the frequency domain is limited but can be maximized using the frame stitching. The transmitted power is minimal due to the UWB regulation; therefore, high gain reader antennas are desirable. Different high gain broadband unidirectional antennas, including horn antennas, Vivaldi antennas, and Antipodal Vivaldi antennas, have been employed in this thesis. The standard gain horn antennas are highly directive but bulky and heavy, thus impractical for real applications. In addition to high-gain, broadband, and unidirectional, Vivaldi antennas and antipodal Vivaldi antennas are light-weight and more compact. In this thesis, the Vivaldi antennas are configured for cross-polarization reading for robustness. In their designs, high isolation between the transmitter and receiver antennas are desirable to minimize polarization leakage. The reader antennas in this thesis have shown their efficacy to work as the front-ends for the chipless RFID sensor readers, but the compactness could be improved.

Regarding features for defect sensing, extractions of resonance frequency features and the PCA-based features have been applied in this thesis. Resonance frequency features can be extracted from either RCS or calibrated transmission coefficients. Since the mechanism of chipless RFID sensors is akin to antenna/resonant sensors, using resonance frequencies or their shifts as features are common and reasoned. This thesis has shown the efficacy of resonance frequency as well as multiple resonance frequency features to characterize defects. In case robustness is required, the statistical feature extraction using PCA can be an alternative feature extraction and selection method. When using a portable reader in a realistic environment, the backscattered signal data contains multiple peaks and is noisy. In such cases, the extraction of resonance frequency features is challenging. Despite the requirements of a large amount of data for training and interpretation for linking the features and physical parameters, PCA is proved effective in this thesis for the robust characterization of defects.

7.2 Limitations

A number of limitations in this research need to be acknowledged. First, the chipless RFID sensor systems demonstrated in this thesis require prior knowledge of the defect location and,

thus, more suitable for monitoring localized defects at safety-critical locations/components. Reading multiple chipless RFID sensors and defect localization remains a challenge. Second, the number bits for ID in a chipless RFID sensor is limited by the frequency bandwidth and the tag surface area. This research emphasizes the sensing functionality rather than the incorporation of ID for tagging. Third, the chipless RFID sensors fabricated in this thesis are made of PCB and can only be used on flat structures. Conformable sensors and integration of sensors to the structure need to be considered in the future. Fourth, the experimentations in this thesis were undertaken with dedicated samples, whereas real defects tend to occur naturally. Chipless RFID sensor systems for real-time SHM could be further investigated. For instance, chipless RFID sensor systems could be used for early detection of strain and structural deformation before crack, as well as early detections of water ingress and humidity before the occurrence of corrosion. Fifth, chipless RFID sensor systems are sensitive to the wireless channel and environmental conditions. In this thesis, the reader position is always fixed, as the wireless channel may cause resonance frequency shifts and signal variations much more than the defect does. The mobility of the reader, changes in the reading distance, misalignment between the reader and sensor, multipath effects can greatly affect the sensing performance. Careful calibration with the environmental background needs to be performed to overcome these challenges. Sixth, the reading distance of the chipless RFID sensor systems may be limited for real applications. From the sensor side, it is a dilemmatic issue as the RCS of a chipless RFID sensor depends on the sensor size. On the one hand, the sensor size needs to be no larger than the defect to be sensitive, as the size of defects is usually tiny. On the other hand, the resonances generated by chipless RFID sensors should be prominent to be readable by the reader, which imposes the sensor size to have a sufficiently large echo area. Many other factors also contribute to the limited reading distance, such as power level restriction, polarization mismatch, and gain of the reader antennas.

7.3 Recommendations for Future Works

The proposed chipless RFID sensor systems have demonstrated the possibilities of using planar resonant structures, such as antennas, FSS, and other RF scatterers, for defect sensing and monitoring. Although the capability of the sensor systems has been validated, there are still significant problems and challenges to solve. Future works can be associated with the integration of sensor array into structures, defect localization, real-time and area monitoring, improvement of RFID sensor reader, dependency to the wireless channel, and integration of the sensor systems with the IoT networks.

For future works, chipless RFID sensors can be extended as an array towards additively manufactured smart coatings for metallic materials. The idea of smart coating is to integrate sensing functionality into complex structures, which is similar to an embedded electromagnetic skin [289]. For a fine spatial resolution, the smart coating could be operated at microwave frequencies higher than 2-6 GHz band, such as Ku-band (12-18 GHz), K-band (18-27 GHz), or mm-waves. With the higher operating frequency, the smart coating could be composed of tiny periodic conductive patches based on metasurface absorbers [290] on thin dielectric paint, powder, or substrate. The implementation could involve multi-material additive manufacturing [291], 3D printing [292], and using emerging 2D nanomaterials such as graphene [293], [294]. Apart from the smart coating for metals, additive manufacturing could also enable functional smart materials and composite structures [295], [296].

More attention should also be given to improve the reader, particularly the antennas. Chipless RFID reader antennas could be realized in a small form factor as in [278] and to have a finer radar resolution if the system operates at higher microwave frequencies. Antennas with narrow beam radiation or beam-steering capability such as array antennas and leaky wave antennas [297] could be investigated so that the backscattered signal is highly directive and reflected from a selective point area. Furthermore, a dielectric lens or other emerging approaches, such as transmit array [298], reflectarray [277], and metamaterial/metasurface lens [299], could be added to achieve focused beam radiation. This could improve spatial resolution for area monitoring and reduce the effects of the surrounding environment and wireless channel.

Regarding the signal processing and feature extraction, the system could exploit real-time monitoring and area scan using actuators or drones to acquire more signal data. Early detection and real-time monitoring of multiple physical variables, such as strain, structural deformation, water ingress, apart from crack and corrosion, could be considered. Real-time monitoring of multiple variables and imaging aspects could open opportunities to explore advanced signal processing, feature extraction techniques in time and frequency domains, synthetic aperture radar (SAR) imaging [300], and artificial intelligence [103].

Beyond the aspects of sensors and smart coating/materials, reader, and signal processing, the developments of IoT based SHM with chipless RFID sensor systems could be exciting future works. Edge computing, big data, and the concept of industry 4.0 are currently in focus. The IoT system architecture, integration of chipless RFID sensor systems with other wireless communication platforms and networks, power and data management, and security could be investigated in the future [301]–[303].

References

- [1] J. P. Lynch, C. R. Farrar, and J. E. Michaels, “Structural health monitoring: technological advances to practical implementations,” *Proceedings of the IEEE*, vol. 104, no. 8, pp. 1508–1512, Aug. 2016.
- [2] R. Doglione and D. Firrao, “Structural collapse calculations of old pipelines,” *International Journal of Fatigue*, vol. 20, no. 2, pp. 161–168, Mar. 1998.
- [3] R. J. H. Wanhill, Molent, S. A. Barter, and E. Amsterdam, “Milestone Case Histories in Aircraft Structural Integrity,” National Aerospace Laboratory NLR, NLR-TP-2015-193, Jan. 2016.
- [4] “Photos: Looking back at the I-35W bridge collapse,” *MPR News*. [Online]. Available: <https://www.mprnews.org/story/2017/08/01/looking-back-photos-of-the-bridge-collapse>. [Accessed: 05-Aug-2020].
- [5] J. Scheerhout, “Pictures and Video: Holiday jet drama at Manchester Airport as pilot aborts take-off after engine fails,” *men*, 24-Jun-2013. [Online]. Available: <http://www.manchestereveningnews.co.uk/news/greater-manchester-news/holiday-jet-drama-pilot-aborts-4705061>. [Accessed: 05-Aug-2020].
- [6] N. Welsh and 2015 | 9:00pm, “Photos of Ruptured Pipeline Finally Released,” *The Santa Barbara Independent*, 09-Jun-2015. [Online]. Available: <https://www.independent.com/2015/06/08/photos-ruptured-pipeline-finally-released/>. [Accessed: 29-Jan-2020].
- [7] Z. C. Petrovic, “Catastrophes caused by corrosion,” *Vojnotehnicki glasnik/Military Technical Courier*, vol. 64, no. 4, pp. 1048–1064, 2016.
- [8] C. R. Farrar and K. Worden, “An introduction to structural health monitoring,” *Philos Trans A Math Phys Eng Sci*, vol. 365, no. 1851, pp. 303–315, Feb. 2007.
- [9] B. Chapuis, “Introduction to Structural Health Monitoring,” in *Sensors, Algorithms and Applications for Structural Health Monitoring*, Springer, Cham, 2018, pp. 1–11.
- [10] A. Moreno-Gomez, C. A. Perez-Ramirez, A. Dominguez-Gonzalez, M. Valtierra-Rodriguez, O. Chavez-Alegria, and J. P. Amezcuita-Sanchez, “Sensors Used in Structural Health Monitoring,” *Arch Computat Methods Eng*, vol. 25, no. 4, pp. 901–918, Nov. 2018.
- [11] C. Cremona and J. Santos, “Structural Health Monitoring as a Big-Data Problem,” *Structural Engineering International*, vol. 28, no. 3, pp. 243–254, Jul. 2018.
- [12] P. Cawley, “Structural health monitoring: Closing the gap between research and industrial deployment,” *Structural Health Monitoring*, vol. 17, no. 5, pp. 1225–1244, Sep. 2018.
- [13] F. Hernandez-Valle, A. R. Clough, and R. S. Edwards, “Stress corrosion cracking detection using non-contact ultrasonic techniques,” *Corrosion Science*, vol. 78, pp. 335–342, Jan. 2014.
- [14] J. García-Martín, J. Gómez-Gil, and E. Vázquez-Sánchez, “Non-Destructive Techniques Based on Eddy Current Testing,” *Sensors*, vol. 11, no. 3, pp. 2525–2565, Mar. 2011.
- [15] A. Sophian, G. Tian, and M. Fan, “Pulsed Eddy Current Non-destructive Testing and Evaluation: A Review,” *Chin. J. Mech. Eng.*, vol. 30, no. 3, pp. 500–514, May 2017.

- [16] G. Y. Tian, Y. Gao, K. Li, Y. Wang, B. Gao, and Y. He, “Eddy Current Pulsed Thermography with Different Excitation Configurations for Metallic Material and Defect Characterization,” *Sensors (Basel)*, vol. 16, no. 6, Jun. 2016.
- [17] H. Zhang, R. Yang, Y. He, A. Foudazi, L. Cheng, and G. Tian, “A Review of Microwave Thermography Nondestructive Testing and Evaluation,” *Sensors (Basel)*, vol. 17, no. 5, May 2017.
- [18] L. Atzori, A. Iera, and G. Morabito, “The Internet of Things: A survey,” *Computer Networks*, vol. 54, no. 15, pp. 2787–2805, Oct. 2010.
- [19] J. Gubbi, R. Buyya, S. Marusic, and M. Palaniswami, “Internet of Things (IoT): A vision, architectural elements, and future directions,” *Future Generation Computer Systems*, vol. 29, no. 7, pp. 1645–1660, Sep. 2013.
- [20] L. D. Xu, W. He, and S. Li, “Internet of Things in Industries: A Survey,” *IEEE Transactions on Industrial Informatics*, vol. 10, no. 4, pp. 2233–2243, Nov. 2014.
- [21] J. Zhang, G. Y. Tian, A. M. J. Marindra, A. I. Sunny, and A. B. Zhao, “A Review of Passive RFID Tag Antenna-Based Sensors and Systems for Structural Health Monitoring Applications,” *Sensors*, vol. 17, no. 2, p. 265, Feb. 2017.
- [22] S. Preradovic and N. C. Karmakar, “Chipless RFID: Bar Code of the Future,” *IEEE Microwave Magazine*, vol. 11, no. 7, pp. 87–97, Dec. 2010.
- [23] S. Tedjini, N. Karmakar, E. Perret, A. Vena, R. Koswatta, and R. E-Azim, “Hold the Chips: Chipless Technology, an Alternative Technique for RFID,” *IEEE Microwave Magazine*, vol. 14, no. 5, pp. 56–65, Jul. 2013.
- [24] S. Dey, J. K. Saha, and N. C. Karmakar, “Smart Sensing: Chipless RFID Solutions for the Internet of Everything,” *IEEE Microwave Magazine*, vol. 16, no. 10, pp. 26–39, Nov. 2015.
- [25] E. M. Amin, N. C. Karmakar, and B. W. Jensen, “Fully printable chipless RFID multi-parameter sensor,” *Sensors and Actuators A: Physical*, vol. 248, pp. 223–232, Sep. 2016.
- [26] C. Herrojo, F. Paredes, J. Mata-Contreras, and F. Martín, “Chipless-RFID: A Review and Recent Developments,” *Sensors (Basel)*, vol. 19, no. 15, Aug. 2019.
- [27] N. C. Karmakar, E. M. Amin, and J. K. Saha, *Chipless RFID Sensors*. John Wiley & Sons, 2016.
- [28] A. M. J. Marindra and G. Y. Tian, “Chipless RFID Sensor Tag for Metal Crack Detection and Characterization,” *IEEE Transactions on Microwave Theory and Techniques*, vol. 66, no. 5, pp. 2452–2462, May 2018.
- [29] A. M. J. Marindra and G. Y. Tian, “Chipless RFID sensor for corrosion characterization based on frequency selective surface and feature fusion,” *Smart Mater. Struct.*, vol. 29, no. 12, p. 125010, Oct. 2020.
- [30] A. M. J. Marindra and G. Y. Tian, “Multiresonance Chipless RFID Sensor Tag for Metal Defect Characterization Using Principal Component Analysis,” *IEEE Sensors Journal*, vol. 19, no. 18, pp. 8037–8046, Sep. 2019.
- [31] L. Pook, “Historical Background,” in *Metal Fatigue*, Springer, Dordrecht, 2007, pp. 7–14.
- [32] W. Cui, “A state-of-the-art review on fatigue life prediction methods for metal structures,” *J Mar Sci Technol*, vol. 7, no. 1, pp. 43–56, Jun. 2002.

- [33] R. Brighenti and A. Carpinteri, "Surface cracks in fatigued structural components: a review," *Fatigue & Fracture of Engineering Materials & Structures*, vol. 36, no. 12, pp. 1209–1222, Dec. 2013.
- [34] A. Bahrami, M. Kiani Khouzani, S. A. Mokhtari, S. Zareh, and M. Yazdan Mehr, "Root Cause Analysis of Surface Cracks in Heavy Steel Plates during the Hot Rolling Process," *Metals*, vol. 9, no. 7, p. 801, Jul. 2019.
- [35] V. Cicek, *Corrosion Engineering*. John Wiley & Sons, 2014.
- [36] D. de la Fuente, I. Diaz, J. Simancas, B. Chico, and M. Morcillo, "Long-term atmospheric corrosion of mild steel," *Corrosion Science*, vol. 53, no. 2, pp. 604–617, Feb. 2011.
- [37] L. T. Popoola, A. S. Grema, G. K. Latinwo, B. Gutti, and A. S. Balogun, "Corrosion problems during oil and gas production and its mitigation," *Int J Ind Chem*, vol. 4, no. 1, pp. 1–15, Dec. 2013.
- [38] Z. Ahmad, *Types of Corrosion: Materials and Environments*. Butterworth-Heinemann, 2006.
- [39] M. Morcillo, D. de la Fuente, I. Diaz, and H. Cano, "Atmospheric corrosion of mild steel," *Revista de Metalurgia*, vol. 47, no. 5, pp. 426–444, Oct. 2011.
- [40] D. Chen, M. Yen, P. Lin, S. Groff, R. Lampo, M. McInerney, and J. Ryan, "A Corrosion Sensor for Monitoring the Early-Stage Environmental Corrosion of A36 Carbon Steel," *Materials (Basel)*, vol. 7, no. 8, pp. 5746–5760, Aug. 2014.
- [41] W. M. Haynes, *CRC Handbook of Chemistry and Physics*. CRC Press, 2014.
- [42] D. Varshney and A. Yogi, "Structural and Electrical conductivity of Mn doped Hematite (α -Fe₂O₃) phase," *Journal of Molecular Structure*, vol. 995, no. 1–3, pp. 157–162, May 2011.
- [43] V. Lair, H. Antony, L. Legrand, and A. Chausse, "Electrochemical reduction of ferric corrosion products and evaluation of galvanic coupling with iron," *Corrosion Science*, vol. 48, no. 8, pp. 2050–2063, Aug. 2006.
- [44] R. Itai, M. Shibuya, T. Matsumura, and G. Ishi, "Electrical Resistivity of Magnetite Anodes," *J. Electrochem. Soc.*, vol. 118, no. 10, p. 1709, Oct. 1971.
- [45] Alaa A Akl, "Microstructure and electrical properties of iron oxide thin films deposited by spray pyrolysis," *Applied Surface Science*, vol. 221, no. 1–4, pp. 319–329, Jan. 2004.
- [46] T. D. Glotch and G. R. Rossman, "Mid-infrared reflectance spectra and optical constants of six iron oxide/oxyhydroxide phases," *Icarus*, vol. 204, no. 2, pp. 663–671, Dec. 2009.
- [47] C. Boller, "Structural Health Monitoring – Its Association and Use," in *New Trends in Structural Health Monitoring*, Springer, Vienna, 2013, pp. 1–79.
- [48] P. J. Shull, *Nondestructive Evaluation: Theory, Techniques, and Applications*. CRC Press, 2002.
- [49] M. Mitra and S. Gopalakrishnan, "Guided wave based structural health monitoring: A review," *Smart Mater. Struct.*, vol. 25, no. 5, p. 053001, Mar. 2016.
- [50] R. Halmshaw, *Visual methods*. Woodhead Publishing, 1996.
- [51] Hareesh K, "Introduction to NDT and Visual Inspection," 16:32:06 UTC.
- [52] Campbell Leslie E., Connor Robert J., Whitehead Julie M., and Washer Glenn A., "Benchmark for Evaluating Performance in Visual Inspection of Fatigue Cracking in Steel Bridges," *Journal of Bridge Engineering*, vol. 25, no. 1, p. 04019128, Jan. 2020.

- [53] J. E. See, C. G. Drury, A. Speed, A. Williams, and N. Khalandi, "The Role of Visual Inspection in the 21st Century," *Proceedings of the Human Factors and Ergonomics Society Annual Meeting*, vol. 61, no. 1, pp. 262–266, Sep. 2017.
- [54] S. Sony, S. Laventure, and A. Sadhu, "A literature review of next-generation smart sensing technology in structural health monitoring," *Structural Control and Health Monitoring*, vol. 26, no. 3, Mar. 2019.
- [55] I.-H. Kim, H. Jeon, S.-C. Baek, W.-H. Hong, and H.-J. Jung, "Application of Crack Identification Techniques for an Aging Concrete Bridge Inspection Using an Unmanned Aerial Vehicle," *Sensors*, vol. 18, no. 6, p. 1881, Jun. 2018.
- [56] X. Kong and J. Li, "Vision-Based Fatigue Crack Detection of Steel Structures Using Video Feature Tracking," *Computer-Aided Civil and Infrastructure Engineering*, vol. 33, no. 9, pp. 783–799, Sep. 2018.
- [57] B. Bastian, N. Jaspreeth, K. Ranjith, and C. V. Jiji, "Visual inspection and characterization of external corrosion in pipelines using deep neural network," *NDT & E International*, vol. 107, p. 102134, Oct. 2019.
- [58] R. Halmshaw, *Penetrant methods*. Woodhead Publishing, 1996.
- [59] C. F. Molina, "Liquid penetrant examination BOK API 653 – An explanation," *Apiexam*, 11-Nov-2016. [Online]. Available: <http://apiexam.com/liquid-penetrant-examination-bok-api-653-an-explanation/>. [Accessed: 10-Feb-2020].
- [60] M. K. Kutman, F. Z. B. Muftuler, C. Harmansah, and O. K. Guldu, "Use of Bacteria as Fluorescent Penetrant for Penetrant Testing (PT)," *J Nondestruct Eval*, vol. 39, no. 1, pp. 1–6, Mar. 2020.
- [61] N. J. Shipway, T. J. Barden, P. Huthwaite, and M. J. S. Lowe, "Automated defect detection for Fluorescent Penetrant Inspection using Random Forest," *NDT & E International*, vol. 101, pp. 113–123, Jan. 2019.
- [62] S. Huang and S. Wang, "Magnetic Flux Leakage Testing," in *New Technologies in Electromagnetic Non-destructive Testing*, Springer, Singapore, 2016, pp. 185–222.
- [63] Y. Shi, C. Zhang, R. Li, M. Cai, and G. Jia, "Theory and Application of Magnetic Flux Leakage Pipeline Detection," *Sensors (Basel)*, vol. 15, no. 12, pp. 31036–31055, Dec. 2015.
- [64] A. G. Antipov and A. A. Markov, "Detectability of Rail Defects by Magnetic Flux Leakage Method," *Russ J Nondestruct Test*, vol. 55, no. 4, pp. 277–285, Apr. 2019.
- [65] Z. Usarek, M. Chmielewski, and L. Piotrowski, "Reduction of the Velocity Impact on the Magnetic Flux Leakage Signal," *J Nondestruct Eval*, vol. 38, no. 1, pp. 1–7, Mar. 2019.
- [66] D. Yang, J. Qiu, H. Di, S. Zhao, J. Zhou, and F. Yang, "Quantitative Evaluation of Corrosion Degrees of Steel Bars Based on Self-Magnetic Flux Leakage," *Metals*, vol. 9, no. 9, p. 952, Sep. 2019.
- [67] M. V. Brook, "Introduction," *Ultrasonic Inspection Technology Development and Search Unit Design*, pp. 1–12, Nov. 2011.
- [68] S. Kumar and D. G. Mahto, "Recent Trends in Industrial and Other Engineering Applications of Non Destructive Testing: A Review," Social Science Research Network, Rochester, NY, SSRN Scholarly Paper ID 2770922, 2013.
- [69] X. F. Wang and Z. A. Tang, "A novel method for digital ultrasonic time-of-flight measurement," *Review of Scientific Instruments*, vol. 81, no. 10, p. 105112, Oct. 2010.

- [70] A. N. Sinclair, J. N. Fortin, B. Shakibi, F. Honarvar, M. Jastrzebski, and M. D. C. Moles, “Enhancement of ultrasonic images for sizing of defects by time-of-flight diffraction,” *NDT & E International*, vol. 43, no. 3, pp. 258–264, Apr. 2010.
- [71] A. Habibpour-Ledari and F. Honarvar, “Three Dimensional Characterization of Defects by Ultrasonic Time-of-Flight Diffraction (ToFD) Technique,” *J Nondestruct Eval*, vol. 37, no. 1, pp. 1–11, Mar. 2018.
- [72] X. Wang, W. Li, Y. Li, Z. Zhou, J. Zhang, F. Zhu, and Z. Miao, “Phased array ultrasonic testing of micro-flaws in additive manufactured titanium block,” *Mater. Res. Express*, vol. 7, no. 1, p. 016572, Jan. 2020.
- [73] Y. Ohara, T. Mihara, and K. Yamanaka, “Nonlinear Ultrasonic Phased Array for Measurement of Closed-Crack Depth,” in *Measurement of Nonlinear Ultrasonic Characteristics*, Springer, Singapore, 2020, pp. 165–234.
- [74] D. Yi, C. Pei, T. Liu, and Z. Chen, “Inspection of cracks with focused angle beam laser ultrasonic wave,” *Applied Acoustics*, vol. 145, pp. 1–6, Feb. 2019.
- [75] M. V. Felice, A. Velichko, and P. D. Wilcox, “Accurate depth measurement of small surface-breaking cracks using an ultrasonic array post-processing technique,” *NDT & E International*, vol. 68, pp. 105–112, Dec. 2014.
- [76] “A novel method for Estimating Time of Flight of ultrasonic echoes through short-time Fourier transforms,” *Ultrasonics*, p. 106104, Feb. 2020.
- [77] Z. Zhu, H. Sui, L. Yu, H. Zhu, J. Zhang, and J. Peng, “Effective Defect Features Extraction for Laser Ultrasonic Signal Processing by Using Time–Frequency Analysis,” *IEEE Access*, vol. 7, pp. 128706–128713, 2019.
- [78] P. Fromme, “Guided Wave Testing,” in *Handbook of Advanced Nondestructive Evaluation*, Springer, Cham, 2019, pp. 141–170.
- [79] Fei Yan, R. L. Royer, and J. L. Rose, “Ultrasonic Guided Wave Imaging Techniques in Structural Health Monitoring,” *Journal of Intelligent Material Systems and Structures*, vol. 21, no. 3, pp. 377–384, Feb. 2010.
- [80] M. Abbas and M. Shafiee, “Structural Health Monitoring (SHM) and Determination of Surface Defects in Large Metallic Structures using Ultrasonic Guided Waves,” *Sensors (Basel)*, vol. 18, no. 11, Nov. 2018.
- [81] W. Zhu, J. L. Rose, J. N. Barshinger, and V. S. Agarwala, “Ultrasonic Guided Wave NDT for Hidden Corrosion Detection,” *Research in Nondestructive Evaluation*, vol. 10, no. 4, pp. 205–225, Jan. 1998.
- [82] D. Dai and Q. He, “Structure damage localization with ultrasonic guided waves based on a time–frequency method,” *Signal Processing*, vol. 96, pp. 21–28, Mar. 2014.
- [83] J. S. Hall and J. E. Michaels, “Multipath ultrasonic guided wave imaging in complex structures,” *Structural Health Monitoring*, vol. 14, no. 4, pp. 345–358, Jul. 2015.
- [84] Z. Chen, C. Jomdecha, and S. Xie, “Eddy Current Testing,” in *Handbook of Advanced Nondestructive Evaluation*, Springer, Cham, 2019, pp. 645–728.
- [85] A. Bernieri, G. Betta, L. Ferrigno, and M. Laracca, “Crack Depth Estimation by Using a Multi-Frequency ECT Method,” *IEEE Transactions on Instrumentation and Measurement*, vol. 62, no. 3, pp. 544–552, Mar. 2013.
- [86] Y. He, G. Tian, H. Zhang, M. Alamin, A. Simm, and P. Jackson, “Steel Corrosion Characterization Using Pulsed Eddy Current Systems,” *IEEE Sensors Journal*, vol. 12, no. 6, pp. 2113–2120, Jun. 2012.

- [87] W. Cheng, “Thickness Measurement of Metal Plates Using Swept-Frequency Eddy Current Testing and Impedance Normalization,” *IEEE Sensors Journal*, vol. 17, no. 14, pp. 4558–4569, Jul. 2017.
- [88] L. U. Daura and G. Y. Tian, “Wireless Power Transfer Based Non-Destructive Evaluation of Cracks in Aluminum Material,” *IEEE Sensors Journal*, vol. 19, no. 22, pp. 10529–10536, Nov. 2019.
- [89] Y. Fu, M. Lei, Z. Li, Z. Gu, H. Yang, A. Cao, and J. Sun, “Lift-off effect reduction based on the dynamic trajectories of the received-signal fast Fourier transform in pulsed eddy current testing,” *NDT & E International*, vol. 87, pp. 85–92, Apr. 2017.
- [90] A. N. AbdAlla, M. A. Faraj, F. Samsuri, D. Rifai, K. Ali, and Y. Al-Douri, “Challenges in improving the performance of eddy current testing: Review,” *Measurement and Control*, vol. 52, no. 1–2, pp. 46–64, Jan. 2019.
- [91] S. Bajracharya, E. Sasaki, and H. Tamura, “Numerical study on corrosion profile estimation of a corroded steel plate using eddy current,” *Structure and Infrastructure Engineering*, vol. 15, no. 9, pp. 1151–1164, Sep. 2019.
- [92] A. S. Repelianto, N. Kasai, K. Sekino, M. Matsunaga, and L. Q. Trung, “Flaw Detection in Aluminum Plates Using a Rotating Uniform Eddy Current Probe with Two Pairs of Excitation Coils,” *Metals*, vol. 9, no. 10, p. 1069, Oct. 2019.
- [93] D. I. Ona, G. Y. Tian, and S. M. Naqvi, “Investigation of Signal Conditioning for Tx-Rx PEC Probe at High Lift-Off Using a Modified Maxwell’s Bridge,” *IEEE Sensors Journal*, vol. 20, no. 5, pp. 2560–2569, Mar. 2020.
- [94] L. Wang, W. Cai, and Z. Chen, “Quantitative evaluation of stress corrosion cracking based on crack conductivity model and intelligent algorithm from eddy current testing signals,” *Nondestructive Testing and Evaluation*, vol. 0, no. 0, pp. 1–17, Dec. 2019.
- [95] S. Kharkovsky and R. Zoughi, “Microwave and millimeter wave nondestructive testing and evaluation - Overview and recent advances,” *IEEE Instrumentation Measurement Magazine*, vol. 10, no. 2, pp. 26–38, Apr. 2007.
- [96] M. Dvorsky, J. Gallion, and R. Zoughi, “Millimeter Wave Imaging and Evaluation of Surface-Breaking Cracks in Metal Structures with Surface Pitting and Corrosion,” *Review of Progress in Quantitative Nondestructive Evaluation*, Jan. 2016.
- [97] R. Zoughi and S. Kharkovsky, “Microwave and millimetre wave sensors for crack detection,” *Fatigue & Fracture of Engineering Materials & Structures*, vol. 31, no. 8, pp. 695–713, Aug. 2008.
- [98] R. Sutthaweeikul and G. Y. Tian, “Steel Corrosion Stages Characterization Using Open-Ended Rectangular Waveguide Probe,” *IEEE Sensors Journal*, vol. 18, no. 3, pp. 1054–1062, Feb. 2018.
- [99] N. Ida, “Microwave and Millimeter Wave Nondestructive Testing and Evaluation,” in *Handbook of Advanced Nondestructive Evaluation*, Springer, Cham, 2019, pp. 929–966.
- [100] “Microwave open-ended waveguide for detection and characterisation of FBHs in coated GFRP pipes,” *Composite Structures*, vol. 225, p. 111080, Oct. 2019.
- [101] X. Zhang, J. Liang, N. Wang, T. Chang, Q. Guo, and H.-L. Cui, “Broadband Millimeter-Wave Imaging Radar-Based 3-D Holographic Reconstruction for Nondestructive Testing,” *IEEE Transactions on Microwave Theory and Techniques*, pp. 1–12, 2019.

- [102] M. Chizh, A. V. Zhuravlev, V. Razevig, S. Ivashov, P. Falorni, and L. Capineri, “Defects investigation in thermal insulation coatings with microwave imaging based on a 22 GHz holographic radar,” *NDT & E International*, vol. 109, p. 102191, Jan. 2020.
- [103] N. H. M. M. Shrifan, M. F. Akbar, and N. A. M. Isa, “Prospect of Using Artificial Intelligence for Microwave Nondestructive Testing Technique: A Review,” *IEEE Access*, vol. 7, pp. 110628–110650, 2019.
- [104] H. Budzier and G. Gerlach, “Active Thermography,” in *Handbook of Advanced Nondestructive Evaluation*, Springer, Cham, 2019, pp. 1401–1418.
- [105] H. Budzier and G. Gerlach, “Passive Thermography, Thermal Imaging,” in *Handbook of Advanced Nondestructive Evaluation*, Springer, Cham, 2019, pp. 1371–1400.
- [106] X. Li, B. Gao, W. L. Woo, G. Y. Tian, X. Qiu, and L. Gu, “Quantitative Surface Crack Evaluation Based on Eddy Current Pulsed Thermography,” *IEEE Sensors Journal*, vol. 17, no. 2, pp. 412–421, Jan. 2017.
- [107] S. Doshvarpassand, C. Wu, and X. Wang, “An overview of corrosion defect characterization using active infrared thermography,” *Infrared Physics & Technology*, vol. 96, pp. 366–389, Jan. 2019.
- [108] T. Krell, M. Wetzel, and J. Holtmannspötter, “Non-destructive, quick and visual,” *Adhes Adhes Sealants*, vol. 9, no. 1, pp. 37–41, Mar. 2012.
- [109] A. Sirikham, Y. Zhao, H. Liu, Y. Xu, S. Williams, and J. Mehnen, “Three-dimensional subsurface defect shape reconstruction and visualisation by pulsed thermography,” *Infrared Physics & Technology*, vol. 104, p. 103151, Jan. 2020.
- [110] H. Wu, K. Zheng, S. Sfarra, Y. Liu, and Y. Yao, “Multi-view learning for subsurface defect detection in composite products: a challenge on thermographic data analysis,” *IEEE Transactions on Industrial Informatics*, pp. 1–1, 2020.
- [111] S. Deane, N. P. Avdelidis, C. Castanedo, H. Zhang, H. Y. Nezaad, A. A. Williamson, T. Mackley, M. J. Davis, X. Maldague, and A. Tsourdos, “Application of NDT thermographic imaging of aerospace structures,” *Infrared Physics & Technology*, vol. 97, pp. 456–466, Mar. 2019.
- [112] X. Wang, B. S. Wong, C. Tan, and C. G. Tui, “Automated Crack Detection for Digital Radiography Aircraft Wing Inspection,” *Research in Nondestructive Evaluation*, vol. 22, no. 2, pp. 105–127, Mar. 2011.
- [113] B. Dong, G. Fang, Y. Liu, P. Dong, J. Zhang, F. Xing, and S. Hong, “Monitoring reinforcement corrosion and corrosion-induced cracking by X-ray microcomputed tomography method,” *Cement and Concrete Research*, vol. 100, pp. 311–321, Oct. 2017.
- [114] P.-J. Chiang, R. Jiang, R. Cunningham, N. Parab, C. Zhao, K. Fezzaa, T. Sun, and A. D. Rollett, “In Situ Characterization of Hot Cracking Using Dynamic X-Ray Radiography,” in *Advanced Real Time Imaging II*, Springer, Cham, 2019, pp. 77–85.
- [115] E. Yahaghi and M. Hosseini-Ashrafi, “Enhanced defect detection in radiography images of welded objects,” *Nondestructive Testing and Evaluation*, vol. 34, no. 1, pp. 13–22, Jan. 2019.
- [116] K. S. Kim, S. Y. Kang, W. S. Kim, H. S. Cho, C. K. Park, D. Y. Lee, G. A. Kim, S. Y. Park, H. W. Lim, H. W. Lee, J. E. Park, D. H. Jeon, Y. H. Lim, U. K. Je, and T. H. Woo, “Improvement of radiographic visibility using an image restoration method based on a simple radiographic scattering model for x-ray nondestructive testing,” *NDT & E International*, vol. 98, pp. 117–122, Sep. 2018.

- [117] T. Burgos, D. A. G. Vargas, R. C. C. Pedraza, D. Agis, and F. Pozo, “Damage Identification in Structural Health Monitoring: A Brief Review from its Implementation to the Use of Data-Driven Applications,” *Sensors*, vol. 20, no. 3, p. 733, Jan. 2020.
- [118] W. Ostachowicz, R. Soman, and P. Malinowski, “Optimization of sensor placement for structural health monitoring: a review,” *Structural Health Monitoring*, vol. 18, no. 3, pp. 963–988, May 2019.
- [119] H.-P. Chen and Y.-Q. Ni, “Sensors and Sensing Technology for Structural Monitoring,” *Structural Health Monitoring of Large Civil Engineering Structures*, pp. 15–49, Mar. 2018.
- [120] J. Moody, “The relationship between SHM, CM and NDT.” [Online]. Available: <https://www.bindt.org/forums/moodys-memoranda/the-relationship-between-shm-cm-and-ndt/>. [Accessed: 26-May-2020].
- [121] Jeffrey Funk, “Smart Sensors for Infrastructure and Structural Health Monitoring,” 20:36:11 UTC.
- [122] Webb G. T., Vardanega P. J., and Middleton C. R., “Categories of SHM Deployments: Technologies and Capabilities,” *Journal of Bridge Engineering*, vol. 20, no. 11, p. 04014118, Nov. 2015.
- [123] C. Scuro, P. F. Sciammarella, F. Lamonaca, R. S. Olivito, and D. L. Carni, “IoT for structural health monitoring,” *IEEE Instrumentation Measurement Magazine*, vol. 21, no. 6, pp. 4–14, Dec. 2018.
- [124] Richard W. Griffiths, “Structural monitoring system using fiber optics,” 18-Mar-1985.
- [125] C. I. Merzbacher, A. D. Kersey, and E. J. Friebele, “Fiber optic sensors in concrete structures: a review,” *Smart Mater. Struct.*, vol. 5, no. 2, pp. 196–208, Apr. 1996.
- [126] D. J. Pines and P. A. Lovell, “Conceptual framework of a remote wireless health monitoring system for large civil structures,” *Smart Mater. Struct.*, vol. 7, no. 5, pp. 627–636, Oct. 1998.
- [127] T. Wang, M. Z. A. Bhuiyan, G. Wang, M. A. Rahman, J. Wu, and J. Cao, “Big Data Reduction for a Smart City’s Critical Infrastructural Health Monitoring,” *IEEE Communications Magazine*, vol. 56, no. 3, pp. 128–133, Mar. 2018.
- [128] G.-D. Zhou and T.-H. Yi, “Recent Developments on Wireless Sensor Networks Technology for Bridge Health Monitoring,” *Mathematical Problems in Engineering*, vol. 2013, 2013.
- [129] W. R. Habel, “Optical Fiber Methods in Nondestructive Evaluation,” in *Handbook of Advanced Nondestructive Evaluation*, Springer, Cham, 2019, pp. 595–642.
- [130] J. M. Lopez-Higuera, L. R. Cobo, A. Q. Incera, and A. Cobo, “Fiber Optic Sensors in Structural Health Monitoring,” *Journal of Lightwave Technology*, vol. 29, no. 4, pp. 587–608, Feb. 2011.
- [131] A. Barrias, J. R. Casas, and S. Villalba, “A Review of Distributed Optical Fiber Sensors for Civil Engineering Applications,” *Sensors*, vol. 16, no. 5, p. 748, May 2016.
- [132] X. W. Ye, Y. H. Su, and J. P. Han, “Structural Health Monitoring of Civil Infrastructure Using Optical Fiber Sensing Technology: A Comprehensive Review,” *The Scientific World Journal*, 2014.
- [133] H. Guo, G. Xiao, N. Mrad, and J. Yao, “Fiber Optic Sensors for Structural Health Monitoring of Air Platforms,” *Sensors*, vol. 11, no. 4, pp. 3687–3705, Apr. 2011.

- [134] K. T. Wan and C. K. Y. Leung, “Applications of a distributed fiber optic crack sensor for concrete structures,” *Sensors and Actuators A: Physical*, vol. 135, no. 2, pp. 458–464, Apr. 2007.
- [135] D. Luo, J. Li, and Y. Li, “A review of fiber-optic corrosion sensor in civil engineering,” *AIP Conference Proceedings*, vol. 1967, no. 1, p. 020055, May 2018.
- [136] P. J. Thomas and J. O. Hellevang, “A distributed fibre optic approach for providing early warning of Corrosion Under Insulation (CUI),” *Journal of Loss Prevention in the Process Industries*, vol. 64, p. 104060, Mar. 2020.
- [137] D.-S. Kim and H. Tran-Dang, “An Overview on Wireless Sensor Networks,” in *Industrial Sensors and Controls in Communication Networks*, Springer, Cham, 2019, pp. 101–113.
- [138] Y. Lee, D. Blaauw, and D. Sylvester, “Ultralow Power Circuit Design for Wireless Sensor Nodes for Structural Health Monitoring,” *Proceedings of the IEEE*, vol. 104, no. 8, pp. 1529–1546, Aug. 2016.
- [139] C. Ayyildiz, H. E. Erdem, T. Dirikgil, O. Dugenci, T. Kocak, F. Altun, and V. C. Gungor, “Structure health monitoring using wireless sensor networks on structural elements,” *Ad Hoc Networks*, vol. 82, pp. 68–76, Jan. 2019.
- [140] Z. Liu and Y. Kleiner, “State-of-the-Art Review of Technologies for Pipe Structural Health Monitoring,” *IEEE Sensors Journal*, vol. 12, no. 6, pp. 1987–1992, Jun. 2012.
- [141] R. F. Wright, P. Lu, J. Devkota, F. Lu, M. Ziomek-Moroz, and P. R. Ohodnicki, “Corrosion Sensors for Structural Health Monitoring of Oil and Natural Gas Infrastructure: A Review,” *Sensors*, vol. 19, no. 18, p. 3964, Jan. 2019.
- [142] G. Sun, G. Yang, and B. Guo, “CoCoMo: Toward controllable and reliable corrosion monitoring with a wireless sensor network,” *International Journal of Distributed Sensor Networks*, vol. 13, no. 10, p. 1550147717734525, Oct. 2017.
- [143] A. B. Noel, A. Abdaoui, T. Elfouly, M. H. Ahmed, A. Badawy, and M. S. Shehata, “Structural Health Monitoring Using Wireless Sensor Networks: A Comprehensive Survey,” *IEEE Communications Surveys Tutorials*, vol. 19, no. 3, pp. 1403–1423, 2017.
- [144] G. Park, K. M. Farinholt, C. R. Farrar, T. Rosing, and M. D. Todd, “Powering Wireless SHM Sensor Nodes through Energy Harvesting,” in *Energy Harvesting Technologies*, Springer, Boston, MA, 2009, pp. 493–506.
- [145] M. Abdulkarem, K. Samsudin, F. Z. Rokhani, and M. F. A. Rasid, “Wireless sensor network for structural health monitoring: A contemporary review of technologies, challenges, and future direction,” *Structural Health Monitoring*, vol. 19, no. 3, pp. 693–735, May 2020.
- [146] K. Ashton, “That ‘Internet of Things’ Thing | RFID JOURNAL.” [Online]. Available: <https://www.rfidjournal.com/that-internet-of-things-thing>. [Accessed: 23-Aug-2020].
- [147] C. A. Tokognon, B. Gao, G. Y. Tian, and Y. Yan, “Structural Health Monitoring Framework Based on Internet of Things: A Survey,” *IEEE Internet of Things Journal*, vol. 4, no. 3, pp. 619–635, Jun. 2017.
- [148] J. Lin, W. Yu, N. Zhang, X. Yang, H. Zhang, and W. Zhao, “A Survey on Internet of Things: Architecture, Enabling Technologies, Security and Privacy, and Applications,” *IEEE Internet of Things Journal*, vol. 4, no. 5, pp. 1125–1142, Oct. 2017.
- [149] H. Lehpamer, *RFID Design Principles*. Artech House, 2008.

- [150] D. M. Dobkin, *The RF in RFID (Chapter 2 - History and Practice of RFID)*. Newnes, 2013.
- [151] S. Zuffanelli, “Introduction,” in *Antenna Design Solutions for RFID Tags Based on Metamaterial-Inspired Resonators and Other Resonant Structures*, Springer, Cham, 2018, pp. 1–45.
- [152] K. V. S. Rao, P. V. Nikitin, and S. F. Lam, “Antenna design for UHF RFID tags: a review and a practical application,” *IEEE Transactions on Antennas and Propagation*, vol. 53, no. 12, pp. 3870–3876, Dec. 2005.
- [153] M.-S. Jian and J.-S. Wu, “RFID Applications and Challenges,” Jun. 2013.
- [154] K. Koski, E. Koski, J. Virtanen, T. Björninen, L. Sydänheimo, L. Ukkonen, and A. Z. Elsherbeni, “Inkjet-printed passive UHF RFID tags: review and performance evaluation,” *Int J Adv Manuf Technol*, vol. 62, no. 1, pp. 167–182, Sep. 2012.
- [155] J. Grosinger, W. Pachler, and W. Bosch, “Tag Size Matters: Miniaturized RFID Tags to Connect Smart Objects to the Internet,” *IEEE Microwave Magazine*, vol. 19, no. 6, pp. 101–111, Sep. 2018.
- [156] T. Björninen, L. Sydänheimo, L. Ukkonen, and Y. Rahmat-Samii, “Advances in antenna designs for UHF RFID tags mountable on conductive items,” *IEEE Antennas and Propagation Magazine*, vol. 56, no. 1, pp. 79–103, Feb. 2014.
- [157] Y. Wu, Q. Z. Sheng, and S. Zeadally, “RFID: Opportunities and Challenges,” in *Next-Generation Wireless Technologies*, Springer, London, 2013, pp. 105–129.
- [158] L. Xie, Y. Yin, A. V. Vasilakos, and S. Lu, “Managing RFID Data: Challenges, Opportunities and Solutions,” *IEEE Communications Surveys Tutorials*, vol. 16, no. 3, pp. 1294–1311, Third 2014.
- [159] B. S. Cook, R. Vyas, S. Kim, T. Thai, T. Le, A. Traille, H. Aubert, and M. M. Tentzeris, “RFID-Based Sensors for Zero-Power Autonomous Wireless Sensor Networks,” *IEEE Sensors Journal*, vol. 14, no. 8, pp. 2419–2431, Aug. 2014.
- [160] R. Bhattacharyya, C. Floerkemeier, and S. Sarma, “Low-Cost, Ubiquitous RFID-Tag-Antenna-Based Sensing,” *Proceedings of the IEEE*, vol. 98, no. 9, pp. 1593–1600, Sep. 2010.
- [161] R. Want, “Enabling ubiquitous sensing with RFID,” *Computer*, vol. 37, no. 4, pp. 84–86, Apr. 2004.
- [162] Z. Meng and Z. Li, “RFID Tag as a Sensor - A Review on the Innovative Designs and Applications,” *Measurement Science Review*, vol. 16, no. 6, pp. 305–315, Dec. 2016.
- [163] L. Cui, Z. Zhang, N. Gao, Z. Meng, and Z. Li, “Radio Frequency Identification and Sensing Techniques and Their Applications—A Review of the State-of-the-Art,” *Sensors*, vol. 19, no. 18, p. 4012, Jan. 2019.
- [164] L. Catarinucci, R. Colella, A. Esposito, L. Tarricone, and M. Zappatore, “RFID Sensor-Tags Feeding a Context-Aware Rule-Based Healthcare Monitoring System,” *J Med Syst*, vol. 36, no. 6, pp. 3435–3449, Dec. 2012.
- [165] A. Wickramasinghe and D. C. Ranasinghe, “Ambulatory Monitoring Using Passive Computational RFID Sensors,” *IEEE Sensors Journal*, vol. 15, no. 10, pp. 5859–5869, Oct. 2015.
- [166] J. Virtanen, L. Ukkonen, T. Björninen, A. Z. Elsherbeni, and L. Sydänheimo, “Inkjet-Printed Humidity Sensor for Passive UHF RFID Systems,” *IEEE Transactions on Instrumentation and Measurement*, vol. 60, no. 8, pp. 2768–2777, Aug. 2011.

- [167] S. F. Pichorim, N. J. Gomes, and J. C. Batchelor, “Two Solutions of Soil Moisture Sensing with RFID for Landslide Monitoring,” *Sensors (Basel)*, vol. 18, no. 2, Feb. 2018.
- [168] S. Zampolli, I. Elmi, E. Cozzani, G. C. Cardinali, A. Scorzoni, M. Cicioni, S. Marco, F. Palacio, J. M. Gómez-Cama, I. Sayhan, and T. Becker, “Ultra-low-power components for an RFID Tag with physical and chemical sensors,” *Microsyst Technol*, vol. 14, no. 4, pp. 581–588, Apr. 2008.
- [169] S. Manzari, A. Catini, G. Pomarico, C. D. Natale, and G. Marrocco, “Development of an UHF RFID Chemical Sensor Array for Battery-Less Ambient Sensing,” *IEEE Sensors Journal*, vol. 14, no. 10, pp. 3616–3623, Oct. 2014.
- [170] A. M. Rady and D. E. Guyer, “Rapid and/or nondestructive quality evaluation methods for potatoes: A review,” *Computers and Electronics in Agriculture*, vol. 117, pp. 31–48, Sep. 2015.
- [171] K.-H. Eom, K.-H. Hyun, S. Lin, and J.-W. Kim, “The Meat Freshness Monitoring System Using the Smart RFID Tag,” *International Journal of Distributed Sensor Networks*, vol. 10, no. 7, p. 591812, Jul. 2014.
- [172] T. Wang, Y. He, Q. Luo, F. Deng, and C. Zhang, “Self-Powered RFID Sensor Tag for Fault Diagnosis and Prognosis of Transformer Winding,” *IEEE Sensors Journal*, vol. 17, no. 19, pp. 6418–6430, Oct. 2017.
- [173] E. DiGiampaolo, A. DiCarlofelice, and A. Gregori, “An RFID-Enabled Wireless Strain Gauge Sensor for Static and Dynamic Structural Monitoring,” *IEEE Sensors Journal*, vol. 17, no. 2, pp. 286–294, Jan. 2017.
- [174] C. Occhiuzzi, S. Caizzzone, and G. Marrocco, “Passive UHF RFID antennas for sensing applications: Principles, methods, and classifications,” *IEEE Antennas and Propagation Magazine*, vol. 55, no. 6, pp. 14–34, Dec. 2013.
- [175] H. Huang, “Antenna Sensors in Passive Wireless Sensing Systems,” in *Handbook of Antenna Technologies*, Z. N. Chen, Ed. Singapore: Springer Singapore, 2015, pp. 1–34.
- [176] X. Yi, C. Cho, J. Cooper, Y. Wang, M. M. Tentzeris, and R. T. Leon, “Passive wireless antenna sensor for strain and crack sensing—electromagnetic modeling, simulation, and testing,” *Smart Mater. Struct.*, vol. 22, no. 8, p. 085009, Jul. 2013.
- [177] S. Caizzzone and E. DiGiampaolo, “Wireless Passive RFID Crack Width Sensor for Structural Health Monitoring,” *IEEE Sensors Journal*, vol. 15, no. 12, pp. 6767–6774, Dec. 2015.
- [178] J. Zhang, G. Y. Tian, and A. B. Zhao, “Passive RFID sensor systems for crack detection & characterization,” *NDT & E International*, vol. 86, pp. 89–99, Mar. 2017.
- [179] R. E. Martínez-Castro, S. Jang, J. Nicholas, and R. Bansal, “Experimental assessment of an RFID-based crack sensor for steel structures,” *Smart Mater. Struct.*, vol. 26, no. 8, p. 085035, Jul. 2017.
- [180] P. Kalansuriya, R. Bhattacharyya, and S. Sarma, “RFID Tag Antenna-Based Sensing for Pervasive Surface Crack Detection,” *IEEE Sensors Journal*, vol. 13, no. 5, pp. 1564–1570, May 2013.
- [181] S. Caizzzone, E. DiGiampaolo, and G. Marrocco, “Wireless Crack Monitoring by Stationary Phase Measurements from Coupled RFID Tags,” *IEEE Transactions on Antennas and Propagation*, vol. 62, no. 12, pp. 6412–6419, Dec. 2014.
- [182] M. Omer, G. Y. Tian, B. Gao, and D. Su, “Passive UHF RFID Tag as a Sensor for Crack Depths,” *IEEE Sensors Journal*, vol. 18, no. 23, pp. 9867–9873, Dec. 2018.

- [183] J. Zhang, B. Huang, G. Zhang, and G. Y. Tian, “Wireless Passive Ultra High Frequency RFID Antenna Sensor for Surface Crack Monitoring and Quantitative Analysis,” *Sensors*, vol. 18, no. 7, p. 2130, Jul. 2018.
- [184] J. Zhang, A. I. Sunny, G. Zhang, and G. Tian, “Feature Extraction for Robust Crack Monitoring Using Passive Wireless RFID Antenna Sensors,” *IEEE Sensors Journal*, vol. 18, no. 15, pp. 6273–6280, Aug. 2018.
- [185] B. Bruciati, S. Jang, and P. Fils, “RFID-Based Crack Detection of Ultra High-Performance Concrete Retrofitted Beams,” *Sensors (Basel)*, vol. 19, no. 7, Apr. 2019.
- [186] W. Leon-Salas, S. Kanneganti, and C. Halmen, “Development of a smart RFID-based corrosion sensor,” in *2011 IEEE SENSORS*, 2011, pp. 534–537.
- [187] S. Bhadra, D. J. Thomson, and G. E. Bridges, “A wireless embedded passive sensor for monitoring the corrosion potential of reinforcing steel,” *Smart Mater. Struct.*, vol. 22, no. 7, p. 075019, Jun. 2013.
- [188] W. D. Leon-Salas and C. Halmen, “A RFID Sensor for Corrosion Monitoring in Concrete,” *IEEE Sensors Journal*, vol. 16, no. 1, pp. 32–42, Jan. 2016.
- [189] L. Lawand, O. Shiryayev, K. Al Handawi, N. Vahdati, and P. Rostron, “Corrosivity Sensor for Exposed Pipelines Based on Wireless Energy Transfer,” *Sensors*, vol. 17, no. 6, p. 1238, Jun. 2017.
- [190] M. Alamin, G. Y. Tian, A. Andrews, and P. Jackson, “Corrosion detection using low-frequency RFID technology,” *The British Institute of Non-Destructive Testing*, vol. 54, no. 2, pp. 72-75(4), Feb. 2012.
- [191] Y. L. He, S. McLaughlin, J. S. H. Lo, C. Shi, J. Lenos, and A. Vincelli, “Radio frequency identification (RFID) based corrosion monitoring sensors Part 1 – Component selection and testing,” *Corrosion Engineering, Science and Technology*, vol. 50, no. 1, pp. 63–71, Feb. 2015.
- [192] Y. L. He, S. McLaughlin, J. S. H. Lo, C. Shi, J. Lenos, and A. Vincelli, “Radio frequency identification (RFID) based corrosion monitoring sensors Part 2 – Application and testing of coating materials,” *Corrosion Engineering, Science and Technology*, vol. 49, no. 8, pp. 695–704, Dec. 2014.
- [193] A. I. Sunny, G. Y. Tian, J. Zhang, and M. Pal, “Low frequency (LF) RFID sensors and selective transient feature extraction for corrosion characterisation,” *Sensors and Actuators A: Physical*, vol. 241, pp. 34–43, Apr. 2016.
- [194] H. Zhang, R. Yang, Y. He, G. Y. Tian, L. Xu, and R. Wu, “Identification and characterisation of steel corrosion using passive high frequency RFID sensors,” *Measurement*, vol. 92, pp. 421–427, Oct. 2016.
- [195] J. Zhang and G. Y. Tian, “UHF RFID Tag Antenna-Based Sensing for Corrosion Detection and Characterization Using Principal Component Analysis,” *IEEE Transactions on Antennas and Propagation*, vol. 64, no. 10, pp. 4405–4414, Oct. 2016.
- [196] A. Zhao, J. Zhang, and G. Y. Tian, “Miniaturization of UHF RFID Tag Antenna Sensors for Corrosion Characterization,” *IEEE Sensors Journal*, vol. 17, no. 23, pp. 7908–7916, Dec. 2017.
- [197] A. I. Sunny, J. Zhang, G. Y. Tian, C. Tang, W. Rafique, A. Zhao, and M. Fan, “Temperature Independent Defect Monitoring Using Passive Wireless RFID Sensing System,” *IEEE Sensors Journal*, vol. 19, no. 4, pp. 1525–1532, Feb. 2019.
- [198] R. R. (Richard R. Fletcher, “Low-cost electromagnetic tagging: design and implementation,” Thesis, Massachusetts Institute of Technology, 2002.

- [199] Mi. G. Pettus, “RFID system utilizing parametric reflective technology,” 21-Jun-2005.
- [200] M. Garbati, E. Perret, and R. Siragusa, *Chipless RFID Reader Design for Ultra-Wideband Technology: Design, Realization and Characterization*. Elsevier, 2018.
- [201] S. Preradovic and N. C. Karmakar, “Introduction,” in *Multiresonator-Based Chipless RFID*, Springer, New York, NY, 2012, pp. 1–8.
- [202] O. Rance, E. Perret, R. Siragusa, and P. Lemaitre-Auger, *RCS Synthesis for Chipless RFID: Theory and Design*. Elsevier Science, 2017.
- [203] T. Athauda and N. Karmakar, “Chipped Versus Chipless RF Identification: A Comprehensive Review,” *IEEE Microwave Magazine*, vol. 20, no. 9, pp. 47–57, Sep. 2019.
- [204] N. C. Karmakar, “Tag, You’re It Radar Cross Section of Chipless RFID Tags,” *IEEE Microwave Magazine*, vol. 17, no. 7, pp. 64–74, Jul. 2016.
- [205] C. Herrojo, M. Moras, F. Paredes, A. Núñez, E. Ramon, J. Mata-Contreras, and F. Martín, “Very Low-Cost 80-Bit Chipless-RFID Tags Inkjet Printed on Ordinary Paper,” *Technologies*, vol. 6, no. 2, p. 52, Jun. 2018.
- [206] R. Rezaiesarlak and M. Manteghi, “A Space–Time–Frequency Anticollision Algorithm for Identifying Chipless RFID Tags,” *IEEE Transactions on Antennas and Propagation*, vol. 62, no. 3, pp. 1425–1432, Mar. 2014.
- [207] V. P. Plessky and L. M. Reindl, “Review on SAW RFID tags,” *IEEE Transactions on Ultrasonics, Ferroelectrics, and Frequency Control*, vol. 57, no. 3, pp. 654–668, Mar. 2010.
- [208] S. Preradovic, I. Balbin, N. C. Karmakar, and G. F. Swiegers, “Multiresonator-Based Chipless RFID System for Low-Cost Item Tracking,” *IEEE Transactions on Microwave Theory and Techniques*, vol. 57, no. 5, pp. 1411–1419, May 2009.
- [209] C. Herrojo, J. Mata-Contreras, A. Núñez, F. Paredes, E. Ramon, and F. Martín, “Near-Field Chipless-RFID System With High Data Capacity for Security and Authentication Applications,” *IEEE Transactions on Microwave Theory and Techniques*, vol. 65, no. 12, pp. 5298–5308, Dec. 2017.
- [210] Lu Zhang, S. Rodriguez, H. Tenhunen, and Li-Rong Zheng, “An innovative fully printable RFID technology based on high speed time-domain reflections,” in *Conference on High Density Microsystem Design and Packaging and Component Failure Analysis, 2006. HDP’06.*, 2006, pp. 166–170.
- [211] R. Rezaiesarlak and M. Manteghi, “Complex-Natural-Resonance-Based Design of Chipless RFID Tag for High-Density Data,” *IEEE Transactions on Antennas and Propagation*, vol. 62, no. 2, pp. 898–904, Feb. 2014.
- [212] O. Rance, R. Siragusa, P. Lemaitre-Auger, and E. Perret, “Toward RCS Magnitude Level Coding for Chipless RFID,” *IEEE Transactions on Microwave Theory and Techniques*, vol. 64, no. 7, pp. 2315–2325, Jul. 2016.
- [213] C. S. Hartmann, “A global SAW ID tag with large data capacity,” in *2002 IEEE Ultrasonics Symposium, 2002. Proceedings.*, 2002, vol. 1, pp. 65–69 vol.1.
- [214] M. Forouzandeh and N. C. Karmakar, “Chipless RFID tags and sensors: a review on time-domain techniques,” *Wireless Power Transfer*, vol. 2, no. 2, pp. 62–77, Sep. 2015.
- [215] C. Herrojo, M. Moras, F. Paredes, A. Nunez, J. Mata-Contreras, E. Ramon, and F. Martin, “Time-Domain-Signature Chipless RFID Tags: Near-Field Chipless-RFID

- Systems With High Data Capacity,” *IEEE Microwave Magazine*, vol. 20, no. 12, pp. 87–101, Dec. 2019.
- [216] J. Alam, M. Khaliel, A. Fawky, A. El-Awamry, and T. Kaiser, “Frequency-Coded Chipless RFID Tags: Notch Model, Detection, Angular Orientation, and Coverage Measurements,” *Sensors*, vol. 20, no. 7, p. 1843, Jan. 2020.
- [217] A. Vena, E. Perret, and S. Tedjini, *Chipless RFID based on RF Encoding Particle: Realization, Coding and Reading System*. Elsevier, 2016.
- [218] F. Babaeian and N. C. Karmakar, “Hybrid Chipless RFID Tags- A Pathway to EPC Global Standard,” *IEEE Access*, vol. 6, pp. 67415–67426, 2018.
- [219] A. Vena, E. Perret, and S. Tedjini, “Chipless RFID Tag Using Hybrid Coding Technique,” *IEEE Transactions on Microwave Theory and Techniques*, vol. 59, no. 12, pp. 3356–3364, Dec. 2011.
- [220] A. Vena, A. A. Babar, L. Sydänheimo, M. M. Tentzeris, and L. Ukkonen, “A Novel Near-Transparent ASK-Reconfigurable Inkjet-Printed Chipless RFID Tag,” *IEEE Antennas and Wireless Propagation Letters*, vol. 12, pp. 753–756, 2013.
- [221] V. Mulloni and M. Donelli, “Chipless RFID Sensors for the Internet of Things: Challenges and Opportunities,” *Sensors*, vol. 20, no. 7, p. 2135, Jan. 2020.
- [222] K. M. Gee, P. Anandarajah, D. Collins, and M. Gee, “A Review of Chipless Remote Sensing Solutions Based on RFID Technology,” *Sensors*, vol. 19, no. 22, p. 4829, Nov. 2019.
- [223] E. M. Amin, J. K. Saha, and N. C. Karmakar, “Smart Sensing Materials for Low-Cost Chipless RFID Sensor,” *IEEE Sensors Journal*, vol. 14, no. 7, pp. 2198–2207, Jul. 2014.
- [224] J. G. D. Hester and M. M. Tentzeris, “Inkjet-Printed Flexible mm-Wave Van-Atta Reflectarrays: A Solution for Ultralong-Range Dense Multitag and Multisensing Chipless RFID Implementations for IoT Smart Skins,” *IEEE Transactions on Microwave Theory and Techniques*, vol. 64, no. 12, pp. 4763–4773, Dec. 2016.
- [225] I. Mohammad, V. Gowda, H. Zhai, and H. Huang, “Detecting crack orientation using patch antenna sensors,” *Meas. Sci. Technol.*, vol. 23, no. 1, p. 015102, Nov. 2011.
- [226] I. Mohammad and H. Huang, “Monitoring fatigue crack growth and opening using antenna sensors,” *Smart Mater. Struct.*, vol. 19, no. 5, p. 055023, Apr. 2010.
- [227] I. Mohammad and H. Huang, “An Antenna Sensor for Crack Detection and Monitoring,” *Advances in Structural Engineering*, vol. 14, no. 1, pp. 47–53, Feb. 2011.
- [228] B. S. Cook, A. Shamim, and M. M. Tentzeris, “Passive low-cost inkjet-printed smart skin sensor for structural health monitoring,” *Antennas Propagation IET Microwaves*, vol. 6, no. 14, pp. 1536–1541, Nov. 2012.
- [229] X. Xu and H. Huang, “Multiplexing passive wireless antenna sensors for multi-site crack detection and monitoring,” *Smart Mater. Struct.*, vol. 21, no. 1, p. 015004, Dec. 2011.
- [230] P. Kalansuriya, R. Bhattacharyya, S. Sarma, and N. Karmakar, “Towards chipless RFID-based sensing for pervasive surface crack detection,” in *2012 IEEE International Conference on RFID-Technologies and Applications (RFID-TA)*, 2012, pp. 46–51.
- [231] S. Dey, P. Kalansuriya, and N. C. Karmakar, “Chipless RFID based high resolution crack sensing through SWB technology,” in *2014 IEEE International Microwave and RF Conference (IMaRC)*, 2014, pp. 330–333.

- [232] C. Cho, X. Yi, D. Li, Y. Wang, and M. M. Tentzeris, “Passive Wireless Frequency Doubling Antenna Sensor for Strain and Crack Sensing,” *IEEE Sensors Journal*, vol. 16, no. 14, pp. 5725–5733, Jul. 2016.
- [233] L. Ke, Z. Liu, and H. Yu, “Characterization of a Patch Antenna Sensor’s Resonant Frequency Response in Identifying the Notch-Shaped Cracks on Metal Structure,” *Sensors*, vol. 19, no. 1, p. 110, Jan. 2019.
- [234] R. Khalifeh, M. S. Yasri, B. Lescop, F. Gallée, E. Diler, D. Thierry, and S. Rioual, “Development of Wireless and Passive Corrosion Sensors for Material Degradation Monitoring in Coastal Zones and Immersed Environment,” *IEEE Journal of Oceanic Engineering*, vol. 41, no. 4, pp. 776–782, Oct. 2016.
- [235] M. H. Zarifi, D. Sameir, and M. Daneshmand, “Wireless passive RFID sensor for pipeline integrity monitoring,” *Sensors and Actuators A: Physical*, vol. 261, pp. 24–29, Jul. 2017.
- [236] M. H. Zarifi, S. Deif, M. Abdolrazzaghi, B. Chen, D. Ramsawak, M. Amyotte, N. Vahabisani, Z. Hashisho, W. Chen, and M. Daneshmand, “A Microwave Ring Resonator Sensor for Early Detection of Breaches in Pipeline Coatings,” *IEEE Transactions on Industrial Electronics*, vol. 65, no. 2, pp. 1626–1635, Feb. 2018.
- [237] S. Deif and M. Daneshmand, “Multi-Resonant Chipless RFID Array System for Coating Defect Detection and Corrosion Prediction,” *IEEE Transactions on Industrial Electronics*, pp. 1–1, 2019.
- [238] C. A. Balanis, *Antenna Theory: Analysis and Design*. John Wiley & Sons, 2016.
- [239] A. Motevasselian and W. G. Whittow, “Miniaturization of a Circular Patch Microstrip Antenna Using an Arc Projection,” *IEEE Antennas and Wireless Propagation Letters*, vol. 16, pp. 517–520, 2017.
- [240] A. Motevasselian and W. G. Whittow, “Patch size reduction of rectangular microstrip antennas by means of a cuboid ridge,” *Antennas Propagation IET Microwaves*, vol. 9, no. 15, pp. 1727–1732, 2015.
- [241] I. Balbin and N. C. Karmakar, “Phase-Encoded Chipless RFID Transponder for Large-Scale Low-Cost Applications,” *IEEE Microwave and Wireless Components Letters*, vol. 19, no. 8, pp. 509–511, Aug. 2009.
- [242] P. Kalansuriya, N. C. Karmakar, and E. Viterbo, “On the Detection of Frequency-Spectra-Based Chipless RFID Using UWB Impulsed Interrogation,” *IEEE Transactions on Microwave Theory and Techniques*, vol. 60, no. 12, pp. 4187–4197, Dec. 2012.
- [243] B. A. Munk, *Frequency Selective Surfaces: Theory and Design*. John Wiley & Sons, 2005.
- [244] F. Costa, S. Genovesi, and A. Monorchio, “A Chipless RFID Based on Multiresonant High-Impedance Surfaces,” *IEEE Transactions on Microwave Theory and Techniques*, vol. 61, no. 1, pp. 146–153, Jan. 2013.
- [245] “Progress in frequency selective surface-based smart electromagnetic structures: A critical review,” *Aerospace Science and Technology*, vol. 66, pp. 216–234, Jul. 2017.
- [246] R. S. Anwar, L. Mao, and H. Ning, “Frequency Selective Surfaces: A Review,” *Applied Sciences*, vol. 8, no. 9, p. 1689, Sep. 2018.
- [247] A. Vena, E. Perret, and S. Tedjni, “A Depolarizing Chipless RFID Tag for Robust Detection and Its FCC Compliant UWB Reading System,” *IEEE Transactions on Microwave Theory and Techniques*, vol. 61, no. 8, pp. 2982–2994, Aug. 2013.

- [248] “Cayenne Radar Development Kit - Bow Tie,” *Flat Earth Online Store*. [Online]. Available: <https://store.flatearthinc.com/products/cayenne-radar-development-kit>. [Accessed: 17-Feb-2019].
- [249] A. Vena, E. Perret, and S. Tedjini, “Design of Compact and Auto-Compensated Single-Layer Chipless RFID Tag,” *IEEE Transactions on Microwave Theory and Techniques*, vol. 60, no. 9, pp. 2913–2924, Sep. 2012.
- [250] N. Karmakar, P. Kalansuriya, R. E. Azim, and R. Koswatta, “Denoising and Filtering Techniques for Chipless RFID,” in *Chipless Radio Frequency Identification Reader Signal Processing*, John Wiley & Sons, Ltd, 2016, pp. 93–110.
- [251] C. R. Farrar and K. Worden, “Damage-Sensitive Features,” *Structural Health Monitoring*, pp. 161–243, Nov. 2012.
- [252] I. T. Jolliffe and J. Cadima, “Principal component analysis: a review and recent developments,” *Philos Trans A Math Phys Eng Sci*, vol. 374, no. 2065, Apr. 2016.
- [253] L. Mujica, J. Rodellar, A. Fernández, and A. Güemes, “Q-statistic and T2-statistic PCA-based measures for damage assessment in structures,” *Structural Health Monitoring: An International Journal*, vol. 10, no. 5, pp. 539–553, Sep. 2011.
- [254] G. Chandrashekar and F. Sahin, “A survey on feature selection methods,” *Computers & Electrical Engineering*, vol. 40, no. 1, pp. 16–28, Jan. 2014.
- [255] U. Stańczyk and L. C. Jain, “Feature Selection for Data and Pattern Recognition: An Introduction,” in *Feature Selection for Data and Pattern Recognition*, Springer, Berlin, Heidelberg, 2015, pp. 1–7.
- [256] R.-T. Wu and M. R. Jahanshahi, “Data fusion approaches for structural health monitoring and system identification: Past, present, and future,” *Structural Health Monitoring*, vol. 19, no. 2, pp. 552–586, Mar. 2020.
- [257] C. Kralovec and M. Schagerl, “Review of Structural Health Monitoring Methods Regarding a Multi-Sensor Approach for Damage Assessment of Metal and Composite Structures,” *Sensors*, vol. 20, no. 3, p. 826, Jan. 2020.
- [258] A. Daliri, A. Galehdar, W. S. Rowe, K. Ghorbani, and S. John, “Utilising microstrip patch antenna strain sensors for structural health monitoring,” *Journal of Intelligent Material Systems and Structures*, vol. 23, no. 2, pp. 169–182, Jan. 2012.
- [259] J. Havlicek, M. Polivka, M. Svanda, and J. Machac, “Capacitively loaded dipoles for chipless RFID transponder,” in *2016 26th International Conference Radioelektronika (RADIOELEKTRONIKA)*, 2016, pp. 446–449.
- [260] K. Song and P. Mazumder, “Design of Highly Selective Metamaterials for Sensing Platforms,” *IEEE Sensors Journal*, vol. 13, no. 9, pp. 3377–3385, Sep. 2013.
- [261] M. I. R. Shishir, S. Mun, H.-C. Kim, J. W. Kim, and J. Kim, “Frequency-selective surface-based chipless passive RFID sensor for detecting damage location,” *Structural Control and Health Monitoring*, vol. 24, no. 12, p. e2028, 2017.
- [262] S. N. Azemi, F. H. Wan Mustaffa, M. F. Jamlos, A. A. Al-Hadi, and P. J. Soh, “Frequency Selective Surface for Structural Health Monitoring,” *IOP Conference Series: Materials Science and Engineering*, vol. 318, p. 012033, Mar. 2018.
- [263] A. Lázaro, R. Villarino, F. Costa, S. Genovesi, A. Gentile, L. Buoncristiani, and D. Girbau, “Chipless Dielectric Constant Sensor for Structural Health Testing,” *IEEE Sensors Journal*, vol. 18, no. 13, pp. 5576–5585, Jul. 2018.

- [264] F. Costa, A. Gentile, S. Genovesi, L. Buoncristiani, A. Lazaro, R. Villarino, and D. Girbau, "A Depolarizing Chipless RF Label for Dielectric Permittivity Sensing," *IEEE Microwave and Wireless Components Letters*, vol. 28, no. 5, pp. 371–373, May 2018.
- [265] F. Costa, S. Genovesi, and A. Monorchio, "Chipless RFIDs for Metallic Objects by Using Cross Polarization Encoding," *IEEE Transactions on Antennas and Propagation*, vol. 62, no. 8, pp. 4402–4407, Aug. 2014.
- [266] N. N. Qaddoumi, W. M. Saleh, and M. Abou-Khousa, "Innovative Near-Field Microwave Nondestructive Testing of Corroded Metallic Structures Utilizing Open-Ended Rectangular Waveguide Probes," *IEEE Transactions on Instrumentation and Measurement*, vol. 56, no. 5, pp. 1961–1966, Oct. 2007.
- [267] P. Bassach, G. Quintana, I. Ferrer, and J. Ciurana, "Studying the relation between corrosion and surface roughness," *AIP Conference Proceedings*, vol. 1431, no. 1, pp. 319–327, Apr. 2012.
- [268] F. Costa and A. Monorchio, "Closed-Form Analysis of Reflection Losses in Microstrip Reflectarray Antennas," *IEEE Transactions on Antennas and Propagation*, vol. 60, no. 10, pp. 4650–4660, Oct. 2012.
- [269] F. Costa, S. Genovesi, A. Monorchio, and G. Manara, "A Circuit-Based Model for the Interpretation of Perfect Metamaterial Absorbers," *IEEE Transactions on Antennas and Propagation*, vol. 61, no. 3, pp. 1201–1209, Mar. 2013.
- [270] W. Elmenreich, "Fusion of Continuous-valued Sensor Measurements using Confidence-weighted Averaging," *Journal of Vibration and Control*, vol. 13, no. 9–10, pp. 1303–1312, Sep. 2007.
- [271] G. Yang, G. Y. Tian, P. W. Que, and Y. Li, "Data fusion algorithm for pulsed eddy current detection," *IET Science, Measurement Technology*, vol. 1, no. 6, pp. 312–316, Nov. 2007.
- [272] C. Zhang, Z.-Q. Li, X. Yang, Z. Chen, and Z. Wang, "Controlling third harmonic generation with gammadion-shaped chiral metamaterials," *AIP Advances*, vol. 6, no. 12, p. 125014, Dec. 2016.
- [273] R. Zhao, L. Zhang, J. Zhou, Th. Koschny, and C. M. Soukoulis, "Conjugated gammadion chiral metamaterial with uniaxial optical activity and negative refractive index," *Phys. Rev. B*, vol. 83, no. 3, p. 035105, Jan. 2011.
- [274] M. Sonkki, D. Sánchez-Escuderos, V. Hovinen, E. T. Salonen, and M. Ferrando-Bataller, "Wideband Dual-Polarized Cross-Shaped Vivaldi Antenna," *IEEE Transactions on Antennas and Propagation*, vol. 63, no. 6, pp. 2813–2819, Jun. 2015.
- [275] H. Zhang, Y. He, B. Gao, G. Y. Tian, L. Xu, and R. Wu, "Evaluation of Atmospheric Corrosion on Coated Steel Using K-Band Sweep Frequency Microwave Imaging," *IEEE Sensors Journal*, vol. 16, no. 9, pp. 3025–3033, May 2016.
- [276] H. Zhang, "Radio Frequency Non-destructive Testing and Evaluation of Defects under Insulation," Ph.D. thesis, Newcastle University, Newcastle upon Tyne, UK, 2014.
- [277] M. Khaliel, A. El-Awamry, A. Fawky, and T. Kaiser, "Long reading range for the frequency coded Chipless RFID system based on reflectarray antennas," *International Journal of Microwave and Wireless Technologies*, vol. 10, no. 2, pp. 187–195, Mar. 2018.
- [278] M. A. Islam and N. C. Karmakar, "Compact Printable Chipless RFID Systems," *IEEE Transactions on Microwave Theory and Techniques*, vol. 63, no. 11, pp. 3785–3793, Nov. 2015.

- [279] S. Shokralla, J. E. Morelli, and T. W. Krause, "Principal Components Analysis of Multifrequency Eddy Current Data Used to Measure Pressure Tube to Calandria Tube Gap," *IEEE Sensors Journal*, vol. 16, no. 9, pp. 3147–3154, May 2016.
- [280] M. Manekiya, M. Donelli, A. Kumar, and S. K. Menon, "A Novel Detection Technique for a Chipless RFID System Using Quantile Regression," *Electronics*, vol. 7, no. 12, p. 409, Dec. 2018.
- [281] M. Alamin, G. Y. Tian, A. Andrews, and P. Jackson, "Principal Component Analysis of Pulsed Eddy Current Response From Corrosion in Mild Steel," *IEEE Sensors Journal*, vol. 12, no. 8, pp. 2548–2553, Aug. 2012.
- [282] F. Costa, S. Genovesi, and A. Monorchio, "Reading chipless RFID located on metallic platforms by using cross-polar scattering," in *2014 XXXIth URSI General Assembly and Scientific Symposium (URSI GASS)*, Beijing, China, 2014, pp. 1–4.
- [283] M. Forouzandeh and N. Karmakar, "Self-Interference Cancellation in Frequency-Domain Chipless RFID Readers," *IEEE Transactions on Microwave Theory and Techniques*, pp. 1–16, 2019.
- [284] A. Daliri, A. Galehdar, W. S. T. Rowe, S. John, C. H. Wang, and K. Ghorbani, "Quality Factor Effect on the Wireless Range of Microstrip Patch Antenna Strain Sensors," *Sensors (Basel)*, vol. 14, no. 1, pp. 595–605, Jan. 2014.
- [285] "Principal component analysis of raw data - MATLAB pca - MathWorks United Kingdom." [Online]. Available: <https://uk.mathworks.com/help/stats/pca.html>. [Accessed: 15-Dec-2020].
- [286] M. Garbati, R. Siragusa, E. Perret, and C. Halopé, "Impact of an IR-UWB Reading Approach on Chipless RFID Tag," *IEEE Microwave and Wireless Components Letters*, vol. 27, no. 7, pp. 678–680, Jul. 2017.
- [287] J. Aliasgari, M. Forouzandeh, and N. Karmakar, "Chipless RFID Readers for Frequency-Coded Tags: Time-Domain or Frequency-Domain?," *IEEE Journal of Radio Frequency Identification*, vol. 4, no. 2, pp. 146–158, Jun. 2020.
- [288] L. Boggioni, L. Monti, S. Terranova, F. Costa, S. Genovesi, and G. Manara, "Low-Cost Portable Reader for Frequency Domain Chipless Tags: Architecture and Experimental Results on Depolarizing Tags," *Electronics*, vol. 8, no. 1, p. 35, Jan. 2019.
- [289] S. Nappi and G. Marrocco, "Space-Filling Electromagnetic Skins for the Wireless Monitoring of Surface Defects," *IEEE Sensors Journal*, vol. 19, no. 23, pp. 11535–11543, Dec. 2019.
- [290] P. Yu, L. V. Besteiro, Y. Huang, J. Wu, L. Fu, H. H. Tan, C. Jagadish, G. P. Wiederrecht, A. O. Govorov, and Z. Wang, "Broadband Metamaterial Absorbers," *Advanced Optical Materials*, vol. 7, no. 3, p. 1800995, Feb. 2019.
- [291] A. Bandyopadhyay and B. Heer, "Additive manufacturing of multi-material structures," *Materials Science and Engineering: R: Reports*, vol. 129, pp. 1–16, Jul. 2018.
- [292] Y. Xu, X. Wu, X. Guo, B. Kong, M. Zhang, X. Qian, S. Mi, and W. Sun, "The Boom in 3D-Printed Sensor Technology," *Sensors*, vol. 17, no. 5, p. 1166, May 2017.
- [293] A. Kamyshny and S. Magdassi, "Conductive Nanomaterials for Printed Electronics," *Small*, vol. 10, no. 17, pp. 3515–3535, Sep. 2014.
- [294] R. Singh, E. Singh, and H. S. Nalwa, "Inkjet printed nanomaterial based flexible radio frequency identification (RFID) tag sensors for the internet of nano things," *RSC Adv.*, vol. 7, no. 77, pp. 48597–48630, Oct. 2017.

- [295] I. T. Garces and C. Ayranci, “A view into additive manufactured electro-active reinforced smart composite structures,” *Manufacturing Letters*, vol. 16, pp. 1–5, Apr. 2018.
- [296] M. Roy, P. Tran, T. Dickens, and A. Schrand, “Composite Reinforcement Architectures: A Review of Field-Assisted Additive Manufacturing for Polymers,” *Journal of Composites Science*, vol. 4, no. 1, p. 1, Mar. 2020.
- [297] D. Comite, S. K. Podilchak, P. Baccarelli, P. Burghignoli, A. Galli, A. P. Freundorfer, and Y. M. M. Antar, “Analysis and Design of a Compact Leaky-Wave Antenna for Wide-Band Broadside Radiation,” *Sci Rep*, vol. 8, no. 1, pp. 1–14, Dec. 2018.
- [298] J. R. Reis, M. Vala, and R. F. S. Caldeirinha, “Review Paper on Transmitarray Antennas,” *IEEE Access*, vol. 7, pp. 94171–94188, 2019.
- [299] S. Mukherjee, Z. Su, L. Udpa, S. Udpa, and A. Tamburrino, “Enhancement of Microwave Imaging Using a Metamaterial Lens,” *IEEE Sensors Journal*, vol. 19, no. 13, pp. 4962–4971, Jul. 2019.
- [300] M. D. Buhari, G. Y. Tian, and R. Tiwari, “Microwave-Based SAR Technique for Pipeline Inspection Using Autofocus Range-Doppler Algorithm,” *IEEE Sensors Journal*, vol. 19, no. 5, pp. 1777–1787, Mar. 2019.
- [301] T. Addabbo, A. Fort, M. Mugnaini, E. Panzardi, A. Pozzebon, and V. Vignoli, “A city-scale IoT architecture for monumental structures monitoring,” *Measurement*, vol. 131, pp. 349–357, Jan. 2019.
- [302] F. Lamonaca, C. Scuro, D. Grimaldi, R. S. Olivito, P. F. Sciammarella, and D. L. Carnì, “A layered IoT-based architecture for a distributed structural health monitoring system System,” *ACTA IMEKO*, vol. 8, no. 2, pp. 45–52, Jun. 2019.
- [303] S. Malik, R. Rouf, K. Mazur, and A. Kontsos, “The Industry Internet of Things (IIoT) as a Methodology for Autonomous Diagnostics in Aerospace Structural Health Monitoring,” *Aerospace*, vol. 7, no. 5, p. 64, May 2020.
- [304] A. M. D. Oliveira, M. B. Perotoni, S. T. Kofuji, and J. F. Justo, “A Palm Tree Antipodal Vivaldi Antenna With Exponential Slot Edge for Improved Radiation Pattern,” *IEEE Antennas and Wireless Propagation Letters*, vol. 14, pp. 1334–1337, 2015.

Appendix A: The Dual-polarized Broadband Vivaldi Antennas Used in Chapter 5

This appendix shows the design and simulated performance parameters of the dual-polarized broadband Vivaldi antennas used for the chipless RFID sensor reader in Chapter 5. The antenna design, including the dimensions in mm, is exhibited in Figure A.1. The dual-polarized design integrates two identical Vivaldi antennas oriented orthogonally, i.e., 90° different, one to another. The antennas were designed using Rogers RO-3035 laminates with a dielectric constant of 3.5, loss tangent of 0.0015, and a thickness of 1.52 mm. A Vivaldi antenna consists of a copper layer that forms a curved opening towards the antenna radiation direction and a metal layer for feeding. The feeding is implemented with a tapered microstrip line and a radial stub, useful for tuning the desired broadband characteristics. One Vivaldi antenna is oriented vertically to operate in vertical polarization, and another antenna is oriented horizontally for horizontal polarization. The Vivaldi antennas were integrated by inserting one antenna into slits created on the other antenna [274]. A square reflector is added at the back of the antennas to enhance the gain and directivity.

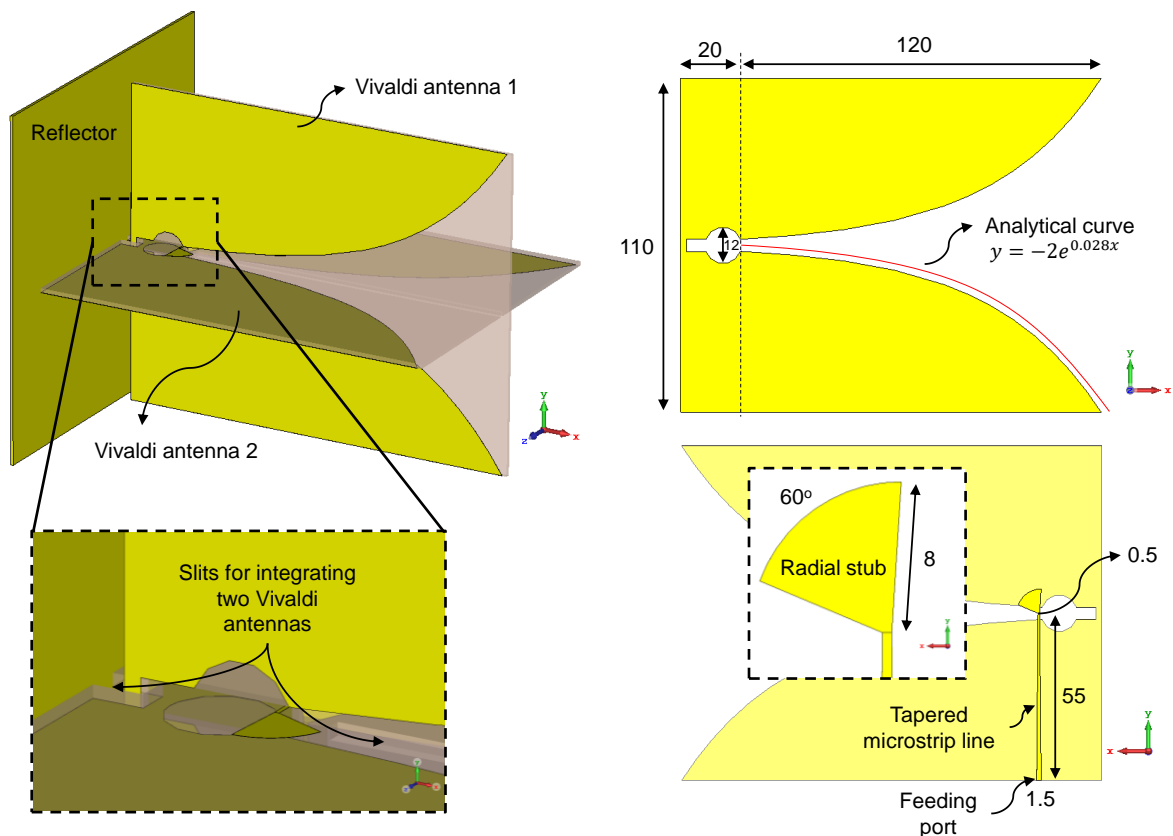


Figure A.1 Design of the dual-polarized broadband Vivaldi antennas used in Chapter 5.

Dimensions are in mm.

The dual-polarized broadband Vivaldi antennas were simulated in CST Microwave Studio. Since the Vivaldi antennas are identical, only $|S_{11}|$ of one of the Vivaldi antennas is shown in Figure A.2. The simulated $|S_{11}|$ is under -10 dB within 2-6 GHz. This confirms that the antennas have a broadband impedance matching at 50Ω over the desired bandwidth. Since there are two Vivaldi antennas combined for providing dual-polarization, there is signal leakage between the antennas. The simulated $|S_{21}|$, which is the leakage between antennas, is shown in Figure A.3 and is below -30 dB within 2-6 GHz. The lower the polarization leakage, the better. The leakage between Vivaldi antennas is adequately low, and therefore, the antennas can be used as a transceiver for a chipless RFID sensor reader.

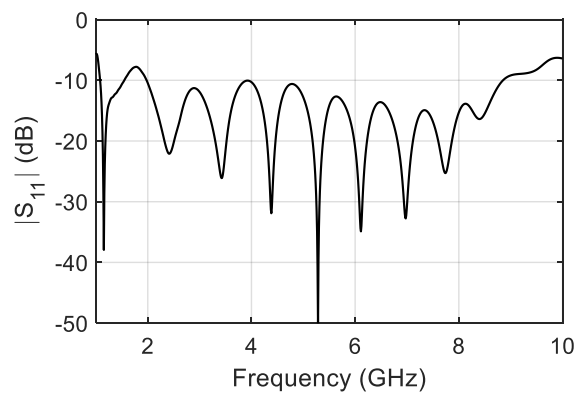


Figure A.2 Simulated $|S_{11}|$ of one of the broadband Vivaldi antenna showing that the $|S_{11}|$ is under -10 dB over 2-6 GHz.

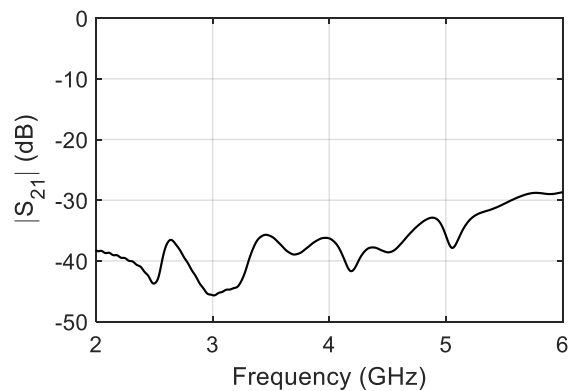


Figure A.3 Simulated $|S_{21}|$ of the dual-polarized Vivaldi antennas showing low leakage mostly under -30 dB over 2-6 GHz.

Figure A.4 shows the simulated gain of the Vivaldi antennas at the boresight, which is between 7 dBi and 11.5 dBi over 2-6 GHz. Figure A.5 illustrates the simulated 3D radiation pattern at 2

GHz, 3 GHz, 4 GHz, 5 GHz, and 6 GHz. The Vivaldi antenna radiation is unidirectional over the desired bandwidth.

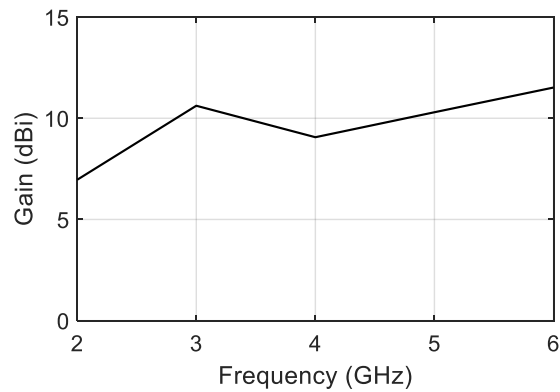


Figure A.4 Simulated gain of the Vivaldi antennas at the boresight showing the gain between 7 dBi and 11.5 dBi over 2-6 GHz.

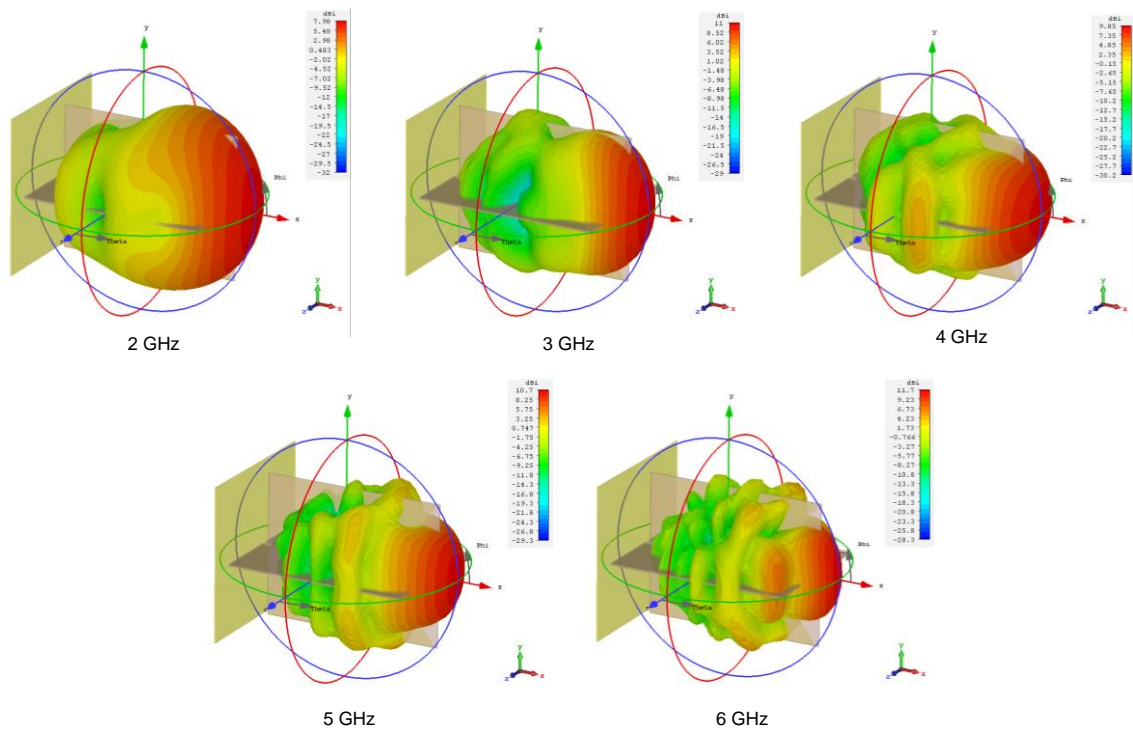


Figure A.5 Simulated 3D radiation pattern of one of the Vivaldi antennas showing unidirectional radiations at 2 GHz, 3 GHz, 4 GHz, 5 GHz, and 6 GHz.

Appendix B: The Broadband Antipodal Vivaldi Antenna Used in Chapter 6

This appendix shows the design and simulated performance parameters of the broadband antipodal Vivaldi antenna used in Chapter 6. The antenna design with the dimensions in mm is exhibited in Figure B.1. The design is similar to the conventional antipodal Vivaldi antenna, except for the additional slots on the edges that aims to enhance the directional radiation pattern of the antenna [304]. The antenna was designed using Rogers RO-3035 laminates with a dielectric constant of 3.5, loss tangent of 0.0015, and a thickness of 1.52 mm.

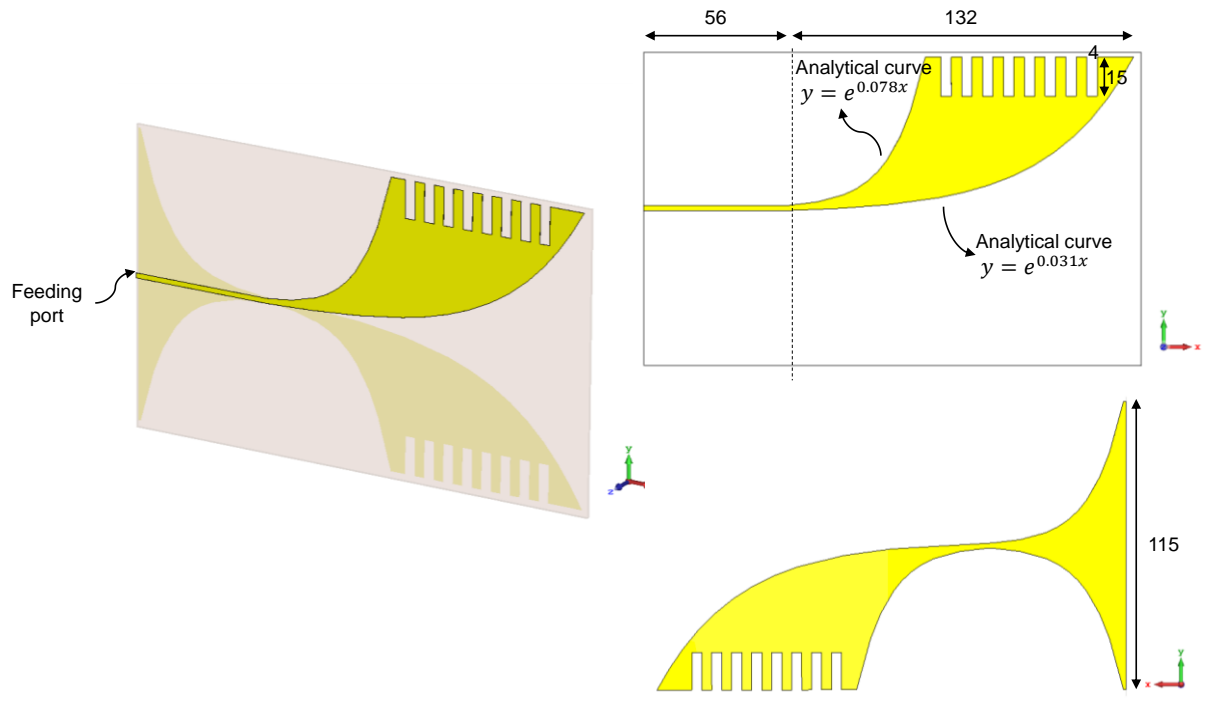


Figure B.1 Design of the broadband antipodal Vivaldi antenna. Dimensions are in mm.

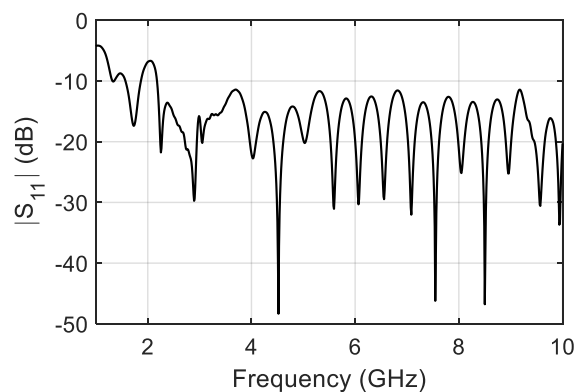


Figure B.2 Simulated $|S_{11}|$ of the broadband antipodal Vivaldi antenna showing that the $|S_{11}|$ is under -10 dB over 2-6 GHz.

Figure B.1 shows that the simulated $|S_{11}|$ is under -10 dB within 2-6 GHz. This indicates that the antenna has a broadband impedance matching at 50Ω over the desired bandwidth. The antenna is, therefore, can be used as a transmitter and receiver for a chipless RFID sensor reader. In Figure B.3, the simulated gain of the antipodal Vivaldi antenna at its boresight is between 7 dBi and 10.2 dBi over 2-6 GHz. The radiation patterns at 2, 3, 4, 5, and 6 GHz (Figure B.4) shows that the antenna radiation is unidirectional over the desired bandwidth.

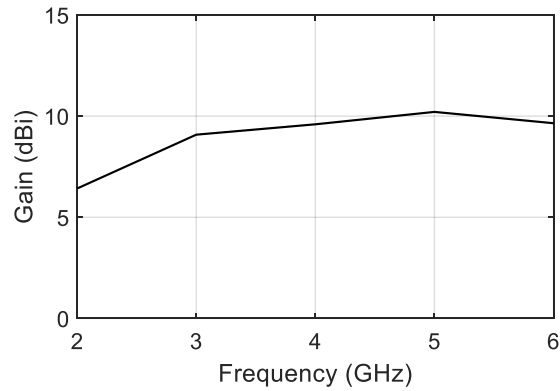


Figure B.3 Simulated gain of the antipodal Vivaldi antenna at the boresight showing the gain between 7 dBi and 10.2 dBi over 2-6 GHz.

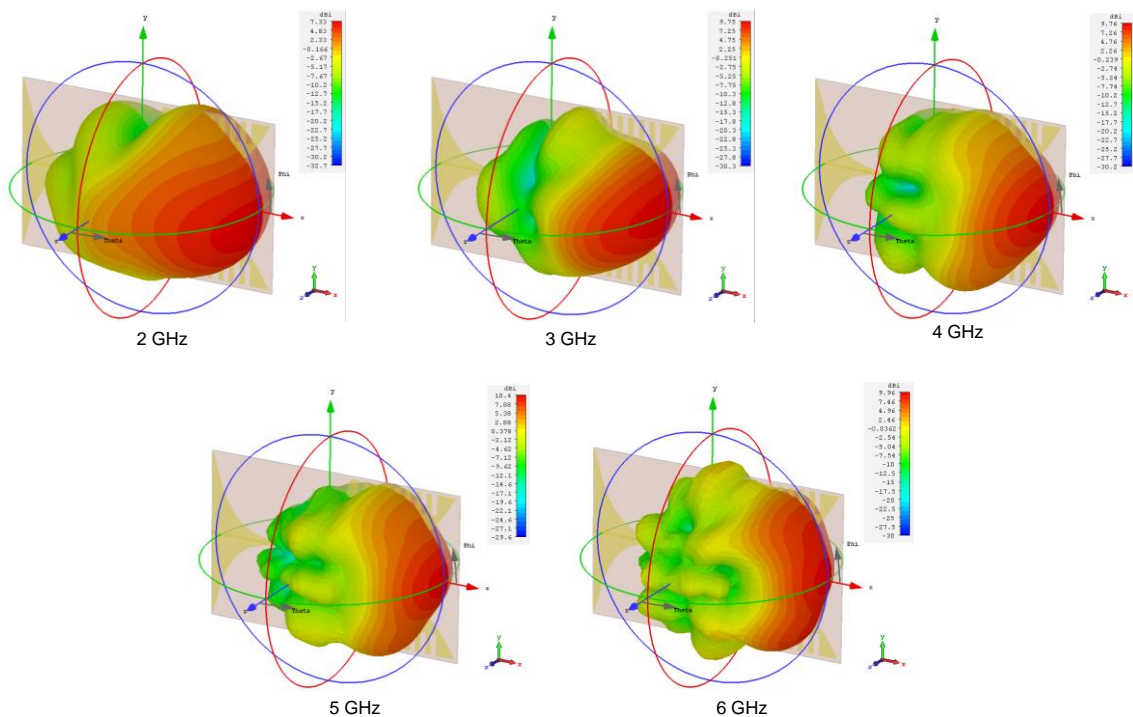


Figure B.4 Simulated 3D radiation pattern of the antipodal Vivaldi antenna showing unidirectional radiations at 2 GHz, 3 GHz, 4 GHz, 5 GHz, and 6 GHz.

Appendix C: Specifications of the Salsa Cayenne Radar Module for Portable Chipless RFID Sensor Reader Used in Chapter 6

Figure C.1 shows one-page specifications of the Salsa Cayenne radar module used for the reference to create Table 6.1 in Section 6.1.2. The Salsa Cayenne radar module was used in Chapter 6 to implement a portable chipless RFID sensor reader. The bow-tie antennas from the module were unused due to their limited gain and replaced by the antipodal Vivaldi antenna given in Appendix B.

CAYENNE

RADAR MODULE



flatearth
UWB radar solutions

The **Salsa Cayenne radar module** is a BeagleBone Black compatible cape based on the XeThru X1 (0.9 - 6.5 GHz) radar technology. The Cayenne module is suitable for ranging, tracking, and positioning applications where the environment can be demanding and penetration capability is essential. Cayenne applications include environmental monitoring, ground penetrating radar, industrial machine control and proximity sensing. Radar applications can be written for the Cayenne using the Salsa software suite. See reverse side for more Salsa details.

System Specifications:

BeagleBone Black Cape Compatible
 Input Voltage: +5VDC & +3.3VDC
 Power Consumption (Continuous Radar):
 • 70 mA @ 5V
 • 30 mA @ 3.3V (450 mW)
 • With CAN Enabled: additional 100 mW @ 3.3V
 Operating Range: -40°C to 85°C
 Dimensions: 2,3 x 2,15 inches

Radar Specifications:

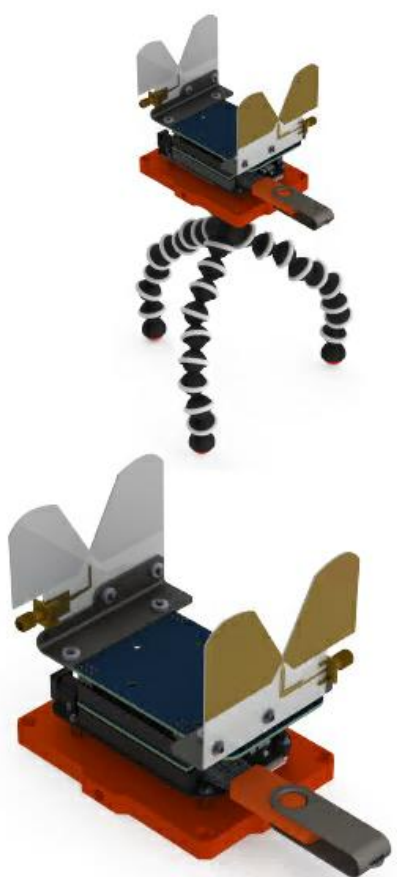
XeThru X1 Transceiver
 • IPG0 Medium-Band Pulse Generator
 Range Accuracy:
 • 4mm (~39 GS/s)
 • 8mm (~20 GS/s)
 • 4cm (~3 GS/s)
 Pulse Repetition Frequency (PRF)
 • Up to 100MHz
 Frame Size
 • 2 meter window
 • 4 meter window
 • 20 meter window
 Operating Bandwidth
 • 0,9 - 6,5 GHz (-10dB)
 Average TX Power
 • -19 dBm
 Integrated LNA
 • NF = 2 dB (@ 6 GHz)
 • Gain = 16 dB (@ 6 GHz)

Memory:

32 KB of EEPROM
 64 KB of Flash

Physical Interfaces:

1 CAN Bus
 1 I²C Bus
 4 User controllable LEDs
 2 x 46-pin Expansion headers (BBB pin-out)
 1 Temp Sensor (± 1 degree)





UWB Radar Solutions

985 Technology Blvd Bozeman, MT 59718
 Phone: 406.587.9520 Skype: flat.earth.01 www.flatearthinc.com

Figure C.1 Specifications of Salsa Cayenne radar module.

Appendix D: Matlab Codes for Collecting Signal Data Using the Portable Chipless RFID Sensor Reader in Chapter 6

This appendix contains the Matlab code that was written for the portable reader, i.e., the Salsa Cayenne radar module, used in Chapter 6. The code requires prior installations of the BeagleBoneBlack (BBB) driver and the SalsaLab Matlab toolbox for interfacing. This Matlab code is to display and record the received signals into the Matlab workspace, which later can be saved as “.mat” files.

```
%%Create the radar object
radar = radarWrapper('192.168.7.2');           %USB Cable
% radar = radarWrapper('192.168.7.2')       %Force a software update
% radar = radarWrapper('192.168.0.198');    %Ethernet IP Address example
% radar = radarWrapper('192.168.10.7');     %Ethernet IP Address example

%% Get a list of the connected modules
modules = radar.ConnectedModules;

%% Open a connection to the radar module
radar.Open(modules{1});

% radar.getEnumItems('Gain')

%% Calibrate the radar module
tic
result = radar.ExecuteAction('MeasureAll');
toc

%% Set the TX voltage on the Ancho Module
% radar.SetVoltage(1.1);

%% Get some register values
IterationsDefaultValue = radar.Item('Iterations');
offsetdistance = radar.Item('OffsetDistanceFromReference');
samplers = radar.Item('SamplersPerFrame');

%% Get the CDF
% cdf = radar.getCDF();

%% Set some register values
% radar.TryUpdateChip('SampleDelayToReference',2.9e-9);
radar.TryUpdateChip('SampleDelayToReference',0);
radar.TryUpdateChip('Iterations','50'); %default 50
radar.TryUpdateChip('DACMin','0');
radar.TryUpdateChip('DACMax','8191'); %default 8191
radar.TryUpdateChip('DACStep','4'); %default 4
radar.TryUpdateChip('PulsesPerStep','64'); %default 16 128 %100
radar.TryUpdateChip('FrameStitch','8'); %default 1
radar.TryUpdateChip('PulseGenFineTune','2'); %2=Fast(1.5-10GHz)
%radar.TryUpdateChip('VGACfg','6');
% Check that it set the value for the iterations value by re-reading it
IterationsSetValue = radar.Item('Iterations');
%% Collect a bunch of raw frames and compute the average FPS
tic;
t1=toc;
plotTime =130;           %Run the plot for this many seconds
fpsFrames = 0;          %Number of frames collected in the time period
%settings of the radar module
VoltRange=1.04;
DACStep= 4;
DACMin= 0; %0
DACMax= 8191; %8191
PulsesPerStep=64;
FrameStitch=8;
%settings of data collection
L=512;                  %Length per frame
N=2^nextpow2(L*FrameStitch);
Fs=radar.Item('SamplesPerSecond'); %get measured sampling rate from dev kit

T=1/Fs;                 %sampling period
t=(0:N-1)*T;           %time range for plotting
```

```

f=Fs/2*linspace(0,1,N/2); %freq range for plotting

fmin=(30*FrameStitch)+1;
fmax=(90*FrameStitch);

rxsignal=zeros(1,N);
%Initialize data collection
n=0;
NFrame=100;
Data=zeros(length(t),NFrame);

while (1)
    fpsFrames= fpsFrames+1;
    newFrame1 = double(radar.GetFrameRaw);
    DACCount=newFrame1;
    NormalDACCount=DACCount*(DACStep/(PulsesPerStep*IterationsSetValue))+DACMin;
    Voltage=NormalDACCount*(VoltRange/(DACMax-DACMin));
    VoltDCRemoved=detrend(Voltage,'linear');
    rxsignal=VoltDCRemoved;
%apply wavelet denoising
    lev=11;
    wname='sym8';
    rxsignaldenoised = wden(rxsignal,'sqtwolog','h','mln',lev,wname);
%apply fourier transform
    Rx=fftshift(fft(rxsignal))/N;
    Rxss=2*(Rx(N/2+1:end));
    Rxdenoised=fftshift(fft(rxsignaldenoised))/N;
    Rxssdenoised=2*(Rxdenoised(N/2+1:end));
%spectrum
    ftag=f(fmin:fmax);
    tag=rxsignal;
    Tag=abs(Rxss(fmin:fmax));
    tagden=rxsignaldenoised;
    Tagden=abs(Rxssdenoised(fmin:fmax));
%Collecting Data
    n=n+1;
    Data(:,n)=tag;
%Showing the time-domain signal in real-time
    figure(1)
    plot(t,tagden,'linewidth',1.5);
    xlabel('Time (s)', 'FontSize', 16,'FontName','Helvetica','fontweight','bold');
    ylabel('Rx Voltage (V)', 'FontSize', 16,'FontName','Helvetica','fontweight','bold');
    set(gca,'FontSize',16,'FontName','Helvetica','linewidth',1);
    drawnow
%Showing the frequency-domain signal in real-time
    figure(2)
    plot(ftag,Tagden,'linewidth',1.5);
    xlabel('Frequency (GHz)', 'FontSize', 16,'FontName','Helvetica','fontweight','bold');
    ylabel('Rx Voltage (V)', 'FontSize', 16,'FontName','Helvetica','fontweight','bold');
    set(gca,'FontSize',16,'FontName','Helvetica','linewidth',1);
    xlim([2e9 6e9]);
    ylim([0 2e-3]);
    ylim([0 0.01]);
    drawnow
%
    if (toc>plotTime)
%
        break
%
    end
    if (n>NFrame)
        break
    end
end
t2=toc;
FPS_RAW = fpsFrames/(t2-t1)

%Command for saving the collected data from the workspace:
%save('file.mat','Data')

```